TECHNISCHE UNIVERSITÄT MÜNCHEN
TUM School of Natural Sciences

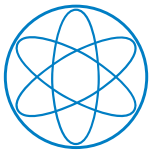

Ultrafast non-equilibrium lasing dynamics of GaAs-based nanowire lasers

Andreas Jakob Thurn, M.Sc. (hon.)

Vollständiger Abdruck der von der TUM School of Natural Sciences der Technischen Universität München zur Erlangung des akademischen Grades eines

Doktors der Naturwissenschaften
(Dr. rer. nat.)

genehmigten Dissertation.

Vorsitzender:	Prof. Dr. David Egger
Prüfer der Dissertation:	1. Prof. Jonathan J. Finley, Ph.D.
	2. Prof. Dr. Andreas Reiserer

Die Dissertation wurde am 09.09.2022 bei der Technischen Universität München eingereicht und durch die TUM School of Natural Sciences am 04.11.2022 angenommen.

Abstract

In recent years, silicon photonics has developed into a broad research field with a wide range of applications in high-speed communications, classical and quantum information processing, artificial intelligence, and metrology. This results in a demand for small, high-speed, CMOS-compatible lasers at telecommunication wavelengths that can be integrated with silicon photonic circuits. One of the promising candidates for on-chip lasers are semiconductor nanowires (NWs). Due to their quasi-one-dimensional geometry, they enable monolithic and site-selective integration of high-quality, direct-gap semiconductors on silicon.

Optically pumped lasing in the spectral range from the near-infrared to the telecommunication bands was demonstrated using NWs made of III-V materials such as gallium arsenide (GaAs), aluminum gallium arsenide (AlGaAs), and indium gallium arsenide. To assess their full potential for ultrafast optoelectronic devices it is crucial to understand their microscopic lasing dynamics. However, the roles played by their resonator geometry and the microscopic processes that mediate energy exchange between the photonic, electronic, and phononic systems during the lasing process are largely unexplored. With this thesis, we close this gap and provide a microscopic understanding of the ultrafast lasing dynamics of GaAs-AlGaAs core-shell NW lasers.

We first investigate their steady-state properties. Thereby, we find that these lasers are strongly affected by gain saturation due to carrier heating, leading to enhanced spontaneous emission and refractive index fluctuations as well as reduced gain-loss compensation. Due to these non-equilibrium effects, these NW lasers exhibit an unusual linewidth behavior that deviates strongly from expectations based on the Schawlow-Townes-Henry theory, but is in excellent agreement with quantum statistical simulations.

We then investigate their ultrafast dynamics and find that the strong mode confinement of GaAs-AlGaAs core-shell NW lasers leads to pronounced non-equilibrium dynamics. For pulsed excitation, these manifest as oscillations of the electron-hole plasma temperature during the lasing process. As a consequence, the output pulses of these NW lasers exhibit intensity and phase oscillations with frequencies ranging from 160 GHz to 260 GHz. These results are achieved through a combined use of femtosecond pump-probe spectroscopy and many-body laser simulation.

The key finding of the thesis is that in GaAs-AlGaAs core-shell NW lasers strong

mode confinement creates a new resonance between the electron-hole plasma temperature and the laser intensity. Taking advantage of this resonance with laser modulation schemes based on terahertz (THz) heating fields could allow direct laser modulation at previously unattainable speed. The theoretical insights of this thesis are general and apply to other nanoscale semiconductor lasers as well. For example, our findings thus illustrate a new approach to how the miniaturization of semiconductor lasers can be used to design their ultrafast dynamical properties.

Zusammenfassung

In den letzten Jahren hat sich die Silizium-Photonik zu einem breiten Forschungsfeld mit einer Vielzahl von Anwendungen in den Bereichen Hochgeschwindigkeitskommunikation, klassische und Quanteninformationsverarbeitung, künstliche Intelligenz und Metrologie entwickelt. Daraus ergibt sich ein Bedarf an kleinen, schnellen, CMOS-kompatiblen Lasern bei Telekommunikationswellenlängen, die in Silizium-Photonik-Schaltungen integriert werden können. Einer der vielversprechenden Kandidaten für On-Chip-Laser sind Halbleiter-Nanodrähte. Aufgrund ihrer quasi-eindimensionalen Geometrie ermöglichen sie die monolithische und ortsselektive Integration qualitativ hochwertiger Halbleiter mit direkter Bandlücke auf Silizium.

Optisch gepumptes Lasing im Spektralbereich vom nahen Infrarot bis zu den Telekommunikationsbändern wurde mit Nanodrähten aus III-V Materialien wie Galliumarsenid (GaAs), Aluminiumgalliumarsenid (AlGaAs) und Indiumgalliumarsenid demonstriert. Um ihr volles Potenzial für ultraschnelle optoelektronische Bauelemente beurteilen zu können, ist es entscheidend, ihre mikroskopische Laserdynamik zu verstehen. Die Auswirkungen ihrer Resonatorgeometrie und der mikroskopischen Prozesse, die den Energieaustausch zwischen den photonischen, elektronischen und phononischen Systemen während des Laserprozesses vermitteln, sind jedoch noch weitgehend unerforscht. Diese Arbeit schließt diese Lücke und schafft ein mikroskopisches Verständnis der Laserdynamik von GaAs-AlGaAs Kern-Schale Nanodrahtlasern.

Zunächst werden ihre stationären Eigenschaften untersucht. Dabei wird festgestellt, dass diese Laser aufgrund von Ladungsträgererwärmung stark von einer Verstärkungssättigung beeinflusst werden, was zu verstärkten spontanen Emissions- und Brechungsindexfluktuationen sowie einer reduzierten Verstärkungs-Verlust-Kompensation führt. Aufgrund dieser Nichtgleichgewichtseffekte weisen diese Nanodrahtlaser ein ungewöhnliches Linienbreitenverhalten auf. Dieses weicht stark von den Erwartungen basierend auf der Schawlow-Townes-Henry Theorie ab, ist aber in ausgezeichneter Übereinstimmung mit quantenstatistischen Simulationen.

Anschließend werden ihre ultraschnellen dynamischen Eigenschaften untersucht. Dabei wird festgestellt, dass der starke Modeneinschluss von GaAs-AlGaAs Kern-Schale Nanodrahtlasern zu einer ausgeprägten Nichtgleichgewichtsdynamik führt. Bei gepulster Anregung manifestiert sich diese als Oszillationen der Temperatur des Elektron-Loch-Plasmas während des Laservorgangs. Infolgedessen weisen die Ausgangspulse dieser

Nanodrahtlaser Intensitäts- und Phasenoszillationen mit Frequenzen im Bereich von 160 GHz bis 260 GHz auf. Diese Ergebnisse wurden durch den kombinierten Einsatz von Femtosekundenspektroskopie und Mehrkörper-Lasersimulation erzielt.

Das Hauptergebnis dieser Arbeit ist, dass in GaAs-AlGaAs Kern-Schale Nanodrahtlasern durch den starken Modeneinschluss eine neue Resonanz zwischen der Temperatur des Elektron-Loch-Plasmas und der Laserintensität entsteht. Die Ausnutzung dieser Resonanz mit Lasermodulationsverfahren, die auf THz-Heizfeldern basieren, könnte eine direkte Lasermodulation mit noch nie dagewesener Geschwindigkeit ermöglichen. Die theoretischen Erkenntnisse dieser Arbeit sind allgemeingültig und gelten auch für andere Halbleiterlaser im Nanomaßstab. Diese Ergebnisse zeigen somit beispielsweise einen neuen Ansatz, wie die Miniaturisierung von Halbleiterlasern genutzt werden kann, um ihre ultraschnellen dynamischen Eigenschaften zu beeinflussen.

Contents

Chapter 1

Introduction

This chapter includes material from

A. Thurn, J. Bissinger, S. Meinecke, P. Schmiedeke, S. S. Oh, W. W. Chow, K. Lüdge, G. Koblmüller and J. J. Finley, 'Self-induced ultrafast electron-hole plasma temperature oscillations in nanowire lasers'. *arXiv:2108.11784* submitted (2021)

The development of semiconductor technology in the twentieth century led to two major inventions: the transistor [1, 2] and the semiconductor laser [3, 4]. The following miniaturization of transistors gave rise to the development of integrated circuits, the foundation of modern electronics [5, 6]. Likewise, semiconductor lasers found wide application in areas such as communications, metrology, machining, and medicine [7–10].

Beginning in the 1980s, researchers increasingly recognized that the combined integration of electronics and photonics on silicon offered great potential for optical interconnects, promising better system synchronization, reduced power dissipation, and larger bandwidths [11]. Silicon is particularly suited as a platform for integrated optoelectronics due to its low cost, high material quality, compatibility with complementary metal-oxide-semiconductor (CMOS) processes, good linear and nonlinear optical properties, as well as the existing infrastructure for high density of integration and high-speed data transmission [12]. Other approaches to integrated optoelectronics include the use of lithium niobate [13], silicon nitride [14], and indium phosphide [15] as platforms, each having unique advantages and disadvantages.

Due to the potential of integrated optoelectronics based on silicon, concerted efforts have been made in recent decades to integrate optical components such as waveguides,

modulators, and photodetectors on this material platform [11, 12, 16]. As a result, silicon photonics developed into a broad research field [17] with applications in high-speed communications [18–20], classical and quantum information processing [21–23], mid-infrared and nonlinear optics [24–26], neuromorphic computing [27], artificial intelligence [28, 29], and metrology [30, 31].

However, since silicon is an indirect semiconductor and thus a very inefficient light source, all these applications are still in need of compact, efficient, high-speed, CMOS-compatible lasers operating at telecommunication wavelengths that can be directly integrated onto silicon [12]. There have been many approaches based on different integration techniques to solve this open problem, as discussed in Refs. [32–38].

One of the promising candidates for on-chip lasers that have emerged in recent years are semiconductor NWs [39–41]. These provide a unique approach to site-selectively and epitaxially integrate high-quality, direct gap semiconductors onto silicon [42–45]. Optically pumped lasing has been demonstrated at room temperature using III-V and II-VI compound semiconductors [46–48], group-II oxides [49], and group-III nitrides [50], with emission wavelengths that can be tuned from the ultraviolet to the telecommunication bands [46–58].

To assess their full potential for ultrafast optoelectronic devices, a detailed understanding of their lasing dynamics is crucial. Previous studies laid the groundwork by investigating several aspects of carrier relaxation, gain dynamics, plasmonic phenomena, and the role of lattice defects in many different material systems [59–67]. However, the microscopic mechanisms and dynamic processes that govern the NW laser dynamics on ultrafast timescales remained largely unexplored. In this context, NWs made of III-V materials such as GaAs, AlGaAs, and indium gallium arsenide are of particular interest as they emit in the near-infrared spectral range [46, 47] and allow tuning of the emission wavelength to the telecommunication bands [54, 55].

Scope of this thesis

In this work, we provide a microscopic understanding of both the ultrafast dynamics and the steady-state properties of GaAs-AlGaAs core-shell NW lasers [68]. The thesis is structured as follows:

- In Chapter 2 we discuss the fundamental properties of GaAs-AlGaAs core-shell NW lasers. We describe their physical dimensions and introduce their structural, electronic, vibrational, and optical properties. We further provide a detailed discussion of their longitudinal and transverse mode properties.

- In Chapter 3, we give an overview of the theoretical models used in this thesis. First, we introduce the two-level rate equation model. We then give a

phenomenological description of the carrier dynamics and discuss two different approaches to describe these theoretically: the relaxation rate approximation and the Boltzmann equation. Subsequently, we introduce the semiconductor Bloch and the quantum statistical laser theory.

- In Chapter 4, we summarize the experimental methods. We outline the nanowire growth, the substrate choice and the sample preparation. In addition, we provide a detailed description of all spectroscopic setups that were developed by the author.

- In Chapter 5, we discuss the continuous wave (CW) lasing characteristics of GaAs-AlGaAs core-shell NW lasers. We observe that the NW laser linewidth deviates strongly from the Schawlow-Townes-Henry theory. We find that the quantum statistical model provides an accurate microscopic description of all experimental results. This allows us to explain the unusual linewidth behavior by significant gain saturation due to carrier heating and the resulting non-equilibrium effects.

- In Chapter 6, we study the dynamics of GaAs-AlGaAs core-shell NW lasers using various experimental and theoretical approaches. We find that the strong gain saturation due to carrier heating predicts an overdamped carrier-photon resonance. However, using femtosecond pump-probe spectroscopy, we show that the NW output pulses exhibit sustained intensity oscillations with frequencies ranging from 160 GHz to 260 GHz. Through extensive many-body simulations, we explain these dynamics by self-induced electron-hole plasma temperature oscillations enabled by the strong mode confinement in NW lasers. Subsequently, we show that these non-equilibrium dynamics are accurately described by a phenomenological three-level rate equation approach that allows for dynamic competition between gain saturation and carrier cooling on picosecond timescales. We then present first experimental results of quasi-degenerate transient reflection spectroscopy performed on a single GaAs-AlGaAs core-shell NW laser.

- In Chapter 7, we conclude by summarizing our main findings from Chapters 2 to 6 and provide a brief outlook on further research enabled by the physical insights obtained in this thesis.

Chapter 2

Fundamentals of GaAs-AlGaAs core-shell nanowire lasers

Contents

This chapter includes material from

A. Thurn, J. Bissinger, S. Meinecke, P. Schmiedeke, S. S. Oh, W. W. Chow, K. Lüdge, G. Koblmüller and J. J. Finley, 'Self-induced ultrafast electron-hole plasma temperature oscillations in nanowire lasers'. *arXiv:2108.11784* submitted (2021)

In this chapter, we introduce the fundamental aspects of GaAs-AlGaAs core-shell NW lasers and explore their structural, electronic, vibrational, and optical properties. This chapter concludes with a discussion of their resonator properties, which are particularly important for laser action and dynamics throughout this thesis.

2.1 Physical dimensions

The GaAs-AlGaAs core-shell NWs studied in this thesis were grown using molecular beam epitaxy (MBE) under ultra-high vacuum conditions on silicon substrates [46, 69]. Information on the NW growth is provided later in Section 4.1. Figure 2.1 shows a sketch of their physical dimensions. The NWs have a hexagonal cross-section, a length (L) in the range of 10 µm – 16 µm, and a nominal diameter of ∼ 340 nm [46, 69]. The diameter was chosen such that the NWs allow the propagation of confined optical modes, see Section 2.6. Radially, the NWs have a core-shell structure consisting of a thick GaAs core with a radius of ∼ 165 nm [46, 69], a 5 nm thick AlGaAs shell to prevent surface recombination [46, 47, 69–75], and a 5 nm thick GaAs capping layer to prevent oxidation of the shell [46, 47, 69, 74, 75].

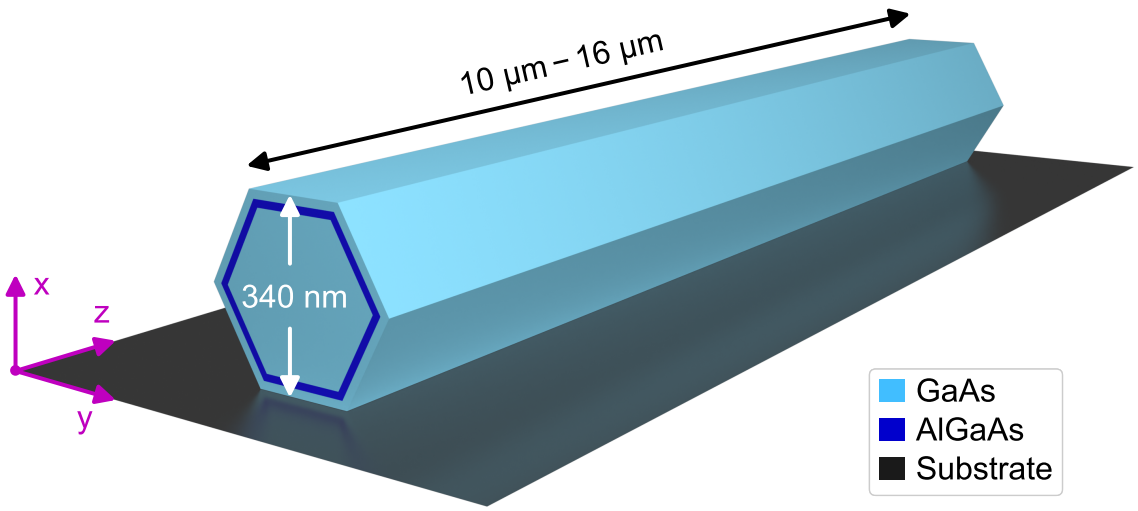

Figure 2.1 | Physical dimensions of GaAs-AlGaAs core-shell NW lasers. Sketch of a NW lying horizontally on top of a substrate. The NWs studied in this thesis typically have a length of 10 µm – 16 µm and a nominal diameter of ∼ 340 nm [46, 69]. Both the AlGaAs shell and the GaAs cap surrounding it have a thickness of 5 nm [46, 69].

2.2 Crystal structure

Both GaAs and AlGaAs are among the best studied and most widely used direct band gap semiconductor materials for optoelectronic applications [76–85]. Thus, this section will be kept very brief, as will Section 2.3 and Section 2.4.

In general, GaAs NWs exhibit a mixed crystal structure with both zinc-blende and wurtzite phases [69, 74, 86–94]. This is in contrast to bulk crystals of GaAs which naturally occur only in the zinc-blende configuration [76–83, 85], unless special efforts are made to produce a wurtzite phase [95, 96]. For the investigated NWs, the growth conditions were chosen such that they predominantly exhibit the zinc-blende phase [69, 74], as checked with reference samples using transmission electron microscopy (TEM) and Raman spectroscopy [69]. For the purposes of this work, we therefore approximate the crystal structure of these NWs as being pure zinc-blende. This simplification is later confirmed in Chapter 5 and Section 6.2 by the excellent agreement of the experimental data with theoretical models using this approximation.

To allow a threading dislocation free shell growth, the lattice constant of the $Al_{0.25}Ga_{0.75}As$ shell (a_{AlGaAs}= 0.5655 nm [69, 85]) was matched to that of the GaAs core (a_{GaAs}= 0.5654 nm [83]) via its aluminum content [69, 85]. More details on the crystal structure of the investigated GaAs-AlGaAs core-shell NWs can be found in Refs. [69, 74].

2.3 Electronic structure

The band structure of a crystal is determined by its crystal structure and the bonds between its constituent atoms [97, 98]. Both GaAs and $Al_{0.25}Ga_{0.75}As$ exhibit a direct band gap at the center of the Brillouin zone (Γ point) [83, 97, 98]. The respective band gap values for the two materials at room temperature are $\epsilon_{g0}(300\,\mathrm{K}) = 1.42\,\mathrm{eV}$ (GaAs [82]) and $\epsilon_{g0}(300\,\mathrm{K}) = 1.73\,\mathrm{eV}$ ($Al_{0.25}Ga_{0.75}As$ [82]). Since GaAs and $Al_{0.25}Ga_{0.75}As$ exhibit a type I band alignment, this band gap difference leads to a potential barrier in the radial direction that traps optically generated charges within the core region and, thus, prevents them from reaching the surface, even at room temperature [46, 47, 69–75].

Since the core region serves as the gain material of the NW laser and is therefore of primary importance, the following discussion will focus on GaAs. When GaAs is cooled, e.g. for experiments at cryogenic temperatures, the lattice constant decreases, resulting in a larger band gap [77, 79, 81–83, 85]. This relationship between the lattice temperature (T_L) and the band gap can be described by the empirical Varshni equation [79, 83, 84]

$$\epsilon_{g0}(T_L) = \epsilon_{g0}(0\,\mathrm{K}) - \frac{aT_L^2}{T_L + b}, \tag{2.1}$$

where $a = 5.405 \times 10^{-4}\,\mathrm{eV\ K^{-1}}$ [84], $b = 204\,\mathrm{K}$ [84], and $\epsilon_{g0}(0\,\mathrm{K}) = 1.5192\,\mathrm{eV}$ is the band gap at 0 K in the absence of excited electrons [99].

In GaAs all the dynamics that are relevant for laser action take place for small wave vectors $\mathbf{k}$ close to the Γ point. Within this region in k-space, GaAs has one

conduction band derived from s anti-bonding orbitals and three valence bands derived from p bonding orbitals [100]. Dipole transitions between the conduction band and all of the three valence bands are therefore allowed [100]. Figure 2.2 shows a schematic representation of this band structure. The three valence bands are labeled heavy-hole (HH), light-hole (LH) and split-off (SO) band [78]. The SO band is separated from the HH and LH bands by the spin-orbit splitting $\Delta_{\mathrm{so}} = 0.34\,\mathrm{meV}$ [78]. Since in this work excitation energies of $< 100\,\mathrm{meV}$ above the band gap were used, this band can be neglected in the following. The slight warping of the HH and LH bands due to the cubic symmetry of the zinc-blende crystal structure [97] is neglected as well, which then allows to approximate all bands as simple parabolas [100]. To describe the physics of semiconductor lasers, it is often also sufficient to consider only the conduction band and the heavy hole band [101]. This is due to the low mass of light holes compared to heavy holes [101]. This leaves us with a simple two-band model (one conduction and one valence band) in which we refer to the heavy holes simply as holes in the following. Using all these approximations, the single-particle conduction ($\epsilon_{\mathbf{ck}}$) and valence ($\epsilon_{\mathbf{vk}}$) band energies can be written as [98, 100]:

$$\epsilon_{\mathbf{ck}} = \frac{\hbar^2\mathbf{k}^2}{2m_{\mathrm{c}}} \tag{2.2}$$

and

$$\epsilon_{\mathbf{vk}} = \frac{\hbar^2\mathbf{k}^2}{2m_{\mathrm{v}}}, \tag{2.3}$$

respectively. Here, $\hbar$ is the reduced Planck constant, m_{c} the effective mass of the conduction band and m_{v} the effective mass of the valence band. For theoretical calculations it is, however, customary to move to an electron-hole description [101], where the electron ($\epsilon_{\mathbf{ek}}$) and hole ($\epsilon_{\mathbf{hk}}$) energies are given by

$$\epsilon_{\mathbf{ek}} = \epsilon_{\mathbf{ck}} = \frac{\hbar^2\mathbf{k}^2}{2m_{\mathrm{e}}}, \tag{2.4}$$

and

$$\epsilon_{\mathbf{hk}} = -\epsilon_{\mathbf{vk}} = \frac{\hbar^2\mathbf{k}^2}{2m_{\mathrm{h}}}, \tag{2.5}$$

where $m_{\mathrm{e}} = m_{\mathrm{c}} = 0.067 \cdot m_0$ and $m_{\mathrm{h}} = -m_{\mathrm{v}} = 0.377 \cdot m_0$, with m_0 being the free electron mass [84, 101]. Equation 2.5, and the relationship between m_{h} and m_{v} is only valid in the single-particle picture and will need to be adjusted once Coulomb interaction among carriers is taken into account [101].

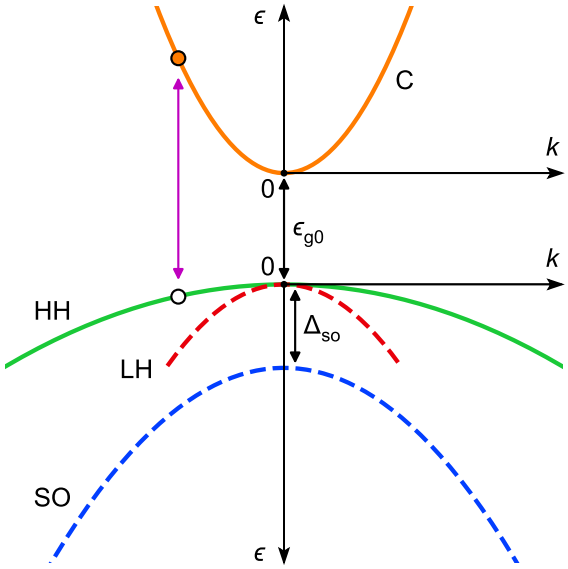

Figure 2.2 | Schematic band structure of GaAs. In the effective mass approximation the bands in the vicinity of the Γ point are approximated as parabolas [100, 101]. The three valence bands are labeled heavy-hole (HH), light-hole (LH) and split-off (SO) band [78]. Transitions (magenta) between the valence bands and the conduction band (C) are dipole allowed and vertical [100]. In a simplified two-band model of a laser only the C and the HH band is considered, while the LH and SO band is neglected (dashed lines) [101].

2.4 Vibrational properties

The periodic lattice of GaAs allows the propagation of quantized vibrational modes, called phonons [97, 102–106]. In general, there are three phonon modes for each atom in the unit cell of a three dimensional crystal [103]. GaAs has two atoms per unit cell and therefore supports six phonon modes, three acoustic and three optical [103]. There is one longitudinal (LA) and two transverse (TA) acoustic phonon modes [103, 106]. Similarly, the optical phonons can be classified into one longitudinal (LO) and two transverse (TO) modes [103, 106]. A detailed discussion of the dispersion of these six phonon branches can be found in literature [103, 107–110].

Scattering of photoexcited carriers with LO phonons is the most important carrier-phonon interaction for hot carrier distributions with temperatures $> 50\,\mathrm{K}$ [106, 111]. This allows us to neglect all other phonon modes for the purpose of this work since the investigated GaAs NW lasers typically operated at carrier temperatures above this range. A further simplification arises from the fact that in this work all the carrier dynamics take place near the band gap. For example, the wave number (q_{PN}) of an electron with an energy of 100 meV above the band gap is only about 7 % of that of an electron at the edge of the Brillouin zone [111]. It is therefore sufficient to consider only phonons with small wave vector $\mathbf{q}_{\mathrm{PN}}$ near the Γ point [111]. This considerably simplifies the discussion, as within this region the dispersion of the LO phonons is

flat [103, 107, 110], with an energy of $\epsilon_{LO} = 36.5\,\text{meV}$ [110].

Since throughout this thesis the excitation energies are $< 100\,\text{meV}$ above the band gap, photoexcited holes do not have enough energy to emit LO phonons and, thus, the carrier dynamics are dominated by the electron-LO-phonon interaction. Due to the s-like wavefunction of the electrons in the Γ valley, this interaction is only mediated via polar coupling (Fröhlich interaction) [106]. In general, both polar and non-polar coupling contributes in other valleys and for holes [106].

2.5 Optical properties

To understand the basic optical properties of a semiconductor, one has to consider several fundamental mechanisms that are involved in light-matter interaction and carrier recombination. As sketched in Fig. 2.3, these are photon absorption, spontaneous emission, stimulated emission and nonradiative recombination [9]. The energy levels depicted on the figure represent single states within the conduction and valence band.

Absorption. In Fig. 2.3a a photon is absorbed by a direct-gap semiconductor, which leads to the dipole allowed transition of an electron from the valence to the conduction band [9]. The resulting vacancy in the valence band is referred to as a hole and the overall excitation as an electron-hole pair [9].

Spontaneous emission. Even if such an electron-hole pair is not subject to any external perturbation, it can spontaneously recombine, creating a photon, see Fig. 2.3b [9]. This is a fundamental quantum mechanical effect [112] and produces a photon with a random phase, polarization, and direction [9].

Stimulated emission. If, however, a resonant photon is incident on such an electron-hole pair, as shown in Fig. 2.3c, it can stimulate recombination. This process creates a new photon that is identical to the incident photon and is thus the fundamental gain mechanism in lasers [9].

Nonradiative recombination. In nonradiative recombination an electron-hole pair recombines without generating a photon [9, 113]. Instead, the energy is transferred to the crystal lattice and thus generates heat. The two important mechanisms that typically need to be considered are sketched in Fig. 2.3d [9]. The first nonradiative mechanism is Shockley-Read-Hall (SRH) recombination, which can occur with the participation of phonons via midgap states due to crystal defects, surfaces, interfaces or impurities [114, 115]. The second nonradiative mechanism is Auger recombination [9, 113]. In this process, the energy of a recombining electron-hole pair is transferred to a third charge carrier (electron or hole) in the form of kinetic energy [9, 113]. The third charge carrier is excited to a higher energy level within the same band and then relaxes back down to the band edge by successively emitting phonons [113]. In general,

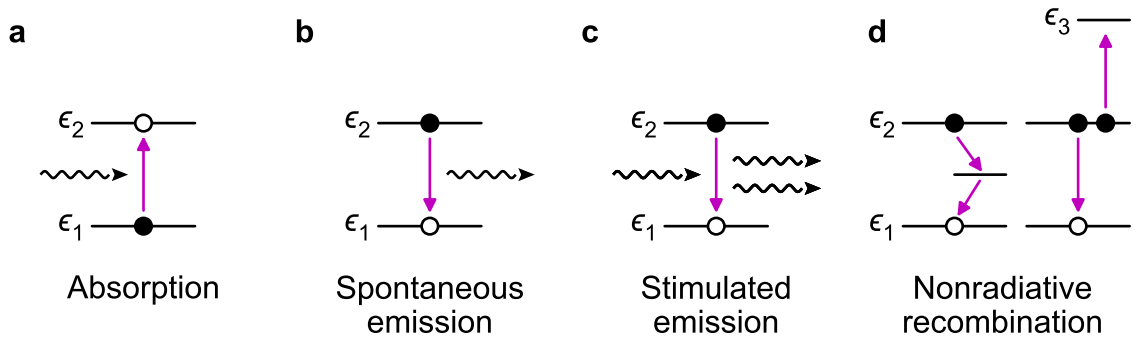

Figure 2.3 | Carrier generation and recombination. **a**, Absorption of a photon leads to the transition (magenta) of an electron from an energy state in the valence band (ϵ_1) to an energy state in the conduction band (ϵ_2). **b**, A spontaneously recombining electron-hole pair creates a photon with a random phase, polarization and propagation direction. **c**, An incident photon stimulates the recombination of an electron-hole pair. This creates a new photon with the same wavelength, phase, polarization and propagation direction as the incident photon. This is the fundamental mechanism of gain in lasers. **d**, Two important nonradiative recombination pathways. Shockley-Read-Hall (SRH) recombination via midgap states [114, 115] and Auger recombination, where the energy of a recombining electron-hole pair is transferred to a third charge carrier (e.g. electron), which thereby transitions to a higher energy state (ϵ_3) within the conduction band [9, 113]. (Adapted from [9])

the rate of the Auger mechanism strongly decreases with decreasing temperature and carrier density [9]. In GaAs, Auger recombination is typically small compared to radiative recombination for carrier densities $<$ (2 to 4) $\times\, 10^{18}\,\mathrm{cm}^{-3}$ [9]. Since in this work all experiments were performed at cryogenic temperatures on GaAs nanowires with high crystal quality and in a carrier density range from $10^{17}\,\mathrm{cm}^{-3}$ to $10^{18}\,\mathrm{cm}^{-3}$, both SRH and Auger recombination will be neglected in the following.

2.6 Resonator properties

In a laser, the lasing process starts with a spontaneously emitted photon, which is then amplified by stimulated emission in the presence of gain and optical feedback [9, 116, 117]. For this to occur, the optical field must overlap with an inverted gain material and be confined in both the longitudinal and transverse directions [9, 116]. This optical confinement is typically achieved by a cavity [9, 116–118]. In the case of a NW, the NW acts as both the cavity and the gain material, and thus naturally provides optimal confinement for the optical field [40, 41, 46, 47, 50, 51, 119–126]. This is made possible by the high refractive index contrast between the NW and the surrounding media [51, 119–123, 127]. In the following, we briefly summarize the resulting transverse and longitudinal mode structure of GaAs NW lasers. A more detailed discussion is given in Ref. [128] by Jochen Bissinger who performed the simulations presented in Section 2.6.1

and 2.6.2. Further information about the numerical implementation can be found in Ref. [129].

2.6.1 Transverse modes

The important properties that characterize a guided optical mode are the spatial profile, the effective refractive index (n_{eff}), the power reflectivity of the NW end facets (R), and the mode confinement factor (Γ) [128]. For a NW in a homogeneous surrounding medium, approximate analytical solutions for these properties can be obtained if the NW is treated as a cylinder [75, 125, 128, 130, 131]. However, if the hexagonal cross-section of the NW must be considered, or the NW is lying on a substrate, as shown in Fig. 2.1, numerical solutions are necessary [69, 128, 129, 132]. Due to the strong index guiding, the obtained solutions are independent of the specific gain [122], which means that the NW material can be modeled as being transparent [133].

In general, a NW can support several types of modes [119–122, 125]. There are transverse electric ($\mathrm{TE}_{0,\mathrm{m}}$), transverse magnetic ($\mathrm{TM}_{0,\mathrm{m}}$), and hybrid modes ($\mathrm{HE}_{\mathrm{n,m},\nu}$ and $\mathrm{EH}_{\mathrm{n,m},\nu}$) [119–122, 125], where the first index (n) describes the azimuthal symmetry, while the second index (m) describes the radial dependence of the field [120]. The hybrid modes have a twofold polarization dependency, which is described by a third index (ν = a,b) for the two possible polarization directions transverse to the NW waveguide [125, 128]. The two transverse modes are characterized by the fact that the $\mathrm{TE}_{0,\mathrm{m}}$ mode does not have a longitudinal electric field component ($E_{\mathrm{z}} = 0$), while the $\mathrm{TM}_{0,\mathrm{m}}$ does not have a longitudinal magnetic field component ($H_{\mathrm{z}} = 0$) [120, 130, 131]. For the nominal dimensions given in Chapter 2.1, GaAs NWs only support a few low order transverse modes [47, 69, 75, 128]. Figure 2.4a shows the simulated profiles of the first four guided modes ($\mathrm{TE}_{0,1}$, $\mathrm{TM}_{0,1}$, $\mathrm{HE}_{1,1,a}$ and $\mathrm{HE}_{2,1,a}$) [128]. The different mode profiles affect the properties of the individual modes and are particularly important for the design of NW lasers with radial heterostructures [52–55, 75, 134–136]. Due to its attractive properties for low-threshold, single mode lasing, the following discussion will focus on the $\mathrm{TE}_{0,1}$ mode [47, 75].

Effective refractive index

The propagation of a mode along the NW axis is described by the effective refractive index (n_{eff}), defined as

$$n_{\mathrm{eff}} = \frac{k_{\mathrm{z}}}{k_0}, \tag{2.6}$$

where k_{z} is the longitudinal component of the wave vector, and $k_0 = 2\pi/\lambda_0$ the wave number of a plane wave in vacuum, with λ_0 being the wavelength [125, 131]. Figure 2.4b shows the numerically calculated n_{eff} for all allowed guided modes of a

GaAs NW lying on a sapphire substrate as a function of $k_0 \cdot R_{NW}$ [128]. Normalized units are used since the results only depend on the ratio between R_{NW} and λ_0 [128]. To facilitate reading specific values for NW laser design, the upper x-axis shows the corresponding NW radius for a fixed wavelength of $\lambda_0 = 820\,nm$, which is approximately the emission wavelength of GaAs NW lasers [46, 47, 137]. As $k_0 \cdot R_{NW}$ increases, n_{eff} varies between the refractive index of the substrate ($n_{sapphire} = 1.76$ [138]) and the refractive index of the NW ($n_{GaAs} = 3.59$ [139]) due to the corresponding change in mode confinement [47]. When n_{eff} crosses the dotted line given by $n_{sapphire}$, the modes are no longer confined [120, 128, 130, 131]. This is called mode cut-off and, for a given wavelength, defines the smallest radius for which a mode is guided [120, 128, 130, 131]. It is also worth noting that the hybrid modes are non-degenerate, as the $HE_{n,m,a}$ modes extend more into the substrate, while the $HE_{n,m,b}$ modes extend more into the surrounding vacuum/air [40]. The simulation results shown in Fig. 2.4b were obtained using the commercial tool Lumerical MODE [128].

End facet reflectivity

When a guided mode impinges on an end facet it gets partially transmitted and reflected due to the high refractive index contrast between the NW and the surrounding medium [51, 120, 125, 126]. Estimating the reflectivity of a mode is difficult because the NW diameter is comparable to the lasing wavelength, which means that the text-book Fresnel formula cannot be applied and that diffraction at the edges must be taken into account [120]. Further complications arise from the possibility that other modes with the same azimuthal symmetry and frequency are excited upon reflection [40, 47, 120], and from the fact that real NW end facets are usually uneven [133]. In the following, the end facets are approximated as perfectly flat and perpendicular to the NW axis [125, 128, 129]. The reflectivity is determined numerically by exciting a guided mode in the NW and then calculating the ratio between the injected and reflected power into that mode [128]. More details on the simulation are provided in Ref. [129]. Figure 2.4c shows the simulated reflectivity for all allowed guided modes as a function of $k_0 \cdot R_{NW}$ [128]. In the investigated range, the hybrid modes have lower reflectivity than the transverse modes. The reflectivity of the $HE_{1,1}$ modes, for example, ranges from $R = 0.32$ to 0.4, which is comparable to the reflectivity ($R = 0.32$) of cleaved GaAs edge-emitters [9, 128]. In contrast, the transverse modes exhibit reflectivities ranging from $R = 0.42$ to 0.74. One of the requirements for a mode to achieve low threshold lasing is having a high reflectivity, see Section 3.1.2. The combination of its high reflectivity over a wide range of $k_0 \cdot R_{NW}$ and the low mode cut-off thus makes the $TE_{0,1}$ mode very attractive for low-threshold, single mode lasing [47, 128]. The simulation results shown in Fig. 2.4c were obtained using Lumerical FDTD [128].

Mode confinement factor

The confinement factor is an important parameter of a laser since it affects both its threshold [9, 119, 121] and its dynamical properties, as will be shown later in Sections 6.2 and 6.3. The confinement factor quantifies how strongly the mode interacts with the gain material and is defined as

$$\Gamma = \frac{2\varepsilon_0 c_0 n_{\text{active}} \int\int_{\text{active}} \mathrm{d}x\mathrm{d}y |\mathbf{E}|^2}{\int\int \mathrm{d}x\mathrm{d}y \, (\mathbf{E} \times \mathbf{H}^* + \mathbf{E}^* \times \mathbf{H}) \cdot \hat{z}}, \tag{2.7}$$

where ε_0 is the vacuum permittivity, c_0 the speed of light in vacuum, n_{active} the refractive index of the active region, and $\hat{z}$ the unit vector along the NW axis [119, 121, 140–142]. The vectors of the electric and magnetic fields are denoted by $\mathbf{E}$ and $\mathbf{H}$, respectively. Equation 2.7 is more general then the energy confinement factor (Γ_0) that is often used in literature and defined as the fraction of energy in the active region compared to the energy in the entire mode [119, 121]. The definition of Γ_0 applies only to the case of weak waveguiding, where wave propagation is quasi-paraxial, and implies that $\Gamma_0 < 1$ [119, 121]. In contrast, Eq. 2.7 is also valid for strong waveguiding, where mode propagation is non-paraxial [119]. The two definitions of confinement (Γ and Γ_0) are related by

$$\Gamma = \frac{n_{\text{g}}}{n_{\text{active}}} \Gamma_0 = \frac{v_{\text{ph}}}{v_{\text{g}}} \Gamma_0, \tag{2.8}$$

where $v_{\text{ph}} = c_0/n_{\text{active}}$ is the phase velocity in the active medium and n_{g} is the group index of the propagating mode, which is connected to the group velocity via $v_{\text{g}} = c_0/n_{\text{g}}$ [119]. For a mode with low v_{g} (large n_{g}) it is thus possible to achieve $\Gamma > 1$ [119, 121]. Figure 2.4d shows the simulated Γ for all allowed guided modes as a function of $k_0 \cdot R_{\text{NW}}$ [128]. The $\text{TM}_{0,1}$ and $\text{HE}_{2,1}$ modes each show a pronounced peak near their cut-off, with a maximum of $\Gamma = 1.57$ for the $\text{HE}_{2,1,a}$ mode [128]. This is in contrast to the $\text{TE}_{0,1}$ and $\text{HE}_{1,1}$ modes, where Γ is relatively constant over the entire simulation range, with an approximate value of $\Gamma = 1.2$ for the $\text{TE}_{0,1}$ mode [128]. Gain modeling shows that the $\text{TE}_{0,1}$ mode is expected to have the lowest threshold over a wide range of $k_0 \cdot R_{\text{NW}}$ [47] and thus $\Gamma = 1.2$ ($\Gamma_0 = 0.84$) will be used throughout the remainder of this work. The simulation results shown in Fig. 2.4d were obtained using COMSOL Multiphysics [128].

2.6.2 Longitudinal modes

In the longitudinal direction, the cavity acts as a Fabry–Pérot resonator with a dispersive medium [116]. The well-known condition for standing waves in such a cavity leads to a series of longitudinal modes [116], each identified by a longitudinal mode number m. The energy (ϵ_{m}) and spacing ($\Delta\epsilon$) of these longitudinal modes is described

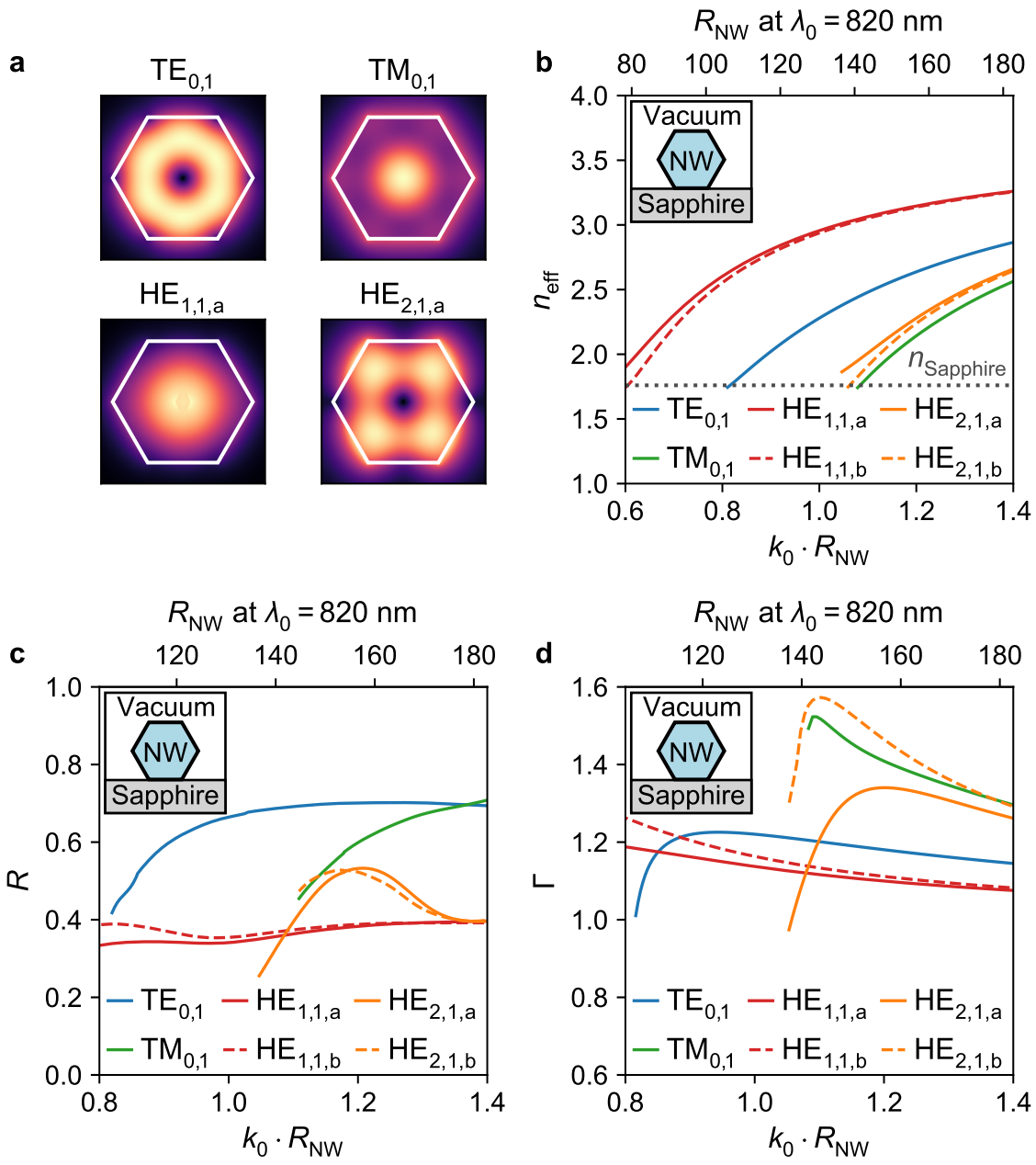

Figure 2.4 | Transverse mode characteristics. **a**, Magnitude of the electric field of the first four guided modes ($\mathrm{TE}_{0,1}$, $\mathrm{TM}_{0,1}$, $\mathrm{HE}_{1,1,a}$ and $\mathrm{HE}_{2,1,a}$). The shown mode profiles are for a NW surrounded by vacuum. **b**, Effective refractive index (n_{eff}) for all guided modes as function of $k_0 \cdot R_{\mathrm{NW}}$. The grey dotted line indicates the refractive index of the sapphire substrate. **c**,**d**, End facet reflectivity (R) and confinement factor (Γ) for each mode as a function of $k_0 \cdot R_{\mathrm{NW}}$. The simulations in **b-d** were performed for a GaAs NW lying on a sapphire substrate, as shown by the inset in each subfigure. Refractive indices of $n_{\mathrm{sapphire}} = 1.76$ [138] and $n_{\mathrm{GaAs}} = 3.59$ [139] were used for all simulations. (Adapted from [128])

by [9, 116]

$$\epsilon_{\mathrm{m}} = m\frac{\pi\hbar c_0}{L n_{\mathrm{eff}}} \tag{2.9}$$

and

$$\Delta\epsilon = \frac{\pi\hbar c_0}{L n_{\mathrm{g}}}. \tag{2.10}$$

The group index n_{g} and the effective refractive index n_{eff} are related by [9]

$$n_{\mathrm{g}} = n_{\mathrm{eff}} + \epsilon\frac{\partial n_{\mathrm{eff}}}{\partial\epsilon}. \tag{2.11}$$

2.7 Summary

In this chapter, we introduced the fundamental properties of GaAs-AlGaAs core-shell NW lasers. They have a nominal diameter of $\sim 340\,\mathrm{nm}$, a length of $10\,\mu\mathrm{m} - 16\,\mu\mathrm{m}$, and a radial heterostructure that prevents surface recombination and oxidation. The crystal structure is predominantly zinc-blende, which, combined with experimental conditions within this thesis, allows to approximate the band structure as being formed from two parabolic bands. At the Γ point, both bands are separated by a direct band gap of $\epsilon_{\mathrm{g0}}\,(0\,\mathrm{K}) = 1.5192\,\mathrm{eV}$. Radiative transitions between these bands are dipole allowed, while nonradiative recombination can be neglected. Regarding the vibrational properties, the zinc-blende crystal structure of the NWs supports six phonon modes. Of these, LO phonons provide the dominant contribution to the charge carrier dynamics via their interaction with electrons. Moreover, the physical shape of the NW allows the propagation of several confined modes, of which the $\mathrm{TE}_{0,1}$ mode is the most likely to lase. The fundamental properties presented here serve as the foundation for the laser theories discussed in the next chapter.

Chapter 3

Semiconductor laser theory

Contents

This chapter includes material from

A. Thurn, J. Bissinger, S. Meinecke, P. Schmiedeke, S. S. Oh, W. W. Chow, K. Lüdge, G. Koblmüller and J. J. Finley, 'Self-induced ultrafast electron-hole plasma temperature oscillations in nanowire lasers'. *arXiv:2108.11784* submitted (2021)

Having discussed the basic properties of GaAs NW lasers in the previous chapter, we now present theoretical models that can be used to describe lasing in such structures. The required level of complexity of these models depends on the nature of the experiment to be simulated.

Section 3.1 introduces a phenomenological two-level rate equation approach [9, 101, 117], which is widely used in literature due to its simplicity. However, its usefulness is limited once quantitative simulations are needed that can be compared to experiments.

This requires an explicit description of the carrier dynamics, for which two different approximations are discussed in Section 3.2. Microscopic laser theories include these carrier dynamics, as well as many-body effects, in a self-consistent manner and thus allow the quantitative description of lasing over a wide range of experimental conditions.

A complete semi-classical laser theory combines the semiconductor Maxwell-Bloch equations with a description of the carrier dynamics within a Boltzmann equation framework [101, 143]. However, such an approach proved to be too computationally expensive for a description of the experiments presented in Section 6.2. For the purposes of this thesis, we therefore used two complementary and less resource-intensive models.

Within the semiclassical laser theory, the carrier dynamics were simplified by a relaxation rate approximation, while keeping the full semiconductor Maxwell-Bloch equations [101, 143]. This approach allowed an efficient description of the amplitude and phase of the emitted electric field of a NW laser, which is crucial for understanding interference phenomena. This model is presented in Section 3.3 and will be referred to as the semiconductor Bloch model in the following.

In contrast, for a detailed study of the carrier dynamics and the laser linewidth, we used the quantum statistical model presented in Section 3.4 [101, 144–150]. This fully quantum mechanical approach describes the laser intensity based on quantum statistical averages of the vector potential and therefore cannot capture the phase dynamics of the emitted electric field [150]. It does, however, allow to keep the full Boltzmann equation for the treatment of the scattering dynamics with reasonable computational effort [148]. Both the semiconductor Bloch and the quantum statistical model use the same set of simulation parameters, listed in Table 5.1 and Table A.1.

In the discussion of all theoretical models, we limit ourselves to the key equations for clarity. The full derivation of these equations can be found in literature [101, 117, 143–158]. A comprehensive summary of this literature is provided in the PhD thesis of Jochen Bissinger [128]. Any required theory that is not discussed in this chapter will be introduced when needed.

3.1 Two-level rate equation model

The single-mode two-level rate equations can be derived from the wave equation for an optical field propagating inside a dielectric medium [117]. They describe the temporal evolution of the carrier number ($\mathcal{N}$), the photon number ($\mathcal{P}$) and the optical phase (ϕ). These equations are given by [9, 117]

$$\frac{d\mathcal{N}}{dt} = \frac{\eta_\mathrm{p} P}{\epsilon_\mathrm{p}} - R_\mathrm{sp} - G_\mathrm{mod}\mathcal{P}, \tag{3.1}$$

$$\frac{d\mathcal{P}}{dt} = \left[G_\mathrm{mod} - \gamma_\mathrm{ph}\right]\mathcal{P} + \beta_\mathrm{sp} R_\mathrm{sp} \tag{3.2}$$

and

$$\frac{d\phi}{dt} = -\frac{n_\mathrm{eff}}{n_\mathrm{g}}\left(\omega - \Omega\right) + \frac{1}{2}\alpha\left(G_\mathrm{mod} - \gamma_\mathrm{ph}\right). \tag{3.3}$$

Here, η_p is the absorption efficiency, P the optical excitation power, ϵ_p the photon energy of the excitation laser, R_sp the total spontaneous emission rate, G_mod the modal gain, γ_ph is the cavity decay rate, β_sp the spontaneous emission coupling factor, ω the angular lasing frequency, Ω the angular cavity-resonance frequency and α the linewidth enhancement factor [117].

3.1.1 Modal and material gain

The modal intensity gain per unit length describes how a mode is amplified as it travels through a gain material [9, 119]. The material gain per unit length, on the other hand, describes the corresponding gain for a plane wave [9, 119]. The relationship between the modal and material gain per unit length is given by [9, 119]

$$G_\mathrm{mod} = \Gamma \cdot G_\mathrm{mat} \tag{3.4}$$

and thus G_mod can be larger or smaller than G_mat, depending on the value of Γ [119]. For rate equations, it is often more convenient to work with modal gain per unit time, which follows from Eq. 3.4 as [9, 117]

$$G_\mathrm{mod} = v_\mathrm{g}\Gamma \cdot G_\mathrm{mat}. \tag{3.5}$$

In both Eq. 3.4 and Eq. 3.5, G_{mat} is usually given in units of [cm^{-1}]. It is useful to note that in literature sometimes the amplitude material gain (g_{mat}) is used instead of the intensity material gain (G_{mat}). These two definitions are related by

$$G_{\mathrm{mat}} = 2 \cdot g_{\mathrm{mat}}. \tag{3.6}$$

3.1.2 Threshold gain

The modal gain that is necessary to overcome the losses is called the threshold modal gain ($G_{\mathrm{th,mod}}$). It is customary to define it in the limiting case of no spontaneous emission [117] and thus Eq. 3.2 yields

$$G_{\mathrm{th,mod}} = \Gamma \cdot G_{\mathrm{th,mat}} = \gamma_{\mathrm{ph}}, \tag{3.7}$$

whereby the cavity decay rate is given by

$$\gamma_{\mathrm{ph}} = v_{\mathrm{g}} \cdot 2\kappa, \tag{3.8}$$

with

$$\kappa = \frac{1}{2}\left(\alpha_{\mathrm{i}} + \alpha_{\mathrm{m}}\right) \tag{3.9}$$

being the electric field amplitude loss per round-trip [117]. Here, α_{i} describes the internal losses of the passive cavity (for example due to scattering or absorption) and

$$\alpha_{\mathrm{m}} = \frac{1}{L}\ln\left(\frac{1}{R}\right) \tag{3.10}$$

the distributed mirror losses [117]. Typical values for the treshold material gain ($G_{\mathrm{th,mat}}$) of GaAs NW lasers range from $200\,\mathrm{cm}^{-1}$ to $1200\,\mathrm{cm}^{-1}$ [47, 75, 128, 133].

3.1.3 Gain approximation

For the purpose of a rate equation analysis, the carrier number dependence of the material gain at the lasing energy is often approximated with either a linear

$$G_{\mathrm{mat}}(\mathcal{N}) = a_{\mathrm{gain}}\left(\mathcal{N} - \mathcal{N}_{\mathrm{tr}}\right) \tag{3.11}$$

or logarithmic function

$$G_{\mathrm{mat}}(\mathcal{N}) = G_0 \ln\left(\frac{\mathcal{N} + \mathcal{N}_{\mathrm{s}}}{\mathcal{N}_{\mathrm{tr}} + \mathcal{N}_{\mathrm{s}}}\right), \tag{3.12}$$

where $\mathcal{N}_{\mathrm{tr}}$ is the transparency carrier number [9]. Here, the free parameters a_{gain}, G_0 and $\mathcal{N}_{\mathrm{s}}$ are used to fit Eq. 3.11 and Eq. 3.12 to precalculated values from a suitable

gain model [9, 101, 128, 133]. In general, the logarithmic approximation is valid over wider range of carrier densities compared to the linear approximation [9, 128].

3.1.4 Gain saturation

Gain saturation describes a reduction in gain due to an increase in photon number at a given carrier number [159–163]. In a real semiconductor laser, this can happen for a variety of reasons, the two most important of which are spectral hole burning and carrier heating [161]. Phenomenologically, gain saturation can be described by

$$G_{\mathrm{mod}}\left(\mathcal{N},\mathcal{P}\right) = \frac{G_{\mathrm{mod}}\left(\mathcal{N}\right)}{\sqrt{1+\mathcal{P}/\mathcal{P}_{\mathrm{sat}}}}, \tag{3.13}$$

where $\mathcal{P}_{\mathrm{sat}}$ is the saturation photon number [159, 161]. As a result of this reduction in gain, the carrier number has to increase above threshold in order to still fulfill the threshold condition given by Eq. 3.7 [9]. This behavior is observed later in Chapter 5 in experiments on GaAs-AlGaAs core-shell NW lasers subject to CW excitation. This is consistent with previous work [128, 133]. There, a rate equation simulation of similar experiments showed that typical values for $\mathcal{P}_{\mathrm{sat}}$ are in the range from 100 to 500 [128, 133]. Gain saturation is crucial for high-speed lasers as it leads to a strong damping of their modulation response [9, 117, 161, 164, 165]. Its effects on the dynamics of GaAs NW lasers will be discussed later in Section 6.1 and Section 6.3.

3.1.5 Spontaneous emission approximation

In case the carrier distributions can be described Maxwell-Boltzmann functions the total spontaneous emission rate is well approximated by a quadratic dependence on the carrier number

$$R_{\mathrm{sp}}(\mathcal{N}) = B \cdot \mathcal{N}^2, \tag{3.14}$$

where B is the bimolecular recombination coefficient [9, 113, 128, 163, 166]. However, when the carrier distributions must be described by Fermi-Dirac functions, this approximation overestimates the spontaneous emission rate [128, 133]. In this regime the spontaneous emission rate increases slower than quadratic with the carrier number and is better approximated by a linear dependence

$$R_{\mathrm{sp}}(\mathcal{N}) = \frac{\mathcal{N}}{\tau_{\mathrm{spon}}}, \tag{3.15}$$

where τ_{spon} is the spontaneous emission lifetime [128, 133]. One of the contributing reasons for this change in carrier number dependence is a reduction of the average optical matrix element as dicussed in Ref. [167]. In Ref. [128] the total spontaneous

emission rate has been calculated for a lattice temperature of $T_\mathrm{L} = 10\,\mathrm{K}$ and a carrier temperature of $T_\mathrm{c} = 55\,\mathrm{K}$ using the quantum statistical theory discussed in Chapter 3.4. Best agreement of Eq. 3.14 with the microscopic calculation in Ref. [128] is achieved for $B = 3.9\times10^{-9}\,\mathrm{cm^3\ s^{-1}}$, which is in accordance with literature values [9] and calculations using different theoretical approaches [133]. Using Eq. 3.15, best agreement is achieved for $\tau_\mathrm{spon} = 740\,\mathrm{ps}$, which is very close to the measured carrier lifetime of $\tau_\mathrm{spon} = 680\,\mathrm{ps}$ in Ref. [69].

3.1.6 Relaxation oscillation frequency

When a laser described by Eqs. 3.1 to 3.3 is abruptly switched on, its output intensity will exhibit damped periodic oscillations [9, 117]. These relaxation oscillations are a manifestation of an intrinsic resonance between $\mathcal{N}$ and $\mathcal{P}$ [9, 117]. The frequency of these relaxation oscillations is crucial for high-speed lasers as it directly influences how fast they can be modulated [9, 117, 164]. As a consequence, great efforts have been made to increase this frequency as much as possible [164, 168]. Their frequency and damping rate can be derived by taking the total differential of both Eq. 3.1 and Eq. 3.2 [117]. This yields linearized equations that can be written in matrix form

$$\begin{pmatrix} \delta\dot{\mathcal{P}} \\ \delta\dot{\mathcal{N}} \end{pmatrix} = \begin{pmatrix} -\Gamma_\mathrm{P} & G_\mathcal{N}\mathcal{P}_0 + \frac{(\partial\beta_\mathrm{sp}R_\mathrm{sp})}{\partial\mathcal{N}} \\ -G_\mathrm{mod} + G_\mathcal{P}\mathcal{P}_0 & \Gamma_\mathrm{N} \end{pmatrix} \begin{pmatrix} \delta\mathcal{P} \\ \delta\mathcal{N} \end{pmatrix}, \tag{3.16}$$

where $\delta\mathcal{P}$ is the differential photon number, $\delta\mathcal{N}$ the differential carrier number, and $\mathcal{P}_0$ the steady-state photon number with $\dot{\mathcal{P}}_0 = 0$ [117]. The damping rate of the carrier (Γ_N) and photon number (Γ_P) is given by

$$\Gamma_\mathrm{N} = \gamma_\mathrm{c} + G_\mathcal{N}\mathcal{P}_0 + \mathcal{N}_0\frac{\partial\gamma_\mathrm{c}}{\mathcal{N}} \tag{3.17}$$

and

$$\Gamma_\mathrm{P} = \frac{\beta_\mathrm{sp}R_\mathrm{sp}}{\mathcal{P}_0} - G_\mathcal{P}\mathcal{P}_0, \tag{3.18}$$

respectively, where $\mathcal{N}_0$ is the steady-state carrier number with $\dot{\mathcal{N}}_0 = 0$ [117]. Further, the differential modal gain with respect to carrier number ($G_\mathcal{N}$) and photon number ($G_\mathcal{P}$) is defined by [117]

$$G_\mathcal{N} = \frac{\partial G_\mathrm{mod}}{\partial\mathcal{N}} \tag{3.19}$$

and

$$G_\mathcal{P} = \frac{\partial G_\mathrm{mod}}{\partial\mathcal{P}}. \tag{3.20}$$

Equation 3.16 can be solved with the Ansatz of an exponentially damped oscillation

$$\begin{pmatrix} \delta\mathcal{P} \\ \delta\mathcal{N} \end{pmatrix} = \begin{pmatrix} \delta\mathcal{P}_0 \\ \delta\mathcal{N}_0 \end{pmatrix} \mathrm{e}^{-ht} \tag{3.21}$$

with the initial amplitudes $\delta\mathcal{P}_0$ and $\delta\mathcal{N}_0$, and the complex decay rate h [117]. Inserting Eq. 3.21 into Eq. 3.16 yields an eigenvalue problem with the complex solutions [117]

$$h_\pm = \Gamma_\mathrm{R} \pm i\Omega_\mathrm{R}. \tag{3.22}$$

Here, the damping rate is given by

$$\Gamma_\mathrm{R} = \frac{1}{2}\left(\Gamma_\mathrm{N} + \Gamma_\mathrm{P}\right), \tag{3.23}$$

while the angular relaxation oscillation frequency is

$$\Omega_\mathrm{R} = \left[G_\mathrm{s}\left(G_\mathcal{N}\mathcal{P} + 2\frac{\partial\left(\beta_\mathrm{sp}R_\mathrm{sp}\right)}{\partial\mathcal{N}}\right) - \frac{1}{4}\left(\Gamma_\mathrm{N} - \Gamma_\mathrm{P}\right)^2\right]^{1/2}, \tag{3.24}$$

where

$$G_\mathrm{s} = G_\mathrm{mod} + G_\mathcal{P}\mathcal{P} \tag{3.25}$$

is the saturated gain [117].

3.1.7 Laser linewidth

For a description of the laser linewidth, Eqs. 3.1 to 3.3 can be extended by Langevin force terms [169–171]. From this, the full width at half maximum (FWHM) of the laser linewidth (Δf) below and above threshold can be derived, which is given by [172]

$$\Delta f = \frac{1}{4\pi}\frac{\beta_\mathrm{sp}R_\mathrm{sp}}{\mathcal{P}}(1 + S_1 + S_2), \tag{3.26}$$

with the summands

$$S_1 = \frac{\epsilon_\mathrm{p}\gamma_\mathrm{c}}{\eta_\mathrm{p}G_\mathcal{N}} \cdot \frac{\mathrm{d}G_\mathrm{mod}}{\mathrm{d}P} \tag{3.27}$$

and

$$S_2 = \left(\alpha G_\mathcal{N} P\right)^2 \cdot \frac{{G_\mathrm{s}}^2 + 2\Gamma_\mathrm{P}G_\mathrm{s} + {\Gamma_\mathrm{P}}^2\left[1 + \gamma_\mathrm{c}\mathcal{N}/\left(\beta_\mathrm{sp}R_\mathrm{sp}\mathcal{P}\right)\right]}{\left({\Omega_\mathrm{R}}^2 + {\Gamma_\mathrm{R}}^2\right)^2}. \tag{3.28}$$

Below threshold, Eq. 3.26 reduces to the Schawlow-Townes linewidth [173]

$$\Delta f_0 = \frac{1}{2\pi}\frac{\beta_\mathrm{sp}R_\mathrm{sp}}{\mathcal{P}}, \tag{3.29}$$

while above it approaches the Schawlow-Townes-Henry linewidth [171]

$$\Delta f_{\infty} = \frac{1}{4\pi} \frac{\beta_{\mathrm{sp}} R_{\mathrm{sp}}}{\mathcal{P}} \left(1 + \alpha^2\right). \tag{3.30}$$

Remarkably, it has been shown in Ref. [133] that the linewidth of GaAs NW lasers cannot be described by Eq. 3.26 and thus follows neither the Schawlow-Townes nor the Schawlow-Townes-Henry linewidth. However, using data obtained during this thesis, it could be demonstrated that the linewidth of these lasers can be described by a quantum statistical laser theory [128], as will be shown later in Chapter 5.

3.2 Carrier dynamics

The primary assumption of the rate equation model discussed in the previous section is that carrier-carrier and carrier-phonon scattering happens on a faster timescale than stimulated emission and the temporal dynamics of the laser output intensity [101]. This is not necessarily the case, especially for experiments on ultrafast timescales such as those discussed later in Section 6.2. In these cases one has to track the occupation of each electron and hole state as a function of time, which is a computationally expensive task [101]. In the following three subsections, we will briefly introduce the typical timescales of carrier dynamics in GaAs and then discuss two approaches to describe these dynamics.

3.2.1 Timescales for carrier dynamics

As shown in Fig. 2.2, the absorption of a photon creates a free electron-hole (e-h) pair. When a semiconductor in thermal equilibrium absorbs an ultrashort laser pulse, a large number of e-h pairs are excited almost simultaneously. The spectral width of this created carrier distribution depends on the linewidth of the exitation laser, while the excess energy of the excited electrons

$$\Delta\epsilon_{\mathrm{e}} = \frac{\epsilon_{\mathrm{p}} - \epsilon_{\mathrm{g0}}}{1 + m_{\mathrm{e}}/m_{\mathrm{h}}} \tag{3.31}$$

and holes

$$\Delta\epsilon_{\mathrm{h}} = \epsilon_{\mathrm{p}} - \epsilon_{\mathrm{g0}} - \Delta\epsilon_{\mathrm{e}} \tag{3.32}$$

with respect to the band edge can be controlled by its photon energy [174]. The subsequent temporal evolution of this photoexcited carrier distribution can approximately be classified into four temporal regimes, as shown in Table 3.1 and discussed in Ref. [106].

Initially, the excited e-h pairs are all in phase with each other and the excitation

Temporal regime	Processes
Coherent ($t < 0.2\,\mathrm{ps}$)	• carrier-carrier scattering • intervalley scattering ($\Gamma \rightarrow L,X$)
Non-thermal ($t < 2\,\mathrm{ps}$)	• carrier-carrier scattering • intervalley scattering ($L,X \rightarrow \Gamma$) • carrier-optical-phonon scattering
Thermal ($t < 100\,\mathrm{ps}$)	• carrier-carrier scattering • carrier-optical-phonon scattering • carrier-acoustic-phonon scattering
Isothermal ($t > 100\,\mathrm{ps}$)	• radiative carrier recombination • nonradiative carrier recombination

Table 3.1 | Carrier relaxation regimes. Typical timescales and relaxation processes in GaAs following excitation with an ultrashort laser pulse. (Adapted from [106])

pulse [106]. However, this coherence decays extremely fast within the first 200 fs because of strong dephasing due to scattering processes [106, 175–184]. After this loss of coherence, the carrier distribution is likely non-thermal [106, 185–187], which means that it cannot be described by either a Maxwell-Boltzmann or Fermi-Dirac function. Carrier-carrier scattering then rapidly thermalizes the electron and hole distributions among themselves within a few hundred femtoseconds [106, 176, 177, 188–195]. At this point, the electrons, holes and the lattice are all described by different temperatures [106]. Due to their different effective masses, the equilibration between the electrons and holes takes slightly longer than the thermalization within each charge carrier species [196] and is typically established after a few picoseconds [106]. Following thermalization, the hot electron and hole distributions then rapidly cool towards the lattice temperature via carrier-phonon scattering within approximately the first hundred picoseconds [106, 111, 175, 197–205]. This transfers the excess energy of the carriers to the lattice and generates a large number of non-equilibrium phonons [106]. Finally, the carriers recombine via radiative and nonradiative recombination pathways and bring the semiconductor back into thermal equilibrium [106].

3.2.2 Boltzmann equation

Within the Boltzmann equation framework, the scattering rates are self-consistently calculated for each k-state in the conduction and valence band [101, 155]. This approach thus allows a detailed microscopic description of the carrier dynamics. The

Boltzmann equation for the **k**-dependent carrier distributions ($n_{\mathrm{a}\mathbf{k}}$) has the form

$$\left.\frac{\partial n_{\mathrm{a}\mathbf{k}}}{\partial t}\right|_{\mathrm{col}} = -\bar{\Sigma}_{\mathrm{a}}^{\mathrm{out}}(\mathbf{k})\, n_{\mathrm{a}\mathbf{k}} + \bar{\Sigma}_{\mathrm{a}}^{\mathrm{in}}(\mathbf{k})\,(1 - n_{\mathrm{a}\mathbf{k}})\,, \tag{3.33}$$

where a ∈ {e,h} for electrons and hole, respectively [101]. It includes contributions from both carrier-carrier and carrier-phonon scattering, and thus the total effective scattering rates into ($\bar{\Sigma}_{\mathrm{a}}^{\mathrm{in}}$) and out ($\bar{\Sigma}_{\mathrm{a}}^{\mathrm{out}}$) of a certain state with wave vector **k** are given by

$$\bar{\Sigma}_{\mathrm{a}}^{\mathrm{b}} = \Sigma_{\mathrm{a,cc}}^{\mathrm{b}} + \Sigma_{\mathrm{a,cp}}^{\mathrm{b}}, \tag{3.34}$$

where $\Sigma_{\mathrm{a,cc}}^{\mathrm{b}}$ is the effective carrier-carrier scattering rate, $\Sigma_{\mathrm{a,cp}}^{\mathrm{b}}$ is the effective carrier-phonon scattering rate and b ∈ {in, out} [101, 128, 155]. The scattering equations given in this section are valid under the Markov and second Born approximation [155].

Carrier-carrier scattering

Carrier-carrier scattering is a direct result of the Coulomb interaction between charge carriers, which is described by the Coulomb hamiltonian

$$\hat{\mathcal{H}}_{\mathrm{C}} = \frac{1}{2}\sum_{\substack{\mathbf{k},\mathbf{k}',\mathbf{q}\\ \mathbf{q}\neq 0}} V_{\mathbf{q}}\left(\hat{a}^{\dagger}_{\mathbf{k}+\mathbf{q}}\hat{a}^{\dagger}_{\mathbf{k}'-\mathbf{q}}\hat{a}_{\mathbf{k}'}\hat{a}_{\mathbf{k}} + \hat{b}^{\dagger}_{\mathbf{k}+\mathbf{q}}\hat{b}^{\dagger}_{\mathbf{k}'-\mathbf{q}}\hat{b}_{\mathbf{k}'}\hat{b}_{\mathbf{k}} - 2\hat{a}^{\dagger}_{\mathbf{k}+\mathbf{q}}\hat{b}^{\dagger}_{\mathbf{k}'-\mathbf{q}}\hat{b}_{\mathbf{k}'}\hat{a}_{\mathbf{k}}\right), \tag{3.35}$$

with the electron and hole creation ($\hat{a}^{\dagger}_{\mathbf{k}}$, $\hat{b}^{\dagger}_{-\mathbf{k}}$) and annihiliation ($\hat{a}_{\mathbf{k}}$, $\hat{b}_{-\mathbf{k}}$) operators, and the Fourier transform ($V_{\mathbf{q}}$) of the Coulomb potential energy (V)

$$V_{\mathbf{q}} = \frac{1}{V_{\mathrm{NW}}}\int \mathrm{d}^3 r e^{-i\mathbf{q}\cdot\mathbf{r}} V(r), \tag{3.36}$$

where **r** is the position vector and r its magnitude [101, 155]. To phenomenologically account for plasma screening, $V_{\mathbf{q}}$ is replaced in the following by a screened Coulomb potential in the static plasmon approximation

$$V_{\mathrm{s}\mathbf{q}} = V_{\mathbf{q}}\left(1 - \frac{\omega_{\mathrm{pl}}^2}{\omega_{\mathbf{q}}^2}\right), \tag{3.37}$$

with the plasma frequency (ω_{pl}) and effective plasmon frequency ($\omega_{\mathbf{q}}$) [101]. The resulting effective carrier-carrier scattering rates include contributions from electron-

electron, hole-hole, and electron-hole scattering and are given by [176, 206]

$$\begin{aligned}\Sigma^{\text{in}}_{\text{a,cc}}(\mathbf{k}) = \frac{2\pi}{\hbar} \sum_{\mathbf{k}',\mathbf{q},\text{b}} & \left[1 - n_{\text{b}\mathbf{k}'}\right] n_{\text{b},\mathbf{k}'+\mathbf{q}} n_{\text{a},\mathbf{k}-\mathbf{q}} \\ & \times \left[V^2_{\text{s}\mathbf{q}} + \left(V_{\text{s}\mathbf{q}} - \delta_{\text{ab}} V^{\text{ex}}_{\mathbf{k}-\mathbf{k}'-\mathbf{q}}\right)^2\right] \\ & \times \delta\left[\epsilon_{\text{a}\mathbf{k}} + \epsilon_{\text{b}\mathbf{k}'} - \epsilon_{\text{a},\mathbf{k}-\mathbf{q}} - \epsilon_{\text{b},\mathbf{k}'+\mathbf{q}}\right]\end{aligned} \tag{3.38}$$

and

$$\begin{aligned}\Sigma^{\text{out}}_{\text{a,cc}}(\mathbf{k}) = \frac{2\pi}{\hbar} \sum_{\mathbf{k}',\mathbf{q},\text{b}} & n_{\text{b}\mathbf{k}'}\left[1 - n_{\text{b},\mathbf{k}'+\mathbf{q}}\right]\left[1 - n_{\text{a},\mathbf{k}-\mathbf{q}}\right] \\ & \times \left[V^2_{\text{s}\mathbf{q}} + \left(V_{\text{s}\mathbf{q}} - \delta_{\text{ab}} V^{\text{ex}}_{\mathbf{k}-\mathbf{k}'-\mathbf{q}}\right)^2\right] \\ & \times \delta\left[\epsilon_{\text{a}\mathbf{k}} + \epsilon_{\text{b}\mathbf{k}'} - \epsilon_{\text{a},\mathbf{k}-\mathbf{q}} - \epsilon_{\text{b},\mathbf{k}'+\mathbf{q}}\right],\end{aligned} \tag{3.39}$$

where a,b $\in$ {e,h}. Here, the exchange term $V^{\text{ex}}_{\mathbf{k}}$ is approximated by

$$V^{\text{ex}}_{\mathbf{k}} = \frac{e_0^2}{\varepsilon_0 \varepsilon_\infty V_{\text{NW}}} \frac{1}{|\mathbf{k}|^2 + \kappa^2_{\text{sc}}}, \tag{3.40}$$

where e_0 is the elementary charge, ε_0 the vacuum permittivity and κ_{sc} the inverse screening length [101, 206]. For additional information on the evaluation of Eq. 3.38 and Eq. 3.39, see Refs. [206] and [128].

Carrier-LO-phonon scattering

As discussed in Section 2.4, the interaction of charge carriers with the crystal lattice is dominated by carrier-LO-phonon scattering. For the case of electrons, this interaction is described by the Fröhlich hamiltonian

$$\hat{\mathcal{H}}_{\text{e-LO}} = \sum_{\mathbf{k},\mathbf{q}} \hbar \mathcal{M}_{\mathbf{q}_{\text{PN}}} \hat{a}^\dagger_{\mathbf{k}+\mathbf{q}_{\text{PN}}} \hat{a}_{\mathbf{k}} \left(\hat{g}_{\mathbf{q}_{\text{PN}}} + \hat{g}^\dagger_{-\mathbf{q}_{\text{PN}}}\right), \tag{3.41}$$

where $\hat{g}_{\mathbf{q}_{\text{PN}}}$ and $\hat{g}^\dagger_{-\mathbf{q}_{\text{PN}}}$ are the annihilation and creation operators for LO phonons with wave vector $\mathbf{q}_{\text{PN}}$ [101, 155]. The Fröhlich interaction matrix element is given by

$$\mathcal{M}^2\left(\mathbf{q}_{\text{PN}}\right) = V_{\text{s}\mathbf{q}} \left(\frac{1}{\varepsilon_\infty} - \frac{1}{\varepsilon_{\text{r}}}\right) \frac{\epsilon_{\text{LO}}\left(\mathbf{q}_{\text{PN}}\right)}{2}, \tag{3.42}$$

where ε_{r} and ε_∞ are the static and optical dielectric constants of the unexcited medium, respectively [101, 155]. Using Eq. 3.41, the scattering rates can be derived and written

as [128, 206–208]

$$\begin{aligned}\Sigma^{\text{in}}_{\text{a,cp}}(\mathbf{k}) = \frac{2\pi}{\hbar}\sum_{\mathbf{q}_{\text{PN}}}\mathcal{M}^2(\mathbf{q}_{\text{PN}})\Big\{ & n_{\text{a},\mathbf{k}+\mathbf{q}_{\text{PN}}}\left[1+n_{\text{PN}}(\mathbf{q}_{\text{PN}})\right] \\ & \times\delta\left[\epsilon_{\text{a},\mathbf{k}+\mathbf{q}_{\text{PN}}}-\epsilon_{\text{a}\mathbf{k}}-\epsilon_{\text{LO}}(\mathbf{q}_{\text{PN}})\right] \\ & + n_{\text{a},\mathbf{k}-\mathbf{q}_{\text{PN}}}n_{\text{PN}}(\mathbf{q}_{\text{PN}}) \\ & \times\delta\left[\epsilon_{\text{a},\mathbf{k}-\mathbf{q}_{\text{PN}}}-\epsilon_{\text{a}\mathbf{k}}+\epsilon_{\text{LO}}(\mathbf{q}_{\text{PN}})\right]\Big\}\end{aligned} \tag{3.43}$$

and

$$\begin{aligned}\Sigma^{\text{out}}_{\text{a,cp}}(\mathbf{k}) = \frac{2\pi}{\hbar}\sum_{\mathbf{q}_{\text{PN}}}\mathcal{M}^2(\mathbf{q}_{\text{PN}})\Big\{ & \left[1-n_{\text{a},\mathbf{k}+\mathbf{q}_{\text{PN}}}\right]n_{\text{PN}}(\mathbf{q}_{\text{PN}}) \\ & \times\delta\left[\epsilon_{\text{a},\mathbf{k}+\mathbf{q}_{\text{PN}}}-\epsilon_{\text{a}\mathbf{k}}-\epsilon_{\text{LO}}(\mathbf{q}_{\text{PN}})\right] \\ & + \left[1-n_{\text{a},\mathbf{k}-\mathbf{q}_{\text{PN}}}\right]\left[1+n_{\text{PN}}(\mathbf{q}_{\text{PN}})\right] \\ & \times\delta\left[\epsilon_{\text{a},\mathbf{k}-\mathbf{q}_{\text{PN}}}-\epsilon_{\text{a}\mathbf{k}}+\epsilon_{\text{LO}}(\mathbf{q}_{\text{PN}})\right]\Big\}.\end{aligned} \tag{3.44}$$

The emission or absorption of a phonon changes the phonon distribution n_{PN}, which can be described by a Bose function in thermal equilibrium [101]. In case the LO phonon generation rate is large enough or the heat contact to the substrate is insufficient, it may be necessary to also introduce a Boltzmann equation for the LO phonon population [206, 208]. In this work, however, using the Bose approximation resulted in excellent agreement with experiments, see Section 6.2. This is consistent with previous work that found excellent heat contact between the NWs and the substrate [46].

3.2.3 Relaxation rate approximation

In case the carrier distributions deviate only slightly from Fermi-Dirac functions, the Boltzmann equation can be simplified as described in the following [101]. When studying the dynamics near the lasing mode with wave vector $\mathbf{k}_{\text{lasing}}$, it is convenient to write the total carrier-carrier scattering rate for this state as

$$\gamma_{\text{cc,a}} = \Sigma^{\text{in}}_{\text{a,cc}}(\mathbf{k}_{\text{lasing}}) + \Sigma^{\text{out}}_{\text{a,cc}}(\mathbf{k}_{\text{lasing}}), \tag{3.45}$$

with $\text{a} \in \{\text{e,h}\}$ [101]. The influence of carrier-carrier scattering on the carrier distributions can then be approximated as

$$\left.\frac{\partial n_{\text{a}\mathbf{k}}}{\partial t}\right|_{\text{col,cc}} = -\gamma_{\text{cc,a}}\left[n_{\text{a}\mathbf{k}} - f_{\text{a}\mathbf{k}}\left(\epsilon_{\text{a}\mathbf{k}},T_{\text{a}},\mu_{\text{a}}\right)\right], \tag{3.46}$$

where

$$f_{\text{a}\mathbf{k}}\left(\epsilon_{\text{a}\mathbf{k}},T_{\text{a}},\mu_{\text{a}}\right) = \frac{1}{\exp\left[\left(\epsilon_{\text{a}\mathbf{k}}-\mu_{\text{a}}\right)/\left(k_{\text{B}}T_{\text{a}}\right)\right]+1} \tag{3.47}$$

is the Fermi-Dirac function, μ_{a} the chemical potential, k_{B} the Boltzmann constant, and T_{a} the respective carrier temperature [101]. The corresponding equations for carrier-phonon scattering are then

$$\gamma_{\mathrm{ap}} = \Sigma^{\mathrm{in}}_{\mathrm{a,cp}}(\mathbf{k}_{\mathrm{lasing}}) + \Sigma^{\mathrm{out}}_{\mathrm{a,cp}}(\mathbf{k}_{\mathrm{lasing}}), \tag{3.48}$$

and

$$\left.\frac{\partial n_{\mathrm{a}\mathbf{k}}}{\partial t}\right|_{\mathrm{col,cp}} = -\gamma_{\mathrm{ap}}\left[n_{\mathrm{a}\mathbf{k}} - f_{\mathrm{a}\mathbf{k}}\left(\epsilon_{\mathrm{a}\mathbf{k}}, T_{\mathrm{L}}, \mu_{\mathrm{aL}}\right)\right], \tag{3.49}$$

with the lattice temperature (T_{L}) and the chemical potential (μ_{aL}) [101]. Within the relaxation rate approximation Equation 3.33 can then be written as

$$\left.\frac{\partial n_{\mathrm{a}\mathbf{k}}}{\partial t}\right|_{\mathrm{col}} = \left.\frac{\partial n_{\mathrm{a}\mathbf{k}}}{\partial t}\right|_{\mathrm{col,cc}} + \left.\frac{\partial n_{\mathrm{a}\mathbf{k}}}{\partial t}\right|_{\mathrm{col,cp}}. \tag{3.50}$$

As a further simplification, the scattering rates in Eq. 3.45 and Eq. 3.48 were approximated as being constant for the semiconductor Bloch model. Their values where chosen with guidance from the full numerical calculation using the Boltzmann equation framework, as discussed in Appendix D.

3.3 Semiconductor Bloch model

For a semiconductor laser, the full semi-classical Hamiltonian (neglecting the carrier-phonon interaction for the moment) depends on the kinetic energy of the charge carriers ($\hat{\mathcal{H}}_{\mathrm{kin}}$), the Coulomb interaction energy between them ($\hat{\mathcal{H}}_{\mathrm{C}}$), and their dipole interaction energy with the electromagnetic field ($\hat{\mathcal{H}}_{\mathrm{dipole}}$) [101, 143]. It is given by

$$\hat{\mathcal{H}} = \hat{\mathcal{H}}_{\mathrm{kin}} + \hat{\mathcal{H}}_{\mathrm{dipole}} + \hat{\mathcal{H}}_{\mathrm{C}}, \tag{3.51}$$

with

$$\hat{\mathcal{H}}_{\mathrm{kin}} = \sum_{\mathbf{k}} \left(\epsilon_{\mathrm{g}0} + \epsilon_{\mathrm{e}\mathbf{k}}\right) \hat{n}_{\mathrm{e}\mathbf{k}} + \sum_{\mathbf{k}} \epsilon_{\mathrm{h}\mathbf{k}} \hat{n}_{\mathrm{h}\mathbf{k}}, \tag{3.52}$$

$$\hat{\mathcal{H}}_{\mathrm{dipole}} = -V_{\mathrm{NW}} \hat{\mathbf{P}} \cdot \mathbf{E}, \tag{3.53}$$

and $\hat{\mathcal{H}}_{\mathrm{C}}$ defined by Eq. 3.35, where $\epsilon_{\mathrm{g}0}$ is the unexcited band gap, $\hat{n}_{\mathrm{e}\mathbf{k}} = \hat{a}^{\dagger}_{\mathbf{k}} \hat{a}_{\mathbf{k}}$ the electron number operator, $\hat{n}_{\mathrm{h}\mathbf{k}} = \hat{b}^{\dagger}_{-\mathbf{k}} \hat{b}_{-\mathbf{k}}$ the hole number operator, $\mu_{\mathbf{k}}$ the dipole matrix element, and $\mathbf{E}$ the classical electric field [101, 143]. Here, $\hat{\mathbf{P}}$ is the macroscopic polarization of the active medium defined by

$$\hat{\mathbf{P}} = \frac{1}{V_{\mathrm{NW}}} \sum_{\mathbf{k}} \left(\mu_{\mathbf{k}} \hat{p}^{\dagger}_{\mathbf{k}} + \mu^{*}_{\mathbf{k}} \hat{p}_{\mathbf{k}}\right), \tag{3.54}$$

where $\hat{p}_{\mathbf{k}} = \hat{b}_{-\mathbf{k}}\hat{a}_{\mathbf{k}}$ is the microscopic polarization operator [101, 143].

3.3.1 Semiconductor Bloch equations

A temporal description of the semiconductor laser dynamics can be obtained by calculating the time dependence of the quantum mechanical expectation values $n_{\mathrm{e}\mathbf{k}} = \langle \hat{n}_{\mathrm{e}\mathbf{k}} \rangle$, $n_{\mathrm{h}\mathbf{k}} = \langle \hat{n}_{\mathrm{h}\mathbf{k}} \rangle$, and $p_{\mathbf{k}} = \langle \hat{p}_{\mathbf{k}} \rangle$ using Equation 3.51 combined with the Heisenberg equation of motion [101, 143]. This yields the semiconductor Bloch equations

$$\frac{\partial p_{\mathbf{k}}}{\partial t} = -i\omega_{\mathbf{k}} p_{\mathbf{k}} - i\Omega_{\mathbf{k}} \left(n_{\mathrm{e}\mathbf{k}} + n_{\mathrm{h}\mathbf{k}} - 1\right) + \left.\frac{\partial p_{\mathbf{k}}}{\partial t}\right|_{\mathrm{col}}, \tag{3.55}$$

$$\frac{\partial n_{\mathrm{a}\mathbf{k}}}{\partial t} = \Lambda_{\mathrm{a}\mathbf{k}} - \gamma_{\mathrm{c}} n_{\mathrm{a}\mathbf{k}} + i\left(\Omega_{\mathbf{k}} p_{\mathbf{k}}^{*} - \Omega_{\mathbf{k}}^{*} p_{\mathbf{k}}\right) + \left.\frac{\partial n_{\mathrm{a}\mathbf{k}}}{\partial t}\right|_{\mathrm{col}}, \tag{3.56}$$

with $\mathrm{a} \in \{\mathrm{e},\mathrm{h}\}$ [101, 143]. In Eq. 3.56, the pump rate $\Lambda_{\mathrm{a}\mathbf{k}}$, and the relaxation term with the total recombination rate γ_{c} were included phenomenologically [101, 143]. The rate γ_{c} takes into account spontaneous emission and non-radiative recombination.

Scattering rates

The terms containing correlations of higher order than Hartree-Fock contributions are included in the partial derivatives $\partial/\partial t|_{\mathrm{col}}$ [101, 143]. In this work, we describe the scattering terms in the relaxation rate approximation, with $\partial n_{\mathrm{a}\mathbf{k}}/\partial t|_{\mathrm{col}}$ being given by Eq. 3.50, while the simplest approximation for the polarization decay is

$$\left.\frac{\partial p_{\mathbf{k}}}{\partial t}\right|_{\mathrm{col}} = -\gamma p_{\mathbf{k}}. \tag{3.57}$$

The dephasing rate γ is given by

$$\gamma = \frac{1}{2}\left(\gamma_{\mathrm{e}} + \gamma_{\mathrm{h}}\right), \tag{3.58}$$

where

$$\gamma_{\mathrm{a}} = \bar{\Sigma}_{\mathrm{a}}^{\mathrm{in}}\left(\mathbf{k}_{\mathrm{lasing}}\right) + \bar{\Sigma}_{\mathrm{a}}^{\mathrm{out}}\left(\mathbf{k}_{\mathrm{lasing}}\right), \tag{3.59}$$

with $\mathrm{a} \in \{\mathrm{e},\mathrm{h}\}$. In general, the rates calculated with the Boltzmann equation cannot be used directly in the relaxation rate approach due to the different nature of these two approximations. Nevertheless, the rates from the Boltzmann equation usually serve as a good starting point for finding suitable scattering rates for the relaxation rate approach. If the computational effort is not a concern, $\partial p_{\mathbf{k}}/\partial t|_{\mathrm{col}}$ and $\partial n_{\mathrm{a}\mathbf{k}}/\partial t|_{\mathrm{col}}$ can also be computed directly within the Boltzmann-equation framework.

Many-body effects

There are three important many-body effects contained in Equations 3.55 and 3.56 [143]. The first is *band gap renormalization* [143]. Here, there transition energy between the bands becomes carrier density dependent and is given by

$$\hbar\omega_{\mathbf{k}} = \frac{\hbar^2\mathbf{k}^2}{2m_\mathrm{e}} + \frac{\hbar^2\mathbf{k}^2}{2m_\mathrm{h}} + \epsilon_{\mathrm{g}0} + \Delta\epsilon_{\mathrm{CH}} + \Delta\epsilon_{\mathrm{SX},\mathbf{k}}, \tag{3.60}$$

where $\Delta\epsilon_{\mathrm{CH}}$ is the Coulomb-hole self energy, and $\Delta\epsilon_{\mathrm{SX},\mathbf{k}}$ the screened exchange shift [101, 143, 155]. This effect reduces the band gap of the excited semiconductor and leads to a shift of the gain spectrum relative to the lasing mode. The second many-body effect is the *renormalization of the angular Rabi frequency*, described by

$$\hbar\Omega_{\mathbf{k}} = \mu_{\mathbf{k}}E + \sum_{\mathbf{k}'\neq\mathbf{k}} V_{\mathrm{s},|\mathbf{k}'-\mathbf{k}|}p_{\mathbf{k}'}, \tag{3.61}$$

with the electric field amplitude E [101, 143, 155]. This effect results in a reshaping and enhancement of the gain compared to a free carrier theory [101, 143, 155]. Physically, this Coulomb enhancement is due to the Coulomb attraction between electrons and holes [101, 143, 155]. As a result, the charge carriers remain in each other's vicinity longer than without this mutual attraction, leading to a longer interaction time and thus a higher probability of optical recombination [101, 143, 155]. Another consequence of the Coulomb attraction between electrons and holes - *plasma screening* - is included in Eq. 3.61 by the use of the screened Coulomb potential as defined in Eq. 3.37.

Electric field envelope

Finally, using Eq. 3.54 and Eq. 3.55 allows to calculate the complex polarization amplitude ($\mathfrak{P}$) according to the procedure described in Refs. [101] and [143]. The dynamics of the complex electric field envelope (E) can then be computed by

$$\frac{\partial E}{\partial t} = \frac{i\omega_0\Gamma}{\varepsilon_0\varepsilon_\mathrm{r}}\mathfrak{P} - (\kappa + i\Delta\omega)\,E, \tag{3.62}$$

where ω_0 is the frequency at the band edge and $\Delta\omega$ the detuning of the lasing mode from the band edge [101, 143].

Numerical modelling

The equations of the semiconductor Bloch model were solved with a fourth order Runge-Kutta method [68]. This required a time discretization of $\Delta t_\mathrm{disc} = 1\times10^{-16}\,\mathrm{s}$, limited by the convergence of the higher k-states [68]. The k-space was discretized with a non-equidistant grid that has an increased density close to the band edge [68].

3.3.2 Many-body gain

To obtain expressions for the amplitude material gain (g_{mat}) and carrier-induced refractive index change ($\Delta n/n$), one first derives the complex susceptibility $\chi = \chi' + i\chi''$, starting from the equation of motion for the microscopic polarization given by Eq. 3.55 [101, 143]. The real (χ') and imaginary (χ'') parts of the complex susceptibility χ are related to g_{mat} and $\Delta n/n$ via

$$g_{\mathrm{mat}} = -\frac{q}{2}\chi'' \tag{3.63}$$

and

$$\frac{\Delta n}{n} = \frac{\chi'}{2}, \tag{3.64}$$

where q is the wave number in the medium [101, 143]. The resulting expressions for g_{mat} and $\Delta n/n$ are then

$$g_{\mathrm{mat}} = \frac{\omega n}{2c_0}\frac{1}{\varepsilon\hbar}\frac{1}{V_{\mathrm{NW}}}\sum_{\mathbf{k}} |\mu_{\mathbf{k}}|^2 \left[n_{\mathrm{e}\mathbf{k}} + n_{\mathrm{h}\mathbf{k}} - 1\right] \mathcal{L}\left(\omega_{\mathbf{k}} - \omega\right)\left[1 + q_{\mathbf{k}}\right] \tag{3.65}$$

and

$$\frac{\Delta n}{n} = -\frac{1}{\varepsilon\hbar}\frac{1}{V_{\mathrm{NW}}}\sum_{\mathbf{k}} \mu_{\mathbf{k}}|^2 \left[n_{\mathrm{e}\mathbf{k}} + n_{\mathrm{h}\mathbf{k}} - 1\right] \mathcal{L}\left(\omega_{\mathbf{k}} - \omega\right)\frac{\omega_{\mathbf{k}} - \omega}{\gamma}\left[1 + q_{\mathbf{k}}\right], \tag{3.66}$$

where $\varepsilon = n^2\varepsilon_0$ is the permittivity,

$$\mathcal{L}\left(\omega_{\mathbf{k}} - \omega\right) = \frac{\gamma}{\left(\omega_{\mathbf{k}} - \omega\right)^2 + \gamma^2} \tag{3.67}$$

a Lorentzian lineshape function, and $q_{\mathbf{k}}$ the Coulomb enhancement factor [101, 143].

3.4 Quantum statistical model

In this chapter we give a brief overview over the key equations of the quantum statistical model. More details can be found in [101, 128, 148–150]. Within this approach, the theory of non-equilibrium Green's functions [157, 209, 210] is used to derive a set of coupled equations for the interacting charge carrier and photon systems of a semiconductor laser [145, 149–152, 158]. This powerful approach allows to self-consistently analyze and simulate semiconductor laser characteristics over a wide range of parameter variations [144–148, 152, 153, 156], which is crucial for the type of experiments analyzed in Section 6.2. In addition, the generality of this theory allows to determine the range of application of simpler models, such as those presented in Section 3.1 and Section 3.3 [101]. The discussion below closely follows

the presentation in Refs. [128, 148]. Details on the numerical modelling are provided in Ref. [128].

3.4.1 Photon kinetics

For a quantized electric field, the semiclassical dipole interaction energy given in Eq. 3.53 becomes

$$\hat{\mathcal{H}}_{\text{dipole}} = -\hbar \sum_{\mathbf{k}} \left(g_{\mathbf{k}}^{*} \hat{c}^{\dagger} \hat{b}_{-\mathbf{k}} \hat{a}_{\mathbf{k}} + g_{\mathbf{k}} \hat{a}_{\mathbf{k}}^{\dagger} \hat{b}_{-\mathbf{k}}^{\dagger} \hat{c} \right), \tag{3.68}$$

where $g_{\mathbf{k}}$ is the interaction matrix element, while $\hat{c}^{\dagger}$ and $\hat{c}$ are the photon creation and annihilation operators, respectively [101]. Applying the non-equilibrium Green's function theory to Eq. 3.51, with Eq. 3.68 expressed in terms of the quantized vector potential, then allows to derive the kinetic equation for the spectral laser intensity [101, 148]

$$\frac{1}{\tilde{F}(\omega)} \frac{1}{c} \frac{\partial I(\omega)}{\partial t} = \left[G_{\text{mod}}(\omega) - \frac{2\kappa}{\tilde{F}(\omega)} \right] I(\omega) + \beta_{\text{sp}} W(\omega) S(\omega), \tag{3.69}$$

where $c = c_0/n(\omega)$ is the renormalized speed of light with the frequency-dependent refractive index $n(\omega)$ [139, 211], while

$$\tilde{F}(\omega) = \frac{2\pi c}{\omega} S(\omega) \tag{3.70}$$

is an approximation of the cavity function $F_{\mathbf{q}}$, as defined in Refs. [101, 128, 148, 152]. Here, $S(\omega)$ is the photon density of states, given by

$$S(\omega) = \frac{\mu_0 e_0^2}{2m_0^2} |\mathcal{M}_{\text{T}}|^2 \frac{1}{V_{\text{NW}}} \sum_{\mathbf{q}} S_{\mathbf{q}}(\omega), \tag{3.71}$$

with the vacuum permeability μ_0, the photon lineshape function $S_{\mathbf{q}}(\omega)$ [101, 148], and the transition matrix element $|\mathcal{M}_{\text{T}}| = (m_0\omega/e_0)|\mu_{\mathbf{k}}|$ [128]. The intensity material gain (G_{mat}) and spontaneous emission rate (W) are frequency-dependent and described by [101, 148]

$$G_{\text{mat}}(\omega) = \frac{\mu_0 e_0^2}{2m_0^2} \frac{c}{\omega} \sum_{\mathbf{k}} |\mathcal{M}_{\text{T}}|^2 \mathcal{L}_{\mathbf{k}}(\omega) \left[n_{\text{e}\mathbf{k}} + n_{\text{h}\mathbf{k}} - 1 \right] \left[1 + 2q_{\mathbf{k}}(\omega) \right] \tag{3.72}$$

and

$$W(\omega) = \frac{\mu_0 e_0^2}{2m_0^2} \frac{c}{\omega} \sum_{\mathbf{k}} |\mathcal{M}_{\text{T}}|^2 \mathcal{L}_{\mathbf{k}}(\omega) n_{\text{e}\mathbf{k}} n_{\text{h}\mathbf{k}} \left[1 + 2q_{\mathbf{k}}(\omega) \right], \tag{3.73}$$

with the Lorentzian lineshape function

$$\mathcal{L}_{\mathbf{k}}(\omega) = 2\frac{\gamma_{\mathrm{eh}}(\mathbf{k})}{\left(\hbar\omega_{\mathbf{k}} - \hbar\omega\right)^2 + \gamma_{\mathrm{eh}}^2(\mathbf{k})}. \tag{3.74}$$

Equation 3.72 together with Eq. 3.4 yields the modal gain in Eq. 3.69. Furthermore, Eq. 3.72 is related to Eq. 3.65 by Eq. 3.6. The wave vector dependent energy broadening in the Lorentzian lineshape function depends on the carrier-carrier and carrier-phonon scattering rates, and is given by [101, 128]

$$\gamma_{\mathrm{eh}}(\mathbf{k}) = \frac{1}{2}\left[\gamma_{\mathrm{e}}(\mathbf{k}) + \gamma_{\mathrm{h}}(\mathbf{k})\right], \tag{3.75}$$

where

$$\gamma_{\mathrm{a}}(\mathbf{k}) = \hbar\left[\bar{\Sigma}_{\mathrm{a}}^{\mathrm{in}}(\mathbf{k}) + \bar{\Sigma}_{\mathrm{a}}^{\mathrm{out}}(\mathbf{k})\right]. \tag{3.76}$$

3.4.2 Carrier kinetics

The dynamics of the carrier distributions are described by the carrier kinetic equation

$$\frac{\partial n_{\mathrm{a}\mathbf{k}}}{\partial t} = \left.\frac{\partial n_{\mathrm{a}\mathbf{k}}}{\partial t}\right|_{\mathrm{col}} + \left.\frac{\partial n_{\mathrm{a}\mathbf{k}}}{\partial t}\right|_{\mathrm{spon}} + \left.\frac{\partial n_{\mathrm{a}\mathbf{k}}}{\partial t}\right|_{\mathrm{stim}} + \left.\frac{\partial n_{\mathrm{a}\mathbf{k}}}{\partial t}\right|_{\mathrm{pump}}, \tag{3.77}$$

with $\mathrm{a} \in \{\mathrm{e}, \mathrm{h}\}$, where the Boltzmann scattering term $\partial n_{\mathrm{a}\mathbf{k}}/\partial t|_{\mathrm{col}}$ is given by Eq. 3.33 [148]. Radiative recombination is accounted for by the spontaneous and stimulated emission contributions, defined by [148]

$$\left.\frac{\partial n_{\mathrm{a}\mathbf{k}}}{\partial t}\right|_{\mathrm{spon}} = -\frac{n_{\mathrm{e}\mathbf{k}} n_{\mathrm{h}\mathbf{k}}}{\tau_{\mathrm{spon}}(\mathbf{k})} \tag{3.78}$$

and

$$\left.\frac{\partial n_{\mathrm{a}\mathbf{k}}}{\partial t}\right|_{\mathrm{stim}} = -\frac{n_{\mathrm{e}\mathbf{k}} + n_{\mathrm{h}\mathbf{k}} - 1}{\tau_{\mathrm{stim}}(\mathbf{k})}, \tag{3.79}$$

whereby the $\mathbf{k}$-dependent spontaneous and stimulated emission lifetimes are given by

$$\tau_{\mathrm{spon}}^{-1}(\mathbf{k}) = \int \frac{\mathrm{d}\omega}{2\pi}\mathcal{L}_{\mathbf{k}}(\omega) S(\omega)\left[1 + q_{\mathbf{k}}(\omega)\right] \tag{3.80}$$

and

$$\tau_{\mathrm{stim}}^{-1}(\mathbf{k}) = \int \frac{\mathrm{d}\omega}{2\pi}\mathcal{L}_{\mathbf{k}}(\omega) I(\omega)\left[1 + q_{\mathbf{k}}(\omega)\right]. \tag{3.81}$$

The last term in Eq. 3.77, describes optical excitation by a pump laser and is given either by

$$\left.\frac{\partial n_{\mathrm{a}\mathbf{k}}}{\partial t}\right|_{\mathrm{pump}} = \Lambda_{\mathrm{a}\mathbf{k}}\left[1 - n_{\mathrm{e}\mathbf{k}}\right]\left[1 - n_{\mathrm{h}\mathbf{k}}\right] \tag{3.82}$$

for continuous-wave excitation, or by

$$\left.\frac{\partial n_{\mathbf{ak}}}{\partial t}\right|_{\text{pump}} = \Lambda_{\mathbf{ak}} \left[1 - n_{\mathbf{ek}}\right] \left[1 - n_{\mathbf{hk}}\right] \operatorname{sech}^2 \left(1.76 \cdot \frac{t - t_0}{\Delta t_{\text{pump}}}\right), \tag{3.83}$$

for pulsed excitation [128]. Here, $\Lambda_{\mathbf{ak}}$ is the pump rate, t_0 the arrival time of the excitation pulse, and Δt_{pump} its FWHM [128].

3.5 Summary

In this chapter, we outlined three semiconductor laser theories with increasing degrees of sophistication. The two-level rate equation approach is the simplest of these and very useful for fast qualitative predictions about specific laser characteristics. However, it is not suitable for quantitative simulations and fails completely when finite carrier relaxation times must to be taken into account. The typical timescales and processes governing carrier relaxation in GaAs after photoexcitation with an ultrashort laser pulse are summarized in Table 3.1. The two most important scattering processes for laser dynamics are carrier-carrier scattering, which leads to thermalization of the carrier distributions, and carrier-LO-phonon scattering, which leads to cooling of the carrier system. Thermalization typically occurs within a few hundred femtoseconds, while carrier cooling takes place on picosecond timescales. The semiconductor Bloch model accounts for these carrier dynamics via a relaxation rate approximation, whereas the quantum statistical model self-consistently calculates all scattering rates for each time step with a Boltzmann equation. The theoretical models outlined here serve as a basis for understanding the experiments discussed in Chapter 5 and Chapter 6.

Chapter 4

Materials and methods

Contents

This chapter describes the sample preparation and the experimental setups that were used to optically characterize the NWs. For each setup, we discuss the key optical elements and their purpose.

4.1 Sample preparation

Sample preparation consisted of NW growth and their subsequent transfer onto a suitable substrate for optical spectroscopy.

4.1.1 Nanowire growth

The investigated NW lasers were grown by Daniel Rudolph on Si(111) substrates using solid source molecular beam epitaxy (Gen II, Veeco) [44, 46, 69, 74, 94]. Prior to growth, the (20 ± 2) nm thick SiO_2 layer of these substrates was thinned to ~ 2 nm by wet chemical etching, resulting in randomly distributed nanoscopic holes in the oxide layer [69, 74]. These act as nucleation sites for the spontaneous growth of NWs [92, 94, 212, 213]. Subsequently, NW synthesis was achieved in a two-step axial and radial growth process using a self-catalyzed vapor-liquid-solid growth mode [94]. To enhance its optical properties, the NW core was overgrown with a 5 nm thick AlGaAs surface passivation layer [46, 47, 69–75], and 5 nm thick GaAs capping layer to prevent oxidation [46, 47, 69, 74, 75]. As shown in Section 2.1, the resulting NWs have a length in the range of 10 µm to 16 µm and a diameter of ~ 340 nm [46, 69]. Further details about the NW growth and their structural characterization are provided in Refs. [46, 69, 74, 92, 94, 214]. The growth wafer used for the samples in this thesis has the identification number 02-27-13.2.

4.1.2 Substrate material

To investigate their lasing characteristics, the grown NWs have to be removed from the growth substrate [46, 47, 69, 75, 136]. This is due to the low refractive index contrast between the NWs ($n_{\mathrm{GaAs}} = 3.65$) and silicon ($n_{\mathrm{silicon}} = 3.67$) [215]. As a result, the reflectivity at the bottom end facet of the NWs is very low ($< 1\%$) [136], which prevents lasing due to the resulting high losses and insufficient optical feedback. For optical experiments, sapphire is a suitable substrate material due to its low refractive index ($n_{\mathrm{sapphire}} = 1.76$) and excellent thermal conductivity at cryogenic temperatures [216]. Figure 4.1a shows the sapphire substrate used in this thesis, which has an area of $\sim 5 \times 5$ mm^2 and a thickness of ~ 300 µm. To facilitate orientation on the substrate, gold markers were added using optical lithography.

4.1.3 Nanowire transfer

The NWs were transferred from the growth wafer to the sapphire substrate using the mechanical transfer process described in Ref. [136]. Figure 4.1b shows the transferred NWs lying on the surface of the sapphire substrate. The sample shown in Fig. 4.1 was used for all measurements presented in this thesis and is identified by the label '2-27-13.2 Bulk GaAs NW laser on sapphire #2'.

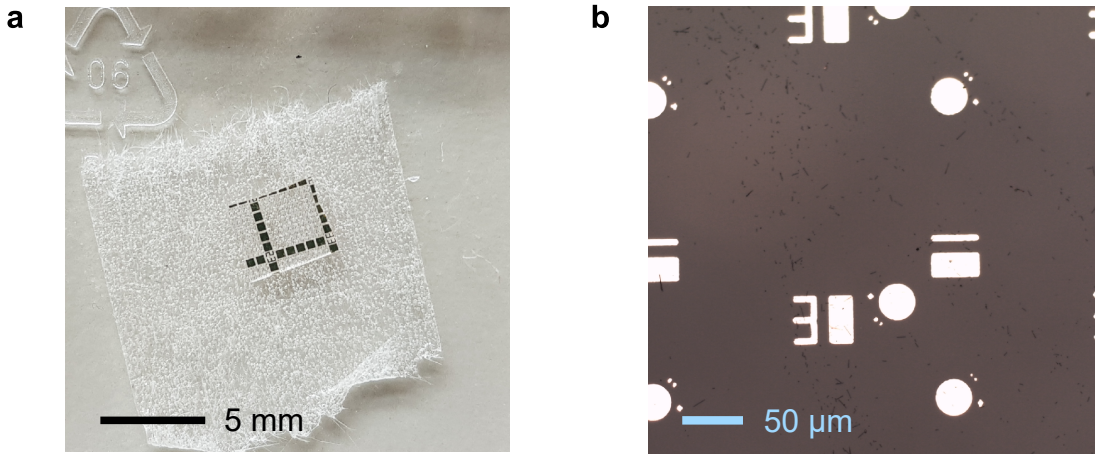

Figure 4.1 | Sample images. **a**, Sapphire substrate with gold markers. **b**, Optical microscope image (20× magnification) of the sample shown in **a** with transferred NWs.

4.2 Optical spectroscopy

The NWs were characterized using a number of different optical spectroscopy techniques, which are presented below.

4.2.1 Microphotoluminescence spectroscopy

Figure 4.2 shows a micro photoluminescence setup for optical characterization of NWs at cryogenic temperatures. The sample was fixed with glue (Fixogum, Marabu) on the cold finger of a liquid helium flow cryostat (Cryovac 8628) (1) that was evacuated to a pressure of $\sim 10^{-6}$ mbar and mounted on top of a manual x-y stage (2). By controlling the flow of liquid helium through the cryostat with valves, the temperature of the cold finger could be adjusted to a value between 10 K and 300 K.

Excitation laser

The excitation source (3) is either pulsed or CW, depending on the experimental requirements. For pulsed excitation, a mode-locked titanium-sapphire laser (Tsunami, Spectra-Physics) was used to generate femtosecond pulses with a duration of ~ 200 fs, a tunable wavelength (~ 750 nm to 850 nm), and a fixed repetition rate of $f_{\mathrm{rep}} = 82$ MHz. For CW excitation, a tunable CW titanium-sapphire laser (Model 3900S, Spectra-Physics) with a wavelength range of ~ 750 nm to 950 nm was used. To prevent back reflections from optical elements in the beam path from reaching the laser cavity, the excitation laser was combined with a broadband Faraday isolator (ISO-05-800-BB, Newport) (4).

Power control

The power and polarization of the laser beam is controlled by a combination of a rotatable polarizer and a polarizing beam splitter (5-6). A thick polarizer is used (PGT 2.05, B-Halle) (5) to avoid back reflections that occur e.g. in thin film polarizers. Additionally, the polarizer (5) is chosen to be sufficiently short, so that beam wandering is negligible as it is rotated.

Back-focal-plane beam-expander

The excitation laser then travels through a lens combination that forms a back-focal-plane beam-expander (7) [217]. This lens combination (7) focuses the excitation laser on the back focal plane of the objective and thus expands the spot size on the sample. This ensures a homogeneous illumination of the NW and simultaneously makes the setup less sensitive to mechanical vibrations.

Objective

After the back-focal-plane beam-expander, the beam is split by a beam splitter (8). The reflected part is directed to a power meter (9) which continuously monitors the excitation power, while the transmitted part passes through an objective (M Plan Apo NIR 50×, Mitutoyo) (10) with a focal length of $f_{\text{focal}} = 4\,\text{mm}$. On the sample, the beam has a spot size of $\sim 17\,\mu\text{m}$. The pupil diameter of the objective (D) is given by $D = 2 \cdot \text{NA} \cdot f_{\text{focal}} = 3.36\,\text{mm}$, where $\text{NA} = 0.42$ is the numerical aperture. The objective itself was mounted on a xyz piezo stage (Tritor 102, Piezosystem Jena) (11) that allowed precise positioning within a volume of $80\,\mu\text{m} \times 80\,\mu\text{m} \times 80\,\mu\text{m}$.

Dispersion

The group delay dispersion (GDD) for a comparable objective (M Plan Apo NIR 100×, Mitutoyo) was measured to be $\sim 4300\,\text{fs}^2$. The GDD for the objective with 50× magnification is thus $< 4300\,\text{fs}^2$. For a 200 fs pulse, this amount of GDD leads only to small corrections of the pulse duration and can therefore be neglected. In addition to GDD, microscope objectives also distort optical pulses through an effect called propagation time difference (PTD) [218, 219]. For comparable objectives, PTD is typically $< 50\,\text{fs}$ [220]. As a result, the pulse duration at the sample is in the range of 200 fs to 250 fs.

Imaging

The sample is illuminated with a Köhler illumination method [221] using an incoherent white light source (12) that can be directed onto the sample with a flip mirror (13).

The back-reflected light is then passed through a suitable low pass filter (14) to remove the excitation laser and imaged onto a charge-coupled device (CCD) (15).

Detection

Precise positioning of the detection spot to collect the photoluminescence of a specific area of the sample was achieved by a 4f lens system (16) in combination with a motorized mirror (8814, Newport) (17). Details on the 4f system are provided in Ref. [69]. For monitoring the detection position as it is moved by the motorized mirror, a fiber coupled alignment laser was sent backwards through the detection beam path. After the motorized mirror, the detection beam is coupled into an optical fiber (PM780-HP, Thorlabs) (18) with an operating wavelength of 770 nm to 1100 nm and a length of 4 m. To avoid interference effects, special care was taken to ensure that the round-trip time of back-reflected pulses within the fiber was not a multiple of the cavity round-trip time of the pulsed titanium-sapphire laser. After outcoupling from the fiber, the light was analyzed using a spectrometer (Triax 550, Horiba) (19) in combination with an InGaAs CCD cooled with liquid nitrogen (20). The spectrometer allowed the use of two different diffraction gratings, one with 150 grooves/mm and a blazing wavelength of 1200 nm, and a second with 1200 grooves/mm and a blazing wavelength of 900 nm.

4.2.2 Pump-probe photoluminescence spectroscopy

The pump-probe photoluminescence setup shown in Fig. 4.3 was used to study various aspects of NW laser dynamics. It is very similar to the microphotoluminescence setup discussed in Section 4.2.1, so we will only discuss the main differences here. For excitation, a mode-locked titanium-sapphire laser (Tsunami 3960, Spectra-Physics) (1) is used. After power and polarization control optics (2-4) the femtosecond pulses are split into two parts by a beam splitter (5). The transmitted part is called pump, the reflected part is called probe. An optical delay stage (M-ILS100PP, Newport) (6) with a bi-directional precision of < 10 fs is used to adjust the delay (Δt) of the probe pulse with respect to the pump pulse. The power of the probe is adjusted by a rotatable polarizer. Subsequently, pump and probe are recombined with a polarizing beam splitter (7) and sent towards the sample. The detection is very similar to the microphotoluminescence setup discussed in Section 4.2.1, except that here photoluminescence is analyzed using a high-resolution ($\Delta E < 40$ µeV) double spectrometer (1403, SPEX) (8) in combination with a peltier-cooled silicon CCD (iDus 416, Andor) (9).

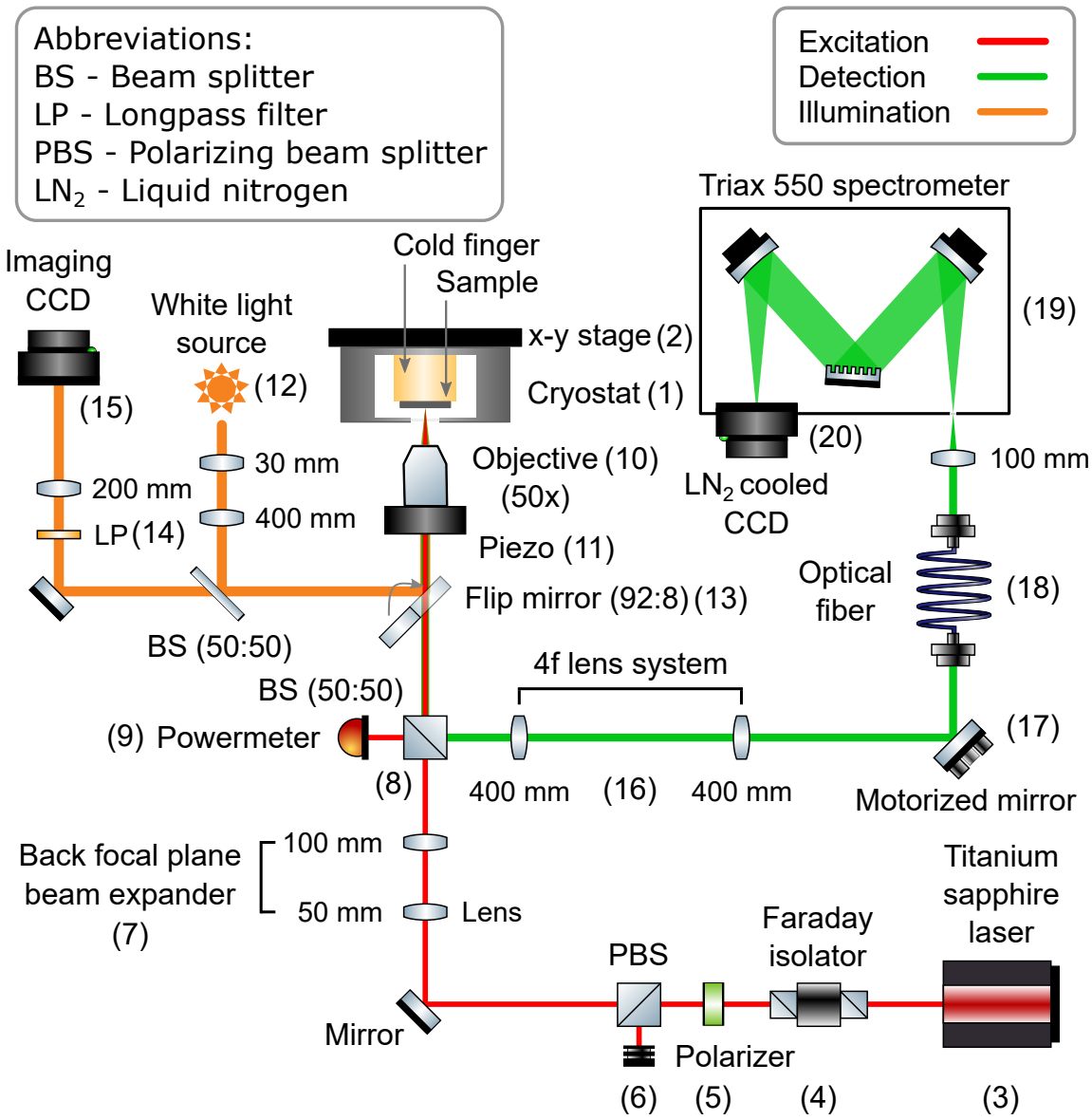

Figure 4.2 | Microphotoluminescence setup. Shown is a simplified sketch of the microphotoluminescence setup. Details are explained in the accompanying text. (The figure was made using graphics from *ComponentLibrary* by Alexander Franzen, licensed under a Creative Commons Attribution-NonCommercial 3.0 Unported License.)

4.2.3 Quasi-degenerate transient reflection spectroscopy

The setup shown in Fig. 4.4 allows to measure the normalized differential reflectivity ($\Delta\mathcal{R}/\mathcal{R}_0$) of a NW as a function of pump-probe delay Δt [106]. Since the experimental layout is very similar to the setup discussed in Section 4.2.2 we will only discuss the key differences.

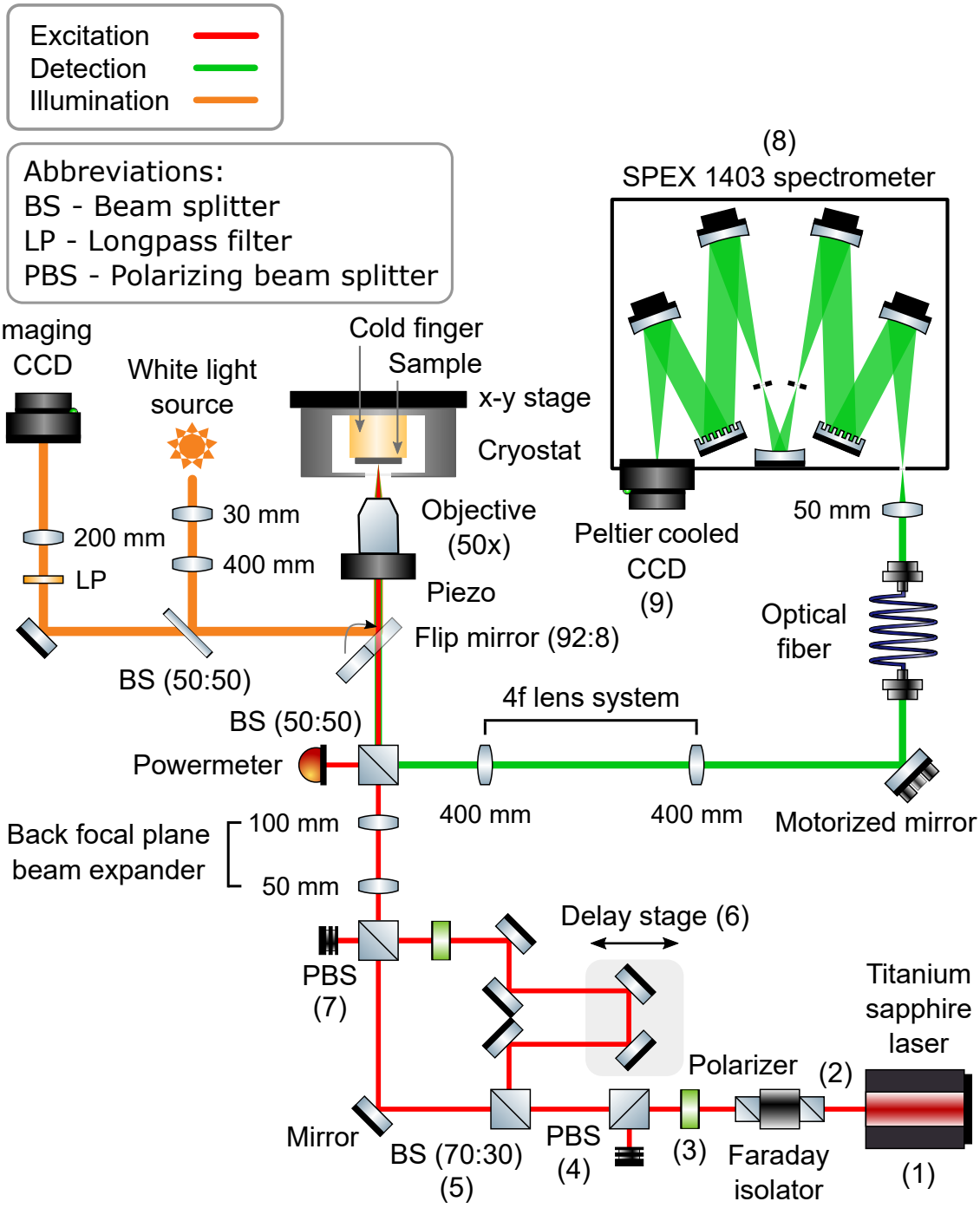

Figure 4.3 | Pump-probe photoluminescence setup. Shown is a simplified sketch of the pump-probe photoluminescence setup. Details are explained in the accompanying text. (The figure was made using graphics from *ComponentLibrary* by Alexander Franzen, licensed under a Creative Commons Attribution-NonCommercial 3.0 Unported License.)

Differential reflectivity

The differential reflectivity is defined by $\Delta\mathcal{R} = \mathcal{R} - \mathcal{R}_0$, were $\mathcal{R}$ and $\mathcal{R}_0$ are the probe reflectivities in the presence and absence of the pump pulse, respectively [106]. In

general, $\Delta\mathcal{R}$ is small and can be approximated by

$$\Delta\mathcal{R} = \frac{\partial\mathcal{R}}{\partial n}\Delta n + \frac{\partial\mathcal{R}}{\partial\kappa_\mathrm{n}}\Delta\kappa_\mathrm{n}, \tag{4.1}$$

with the real (n) and imaginary (κ_n) part of the complex refractive index

$$\tilde{n} = n + i\kappa_\mathrm{n} = \sqrt{1+\chi}, \tag{4.2}$$

where χ is the complex susceptibility [222, 223]. Equations 3.63 to 3.66 in combination with Eq. 4.1, can be combined to show that this method provides access to the temporal dynamics of g_mat and $\Delta n/n$, which in turn are governed by the time-dependent carrier distribution functions $n_{\mathrm{e}\mathbf{k}}$ and $n_{\mathrm{h}\mathbf{k}}$. Further information about transient reflection/absorption techniques is provided in Refs. [106, 222–232].

Experimental setup

As in Section 4.2.2, a beam splitter (1), an optical delay line (2) and polarization optics (3) were used to generate pump and probe pulses with adjustable relative power and time delay (Δt). To generate a differential signal, the pump beam was modulated with an optical chopper system (MC2000B-EC, Thorlabs) (4) at a frequency of 10 kHz. For better distinguishability between pump and probe [228], the pump beam is spectrally filtered by a narrow band pass filter (OSE-VPFHT-12.5C-8080, Laser 2000) (5), which transmits only the high energy part of the pulse spectrum, as shown by the inset (6). Subsequently, the pump beam travels through a back-focal-plane beam-expander (7). This serves a dual purpose. First, it leads to a large spot size on the sample, which allows homogeneous excitation of the NWs. Second, it results in a diverging pump beam in the detection part of the setup, which allows *spatial filtering* of the pump light. Pump and probe are then recombined on a polarizing beam splitter (8). As a result, pump and probe have orthogonal polarization directions, which allows for *polarization filtering* in the detection beam path. After reflection from the sample, the pulses travel through polarization optics (9-11), that correct for any birefringence in the setup and select the polarization direction of the probe. Next, the light is *spectrally filtered* by a long pass filter (FELH0800, Thorlabs) (12) that rejects the pump but transmits the low energy part of the probe. Finally, the light is spatially filtered by an optical fiber before being detected by an avalanche photodiode (APD) (A-CUBE-S500-01, Lasercomponents) (13). The output signal of the APD consists of a DC and an AC voltage component. The DC component gives access to $\mathcal{R}_0$, while the AC component is analyzed by a lock-in amplifier (SR830, Stanford Research Systems) (14) and gives access to $\Delta\mathcal{R}$.

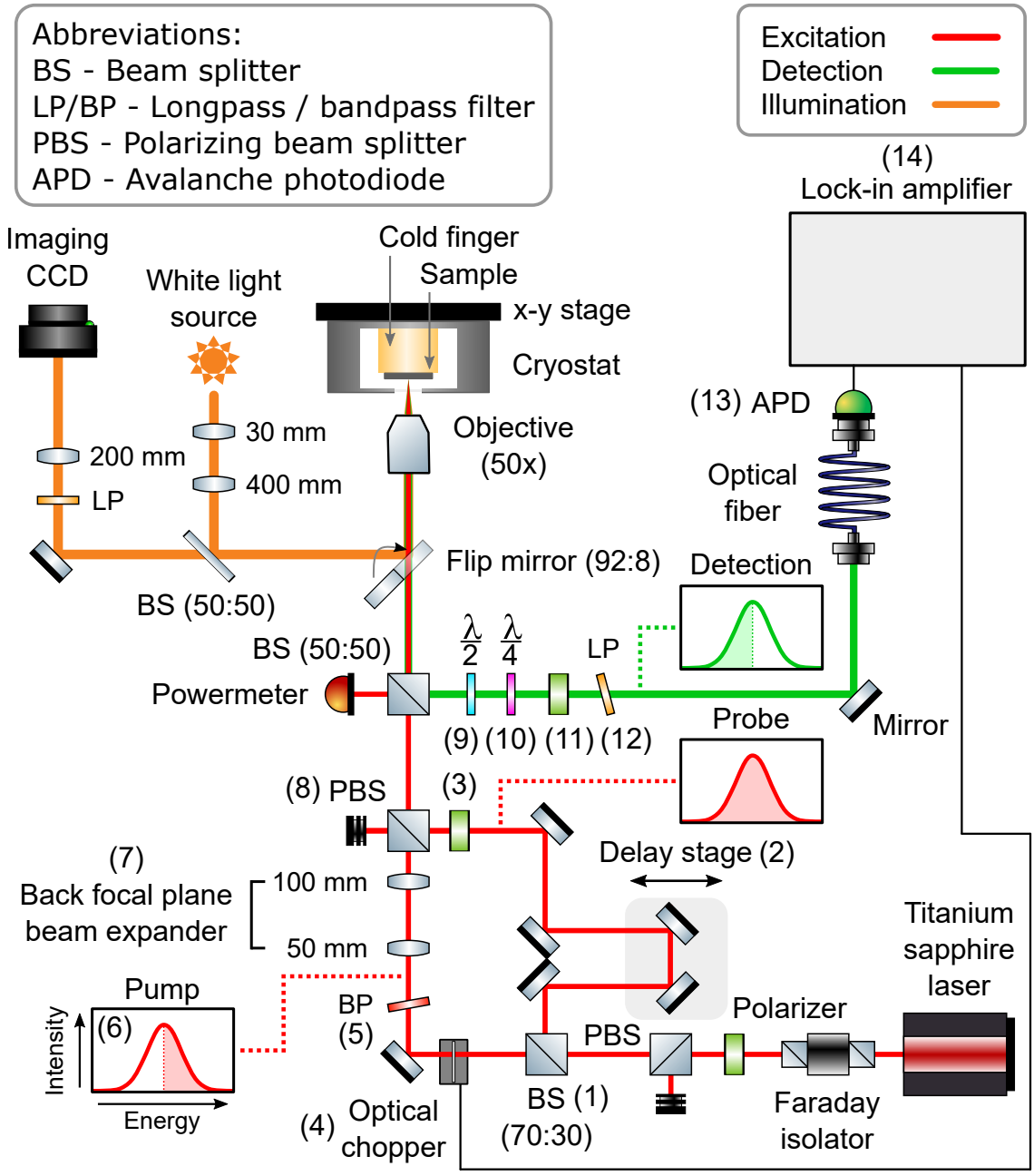

Figure 4.4 | Quasi-degenerate transient reflection setup. Shown is a simplified sketch of the quasi-degenerate transient reflection setup. The insets show sketches of the femtosecond titanium-sapphire laser spectrum. The high energy side of the spectrum is used to pump the sample while the probe uses the entire spectrum. The detection analyzes the low-energy side of the back-reflected laser spectrum and thus detects only the probe. Details are explained in the accompanying text. (The figure was made using graphics from *ComponentLibrary* by Alexander Franzen, licensed under a Creative Commons Attribution-NonCommercial 3.0 Unported License.)

4.3 Summary

In this chapter, we have described the sample preparation and the experimental techniques used to optically characterize the GaAs-AlGaAs core-shell NW lasers. The NWs were grown on Si(111) wafers by molecular beam epitaxy and then mechanically transferred to sapphire substrates for optical investigation. Three different experimental setups were described allowing either microphotoluminescence, pump-probe photoluminescence, or quasi-degenerate transient reflection spectroscopy. The experimental setups presented in this chapter were used to obtain the data analyzed in Chapter 5 and Chapter 6.

Chapter 5

Continuous wave lasing characteristics

Contents

This chapter includes material from

A. Thurn, J. Bissinger, S. Meinecke, P. Schmiedeke, S. S. Oh, W. W. Chow, K. Lüdge, G. Koblmüller and J. J. Finley, 'Self-induced ultrafast electron-hole plasma temperature oscillations in nanowire lasers'. *arXiv:2108.11784* submitted (2021)

In the previous chapters, we have presented the necessary theoretical and experimental background for a detailed study of GaAs-AlGaAs core-shell NW lasers. The ultimate goal of this work is to understand their ultrafast dynamics. However, to achieve this, it is crucial to first gain a detailed understanding of their steady-state properties. In this chapter, we discuss their continuous wave lasing characteristics and show excellent

quantitative agreement with quantum statistical simulations. This direct experiment-theory comparison enables the determination of important laser parameters and shows that the laser linewidth is strongly influenced by non-equilibrium carrier dynamics. The results in this chapter highlight the importance of microscopic theoretical models for a realistic description of GaAs-AlGaAs core-shell NW lasers.

5.1 Method

For an accurate description of the ultrafast dynamical behaviour of NW lasers, finding reliable simulation parameters is crucial. We took advantage of the fact that important parameters such as the end-facet reflectivity (R) and the spontaneous emission factor (β) are approximately the same whether the NW is excited continuously or in a pulsed manner. We therefore measured CW photoluminescence spectra of a NW laser (NW-A) as a function of excitation power and simulated the results using the quantum statistical model. The ultrafast dynamics of the same NW laser will later be investigated in Chapter 6. The CW measurements were performed with an excitation energy of $\epsilon_\mathrm{p} = 1.588\,\mathrm{eV}$ and at a lattice temperature of $T_\mathrm{L} = 10\,\mathrm{K}$. During CW excitation, the laser is in a steady state. This allows to extract the excitation power dependence of properties such as the carrier density (N), carrier temperature (T_c), renormalized band gap energy (ϵ_g) and the broadening of the energy states near the band gap (γ_0) directly from time-integrated measurements of the spontaneous emission spectra. Together with the power dependence of the output intensity (I) and the energy of the lasing mode (ϵ_L), this provides an experimental data set that can be used to adjust and test the simulation parameters of the quantum statistical model. In the following, we first describe the approach used to determine all aforementioned parameters and then present the experimental and simulated results in detail.

5.2 Theoretical model for spontaneous emission spectra

To determine N, T_c, ϵ_g and γ_0 from a measured spontaneous emission spectrum, we fitted it with the theoretical spontaneous emission spectrum given by [9]

$$r_\mathrm{sp}(\omega) = \frac{n_\mathrm{active} e_0^2 \omega}{\hbar \pi c_0^3 \varepsilon_0 m_0^2} |\mathcal{M}_\mathrm{T}|^2 \int_{\epsilon=0}^{\infty} \rho_\mathrm{r}(\epsilon) f_\mathrm{c}(\epsilon)[1 - f_\mathrm{v}(\epsilon)] \mathcal{L}(\epsilon_\mathrm{g} + \epsilon - \hbar\omega) \mathrm{d}\epsilon \,. \tag{5.1}$$

Equation 5.1 can be derived from Eq. 3.73 [128]. For our purposes, it is sufficient to note that the model described by Eq. 5.1 neglects Coulomb enhancement and assumes thermal equilibrium between electrons and holes [128]. Here, ω is the angular frequency, n_active is the refractive index of the NW material and $\mathcal{M}_\mathrm{T}$ the transition

matrix element. Furthermore, e_0 is the elementary charge, $\hbar$ the reduced Planck constant, c_0 the speed of light in vacuum, ε_0 the vacuum permittivity and m_0 the free electron mass. The reduced density of states (ρ_r) and the Fermi functions in the valence (f_v) and conduction band (f_c) depend on the energy (ϵ) and are determined by [9]

$$\rho_\mathrm{r}(\epsilon) = \frac{1}{2\pi^2}\left[\frac{2m_\mathrm{r}}{\hbar^2}\right]^{3/2}\epsilon^{1/2}\,, \tag{5.2}$$

$$f_\mathrm{c}(\epsilon) = \frac{1}{1+\exp\{[\epsilon_\mathrm{g}+(m_\mathrm{r}/m_\mathrm{c}\epsilon-\mu_\mathrm{c})]/[k_\mathrm{B}T_\mathrm{c}]\}} \tag{5.3}$$

and

$$f_\mathrm{v}(\epsilon) = \frac{1}{1+\exp\{[-(m_\mathrm{r}/m_\mathrm{v}\epsilon-\mu_\mathrm{v})]/[k_\mathrm{B}T_\mathrm{c}]\}}\,, \tag{5.4}$$

where k_B is the Boltzmann constant. The quasi-Fermi levels in the valence (μ_v) and conduction band (μ_c) are related to N by the Fermi-Dirac integral. The reduced effective mass $m_\mathrm{r} = m_\mathrm{c}m_\mathrm{v}/(m_\mathrm{c}+m_\mathrm{v})$ is determined by the effective mass of the valence (m_v) and conduction band (m_c), respectively [9]. The broadening of the energy states results mainly from scattering and recombination, and is included in equation (5.1) by the lineshape function $\mathcal{L}(\epsilon)$, which is commonly expressed by a Lorentzian [9]:

$$\mathcal{L}(\epsilon) = \frac{\gamma_\mathrm{L}(\epsilon)}{2\pi}\frac{1}{\epsilon^2+(\gamma_\mathrm{L}(\epsilon)/2)^2}\,. \tag{5.5}$$

Figure 5.1a presents an exemplary spectrum of a NW on a semi-logarithmic scale, measured with a CW excitation power of $P/P_\mathrm{th} \sim 1.7$. Here, the lasing peak ($\sim$ 1.51 eV) is relatively weak, since for this measurement the detection spot was centered in the middle of the NW resonator to maximize the amount of collected spontaneous emission. For the fitting procedure, the lasing peak and Fabry-Pérot modes (blue) were manually removed from the data, leaving only the spontaneous emission spectrum (black). Additionally, the spectrum was normalized to the highest spontaneous emission value. To properly fit both the low and high energy sides of the spectrum, both a Lorentzian line shape function and an energy dependent broadening factor $\gamma_\mathrm{L}(\epsilon)$ are required, as described by equation Eq. 5.5. Phenomenologically, the broadening of the energy states is strong on the low- and weak on the high-energy side of the spectrum and can be described by Landsberg broadening [233–235]

$$\frac{\gamma_\mathrm{L}}{\gamma_0} = 1 - 2.229\left(\frac{\epsilon}{\mu_\mathrm{a}}\right)^1 + 1.458\left(\frac{\epsilon}{\mu_\mathrm{a}}\right)^2 - 0.229\left(\frac{\epsilon}{\mu_\mathrm{a}}\right)^3\,, \tag{5.6}$$

where $\mathrm{a} \in \{\mathrm{e},\mathrm{h}\}$. The Landsberg broadening is valid for $0 \leq \epsilon \leq \mu_\mathrm{a}$, reaches a maximum value of γ_0 at the band edge and approaches zero at the quasi-Fermi level.

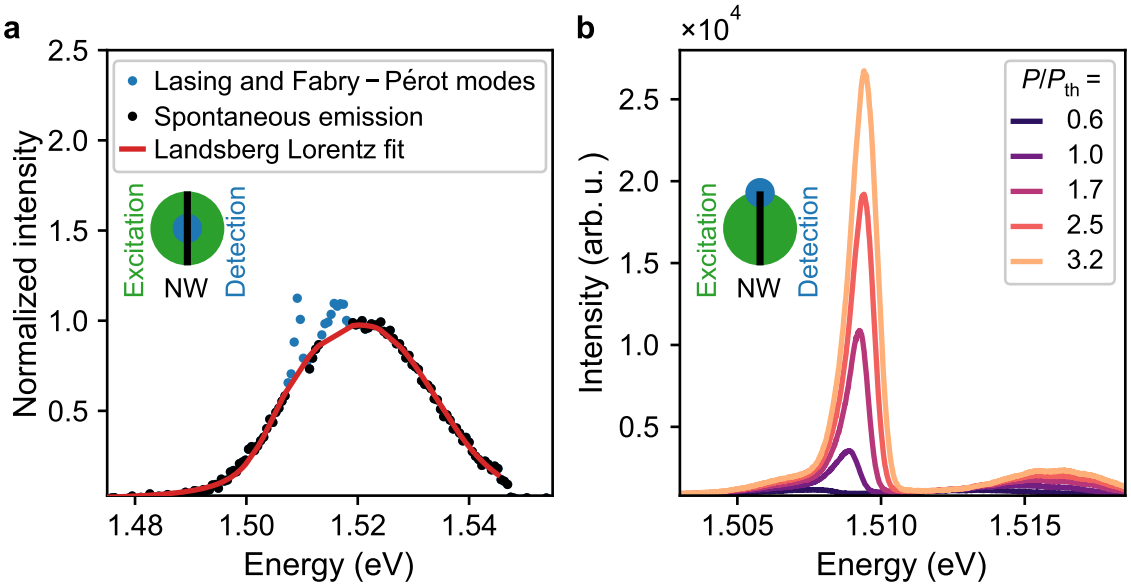

Figure 5.1 | Examples of CW lasing spectra. **a**, Selected spectrum of a NW laser under CW excitation on a semi-logarithmic scale. The spontaneous emission spectrum was obtained by removing the lasing peak and the Fabry-Pérot modes, and was fitted with the model described in equation (5.1). From the fit we obtained the renormalized band gap $\epsilon_g \sim 1.509\,\mathrm{eV}$, the carrier temperature $T_c = (62 \pm 4)\,\mathrm{K}$, the broadening $\gamma_0 = (8.1 \pm 0.8)\,\mathrm{meV}$, and the carrier density $N = (4.0 \pm 0.4) \times 10^{17}\,\mathrm{cm}^{-3}$. The best fit parameters together with their 95 % CIs are given in the plot. **b**, Selected high resolution spectra of the lasing peak for various pump powers (P) relative to threshold (P_{th}). The insets in **a**,**b** show the relative position of the NW (black), excitation spot (green) and detection spot (blue). (Adapted from [68])

Figure 5.1a shows that the fitted Landsberg broadened spectrum shows excellent agreement with the measured data. By fitting each spectrum of a power series in this way, we obtained the values and the power dependence of N, T_c, ϵ_g and γ_0. The best fit parameters for the selected example are listed in Fig. 5.1a.

Additional information about the CW lasing characteristics of NW lasers is obtained from detailed spectra of the lasing peak. Of particular interest for comparison with the simulation is how the laser output power and ϵ_L change with excitation power. For a better resolution of the lasing mode, we repeated the CW excitation measurement from before on the same nanowire but this time detected the NW emission with a double spectrometer (1403, SPEX), allowing a spectral resolution of $\Delta\epsilon < 40\,\mu eV$. For this measurement, the detection spot was positioned on one of the end-facets of the NW laser to maximize the amount of collected stimulated emission. Figure 5.1b shows how the NW emission changes when the excitation power is increased from $P/P_{th} \sim 0.3$ to $P/P_{th} \sim 3.2$. The spectra in Fig. 5.1b show a clear blue shift of the lasing peak and an increase in intensity with increasing excitation power. To determine I, the spontaneous emission was removed from the spectrum and the area under the peak was integrated.

In the following sections below we describe the experimental results, obtained with the procedure outlined above, and discuss the corresponding simulated data, both of which are presented in Fig. 5.2. The simulation parameters of the quantum statistical model are listed in Table 5.1 and Table A.1.

5.3 Light-in light-out curve

Figure 5.2a shows the measured (black) and simulated (red) I as a function of normalized excitation power (P/P_{th}). To allow comparison between experiment and simulation, I was also normalized to its threshold value (I_{th}). We fitted the output intensity above threshold with a linear function (solid cyan line) and determined a CW threshold excitation power of $P_{th} = (4.36 \pm 0.23)\,mW$ via the intersection of the fit with the horizontal axis. With a spot diameter of $\sim 14\,\mu m$ for the CW excitation laser, this corresponds to a power density of $p_{th} = (2.83 \pm 0.15)\,kW\ cm^{-2}$, which is comparable to the CW threshold power density of tin-doped cadmium sulfide NW lasers [236]. The measured light-in light-out curve shows a pronounced nonlinearity around threshold and a linear dependence above, which is a clear indication of lasing and is typical for this type of NW laser. For reasons described in the following, we adjusted the simulated I/I_{th} to the experimental data for one data point above P_{th}, where spontaneous emission is negligible. The resulting agreement of the simulation with the experiment is excellent for all data points above threshold. At and below threshold, the measured

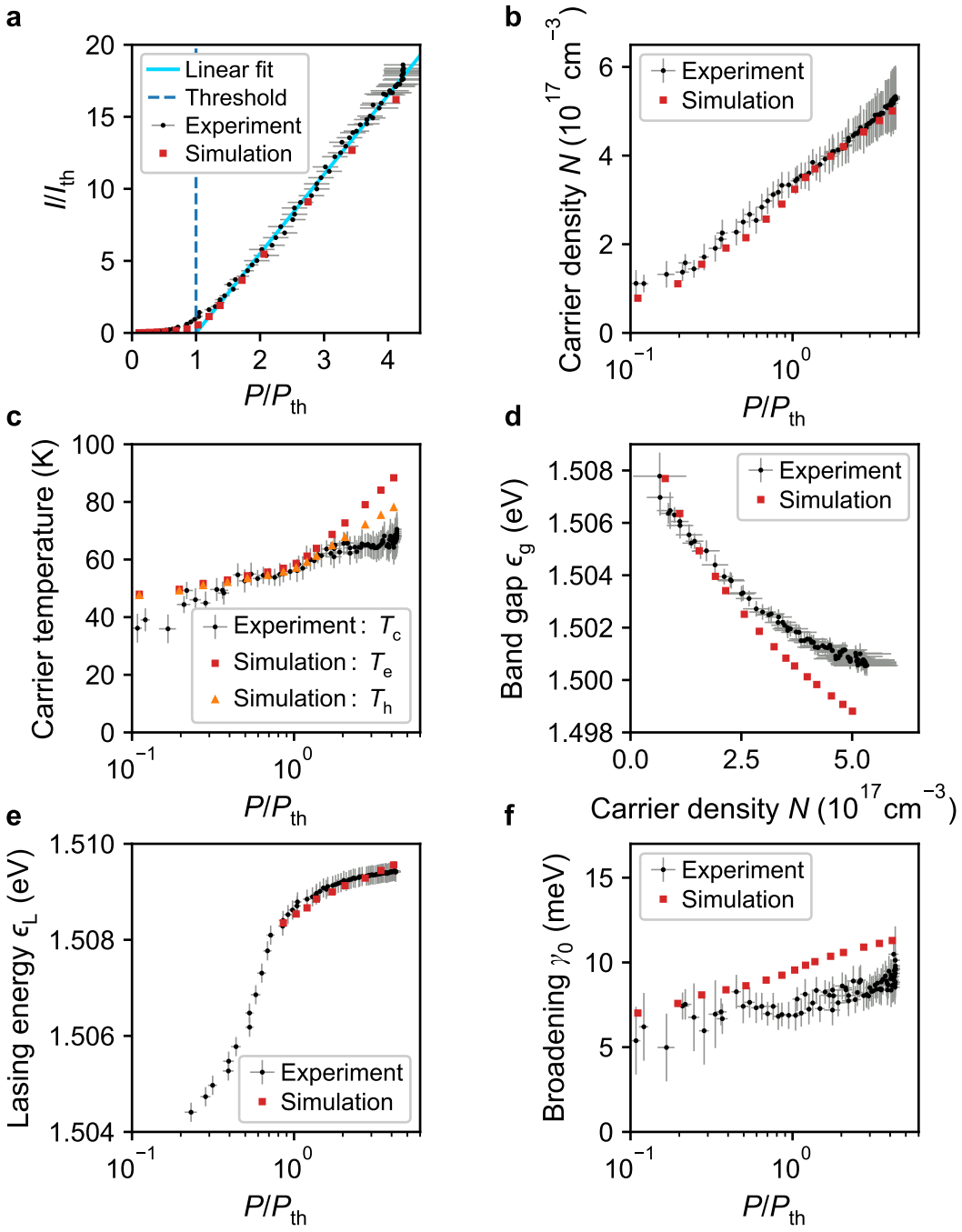

Figure 5.2 | CW lasing characteristics. **a**, Light-in light-out curve on a linear scale. The integrated intensity (I) and excitation power (P) are normalized to their respective threshold values I_{th} and P_{th}. The threshold is determined via the intersection of the linear fit with the horizontal axis. **b**,**c**, The carrier density (N) and the carrier temperatures (T_{c}, T_{e} and T_{h}) are only partially clamped for $P/P_{\mathrm{th}} > 1$ due to carrier heating via stimulated emission. The apparent saturation of T_{c} in **c** for $P/P_{\mathrm{th}} > 2$ is a measurement artefact. **d**, The band gap ϵ_{g} redshifts with increasing N. **e**, Changes in the refractive index lead to a strong blueshift of the lasing energy ϵ_{L}, which weakens for $P/P_{\mathrm{th}} > 1$ due to partial gain clamping. **f**, The simulated broadening γ_0 is in good agreement with the values obtained from experiment using the phenomenological Landsberg model, as described by Eq. 5.6. All error bars represent $95\,\%$ CIs of the mean. In **e**, the error bars reflect the calibration of the spectrometer, whereas in **b**-**d** and **f** the uncertainties result from the fit of equation Eq. 5.1 to the measured spontaneous emission spectra. For all panels, the uncertainty of the excitation power follows from the determination of P_{th}, see **a**. (Adapted from [68])

intensities are slightly larger ($\sim 10\,\%$) than the values predicted by the simulation. There are two main reasons for this behaviour. The first is the measurement geometry. We excited the NW, that was lying horizontally on a substrate, from the top, using the same objective for excitation and detection. Since spontaneous emission has an isotropic radiation characteristic compared to stimulated emission, which is directed along the NW axis, this measurement geometry leads to an overestimation of the amount of spontaneous emission into the lasing mode. The second reason is that the determination of the emission into the laser mode below threshold is challenging. The shape of the simulated data can be adjusted by β_{sp}. For this NW laser we achieved best agreement with the experimental data above P_{th} for $\beta_{\mathrm{sp}} = 0.1$, which is in full accord with values found in literature [44, 47, 237].

5.4 Carrier density and carrier temperature

In Fig. 5.2b we observe that N increases with P/P_{th}. It increases even above P_{th}, although with a slightly reduced slope. Thereby, N changes from $N = (3.4 \pm 0.3) \times 10^{17}\,\mathrm{cm}^{-3}$ at P_{th} to $N = (5.3 \pm 0.6) \times 10^{17}\,\mathrm{cm}^{-3}$ at $P/P_{\mathrm{th}} \sim 4.3$. For the whole range of excitation powers the simulated carrier densities are in excellent quantitative agreement with the experimental data.

Figure 5.2c shows that, similar to N, also the measured T_{c} increases with P/P_{th}, even above threshold. It ranges from $T_{\mathrm{c}} = (36 \pm 5)\,\mathrm{K}$ at $P/P_{\mathrm{th}} \sim 0.11$ to $T_{\mathrm{c}} = (70 \pm 6)\,\mathrm{K}$ at $P/P_{\mathrm{th}} \sim 4.3$. The apparent saturation of T_{c} for $P/P_{\mathrm{th}} > 2$ is a measurement artefact due to a longpass filter that was used to remove the excitation laser. This filter sharply cuts off the NW emission at $\sim 1.55\,\mathrm{eV}$, leading to a systematic underestimation of T_{c} in this range by a few K, while leaving the other fit parameters unaffected. This argument is substantiated by the fact that for $P/P_{\mathrm{th}} > 2$ the carrier density N in Fig. 5.2b keeps increasing, which is only possible if the T_{c} increases simultaneously. This increase in T_{c} is caused by the increased stimulated emission rate with increased P/P_{th}, which heats up the carrier distribution, as will be discussed later in Section 6.2. Due to this photoinduced heating of the carrier distribution, an increase in N is necessary to maintain the gain required for lasing. Thus, the gain is only partially clamped above threshold.

For excitation powers from $P/P_{\mathrm{th}} \sim 0.2$ to $P/P_{\mathrm{th}} \sim 2$, the simulated electron (T_{e}) and hole (T_{h}) temperatures are in excellent quantitative agreement with the measurement, whereas for $P/P_{\mathrm{th}} < 0.2$ they slightly overestimate the experimental results. For high excitation powers ($P/P_{\mathrm{th}} > 2$) the simulated carrier temperatures are observed to further increase, as expected from the behaviour of the simulated N in Fig. 5.2b. Over the investigated range of excitation powers, T_{e} and T_{h} reach maximum

values of $T_e = 88\,K$ and $T_h = 78\,K$, respectively. The model additionally predicts that T_e is slightly larger than T_h with an increasing gap between the two as P/P_{th} increases. However, this cannot be tested with our experimental approach.

The main simulation parameter which influences the behaviour of T_e and T_h and also the power dependence of the T_c is the end-facet reflectivity R of the NW. A higher reflectivity leads to an increased stimulated emission rate, which results in a stronger increase of T_e, T_h and N as a function of P/P_{th}. Best agreement with the experiment was achieved for an end-facet reflectivity of $R = 0.5$, which is in full accord with values in literature [46, 47].

5.5 Band gap narrowing

Figure 5.2d shows the measured ϵ_g (black) as a function of N taken from Fig. 5.2b. As N is increased from $(0.7 \pm 0.6) \times 10^{17}\,cm^{-3}$ to $(5.3 \pm 0.7) \times 10^{17}\,cm^{-3}$, the measured ϵ_g decreases from $\sim 1.508\,eV$ to $\sim 1.501\,eV$. A similar decrease of ϵ_g is calculated with the simulation (red). We observe very good quantitative agreement between experiment and theory, although for $N > 2.5 \times 10^{17}\,cm^{-3}$ the simulated band gap narrowing is slightly overestimated, with a maximum deviation of $\sim 2\,meV$. The band gap energy of unexcited bulk GaAs at $T_L = 10\,K$ was taken from literature [99], see Table A.1. The simulated band gap narrowing is determined purely from many-body Coulomb interactions and is not directly adjusted by any simulation parameter. Thus, the comparison with the experiment in Fig. 5.2d provides a good validation of our simulation model.

5.6 Lasing energy

From spectra such as in Fig. 5.1b, ϵ_L was determined as a function of P/P_{th}. In the experimental data this was reliably possible for excitation powers $P/P_{th} > 0.2$. In Fig. 5.2e, we observe a strong increase of ϵ_L from $(1.5044 \pm 0.0002)\,eV$ to $(1.5086 \pm 0.0002)\,eV$ as the excitation power is increased from $P/P_{th} \sim 0.2$ up to threshold. The reason for this increase is explained by a decrease in refractive index, which is caused by the combined interplay of band gap renormalization and the increased gain with larger N. Above threshold, the gain is partially clamped, resulting in a reduced blueshift, with ϵ_L further increasing up to $(1.5094 \pm 0.0002)\,eV$ at $P/P_{th} \sim 4.2$. For the simulations, we used a heuristic refractive index model of bulk GaAs from literature [139, 211]. Its input parameters do not include any external fit parameters and were exclusively calculated using the quantum statistical model, i.e. a shift in ϵ_L is caused entirely by a change in the microscopic dynamic variables. Only the

absolute value of the simulated ϵ_L at threshold was adjusted to the experiment. We achieved this by first setting the laser length to $L \sim 10\,\mu m$ using the microscope image in Fig. 6.5 and then slightly fine-tuning it to $L \sim 10.15\,\mu m$. This last step had no effect on the lasing dynamics. As can be seen in Fig. 5.2e, our approach resulted in excellent quantitative agreement with the experiment.

5.7 Broadening

Figure 5.2f shows the experimentally determined γ_0 as a function of P/P_{th}. The values range from $\gamma_0 = (5.0 \pm 2.0)\,meV$ at $P/P_{th} \sim 0.17$ to $\gamma_0 = (10.5 \pm 1.0)\,meV$ at $P/P_{th} \sim 4.2$. It is observed that γ_0 does not increase continuously with increasing P/P_{th}, but exhibits a small decrease to $\gamma_0 = (6.9 \pm 0.9)\,meV$ near threshold.

In the quantum statistical model, the energy broadening is given by Eq. 3.75. Similar to the Landsberg model, this simulated broadening is in general energy dependent. In Fig. 5.2f we therefore only compare the broadening values near the band edge ($\gamma_{eh}(0) = \gamma_0$). Over the investigated range of P/P_{th}, the simulated γ_0 exhibits a continuous increase from $\sim 7\,meV$ to $\sim 11.3\,meV$. Remarkably, the simulated results are very close to the experimental values that were determined using the phenomenological Landsberg model and also exhibit a very similar behaviour above threshold. We emphasize that the simulated γ_0 contained no fit parameters, as it was calculated solely from the scattering rates of the quantum statistical model.

5.8 Simulation parameters

Table 5.1 summarizes the parameters used for the quantum statistical simulations in Fig. 5.2. We note that β_{sp} and R were the only free parameters. The same set of parameters is later used in Section 6.2 to simulate the NW laser dynamics following pulsed excitation.

5.9 Comparison of different nanowire lasers

To demonstrate that the CW lasing characteristics of NW-A are typical, we present in Fig. 5.3 data recorded from several other NW lasers (NW-B to NW-F) from the same sample. For all NWs, the excitation power dependence of output power, carrier density, carrier temperature, and lasing energy is very similar and behaves as discussed in Section 5.1 to Section 5.7. In addition, in Fig. 5.3e we present the excitation power dependence of their linewidth given in terms of the full width at half maximum (FWHM). For all NW lasers, a characteristic decrease in linewidth can be observed

Name	Symbol	Value	Source
Confinement factor	Γ	1.2	COMSOL Multiphysics
Excitation pulse duration	Δt_{pump}	200 fs	Measurement
Excitation photon energy	ϵ_{p}	1.588 eV	Measurement
Lattice temperature	T_{L}	10 K	Measurement
Nanowire length	L	10 µm	Microscope images
Nominal nanowire radius	R_{NW}	170 nm	Growth protocol
End-facet reflectivity	R	0.5	Free parameter
Spontaneous emission factor	β_{sp}	0.1	Free parameter

Table 5.1 | Simulation parameters of the many-body laser theories. The listed parameters were used for both the quantum statistical and the semiconductor Bloch model. The values for Γ, L, R and β_{sp} are in full accord with literature [44, 46, 47, 237]. Natural constants and material parameters are listed in Table A.1. (Adapted from [68])

when the excitation power is increased up to threshold [117, 173]. Above threshold, the linewidth then increases again. This behavior is typical for GaAs-AlGaAs core-shell NW lasers and is consistent with the results of previous work [133, 238]. From Fig. 5.3d,e it can be seen that the FWHM is depends on the lasing energy ϵ_{L}. This is summarized in Fig. 5.3f, which shows that the FWHM at threshold increases with increasing ϵ_{L}.

One can qualitatively understand this dependence with the help of Fig. 5.4, where we show an example of material gain (G_{mat}) and differential material gain spectra ($\partial G_{\mathrm{mat}}/\partial T_{\mathrm{c}}$) for a carrier temperature of $T_{\mathrm{c}} = 50\,\mathrm{K}$ and a carrier density of $N = 6 \times 10^{17}\,\mathrm{cm}^{-3}$ [128]. For this simulation, electrons and holes were considered to be in thermal equilibrium and the energy broadening was set to a constant value of $\gamma_{\mathrm{eh}} = 8\,\mathrm{meV}$ [128]. Compared to the material gain maximum, the differential material gain maximum is shifted towards higher energies, which is consistent with expectations from literature [239–241]. The important point of Fig. 5.4 is that within the spectral range where NW modes can lase ($G_{\mathrm{mat}} > 0$), the differential material gain increases as a function of energy.

A phenomenological explanation of why this increases the linewidth is given in Ref. [242]. In short, carrier heating leads to an output power dependent α-factor, which introduces additional broadening terms in the Schawlow-Townes-Henry linewidth given by Eq. 3.30 [242]. Since the strength of carrier heating is directly related to $\partial G_{\mathrm{mat}}/\partial T_{\mathrm{c}}$, this means that a larger $\partial G_{\mathrm{mat}}/\partial T_{\mathrm{c}}$ leads to a broader linewidth, as demonstrated by the data in Fig. 5.3f and Fig. 5.4. A more sophisticated theoretical description is presented in Section 5.10, using the quantum statistical model.

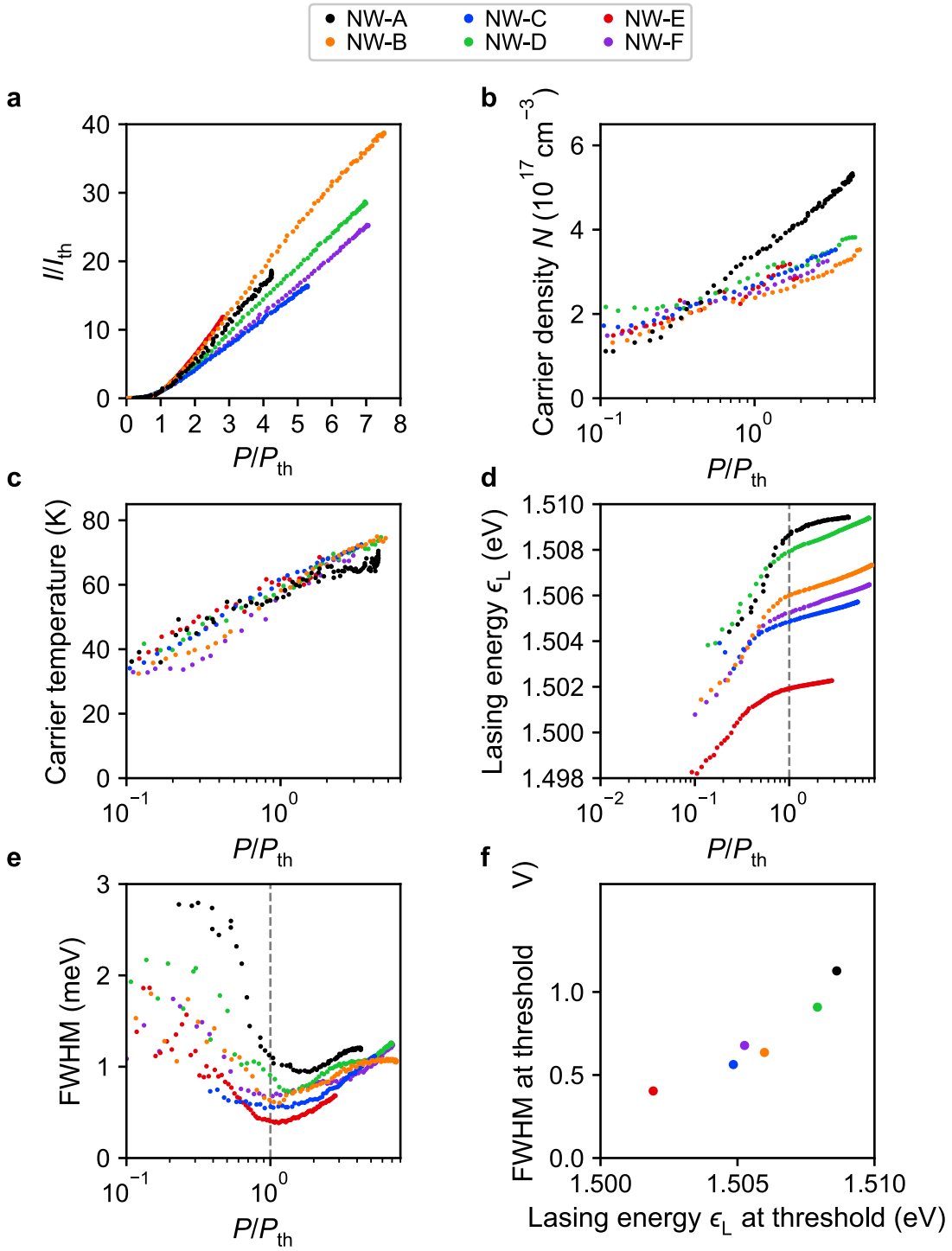

Figure 5.3 | CW lasing characteristics of several nanowire lasers. NW-A was discussed in Section 5.3 to Section 5.8. **a**, Light-in light-out curve on a double logarithmic scale. The integrated intensity (I) and excitation power (P) are normalized to their respective threshold values I_{th} and P_{th}. **b**-**e** All NW lasers show similar behaviour in the excitation power dependence of the carrier density (N), carrier temperature (T_{c}), lasing energy (ϵ_{L}), and full width at half maximum (FWHM) of the lasing mode. All lasing modes show a characteristic drop in linewidth as the excitation power is increased from below to above threshold. **f**, The FWHM strongly depends on the lasing energy ϵ_{L} of the lasing mode at threshold. The threshold values of the FWHM and lasing energy were taken from **d** and **e**, respectively, as indicated by vertical dashed lines.

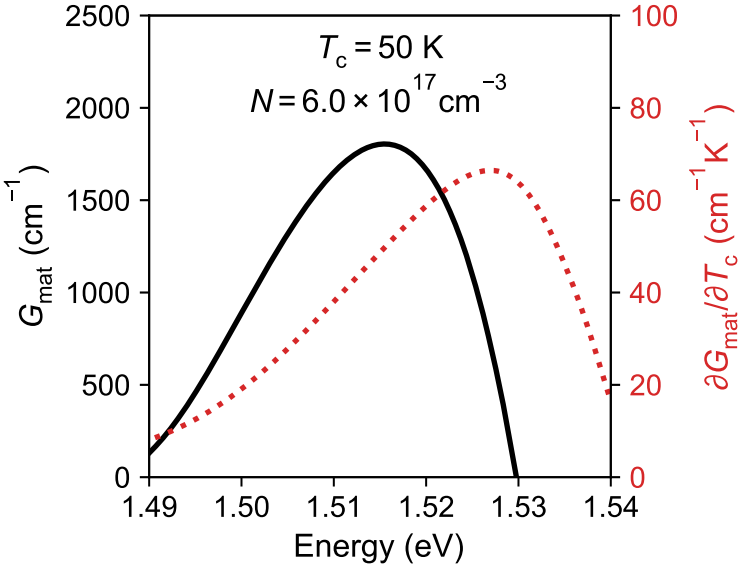

Figure 5.4 | Material and differential material gain spectrum. Exemplary material gain (G_{mat}) spectrum for a carrier temperature of $T_{\mathrm{c}} = 50\,\mathrm{K}$ and a carrier density of $N = 6 \times 10^{17}\,\mathrm{cm}^{-3}$. For this simulation, electrons and holes are considered to be in thermal equilibrium. Furthermore, a constant broadening of $\gamma_{\mathrm{eh}} = 8\,\mathrm{meV}$ was used. The corresponding differential material gain spectrum with respect to carrier temperature ($\partial G_{\mathrm{mat}}/\partial T_{\mathrm{c}}$) is shown in red. Compared to the material gain maximum, the differential material gain maximum is shifted towards higher energies. (Adapted from [128])

5.10 Laser linewidth

A detailed theoretical analysis of the CW data from NW-B measured in this thesis was performed by Jochen Bissinger in Ref. [128]. Here, we focus on the CW linewidth of NW-B, which is shown in Fig. 5.5 as a function of NW output intensity (I) normalized to its threshold value (I_{th}) [128]. As the output power increases, the linewidth first decreases from $\sim 1\,\mathrm{meV}$ well below threshold to $\sim 0.6\,\mathrm{meV}$ at threshold and then increases again to $\sim 1\,\mathrm{meV}$ far above threshold. Along with the experimental data, we also show the corresponding simulations with both the two-level rate equation approach (RE) and the quantum statistical model (QS) [128]. The rate equation simulation is based on Eq. 3.26 and shown for three different values of the linewidth enhancement factor α, with $\alpha \in \{1.5, 3, 4.5\}$. All rate equation simulation parameters are listed in Ref. [128]. It is clear that regardless of the value of α, the rate equation approach is unable to describe the NW laser linewidth. This is in contrast to the quantum statistical model, which yields excellent quantitative agreement over the entire measurement range. It reveals that the increase in linewidth above threshold results from non-equilibrium carrier dynamics that lead to increased spontaneous emission and refractive index fluctuations and a reduction in gain-loss compensation [153, 243]. These results and conclusions are consistent with earlier work on the linewidth of

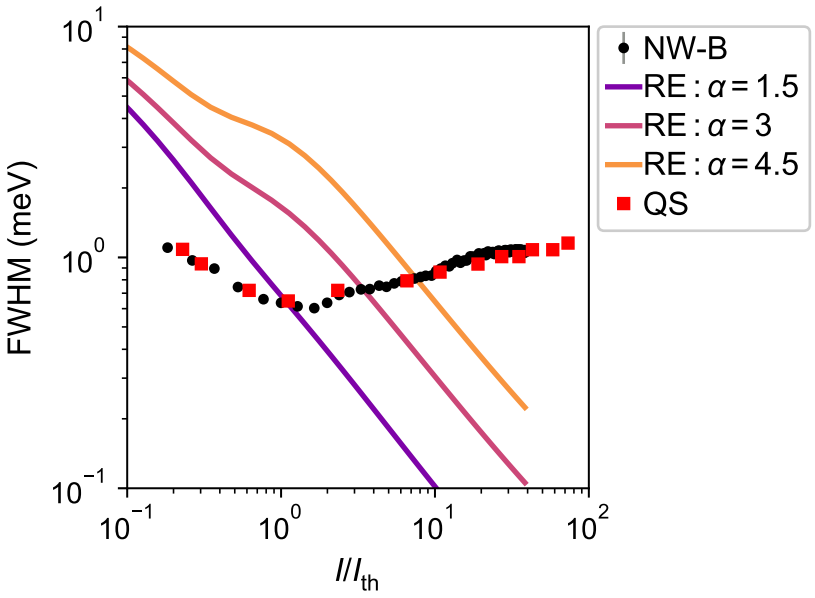

Figure 5.5 | CW laser linewidth. The measured CW linewidth of NW-B was simulated with both the two-level rate equation approach (RE) and the quantum statistical model (QS). The rate equation simulation based on Eq. 3.26 is shown for three different values of the linewidth enhancement factor α. It is clear that the Schawlow-Townes and Schawlow-Townes-Henry theory is unable to describe the NW linewidth, while the quantum statistical model provides excellent quantitative agreement over the entire measurement range. The NW output intensity (I) is normalized to its threshold value (I_{th}). (Adapted from [128])

semiconductor microdisk lasers [153]. Returning to Fig. 5.3b-c, it is thus mainly the pronounced increase in carrier temperature and the resulting depinning of the carrier density above threshold that leads to the strong deviation of the NW linewidth from the Schawlow-Townes-Henry theory [153]. These insights are crucial for a detailed understanding of GaAs-AlGaAs core-shell NW lasers and critical for the design of future NW laser systems for e.g. on-chip optical communication. For further discussion about the linewidth of semiconductor lasers, see Refs. [101, 117, 152, 244–247].

5.11 Summary

In this chapter, we studied the CW lasing characteristics of GaAs-AlGaAs core-shell NW lasers in detail. First, we discussed how several important laser parameters, including carrier density and temperature, can be determined from a spectrum. We then measured these CW lasing parameters as a function of excitation power and simulated the results using the quantum statistical model. This yielded excellent quantitative agreement between experiment and theory and demonstrated that the quantum statistical model provides an accurate microscopic model for the investigated NW lasers. We then analyzed several NW lasers experimentally and showed that they all exhibit very similar properties. In doing so, we found that the laser linewidth broadened

with increasing lasing energy ϵ_{L}. This observation was qualitatively explained by the fact that $\partial G_{\mathrm{mat}}/\partial T_{\mathrm{c}}$ increases with energy, which then leads to a broadened linewidth as described by an extended rate equation theory [242]. Finally, we studied in detail the excitation power dependence of the NW linewidth and demonstrated that it deviates strongly from expectations based on the Schawlow-Townes-Henry theory. The main reason for this is the pronounced increase in carrier temperature above threshold and the resulting depinning of the carrier density, which leads to enhanced spontaneous emission and refractive index fluctuations as well as reduced gain-loss compensation [153]. The results in this chapter are critical to the microscopic understanding of NW lasers and serve as a basis for understanding their ultrafast temporal dynamics, which will be investigated in the next chapter.

Chapter 6

Lasing dynamics

Contents

This chapter includes material from

A. Thurn, J. Bissinger, S. Meinecke, P. Schmiedeke, S. S. Oh, W. W. Chow, K. Lüdge, G. Koblmüller and J. J. Finley, 'Self-induced ultrafast electron-hole plasma temperature oscillations in nanowire lasers'. *arXiv:2108.11784* submitted (2021)

In the previous chapter, we showed that the CW lasing characteristics of GaAs-AlGaAs core-shell NW lasers are strongly influenced by non-equilibrium carrier dynamics. In this chapter, we continue to investigate how these non-equilibrium effects influence their lasing dynamics. Using the two-level rate equation approach, we first analyze their response to modulation and pulsed excitation, taking into account gain saturation. This discussion yields a simple prediction for their output pulse shape, which will be proven to be incomplete in the next section. There, we use a combined experimental and theoretical approach to show that the NW output pulses exhibit sustained intensity oscillations with frequencies ranging from 160 GHz to 260 GHz. We demonstrate that these oscillations correspond to an exceptionally strong non-equilibrium analog of relaxation oscillations [150], which are enabled by the miniaturized dimensions of the laser and the resulting competition between carrier heating and cooling in the electron-hole plasma during lasing operation. In the next section, we then show that fundamental aspects of these non-equilibrium NW laser dynamics can be reproduced by phenomenologically extending the two-level rate equation approach to a three-level system. Using this model, we reveal that the oscillations discussed in the previous section correspond to a previously unknown resonance between the carrier temperature and the photon density. In the final section, we then present first experimental results based on quasi-degenerate transient reflection spectroscopy.

6.1 Two-level rate equation analysis

The two-level rate equation approach allows to obtain an approximate understanding of the dynamics of GaAs-AlGaAs core-shell NW lasers. This understanding is then developed in greater detail in the following sections using more sophisticated models.

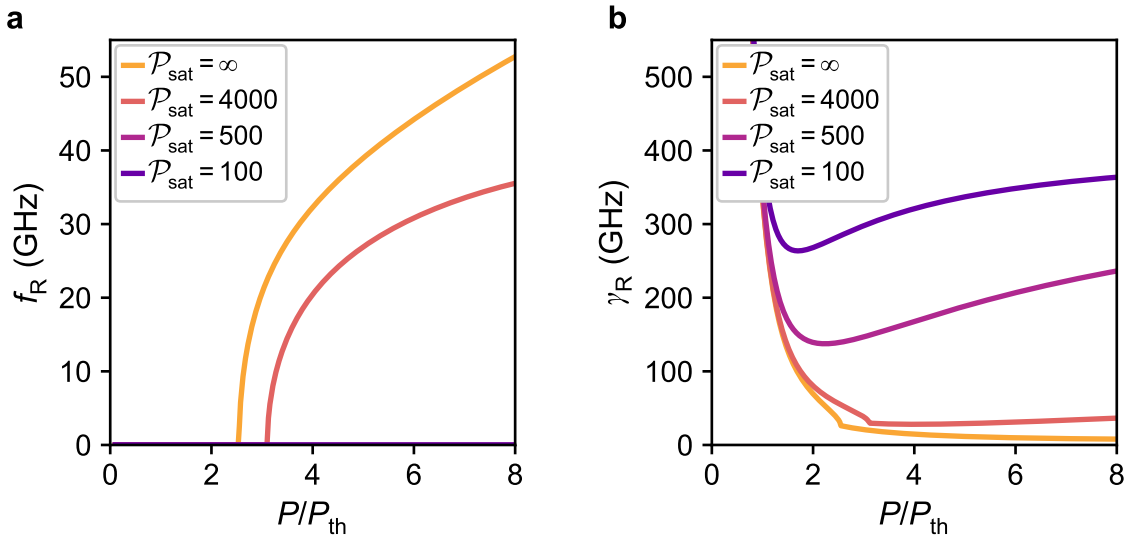

Figure 6.1 | Relaxation oscillation frequency and damping rate. a,**b**, Relaxation oscillation frequency $f_R = \frac{\Omega_R}{2\pi}$ and damping rate of relaxation oscillations $\gamma_R = \frac{\Gamma_R}{2\pi}$ as a function of excitation power (P) normalized to its threshold value (P_{th}). An ideal NW laser ($\mathcal{P}_{sat} = \infty$) exhibits relaxation oscillations. When gain saturation is taken into account, γ_R increases and f_R decreases. For gain saturation values expected for NW lasers ($\mathcal{P}_{sat} = 100$ to 500 [128, 133]), relaxation oscillations are overdamped and f_R is equal to zero. The simulation parameters are listed in Table 6.1.

6.1.1 Relaxation oscillation frequency

One of the most important dynamical properties of a laser is the frequency of relaxation oscillations $f_R = \frac{\Omega_R}{2\pi}$ [9, 117]. This is the natural resonance frequency between the carrier number $\mathcal{N}$, described by Eq. 3.1, and the photon number $\mathcal{P}$, described by Eq. 3.2. The associated resonance is called carrier-photon resonance [248]. Figure 6.1 shows f_R and the corresponding damping rate of the relaxation oscillations $\gamma_R = \frac{\Gamma_R}{2\pi}$ as a function of normalized excitation power (P/P_{th}). Both f_R and γ_R were obtained from Eq. 3.22 after numerically solving the rate equations given by Eq. 3.1 and Eq. 3.2. Figure 6.1a shows, that for an ideal NW laser ($\mathcal{P}_{sat} = \infty$), the relaxation oscillation frequency scales as $f_R \propto P^{1/2} \propto \mathcal{P}^{1/2}$, which is consistent with expectations from literature [9, 117]. From comparison with Fig. 6.1b it can be seen that relaxation oscillations appear as soon as γ_R is sufficiently small. When gain saturation is taken into account, γ_R increases while f_R decreases. For the gain saturation values expected for NW lasers ($\mathcal{P}_{sat} = 100$ to 500 [128, 133]), γ_R becomes too large for oscillations to occur and f_R becomes equal to zero. As a result, relaxation oscillations are not expected for the GaAs-AlGaAs core-shell NW lasers studied in this thesis. This is consistent with modulation experiments performed on indium phosphide based NW lasers [249].

Name	Symbol	Value	Source
Confinement factor	Γ	1.2	COMSOL Multiphysics
Group index	n_g	7	COMSOL Multiphysics
Nanowire length	L	10 µm	Microscope images
Nominal nanowire radius	R_{NW}	170 nm	Growth protocol
Spont. emission lifetime	τ_{spon}	740 ps	Quantum stat. model
Spont. emission factor	β_{sp}	0.1	Quantum stat. model
Gain parameter	G_0	$3.98 \times 10^3\,\mathrm{cm}^{-1}$	Log. gain approx.
Gain parameter	$\mathcal{N}_s/V_{NW}$	$2.38 \times 10^{17}\,\mathrm{cm}^{-3}$	Log. gain approx.
Gain parameter	$\mathcal{N}_{tr}/V_{NW}$	$2.2 \times 10^{17}\,\mathrm{cm}^{-3}$	Log. gain approx.
End facet reflectivity	R	0.3	Free parameter

Table 6.1 | Simulation parameters of the two-level rate equation theory. The gain parameters where determined by fitting the logarithmic gain approximation given by Eq. 3.12 to a microscopic gain model using a lattice temperature of $T_L = 10\,\mathrm{K}$ and a carrier temperature of $T_c = 55\,\mathrm{K}$ [128]. In order for the rate equation model to have a threshold carrier density that is close to the experiment and the quantum statistical model ($N_{th} \sim 3.4 \times 10^{17}\,\mathrm{cm}^{-3}$), R was adjusted to 0.3. The values listed here were used for all two-level rate equation simulations, unless specified otherwise. (Values were taken from [128] and [68])

6.1.2 Modulation response

Figure 6.1a provides the relaxation oscillation frequency f_R but not any information about the strength of the corresponding carrier-photon resonance. To calculate this missing information, we introduce in Eq. 3.1 a time-dependent pump power according to

$$P(t) = P + \delta P(t). \tag{6.1}$$

Here, P is a constant, while the time-dependent modulation is given by

$$\delta P(t) = \delta P_0 \sin(2\pi f_{mod} t), \tag{6.2}$$

where δP_0 is the modulation amplitude and f_{mod} the modulation frequency. For the following calculations we choose $\delta P_0 = 0.05 \cdot P$. The time-dependent modulation power $\delta P(t)$ translates to a time-dependent deviation in the photon number described by

$$\delta \mathcal{P}(t) = \delta \mathcal{P}_0(f_{mod}) \sin(2\pi f_{mod} t), \tag{6.3}$$

where the amplitude $\delta \mathcal{P}_0$ depends on f_{mod}. Expressions similar to Eq. 6.3 hold for the carrier number $\mathcal{N}$ and the phase ϕ. Using Eq. 6.3, the modulation response is defined as [117]

$$M(f_{mod}) = 10 \log_{10}\left(\frac{\delta \mathcal{P}_0(f_{mod})}{\delta \mathcal{P}_0(0)}\right). \tag{6.4}$$

The expression $\delta\mathcal{P}_0(0)$ is understood to be defined in the limit $f_{\mathrm{mod}} \to 0$. Figure 6.2 shows M as a function of f_{mod} and P/P_{th} for an ideal NW laser with $\mathcal{P}_{\mathrm{sat}} = \infty$. The modulation response exhibits a clear resonance, centered around the relaxation oscillation frequency f_{R}, with an overall maximum of $\sim 5\,\mathrm{dB}$. To illustrate how the carrier-photon resonance changes with gain saturation, Fig. 6.2b shows cuts through the surface for $P/P_{\mathrm{th}} = 8$. The position of the cuts is indicated in Fig. 6.2a by the blue line. As gain saturation increases (smaller $\mathcal{P}_{\mathrm{sat}}$), the resonance peak shifts to lower frequencies and decreases. For $\mathcal{P}_{\mathrm{sat}}$ in the range from 100 to 500 the resonance disappears completely. This means that no relaxation oscillations are possible for these types of NWs. This is a significant drawback if GaAs-AlGaAs-core-shell NW lasers are to be used for high-speed data communication using standard modulation techniques [9].

For practical purposes, the frequency up to which a semiconductor laser can be modulated is defined as $M(f_{3\mathrm{dB}}) = -3\,\mathrm{dB}$ [117, 168]. In Fig. 6.1b the 3 dB frequencies for $\mathcal{P}_{\mathrm{sat}} = 100$ and $\mathcal{P}_{\mathrm{sat}} = 500$ are indicated by vertical dashed lines. For realistic excitation powers ($P/P_{\mathrm{th}} \leq 8$), GaAs-AlGaAs core-shell NW lasers are therefore expected to have 3 dB frequencies in the range from $\sim 3\,\mathrm{GHz}$ to $\sim 15\,\mathrm{GHz}$. These 3 dB frequencies are in agreement with modulation experiments performed on indium phosphide based NW lasers [249] and lower than the values reported in literature for other semiconductor lasers [168]. However, it should be kept in mind that the studied NW lasers have not yet been optimized for modulation speed and that NW lasers have the unique advantage that they can be grown site-selectively and monolithically on silicon waveguides. One possible way to improve the 3 dB frequency of NW lasers could be to use radial quantum wells as the gain medium [52, 54].

6.1.3 Pulsed excitation

For the understanding of the experiments presented in the next section, the response of GaAs-AlGaAs core-shell NW lasers to excitation with ultrashort pump pulses is of primary interest. For the simulation presented in Fig. 6.3, the excitation pulses were modeled using Dirac delta distributions and the normalized excitation power was set to $P/P_{\mathrm{th}} = 3$. It can be seen from Fig. 6.3a that gain saturation has a significant effect on the NW output pulse length and shape. As gain saturation increases, the output pulses become longer and increasingly asymmetric in time, with a sharp rise and a long tail, consistent with expectations from literature [250, 251]. While for an ideal NW laser without gain saturation the total output pulse length is $< 1\,\mathrm{ps}$, for strong gain saturation with $\mathcal{P}_{\mathrm{sat}} = 100$ it can be $> 100\,\mathrm{ps}$. For GaAs-AlGaAs core-shell NW lasers, typical values for $\mathcal{P}_{\mathrm{sat}}$ are in the range from 100 to 500 [128, 133]. It should be noted that the output pulse length in the ideal case is certainly underestimated,

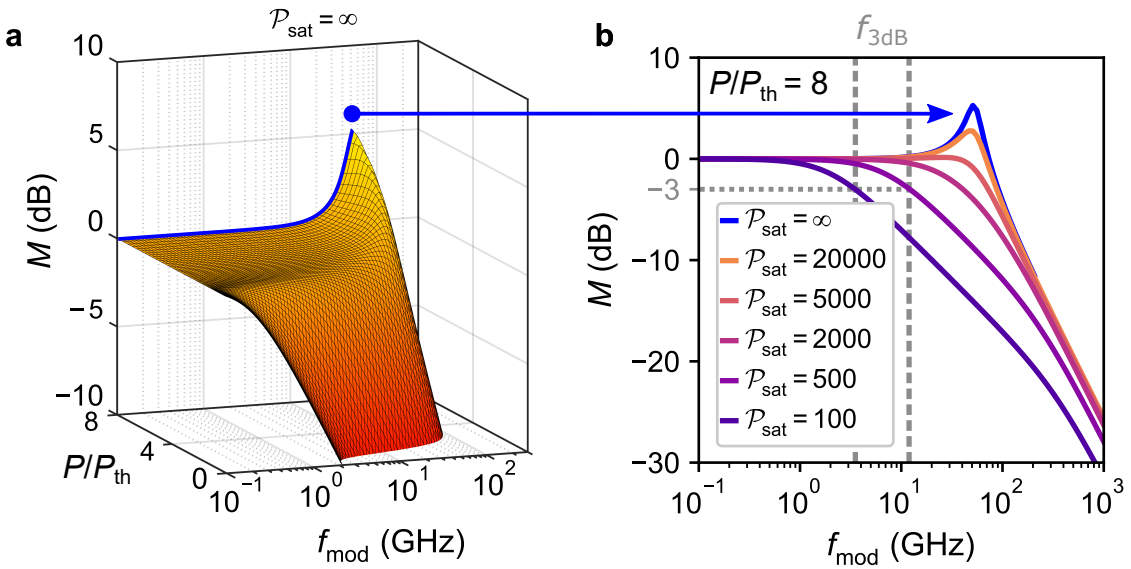

Figure 6.2 | Impact of gain saturation on modulation response. **a**, Modulation response M of an ideal NW laser ($\mathcal{P}_{\mathrm{sat}} = \infty$) as a function of modulation frequency (f_{mod}) and normalized excitation power (P/P_{th}). The modulation response M exihibts a pronounced resonance when f_{mod} approaches the relaxation oscillation frequency f_{R} shown in Fig. 6.1a. The blue line indicates a cut through the surface for $P/P_{\mathrm{th}} = 8$. This cut is shown in **b**, as illustrated by the blue arrow. **b**, Modulation response M as a function of f_{mod} for a fixed normalized excitation power of $P/P_{\mathrm{th}} = 8$. As gain saturation increases (smaller $\mathcal{P}_{\mathrm{sat}}$), the carrier-photon resonance disappears due to stronger damping. For GaAs-AlGaAs core-shell NW lasers, typical values for $\mathcal{P}_{\mathrm{sat}}$ are in the range from 100 to 500 [128, 133]. The $3\,\mathrm{dB}$ frequencies ($f_{3\mathrm{dB}}$) for $\mathcal{P}_{\mathrm{sat}} = 100$ and $\mathcal{P}_{\mathrm{sat}} = 500$ are indicated by vertical dashed lines. Note that f_{mod} is shown on a logarithmic scale in both **a** and **b**. The simulation parameters are listed in Table 6.1.

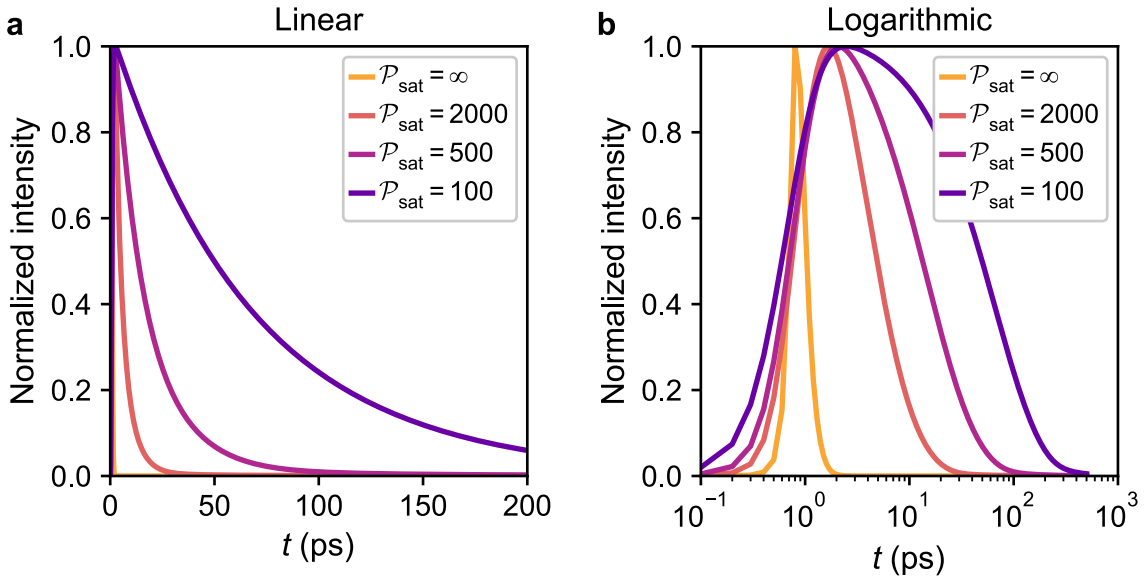

Figure 6.3 | Impact of gain saturation on NW output pulses. **a**, Normalized NW output intensity as a function of time (t). Gain saturation has a significant effect on the output pulse length. The stronger the gain saturation, the longer the output pulses. **b**, The same data as in **a**, but on a logarithmic time axis to make all output pulses equally visible. The simulation parameters are listed in Table 6.1.

since the finite relaxation rate of photoexcited carriers is not considered in this simple model. To make all output pulses equally visible, Fig. 6.3b shows the same data as Fig. 6.3a, but on a logarithmic time axis.

The two-level rate equation model therefore predicts that the output pulses of GaAs-AlGaAs core-shell NW lasers are longer than ~ 50 ps and strongly asymmetric in time, with a sharp rise and a long tail. As will be shown in Section 6.2, both of these predictions are in agreement with experimental results and simulations based on many-body laser theories. Thus, although the two-level rate equation model does not capture all the details of ultrafast dynamics on picosecond timescales, it correctly describes the overall behavior of these lasers.

6.2 Ultrafast non-equilibrium dynamics

In this section we use a combined experimental and theoretical approach to study the ultrafast lasing dynamics of GaAs-AlGaAs core-shell NW lasers in detail. We demonstrate that these NW lasers exhibit ultrafast intensity and phase oscillations that correspond to an exceptionally strong non-equilibrium analog of relaxation oscillations [150], with frequencies ranging from 160 GHz to 260 GHz. We show that these unique dynamics are enabled by the miniaturized dimensions of the laser and the resulting competition between carrier heating and cooling in the electron-hole plasma during lasing operation. Our experimental results are supported by comple-

Name	Symbol	Value
Excitation pulse duration	Δt_{pump}	200 fs
Electron excess energy	$\Delta\epsilon_{\mathrm{e}}$	60 meV
Excitation spot diameter	d_{exc}	17 µm
Detection spot diameter	d_{det}	11 µm
Lattice temperature	T_{L}	10 K

Table 6.2 | Experimental parameters for pump-probe luminescence spectroscopy. At $T_{\mathrm{L}} = 10\,\mathrm{K}$, the electron excess energy of $\Delta\epsilon_{\mathrm{e}} \sim 60\,\mathrm{meV}$ corresponds to an excitation photon energy of $\epsilon_{\mathrm{p}} = 1.588\,\mathrm{eV}$. For experiments at higher lattice temperatures, ϵ_{p} was tuned to keep $\Delta\epsilon_{\mathrm{e}}$ constant. The listed parameters were used for all experiments in Section 6.2, unless specified otherwise.

mentary microscopic simulations based on the semiconductor Bloch [101, 143] and the quantum statistical model [149], which were introduced in Section 3.3 and Section 3.4, respectively.

6.2.1 Laser threshold

The threshold excitation power of NW-A was determined using single-pulse excitation. Details of the experimental setup are summarized in Section 4.2.1. The experiment was performed using the parameters listed in Table 6.2.

Figure 6.4a presents NW emission spectra at selected excitation powers (P) relative to threshold (P_{th}). It shows that the NW laser remains single modal at an energy of $\sim 1.51\,\mathrm{eV}$ for excitation powers $P/P_{\mathrm{th}} < 2.5$. It further demonstrates that, for the range of excitation powers investigated, the mode at $\sim 1.52\,\mathrm{eV}$ is always more than an order of magnitude weaker than the dominant mode. We can therefore neglect this weak second mode at higher energy and treat the laser as being single modal in all simulations. To obtain the characteristic light-in light-out curve we determined the output intensity (I) by spectrally integrating the dominant lasing peak at $\sim 1.51\,\mathrm{eV}$. The resulting I is normalized to its threshold value (I_{th}) and presented in Fig. 6.4b as a function of P/P_{th}, demonstrating a clear transition into lasing. We fitted the output intensity above threshold with a linear function (solid red line) and determined a continuous wave (CW) equivalent threshold excitation power of $P_{\mathrm{th}} = (0.84 \pm 0.04)\,\mathrm{mW}$ (dashed blue line) by the intersection of the fit with the horizontal axis. This corresponds to a threshold fluence of $F_{\mathrm{th}} = (4.5 \pm 0.2)\,\mu\mathrm{J\ cm^{-2}}$. The error on P_{th} and F_{th} represents the 95 % confidence interval (CI), obtained from the linear fit. Figure 6.5 presents an optical microscope image of NW-A pumped into the lasing regime during the measurement shown in Fig. 6.4. The coherence of the NW emission is apparent from the clearly visible spatial interference pattern. The observed interference pattern is very similar to that expected from two coherent dipole

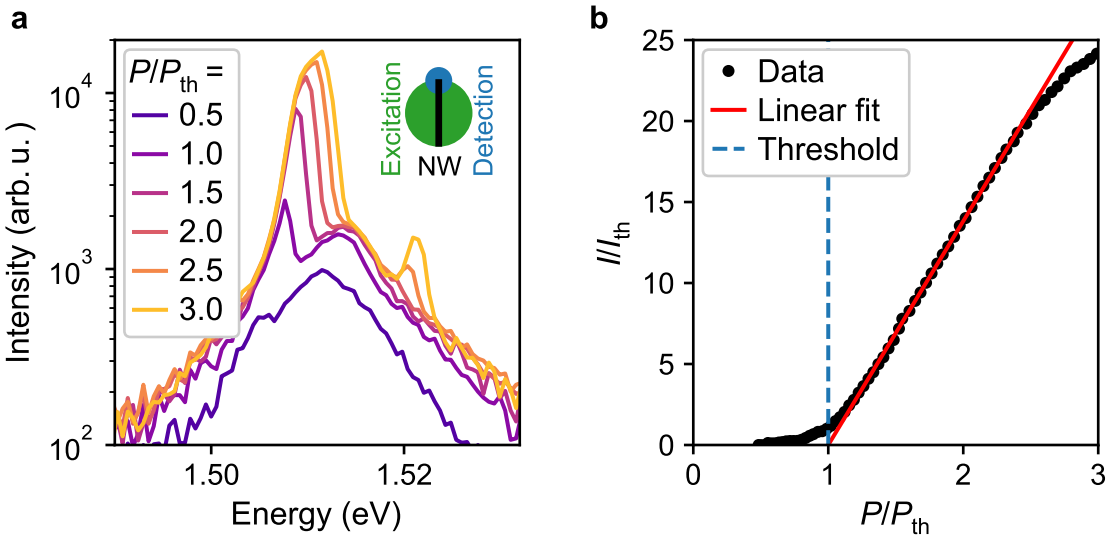

Figure 6.4 | Lasing spectra and light-in light-out curve for single-pulse excitation. **a**, Spectra of the NW emission at selected excitation powers (P) relative to threshold (P_{th}). The second mode at $\sim 1.52\,\mathrm{eV}$ is more than one order of magnitude weaker than the main mode at $\sim 1.51\,\mathrm{eV}$ and can therefore be neglected. **b**, Characteristic light-in light-out curve showing a clear transition into lasing. The intersection of the linear fit with the horizontal axis defines P_{th}. The output intensity (I) is normalized to its threshold value (I_{th}). The insets in **a**,**b** show the relative position of the NW (black), excitation spot (green) and detection spot (blue). (Adapted from [68])

emitters located at the positions of the two NW end facets [46, 47, 252, 253].

6.2.2 Pump-probe measurement and simulation

Femtosecond pump-probe spectroscopy was performed on single NWs with a carefully timed pair of *pump* and *probe* pulses, separated by a time delay Δt. Details of the experimental setup are described in Section 4.2.2, while the experimental parameters are listed in Table 6.2. Figure 6.6 illustrates the pump-probe excitation scheme. The pump pulse power (P_{pump}) and probe pulse power (P_{probe}) are above and below the threshold (P_{th}) of the NW laser, respectively. After excitation, the NW laser emits two modulated output pulses, separated by a time delay Δt.

Figure 6.7a presents typical results of a pump-probe measurement as a function of Δt. Here, we normalized the spectra to their maximum value and set the excitation power to $P_{\mathrm{pump}}/P_{\mathrm{th}} \sim 2.7$ and $P_{\mathrm{probe}}/P_{\mathrm{th}} \sim 0.7$, such that the probe pulse alone cannot induce lasing. We observe a delayed onset of two-pulse interference fringes, reflecting the turn-on time (t_{on}) of the laser, which depends on both the excitation conditions *and* the initial relaxation of the photoexcited carriers [59, 60, 65, 66]. Experimentally, $t_{\mathrm{on}} = (6.3 \pm 0.8)\,\mathrm{ps}$ was determined from the Δt dependence of the spectrally integrated mode intensity, using the transient depletion of the probe absorption [59], as discussed

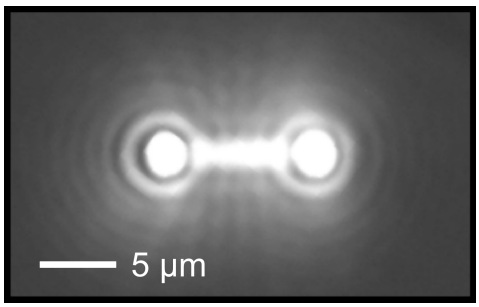

Figure 6.5 | Microscope image. Optical microscope image of NW-A pumped into the lasing regime at a lattice temperature of $T_{\mathrm{L}} = 10\,\mathrm{K}$. Stimulated emission is emitted from both NW end facets. Excitation was performed using optical pulses with an energy of $\epsilon_{\mathrm{p}} = 1.588\,\mathrm{eV}$ and a full width at half maximum of $200\,\mathrm{fs}$. For taking the image, the pump laser was blocked by a filter in front of the imaging CCD. (Adapted from [68])

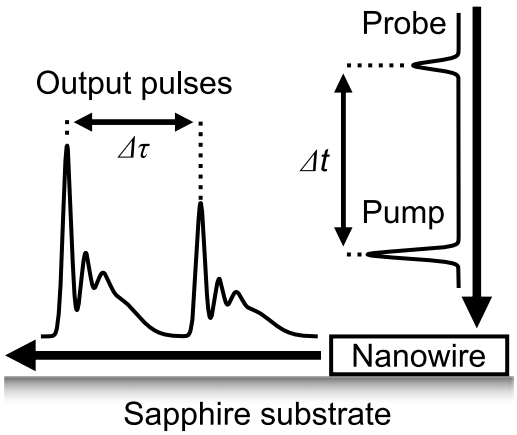

Figure 6.6 | Pump-probe excitation scheme. Schematic of a NW laser subject to pump-probe excitation with delay Δt, emitting two temporally asymmetric and modulated pulses, separated by $\Delta\tau$. (Adapted from [68])

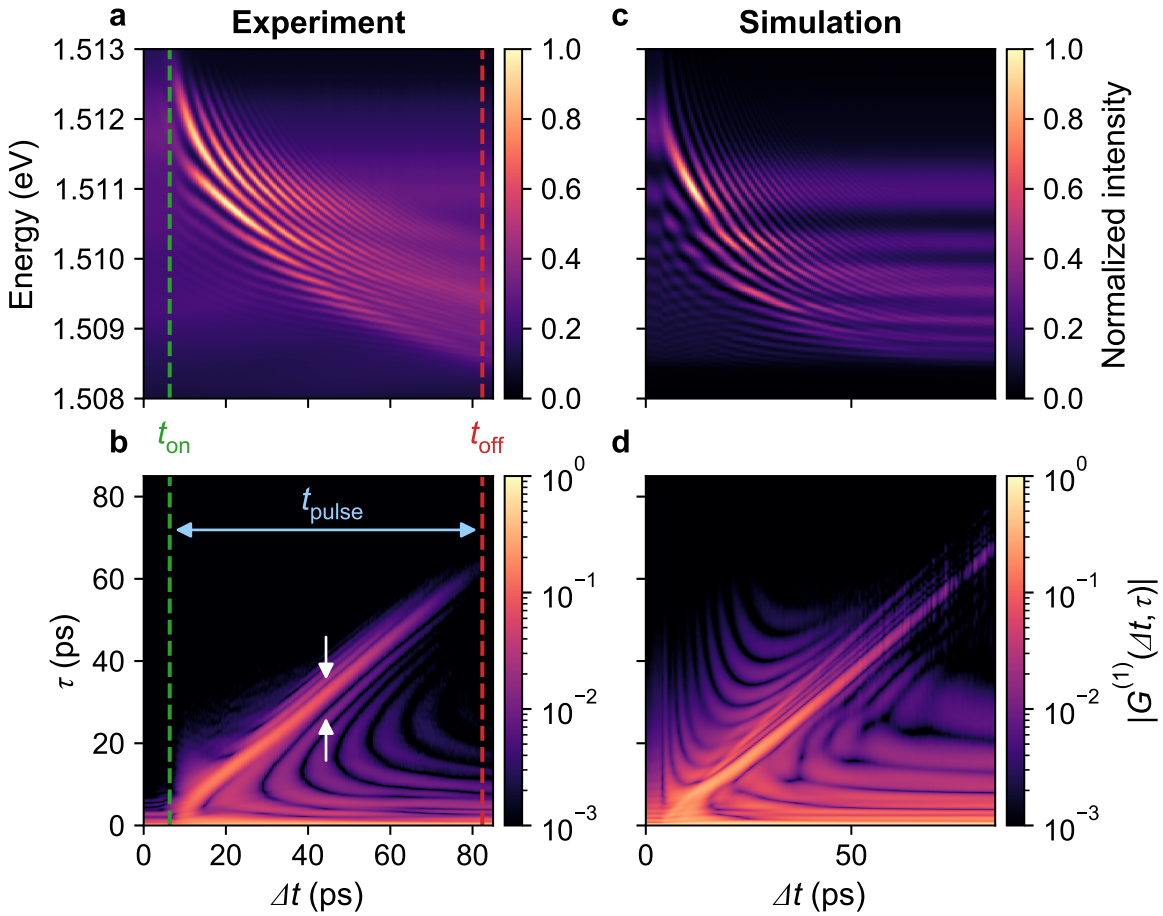

Figure 6.7 | Pump-probe measurement and simulation. **a**, Time-integrated spectra, showing typical two-pulse interference fringes with additional beating patterns along the energy axis. **b**, Normalized magnitude of the electric field autocorrelation ($|G^{(1)}(\Delta t,\tau)|$), exhibiting pronounced oscillations along τ above and below the main sideband (indicated by white arrows), resulting from the beating patterns in **a**. In **a**,**b** we indicated the laser turn-on time (t_{on}) and the disappearance of the sideband (t_{off}). Their difference, $t_{\mathrm{pulse}} \sim t_{\mathrm{off}} - t_{\mathrm{on}}$, gives a measure of the total output pulse length. **c**,**d**, Corresponding semiconductor Bloch simulation of the respective experimental data in **a**,**b**. (Adapted from [68])

in Appendix B. For increasing Δt, the interference fringes increase linearly in frequency. Their existence further shows that the weak probe pulse restarts lasing, whereby the probe-induced output pulse partially adopts the phase of the residual electric field in the cavity defined by the previous output pulse [65]. Hence, the strong pump pulse leaves considerable excitation for an extended period of time, which decays with increasing Δt. This, in turn, leads to a change in refractive index and, thus, to a pronounced redshift of the interference pattern. Meanwhile, the fringes become weaker and finally disappear at a delay $\Delta t = t_{\mathrm{off}}$.

For ease of interpretation, we move to the time domain by Fourier transforming the energy axis in Fig. 6.7a. This yields the electric field autocorrelation $G^{(1)}(\Delta t,\tau)$ as a function of Δt and time shift τ [59, 254]. Its normalized magnitude $|G^{(1)}(\Delta t,\tau)|$ is

presented in Fig. 6.7b on a logarithmic scale. For normalization, we used the respective maximum value at $\tau = 0$ for each Δt to facilitate comparison with theory. The fringes in Fig. 6.7a lead to a linear sideband, with a full width at half maximum (FWHM) of $\sim 3\,\mathrm{ps}$, that sets on at a delay $\Delta t = t_{\mathrm{on}}$ and disappears at $\Delta t = t_{\mathrm{off}}$. We quantified $t_{\mathrm{off}} = (82.4 \pm 0.4)\,\mathrm{ps}$ as the delay time where the main sideband amplitude decreased to 1% of its maximum value. Since the photon lifetime of the resonator is $< 1\,\mathrm{ps}$ [46], the disappearance of the main sideband marks the termination of the first NW laser output pulse. Thus, $t_{\mathrm{pulse}} \sim t_{\mathrm{off}} - t_{\mathrm{on}} = (76.1 \pm 0.9)\,\mathrm{ps}$ is a measure for the overall output pulse duration, which is consistent with our expectations from the rate equation analysis in Section 6.1.3. In addition to the main sideband, we also observe pronounced oscillations above and below, as indicated by white arrows in Fig. 6.7b. These reflect the beating patterns in the spectral interference fringes in Fig. 6.7a. Weak indications of these oscillations can be found in previous work [59, 65], but their significance has not been scrutinized until now. Together, the long t_{pulse}, the short FWHM of the main sideband, and the oscillations indicate that the NW output pulses are strongly asymmetric and modulated in time.

To understand the origin of the oscillating features in Fig. 6.7b, we first used the semiconductor Bloch model to simulate the experimental data. For these simulations, we used the parameters listed in Table 5.1. As discussed in Chapter 5, the end-facet reflectivity ($R = 0.5$) and the spontaneous emission coupling factor ($\beta_{\mathrm{sp}} = 0.1$) were determined using a quantum statistical simulation of the continuous-wave lasing characteristics of NW-A. It should be noted that β_{sp} generally depends on the carrier density [255, 256]. For our purposes, however, it is possible to approximate β_{sp} as a constant, since the dynamics of the NW laser depends only weakly on this parameter, see Appendix C. The result of this semiconductor Bloch approach is presented in Fig. 6.7c,d, whereby we used the same excitation powers as in the experiment. The simulation exhibits excellent qualitative agreement with all observed features of the experimental data in Fig. 6.7a,b. It reproduces the delayed onset of interference fringes, the temporal asymmetry of the output pulses and the oscillations both above and below the main sideband. Moreover, the model reveals that these originate from carrier temperature oscillations, see Appendix D.

6.2.3 Quantum statistical simulation

However, to uncover the full significance of these oscillations and to enable a theoretical description of measurement series within which scattering rates vary, it is necessary to go beyond the relaxation rate approximation used in the semiconductor Bloch model. For this purpose, we used a quantum statistical model that self-consistently calculates the rates for carrier-carrier and carrier-phonon scattering.

Figure 6.8 displays the results of this approach for a pump-probe excitation with $\Delta t = 40\,\mathrm{ps}$. The excitation powers used were the same as in Fig. 6.7. In Fig. 6.8a, we present the laser intensity as a function of time and determine $t_{\mathrm{on}} \sim 5.7\,\mathrm{ps}$ as the time it takes to reach $1/e$ of the first output pulse maximum. After turn-on, the NW pulses are observed to be strongly asymmetric in time with a pronounced initial peak (FWHM $\sim 1.3\,\mathrm{ps}$), following oscillations with a frequency of $\nu_{\mathrm{S}} = 222\,\mathrm{GHz}$ and a long tail. This is in qualitative agreement with both the experiment and the simulation in Fig. 6.7. Following up on the results of the semiconductor Bloch model, we investigated the temporal evolution of the carrier distributions by determining the instantaneous electron (T_{e}) and hole (T_{h}) temperatures for each time step, see Appendix E. Fig. 6.8b shows that the carrier temperatures cool to $T_{\mathrm{e}} \sim 79\,\mathrm{K}$ and $T_{\mathrm{h}} \sim 76\,\mathrm{K}$ after $t \sim 5.3\,\mathrm{ps}$, shortly before the laser turns on, which is in full accord with literature [197, 202]. This cooling primarily takes place via scattering of carriers with longitudinal optical (LO) phonons [106, 174, 257]. After the first temperature minimum at $t \sim 5.3\,\mathrm{ps}$ and during turn-on, we observe a pronounced initial increase of the carrier temperatures by $\Delta T_{\mathrm{e}} \sim 19.8\,\mathrm{K}$ and $\Delta T_{\mathrm{h}} \sim 4.2\,\mathrm{K}$ for electrons and holes, respectively. Subsequently, the carrier temperatures show clear oscillations with a frequency of 222 GHz, mirrored by the laser intensity in Fig. 6.8a. Since T_{e} changes the most, we highlight in Fig. 6.8a-d its first heating and cooling cycle in red and blue, respectively. As is observed in Fig. 6.8c, the carrier temperature dynamics are also mirrored in the time dependence of the electron scattering rates near the lasing energy. While these time variations in the scattering rates are not necessary for the existence of the oscillations in Fig. 6.8a,b, they likely do increase their strength, see Appendix D. Near t_{on}, the carrier-carrier scattering rate of electrons is $\gamma_{\mathrm{cc,e}} \sim 8.6\,\mathrm{ps}^{-1}$, while the electron-LO-phonon scattering rate is $\gamma_{\mathrm{ep}} \sim 0.3\,\mathrm{ps}^{-1}$. In contrast to the oscillations in Fig. 6.8a-c, the carrier density in Fig. 6.8d shows a monotonic, step-like decrease starting from an initial value of $N \sim 5.2 \times 10^{17}\,\mathrm{cm}^{-3}$, besides the injection of additional carriers at $t = 40\,\mathrm{ps}$.

To visualize the carrier dynamics in the parabolic bands, Fig. 6.9 shows the energy-dependent carrier inversion as a function of time in a semi-logarithmic contour plot. The optical pump-probe excitation is indicated by white arrows. Within a few picoseconds, relaxation of the injected carriers leads to build up of inversion at the lasing energy (solid green line), as shown in Appendix F. After the onset of lasing (t_{on}, green point), clear oscillations of the inversion are visible, which are directly connected to the carrier temperature oscillations in Fig. 6.8b. From Fig. 6.9, we further observe no signs of spectral hole burning. This results from the fast carrier-carrier scattering, that continuously thermalizes the electron-hole plasma, and the low end-facet reflectivity R, which reduces the stimulated emission rate (γ_{lasing}).

To explain the origin of these oscillations, Fig. 6.10 shows a schematic representation of two electron distributions having similar densities in the conduction band; one

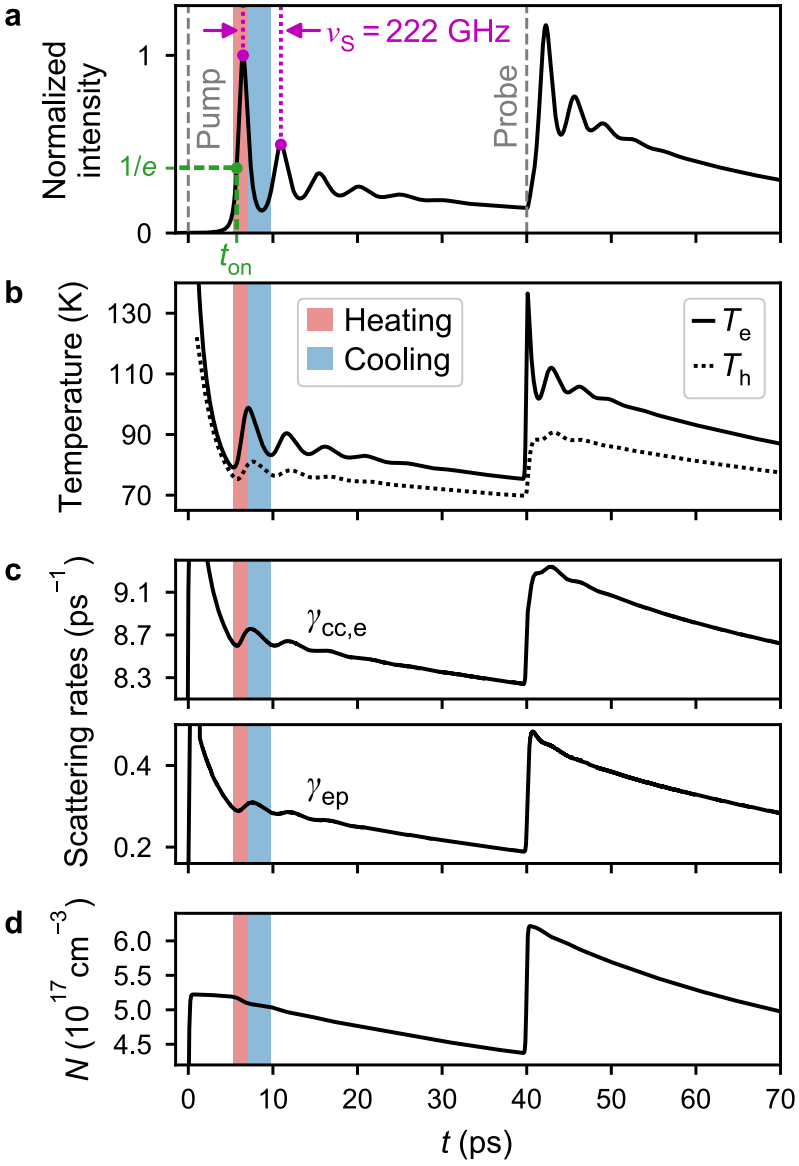

Figure 6.8 | Quantum statistical simulation of the time-resolved pump-probe response. **a**, Time-dependent output intensity for a pump-probe delay of $\Delta t = 40\,\mathrm{ps}$. From the first output pulse we determine t_{on} and the oscillation frequency ν_{S}. **b-d**, Corresponding time-dependent electron (T_{e}) and hole (T_{h}) temperature, carrier-carrier scattering rate of electrons ($\gamma_{\mathrm{cc,e}}$), electron-LO-phonon scattering rate (γ_{ep}) and carrier density (N). In **a-d**, the shaded areas highlight the first heating and cooling cycle of T_{e}. (Adapted from [68])

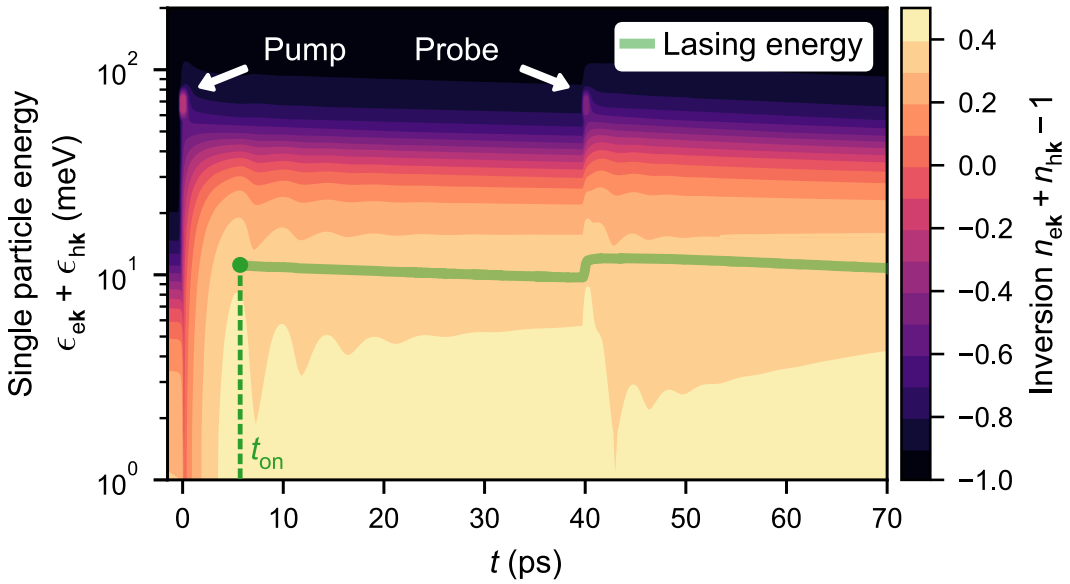

Figure 6.9 | Inversion as a function of time. Energy-resolved inversion, illustrating the time-dependent carrier dynamics during the lasing process. Here, $n_{c\mathbf{k}}$ and $\epsilon_{c\mathbf{k}}$, with $c \in \{e,h\}$, are respectively the occupation probability and energy of electrons and holes with wave vector $\mathbf{k}$. (Adapted from [68])

characterized by a colder T_e (yellow) than the other (orange). The lasing energy (ϵ_L) is below the respective average kinetic energy (ϵ_{avg}^{cold}, ϵ_{avg}^{hot}). Thus, stimulated emission at a rate γ_{lasing} heats the remaining electron distribution [146, 160, 250, 258–260]. In case this heating via γ_{lasing} is sufficiently strong to overcome the cooling via γ_{ep}, T_e rises. Consequently, γ_{ep} increases, whereas γ_{lasing} decreases due to the reduction in material gain (G_{mat}) [258, 259]. Partial recovery of G_{mat} via γ_{ep} then restarts the cycle. A similar discussion applies to holes.

However, in previous investigations of microcavity and nanoscale lasers this intuitive effect of ultrafast self-induced temperature oscillations was strongly damped, preventing the observation of sustained oscillations [150, 240, 241, 250, 260]. We explain the observations in Fig. 6.8a-d and Fig. 6.9 for NW lasers by noting that the modal gain (G_{mod}) and G_{mat} are linked by $G_{mod} \propto \Gamma \cdot G_{mat}$, where Γ is the modal confinement factor [9]. The corresponding differential gains with respect to carrier temperature (T_c, with $c \in \{e,h\}$) are, therefore, to a good approximation related by $\partial G_{mod}/\partial T_c \propto \Gamma \cdot \partial G_{mat}/\partial T_c$. Thus, large Γ leads to enhanced interactions between the lasing mode and the gain material. For NW lasers, this effect is especially pronounced due to their wavelength-scale dimensions and unique resonator geometry, that allows exceptionally strong mode confinement with $\Gamma > 1$ [47, 119, 121]. We further note that the large Γ of NW lasers is, in part, due to the strong lateral optical confinement and the resulting strongly non-paraxial mode propagation [119, 121]. Moreover, here, there exists a balanced interplay between the rates of stimulated emission, carrier-carrier scattering, and carrier-LO-phonon scattering. As mentioned above, carrier-carrier

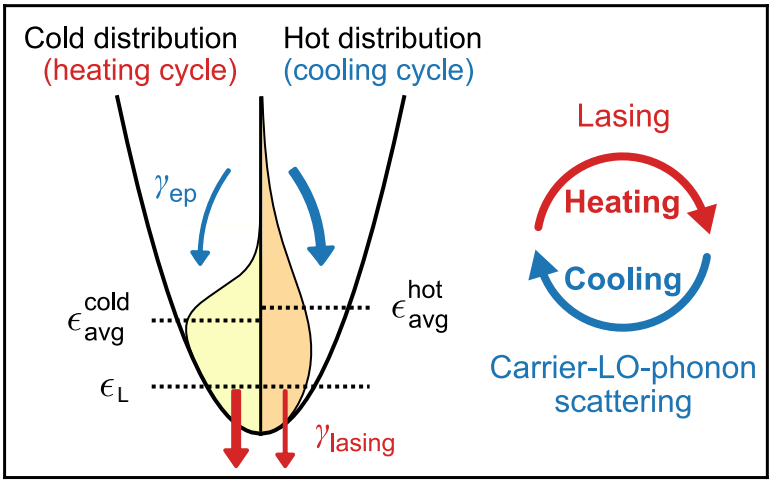

Figure 6.10 | Oscillation mechanism. Sketch of the oscillation mechanism enabled by the exceptionally large modal confinement factor Γ of NW lasers. Here, γ_{lasing} is the stimulated emission rate of the lasing mode with energy ϵ_{L}, while $\epsilon_{\text{avg}}^{\text{cold}}$ and $\epsilon_{\text{avg}}^{\text{hot}}$ are the average kinetic energies of the respective distributions. (Adapted from [68])

scattering is sufficiently fast to maintain Fermi-Dirac distributions, and heating via stimulated emission strong enough to compete with cooling via carrier-LO-phonon scattering, such that light-matter coupling is manifested as a strongly oscillating carrier temperature. In our NW lasers, it is precisely this combination of large Γ with these carrier dynamics that leads to the observed sustained oscillations. This is confirmed in Section 6.2.4 by a comparison of the simulated laser dynamics with $\Gamma = 1.2$ (used here) and $\Gamma = 0.12$.

6.2.4 Confinement factor dependence

Using the quantum statistical model, we illustrate the strong influence of Γ on the lasing dynamics by comparing two similar lasers with markedly different Γ. Both lasers were excited with single pulses and an excitation power of $P/P_{\text{th}} = 2.5$. Figure 6.11a shows the intensity dynamics of NW-A, with a confinement factor of $\Gamma = 1.2$ and a length of $L \sim 10\,\mu\text{m}$. The corresponding peak material gain ($\bar{G}_{\text{mat}}$) is presented in Fig. 6.11b. For comparison, Fig. 6.11c and Fig. 6.11d show the intensity and $\bar{G}_{\text{mat}}$ of a laser with $\Gamma = 0.12$, respectively. A similar threshold and $\bar{G}_{\text{mat}}$ as for the case with high Γ was achieved by adjusting the losses via L. No intensity oscillations are observed in this case, demonstrating the important role Γ plays for the ultrafast dynamics in Fig. 6.11a. Except Γ and L, all parameters were the same for both simulations and are listed in Table 5.1.

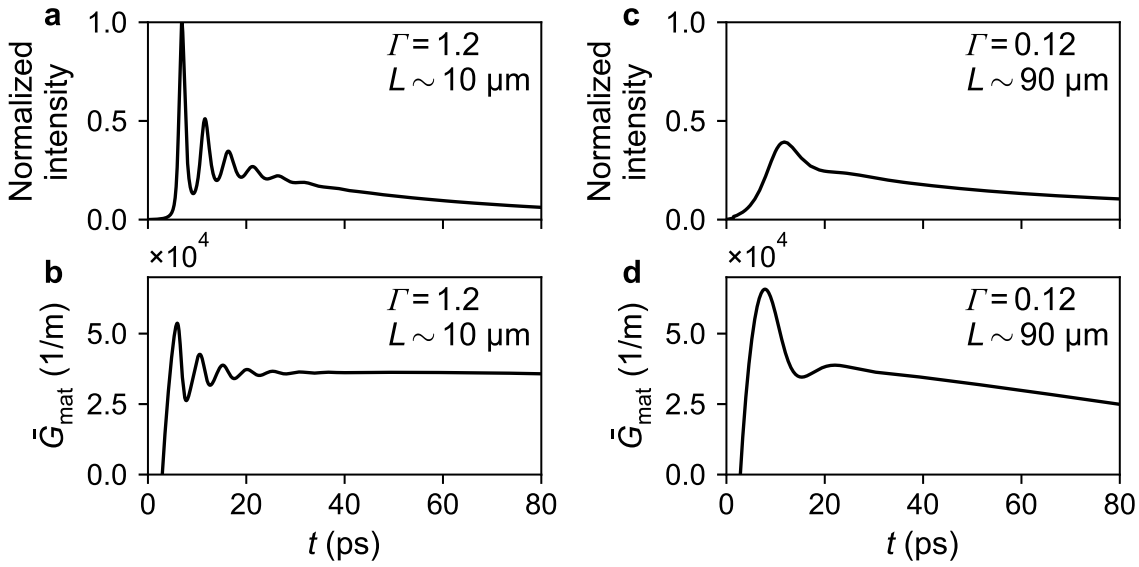

Figure 6.11 | Confinement factor and lasing dynamics. **a**,**b**, Intensity and peak material gain ($\bar{G}_{\mathrm{mat}}$) of a NW laser with a confinement factor of $\Gamma = 1.2$ and a length of $L \sim 10\,\mu\mathrm{m}$, exhibiting clear oscillations in the laser output intensity. **c**,**d**, Dynamics of a similar laser with $\Gamma = 0.12$ and $L \sim 90\,\mu\mathrm{m}$, showing no oscillations in the laser output. The intensities in **a**,**c** were normalized to the maximum value in **a**. The simulations in **a**-**d** were performed using a normalized excitation power of $P/P_{\mathrm{th}} = 2.5$. All simulation parameters that are not explicitly mentioned here are listed in Table 5.1. (Adapted from [68])

6.2.5 Excitation power dependence

To test the above hypothesis for the origin of the observed ultrafast oscillations, we experimentally studied the excitation power and T_{L} dependence of the NW laser dynamics and compared with the predictions of the quantum statistical model.

Figure 6.12 presents the results of the excitation power dependent measurement, with which we investigated in detail how the lasing dynamics depend on N and γ_{lasing}. As shown in Figure 6.12a, t_{on} decreases from $(9.9 \pm 0.4)\,\mathrm{ps}$ to $(5.5 \pm 0.4)\,\mathrm{ps}$ as the pumping level increases from $P_{\mathrm{pump}}/P_{\mathrm{th}} \sim 1.8$ to ~ 3.0. This decrease is in excellent quantitative agreement with theory. It results from the increase in N with increasing $P_{\mathrm{pump}}/P_{\mathrm{th}}$, allowing the laser to turn on at higher carrier temperatures.

To estimate the frequency (f_{E}) of the oscillations in $|G^{(1)}(\Delta t,\tau)|$ from our measurements, we determined the time interval between the main sideband and the first oscillation above, as described in Appendix G. As shown in Fig. 6.12b, f_{E} increases with stronger excitation power from $(231 \pm 14)\,\mathrm{GHz}$ to $(344 \pm 18)\,\mathrm{GHz}$. Since $|G^{(1)}(\Delta t,\tau)|$ and, thus, the simulated oscillation frequency (f_{S}) cannot be directly obtained from the quantum statistical model, we computed the oscillation frequency ν_{S}. Here, we observe an increase from $\sim 166\,\mathrm{GHz}$ to $\sim 238\,\mathrm{GHz}$, over the same range of excitation powers. Nonetheless, an approximate relationship between ν_{S} and f_{S} can be established using the semiconductor Bloch model. In the present case, f_{S} is related to ν_{S} by $f_{\mathrm{S}} = 1.38 \cdot \nu_{\mathrm{S}}$,

see Appendix H. Applying this relationship to the frequencies ν_S in Fig. 6.12b leads to remarkable quantitative agreement between f_S and f_E over the entire range of excitation powers. The increase of the oscillation frequencies with stronger excitation power results from the complex interplay of various effects. As the main reason, we identified the increased γ_{lasing}, leading to enhanced carrier temperature oscillations and, hence, shorter heating and cooling cycles.

6.2.6 Lattice temperature dependence

Complementary to the excitation power series, varying T_L allowed to tune $\partial G_{\text{mat}}/\partial T_c$, and to shift the operating point of the laser towards higher carrier temperatures. All experimental data in Fig. 6.13 and Fig. 6.14 were measured with $P_{\text{pump}}/P_{\text{th}} \sim 2.5$ and $P_{\text{probe}}/P_{\text{th}} \sim 0.5$. For illustration, Fig. 6.13 presents the measured $|G^{(1)}(\Delta t,\tau)|$ for $T_L = 40\,\text{K}$, 60 K and 80 K. As T_L increases, the data show that t_{on} decreases, f_E increases and t_{pulse} decreases, see Appendix I.

As shown by the data in Fig. 6.14a, t_{on} remains approximately constant at $\sim 6\,\text{ps}$ up to 40 K and then decreases to $(2.6 \pm 0.4)\,\text{ps}$ as T_L further increases to 100 K. This behaviour can be understood on the basis of the T_L dependence of P_{th}, shown in Fig. 6.14b. For $T_L \leq 40\,\text{K}$, P_{th} remains almost constant, whereas at higher T_L it increases exponentially with a characteristic temperature $T_0 = (57 \pm 11)\,\text{K}$. Since the pumping level is fixed relative to P_{th}, this increase leads to a larger initial N. Consequently, t_{on} decreases, as observed in Fig. 6.14a. The simulations presented in Fig. 6.14a,b quantitatively reproduce the experimental data and, thus, confirm our interpretation.

The T_L dependence of P_{th} is, in turn, accounted for by the variation of the electron ($T_{e,\text{on}}$) and hole ($T_{h,\text{on}}$) temperatures at laser turn-on, as shown in Fig. 6.14c. For increasing T_L, they are initially constant at $\sim 62\,\text{K}$, reflecting the fact that the cooling rate due to carrier-LO-phonon scattering decreases rapidly for low carrier temperatures ($\lesssim 50\,\text{K}$) [197, 257]. Both $T_{e,\text{on}}$ and $T_{h,\text{on}}$ only rise as T_L becomes comparable, shifting the operating point of the laser towards higher carrier temperatures. The carrier distributions therefore spread out towards higher energies, which reduces G_{mat} at the lasing energy for a given N. Hence, P_{th} increases, explaining the observed trend in Fig. 6.14b.

We are now in a position to explain the T_L dependence of the oscillation frequencies in Fig. 6.14d. Up to 40 K, f_E remains approximately constant at $\sim 270\,\text{GHz}$ and then increases to $(350 \pm 20)\,\text{GHz}$ at $T_L = 80\,\text{K}$. Similarly, ν_S increases from 213 GHz to 259 GHz. We again calculated f_S from ν_S, using the proportionality factor 1.38 stated above, and obtained remarkable agreement with f_E. The trend of the oscillation frequencies is strongly influenced by the T_L dependence of P_{th} in Fig. 6.14b. As P_{th}

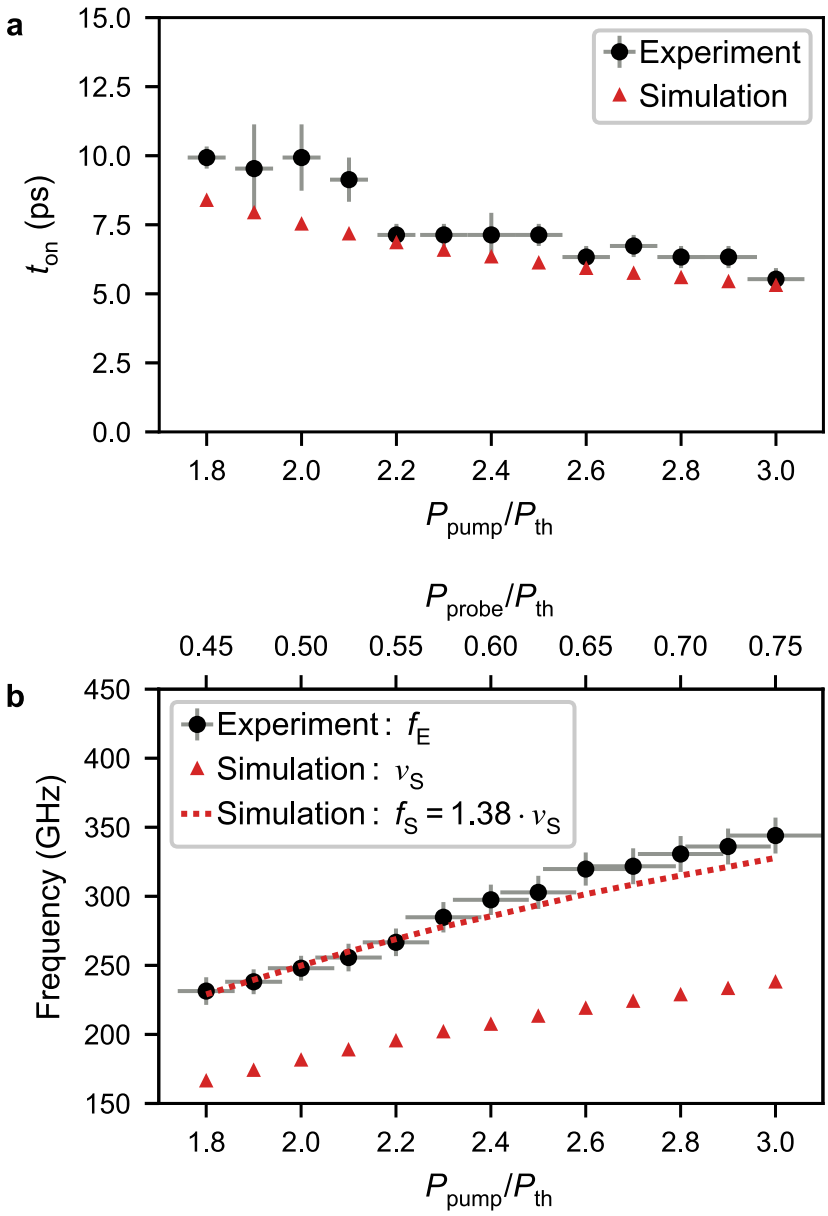

Figure 6.12 | Excitation power dependence of the NW laser dynamics. **a**, A stronger pump pulse power ($P_{\mathrm{pump}}/P_{\mathrm{th}}$) produces a greater initial carrier density N, allowing the laser to turn on faster. Here, $P_{\mathrm{probe}}/P_{\mathrm{th}} \sim 0.5$ was kept constant. **b**, The increase in oscillation frequencies with excitation power depends on a complex interplay of several effects, but is mainly driven by the increased stimulated emission rate γ_{lasing}. Here, we kept the ratio $P_{\mathrm{pump}}/P_{\mathrm{probe}} = 4:1$ constant to ensure that the intensities of both output pulses remained comparable. All error bars represent $95\,\%$ confidence intervals (CIs) of the mean and result from the methods used to determine P_{th}, t_{on} and f_{E}, as described in Section 6.2.1, Appendix B and Appendix G, respectively. In **b**, the uncertainty in excitation power refers to the bottom axis. (Adapted from [68])

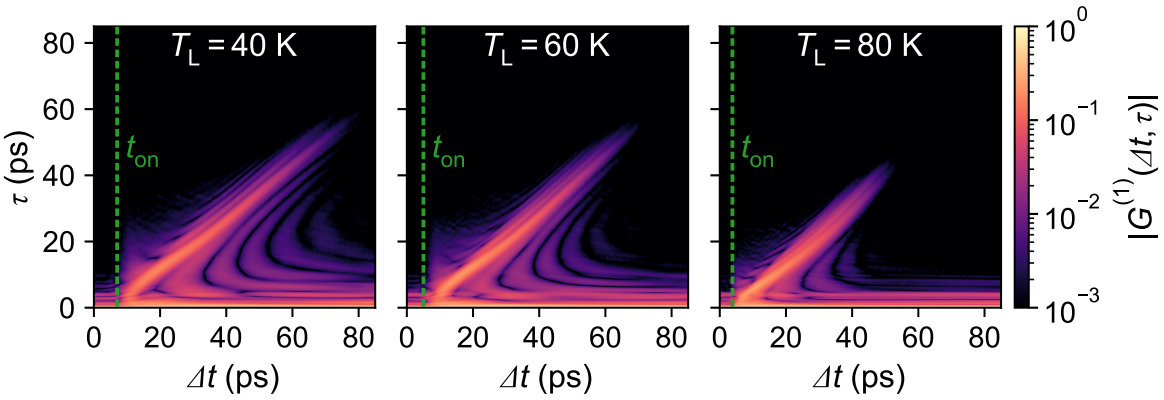

Figure 6.13 | Lattice temperature dependence of the NW laser dynamics. a, Three exemplary pump-probe measurements, illustrating the changes that occur with increasing T_L. (Adapted from [68])

increases, the correspondingly larger initial N blueshifts the lasing mode due to the associated change in refractive index, and broadens the gain spectrum as a result of band gap renormalization and band filling. Simultaneously, the band gap and the lasing mode redshift with increasing T_L, whereby the redshift of the lasing mode is smaller than the other effects. In combination, these processes effectively shift the lasing mode towards the high-energy side of the gain spectrum, where $\partial G_{mat}/\partial T_c$ is larger. This leads to the observed increase in oscillation frequencies. No oscillations were observed for $T_L = 100\,K$, which coincided with the laser becoming multimodal. In addition, as shown in Fig. 6.14c, the carrier temperatures increase for higher T_L, which reduces $\partial G_{mat}/\partial T_c$ [261]. This counteracts the increases due to the shift of the lasing mode towards the high-energy side of the gain spectrum and at some point will compensate them. The oscillations are therefore expected to disappear at sufficiently high T_L, here $> 80\,K$.

6.2.7 Discussion

In Section 6.2, we investigated the microscopic lasing dynamics of GaAs-AlGaAs core-shell NW lasers on picosecond timescales. The following discussion puts the results into a broader context.

Ultrafast laser modulation using terahertz heating fields

Direct laser modulation based on changing the carrier density takes advantage of the carrier-photon resonance to achieve fast modulation speeds, which are currently limited to $< 60\,GHz$ without the use of photonic feedback effects [168]. Similarly, we believe that the new resonance between the carrier temperature and the laser intensity discussed here can be used for ultrafast laser modulation. Considering the

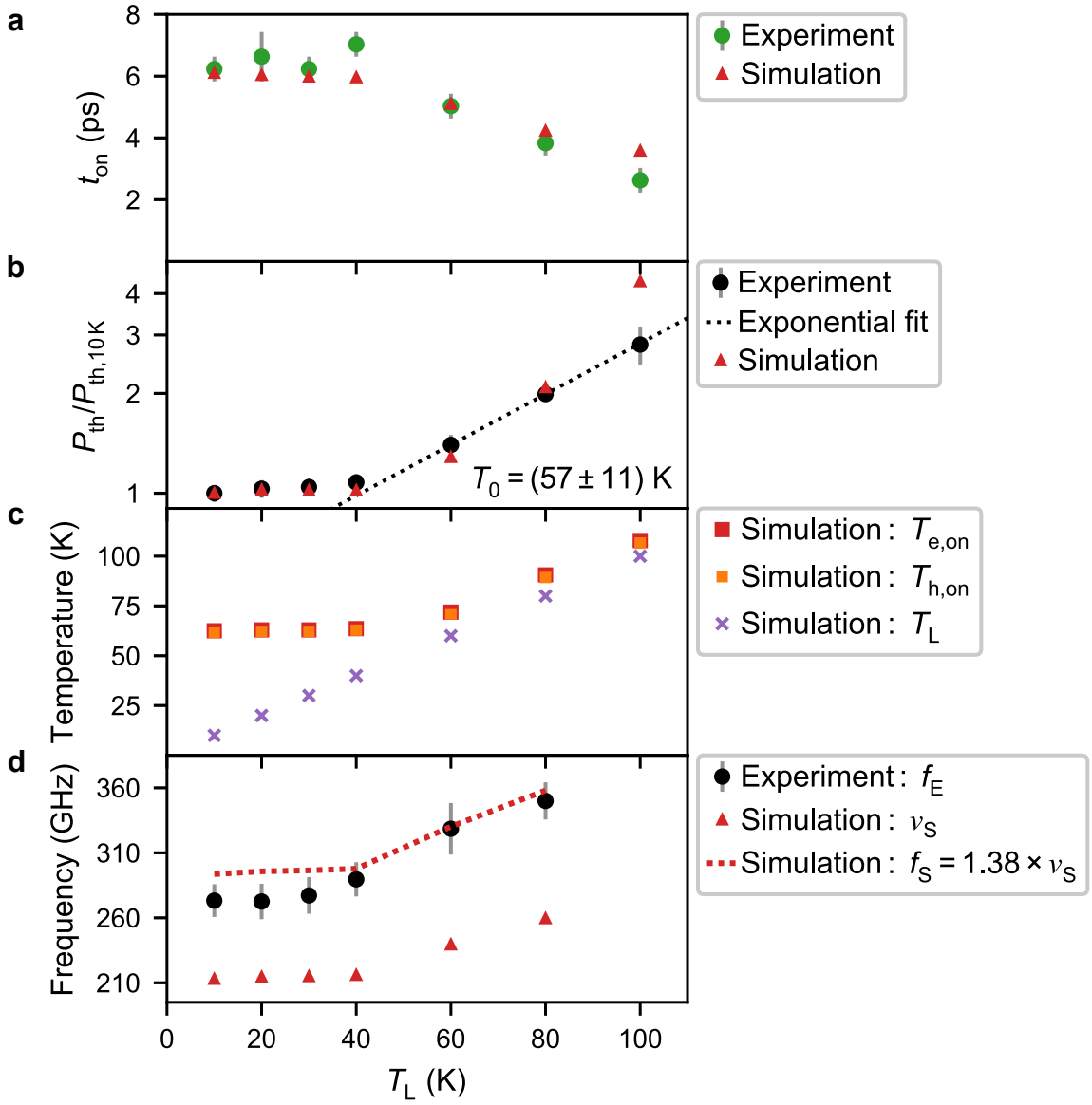

Figure 6.14 | Lattice temperature dependence of the NW laser dynamics. **a**, As T_L increases, t_on is at first constant and then decreases. **b**, Above $40\,\mathrm{K}$, P_th increases with a characteristic temperature T_0, as obtained from an exponential fit. This increase leads to the decrease of t_on in **a**. The data were normalized to the smallest threshold ($P_\mathrm{th,10\,K}$). **c**, Electron ($T_\mathrm{e,on}$) and hole ($T_\mathrm{h,on}$) temperatures at times $t = t_\mathrm{on}$ as a function of T_L, whereby the excitation power was set to $P_\mathrm{pump}/P_\mathrm{th} \sim 1$. The rise of $T_\mathrm{e,on}$ and $T_\mathrm{h,on}$ causes the increase of P_th in **b**. **d**, The oscillation frequencies increase as the lasing mode shifts towards the high-energy side of the gain spectrum, where $\partial G_\mathrm{mat}/\partial T_\mathrm{c}$ is larger. All error bars represent $95\,\%$ CIs of the mean and result from the methods used to determine P_th, t_on and f_E, as described in Section 6.2.1, Appendix B and Appendix G, respectively. In **b**, some error bars are smaller than the symbol size. (Adapted from [68])

observed resonance frequencies of 160 GHz to 260 GHz, we therefore anticipate that NW lasers could substantially improve previously proposed laser modulation schemes based on THz heating fields [261]. This is because their large $\partial G_{\mathrm{mod}}/\partial T_{\mathrm{c}}$ makes them highly susceptible to applied electric fields in contrast to lasers with low mode confinement. Our findings thus illustrate a new approach to how the miniaturization of semiconductor lasers can be used to design their ultrafast dynamical properties.

Comparison with other laser modulation approaches

This is complementary to previous research that investigated accelerated laser dynamics based on Purcell enhancement [256, 262] and plasmonic effects [59, 263]. We note that no Purcell enhancement is expected for our NW lasers since their effective mode volume is $\sim$ 140 times larger than that of the photonic crystal laser studied in Ref. [262]. Other approaches to ultrafast laser modulation include mode field switching [264] and the use of photonic feedback effects [168]. Both approaches typically require larger device structures. The potential of mode field switching is not yet known, as direct time-dependent modulation of a laser has not yet been demonstrated with this method [264]. However, with both photonic feedback on a silicon carbide substrate [168] and Purcell enhancement in a GaAs material system [262] modulation frequencies of up to $\sim$ 100 GHz have been demonstrated, although the latter could not be confirmed theoretically [255, 265]. Thus, the combination of THz modulation with NWs or other suitably designed lasers could enable direct laser modulation at previously unattainable speeds (160 GHz to 260 GHz).

Similarities and differences to the two-level rate equation approach.

Comparison of Fig. 6.3a and Fig. 6.11a shows that the two-level rate equation model and the quantum statistical model agree on the overall behavior of the NW laser. The output pulses are long ($>$ 50 ps) and strongly asymmetric in time, with a sharp rise and a long tail. However, the detailed dynamics on picosecond timescales are substantially different. This shows the limitations of the two-level rate equation approach and illustrates that it does not take into account important physical processes. The main reason for this is the way gain saturation is implemented in this model. This will be shown in Section 6.3, where we demonstrate that a simple modification of the two-level rate equation approach allows to reproduce the main experimental and theoretical results of Section 6.2. A more sophisticated rate equation theory that directly includes the carrier temperature as a dynamical variable is described in Ref. [266].

6.3 Three-level rate equation analysis

In Section 6.2, we investigated the microscopic lasing dynamics of GaAs-AlGaAs core-shell NW lasers with a combined experimental and theoretical approach. Using many-body laser simulations, we showed that strong mode confinement can lead to pronounced carrier temperature oscillations that modulate both the amplitude and phase of the emitted electric field.

The results of the two-level rate equation approach in Section 6.1 are consistent with the overall length and the strong temporal asymmetry of the NW output pulses observed in Section 6.2. However, this approach did not capture the unique non-equilibrium dynamics revealed in Section 6.2. The reason for this can be understood using Eq. 3.13. According to Eq. 3.13 and Eq. 3.4, changes in the material gain G_{mat} and the photon number $\mathcal{P}$ always occur simultaneously. This approximation works well for slowly varying G_{mat} and $\mathcal{P}$. On picosecond timescales, however, it fails because the finite heating and cooling rates of the electron-hole plasma must also be taken into account. This is illustrated in Fig. 6.15, where the data from Fig. 6.11a,b are reproduced on the same axis for better comparison. It is evident that the oscillations in the laser intensity (proportional to $\mathcal{P}$) and the peak value of the material gain ($\bar{G}_{\mathrm{mat}}$) are shifted in time with respect to each other.

Since these many-body laser simulations are demanding and time-consuming, it would be very useful for basic studies to have a simple model that phenomenologically captures these non-equilibrium effects. In the following, we introduce such a model and compare its predictions with those of the quantum statistical laser theory and with the main experimental results presented in Section 6.2.

6.3.1 Three-level rate equations

This section extends the two-level rate equation model discussed in Section 6.1 to a three-level system. As illustrated in Fig. 6.10, an increase in carrier temperature corresponds to a redistribution of carriers towards higher energy states within their respective bands. In the subsequent cooling cycle, these carriers then relax back towards the band edge and the lasing level. In the simplest rate equation approximation, this redistribution of charge carriers can be modeled by introducing an additional energy level (representing carriers in high energy states) and corresponding transition rates, as illustrated in Fig. 6.16. Carrier cooling is represented by a constant rate γ_{cool}, while carrier heating is represented by a time-dependent rate $\gamma_{\mathrm{heat}} = \xi G_{\mathrm{mod}}$, where ξ is a dimensionless proportionality constant. The corresponding equations for this

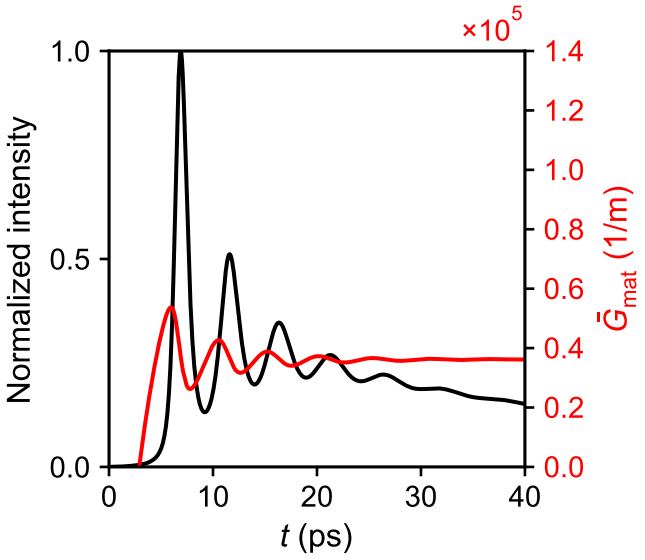

Figure 6.15 | Time delay between laser intensity and peak material gain. Quantum statistical simulation of the NW laser intensity and peak material gain ($\bar{G}_{\mathrm{mat}}$) as a function of time (t) for single-pulse excitation with $P/P_{\mathrm{th}} = 2.5$. The simulation shows that the oscillations in the laser intensity and the peak material gain are shifted in time respect to each other. The data were taken from Fig. 6.11a,b. (Adapted from [68])

three-level system are

$$\frac{d\mathcal{N}_{\mathrm{hot}}}{dt} = \frac{\eta_{\mathrm{p}} P}{\epsilon_{\mathrm{p}}} - \gamma_{\mathrm{cool}} \mathcal{N}_{\mathrm{hot}} + \gamma_{\mathrm{heat}} \mathcal{P}, \tag{6.5}$$

$$\frac{d\mathcal{N}}{dt} = -R_{\mathrm{sp}} - G_{\mathrm{mod}} \mathcal{P} + \gamma_{\mathrm{cool}} \mathcal{N}_{\mathrm{hot}} - \gamma_{\mathrm{heat}} \mathcal{P} \tag{6.6}$$

and

$$\frac{d\mathcal{P}}{dt} = \left[G_{\mathrm{mod}} - \gamma_{\mathrm{ph}} \right] \mathcal{P} + \beta_{\mathrm{sp}} R_{\mathrm{sp}}, \tag{6.7}$$

where $\mathcal{N}_{\mathrm{hot}}$ describes the number of carriers in high energy states. Here, G_{mod} always represents the unsaturated gain, since in the three-level rate equation model, gain saturation is effectively described by the heating and cooling terms.

6.3.2 Determination of effective heating and cooling rates

The rate γ_{cool} and the proportionality constant ξ are free parameters and were determined by fitting the three-level rate equation model to both the experimental data and the results of the quantum statistical model.

The cooling rate γ_{cool} describes the initial relaxation of photoexcited carriers towards the band edge and thus strongly influences the turn-on time (t_{on}) of the NW laser. The turn-on time data previously presented in Fig. 6.12a were therefore used to determine γ_{cool}. These data are presented in Fig. 6.17a together with the simulation results of

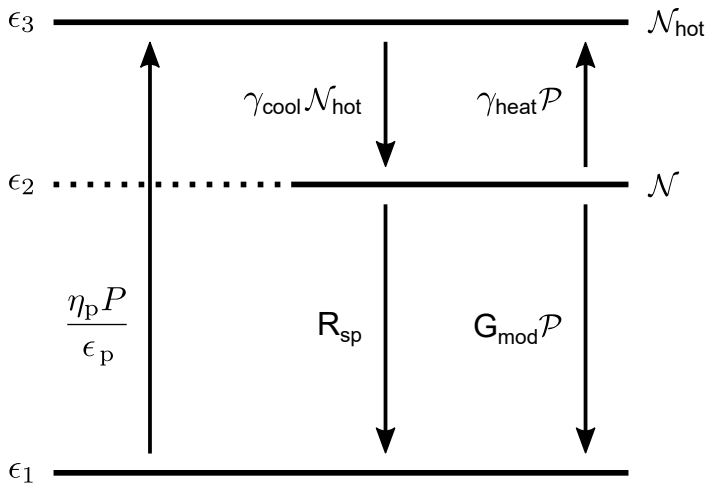

Figure 6.16 | Three-level rate equation model. Sketch of three levels with energies ($\epsilon_1 < \epsilon_2 < \epsilon_3$) and the corresponding terms describing the transition of carriers between them. The number of carriers in high energy states is denoted by $\mathcal{N}_{\text{hot}}$. Heating and cooling of carriers is phenomenologically described by effective rates γ_{heat} and γ_{cool}, respectively. Apart from the new terms, the notation is the same as for the two-level model.

the three-level rate equation model (RE). Best agreement with the experimental data and the quantum statistical (QS) model was obtained for $\gamma_{\text{cool}} = 0.125\,\text{ps}^{-1}$. This corresponds to an upper state lifetime of 8 ps and is consistent previous work [65]. As can be seen in Fig. 6.17a, the rate equation simulation is in excellent agreement with the experimental data and the quantum statistical simulation over the entire measurement range.

Once γ_{cool} is chosen, the heating rate γ_{heat} determines the oscillation frequency. The oscillation frequency data previously presented in Fig. 6.12b were therefore used to determine ξ. These data are shown in Fig. 6.17b together with the simulation results of the three-level rate equation model (RE). Best agreement with the experimental data and the quantum statistical (QS) model was obtained for $\xi = 5$. Physically, this means that for each photon created via stimulated emission, five charge carriers are transferred from the lasing level to the higher energy level. Over the entire measurement range, the results of the three-level rate equation simulation are in excellent agreement with both the experimental data and the quantum statistical simulation.

6.3.3 Output pulse shape

The three-level rate equation (RE) model was further verified by comparing its prediction for the output pulse shape with that of the quantum statistical (QS) laser theory. For this purpose, the data presented in Fig. 6.11a,c were used as a reference.

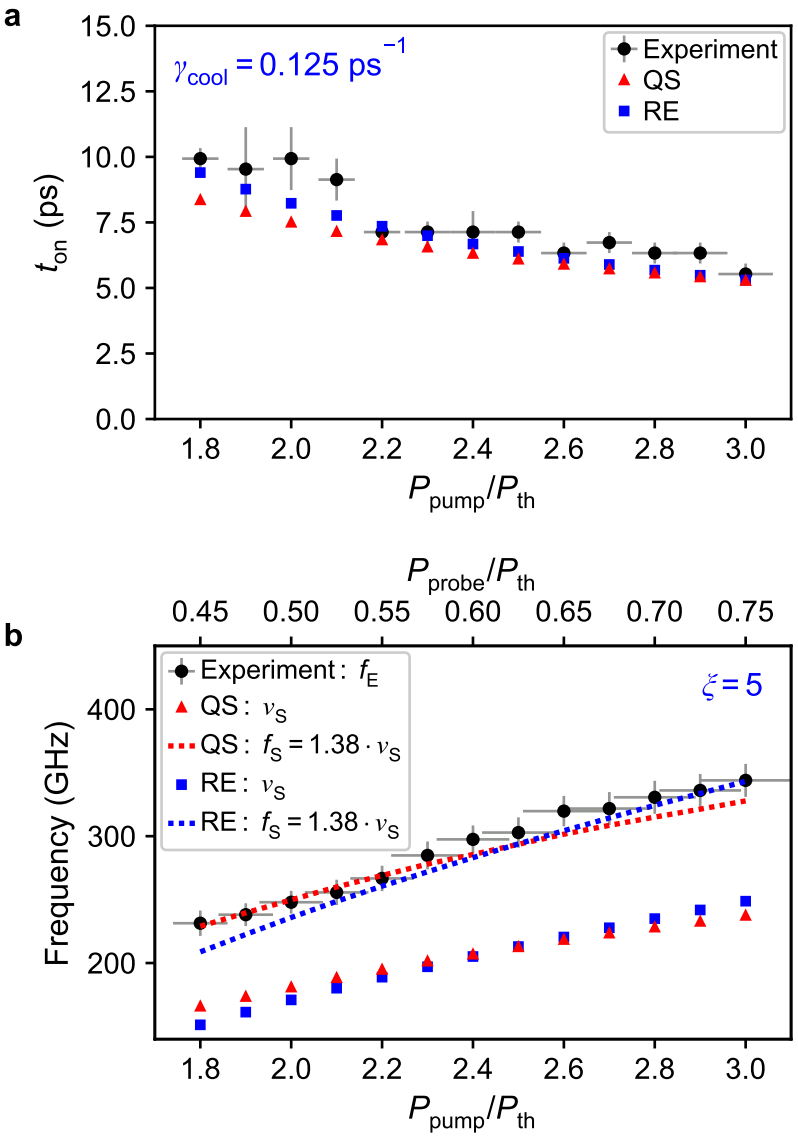

Figure 6.17 | Determination of heating and cooling parameters for NW-A. a, The turn-on time (t_{on}) of the three-level rate equation model was adjusted to the experimental data and the results of the quantum statistical laser theory using the cooling rate γ_{cool} as a fit parameter. Best agreement was achieved for $\gamma_{cool} = 0.125\,\mathrm{ps}^{-1}$. **b**, The proportionality factor ξ, and thus the heating rate γ_{heat}, was determined by adjusting the oscillation frequency to the results of the experiment and the quantum statistical model. Best agreement was achieved for $\xi = 5$. The simulation parameters of the three-level rate equation model are listed in Table 6.3. The experimental data and the results of the quantum statistical model were taken from Fig. 6.12.

Name	Symbol	Value	Source
Confinement factor	Γ	1.2	COMSOL Multiphysics
Group index	n_g	7	COMSOL Multiphysics
Nanowire length	L	10 µm	Microscope images
Nominal nanowire radius	R_{NW}	170 nm	Growth protocol
Spont. emission lifetime	τ_{spon}	740 ps	Quantum stat. model
Spont. emission factor	β_{sp}	0.1	Quantum stat. model
Gain parameter	G_0	$3.98 \times 10^3\,\mathrm{cm}^{-1}$	Log. gain approx.
Gain parameter	$\mathcal{N}_s/V_{NW}$	$2.38 \times 10^{17}\,\mathrm{cm}^{-3}$	Log. gain approx.
Gain parameter	$\mathcal{N}_{tr}/V_{NW}$	$2.2 \times 10^{17}\,\mathrm{cm}^{-3}$	Log. gain approx.
End facet reflectivity	R	0.3	Free parameter
Cooling rate	γ_{cool}	$0.125\,\mathrm{ps}^{-1}$	Free parameter
Proportionality factor	ξ	5	Free parameter

Table 6.3 | Simulation parameters of the three-level rate equation theory. Except for γ_{cool} and ξ, all parameters are the same as for the two-level rate equation model, see Table 6.1. In order for the three-level rate equation model to have a threshold carrier density that is close to the experiment and the quantum statistical model ($N_{th} \sim 3.4 \times 10^{17}\,\mathrm{cm}^{-3}$), R was adjusted to 0.3. The values listed here were used for all three-level rate equation simulations, unless specified otherwise. (Values were taken from [128] and [68])

These data are shown in Fig. 6.18a,b together with the results of the three-level rate equation simulation. The presented simulations were performed for a normalized excitation power of $P/P_{th} = 2.5$. All simulation parameters of the three-level rate equation model are listed in Table 6.3.

The excellent agreement between the two theoretical models in Fig. 6.18a demonstrates that the three-level rate equation approach correctly describes the most important physical processes of the NW laser dynamics. The slightly larger oscillation amplitude in the quantum statistical simulation is likely due to the fact that in this model the effective cooling rate is a function of time, whereas in the three-level rate equation approach γ_{cool} is approximated as a constant.

Figure 6.18b shows that for low confinement ($\Gamma = 0.12$), the oscillations also completely disappear in the rate equation simulation. In addition, the overall output pulse shape is in good agreement with that of the quantum statistical model. These findings further confirm the importance of Γ for the ultrafast non-equilibrium dynamics shown in Fig. 6.18a and discussed in detail in Section 6.2.

6.3.4 Resonance frequency

From Fig. 6.17b and Fig. 6.18a, it is evident that the three-level rate equation model described by Eq. 6.5 to Eq. 6.7 exhibits an internal resonance. The frequency of this

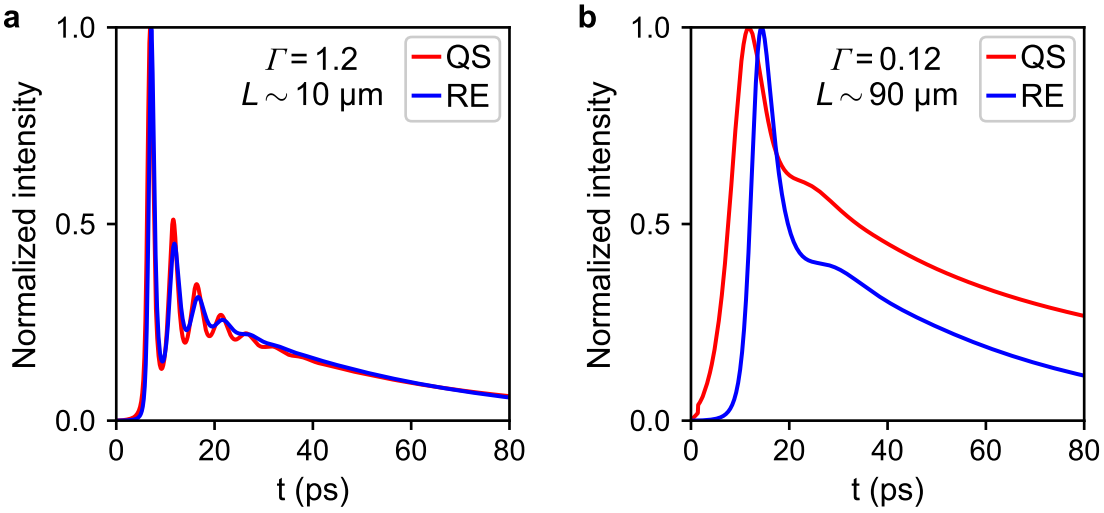

Figure 6.18 | Comparison of simulated output pulse shapes. a, Normalized output intensities as a function of time for NW-A. The simulations were performed with a confinement factor of $\Gamma = 1.2$ and a length of $L = 10\,\mu\mathrm{m}$. The three-level rate equation (RE) model is in excellent agreement with the quantum statistical (QS) model. **b**, Simulated intensity dynamics of a similar laser with $\Gamma = 0.12$ and $L = 90\,\mu\mathrm{m}$. Consistent with the quantum statistical laser theory, the three-level rate equation model also predicts that the ultrafast non-equilibrium dynamics disappear for low mode confinement. In both **a** and **b**, the normalized excitation power was set to $P/P_{\mathrm{th}} = 2.5$. The simulation parameters of the rate equation model are listed in Table 6.3. The data of the quantum statistical model were taken from Fig. 6.11a,c.

resonance can be calculated analogously to the discussion in Section 3.1.6. The only difference is that here the linearized system of equations is described by a 3×3 matrix. As a consequence, there are three eigenvalues resulting in three resonance frequencies (f_r) and damping rates (γ_r).

Figure 6.19a presents the three resonance frequencies ($f_{\mathrm{r}1}$, $f_{\mathrm{r}2}$, $f_{\mathrm{r}3}$) for NW-A as a function of normalized CW excitation power (P/P_th). One of the frequencies ($f_{\mathrm{r}1}$) is identical to zero except for one data point. The absolute values of the other two resonance frequencies ($f_{\mathrm{r}2}$ and $f_{\mathrm{r}3}$) are larger than the relaxation oscillation frequency f_R of the corresponding ideal two-level system, but otherwise behave similarly as a function of excitation power. The frequencies are smaller than in Fig. 6.17b since for pulsed excitation the peak photon number inside the resonator is much higher than under steady-state conditions for a given normalized excitation power.

The corresponding damping rates are shown in Fig. 6.19b. Here, the most notable characteristic is that for a certain range of excitation powers there are solutions with negative γ_r. This means, that small deviations from the steady-state photon number will be amplified until the damping becomes positive and sufficiently strong [117]. As a result, the steady state is unstable in this region, which can lead to self-pulsation, a well-known phenomenon in other types of lasers that can have many different causes apart from carrier temperature effects [267–272]. Whether this negative damping predicted here does in fact lead to observable physical effects such as self-pulsation or chaotic behavior could be clarified by experimentally observing the CW laser output as a function of time in future experiments.

6.3.5 Modulation response

Analogous to Section 6.1.2, the modulation response provides information about the strength of the resonance associated with the resonance frequency discussed in Section 6.3.4. In the three-level system, there are two possible types of modulation, both of which are illustrated in Fig. 6.20.

Interband modulation

Figure 6.20a shows a sketch of *interband* modulation. Here, the modulation (red) is applied between the valence and the conduction band. More specifically, it is applied between the lowest and the highest energy level of the three-level system. This type of modulation is very similar to the one used previously in Section 6.1.2. To describe the modulation, Eq. 6.5 was adapted according to Figure 6.20a.

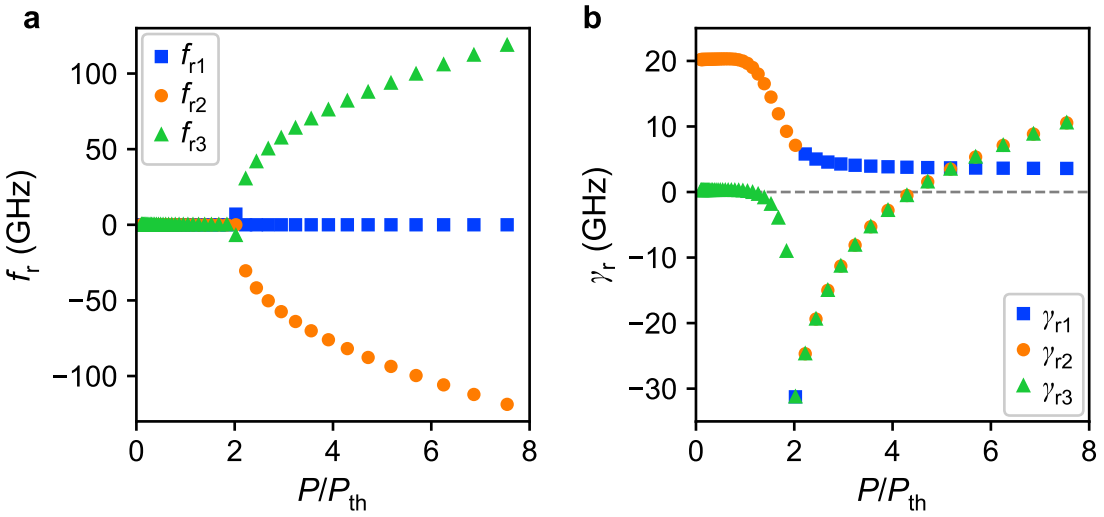

Figure 6.19 | Resonance frequency and damping rate. a,**b**, Resonance frequency and damping rate as a function of excitation power (P) normalized to its threshold value (P_{th}). Since the three-level rate equation model is described by three equations, there are three different eigenfrequencies (f_{r1}, f_{r2}, f_{r3}) with corresponding damping rates (γ_{r1}, γ_{r2}, γ_{r3}). **b**, For a certain region of excitation powers, γ_{r} is negative. This means that the steady-state is unstable in this region, which can lead to self-pulsation [117, 267–272].

Intraband modulation

Figure 6.20b shows a sketch of *intraband* modulation. In this case, the pump power between the valence and the conduction band is constant, while the modulation (red) periodically transfers carriers within a given band to a higher energy state. Physically, this type of modulation corresponds to a periodic heating of the carrier temperature and could be realized by applying THz heating fields to a CW laser as discussed in Refs. [261, 273]. To describe the modulation, Eq. 6.5 and Eq. 6.6 were adapted according to Figure 6.20b.

Simulation results

The simulation results for *interband* modulation are summarized in Fig. 6.21a for a CW excitation power of $P/P_{\mathrm{th}} = 8$. The orange curve shows the interband modulation response of a NW with a mode confinement factor of $\Gamma = 1.2$ and a length of $L = 10\,\mu\mathrm{m}$. The blue curve shows the corresponding interband modulation response of a similar laser with $\Gamma = 0.12$ and $L = 90\,\mu\mathrm{m}$. The NW laser exhibits a weak resonance at a frequency of $f_{\mathrm{r}} = 120\,\mathrm{GHz}$, which is absent in the laser with low mode confinement. Physically, this is a resonance between the carrier temperature and the laser intensity. It is further evident that both the orange and the blue curve do not exhibit a carrier-photon resonance. This is consistent with the results of the two-level rate equation

approach shown previously in Fig. 6.2b. For better comparison, the orange shaded area indicates the two-level rate equation modulation response of a NW laser with gain saturation values between $\mathcal{P}_{\mathrm{sat}} = 100$ (lower bound) and $\mathcal{P}_{\mathrm{sat}} = 500$ (upper bound). If the three-level rate equation model correctly describes the gain saturation dynamics, then one would expect the modulation response far from the resonance frequency f_{r} to behave similarly to the simpler two-level approach. Figure 6.21a shows that this is indeed the case. We thus have the interesting situation that the same effect that strongly dampens relaxation oscillations creates a new resonance at even higher frequencies. In addition, the 3 dB frequency ($f_{3\mathrm{dB}} \sim 6\,\mathrm{GHz}$) is in excellent agreement with the expectations from the two-level rate equation model ($f_{3\mathrm{dB}} \sim 3\,\mathrm{GHz}$ to $15\,\mathrm{GHz}$) as well.

The corresponding simulation results for *intraband* modulation are summarized in Fig. 6.21b. Here, the NW laser exhibits a strong resonance at $f_{\mathrm{r}} = 120\,\mathrm{GHz}$. Similarly to **a**, this resonance does not exist for the laser with low mode confinement. The 3 dB frequency seems to be very high for both types of lasers (close to 1 THz). However, for a real laser this is unlikely to be the case due to additional saturation mechanisms not captured by the rate equation model [261, 273]. In reality, the decrease in modulation response for frequencies $> f_{\mathrm{r}}$ is thus expected to be faster than predicted by the rate equation simulation.

The results presented in Fig. 6.21 clearly illustrate that for GaAs-AlGaAs core-shell NW lasers it is the strong mode confinement that creates a new resonance between the carrier temperature and laser intensity. This *temperature-photon* resonance occurs at very high frequencies (here: $f_{\mathrm{r}} = 120\,\mathrm{GHz}$), much faster than relaxation oscillations. Taking advantage of intraband modulation with THz heating fields [261, 273], this could enable ultrafast laser modulation at previously unattainable speeds [168], as already noted in the discussion of Section 6.2.

6.4 Quasi-degenerate transient reflection spectroscopy

In Section 6.2, we used an indirect method to measure the ultrafast non-equilibrium dynamics of GaAs-AlGaAs core-shell NW lasers. This experimental method has the disadvantage that it required the introduction of a proportionality factor of 1.38 to compare the simulated oscillation frequency with that of the experiment. The underlying reason is the chirp of the NW output pulses, which slightly distorts the measurement data, e.g. in Fig. 6.7b. This problem can be circumvented by using an experimental method capable of directly temporally resolving the NW laser dynamics with subpicosecond resolution.

There are three main methods to achieve this: optical Kerr gating [63, 67], photolumi-

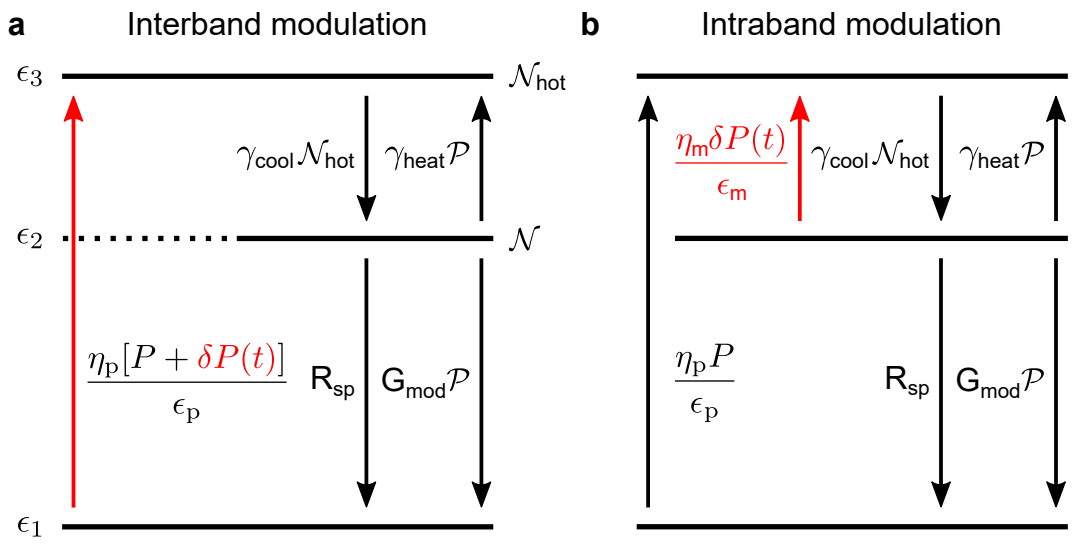

Figure 6.20 | Interband and intraband modulation. **a**, Sketch of interband modulation. **b**, Sketch of intraband modulation. Here, η_{m} and ϵ_{m} describes the absorption efficiency and the photon energy of the pump source that is used for modulation. This type of modulation can be realized using THz radiation [261, 273]. In **a**,**b**, the time-dependent modulation is marked in red.

nescence upconversion [64, 274], and transient absorption/reflection spectroscopy [275, 276]. With any of these techniques, achieving a signal-to-noise ratio sufficient for a detailed measurement of a single GaAs-AlGaAs core-shell NW laser is a nontrivial task. Here we used transient reflection spectroscopy since this method is directly compatible with the pump-probe photoluminescence setup described in Section 4.2.2, whereas optical Kerr-gating and photoluminescence upconversion require dedicated setups with suitable pump lasers.

In this chapter, we present the first experimental results of transient reflection spectroscopy on a single GaAs-AlGaAs core-shell NW laser, using the optical setup described in Section 4.2.3. The experimental parameters are listed in Table 6.4.

6.4.1 Laser threshold

Figure 6.22a shows the light-in light-out curve of the investigated NW (NW-G). A linear fit was used to determine a threshold excitation power of $P_{\text{th}} = (0.36 \pm 0.02)\,\text{mW}$, which corresponds to a threshold fluence of $F_{\text{th}} = (1.9 \pm 0.1)\,\mu\text{J cm}^{-2}$. The threshold of NW-G is thus approximately a factor of 2.4 smaller than that of NW-A, which was studied in Section 6.2.

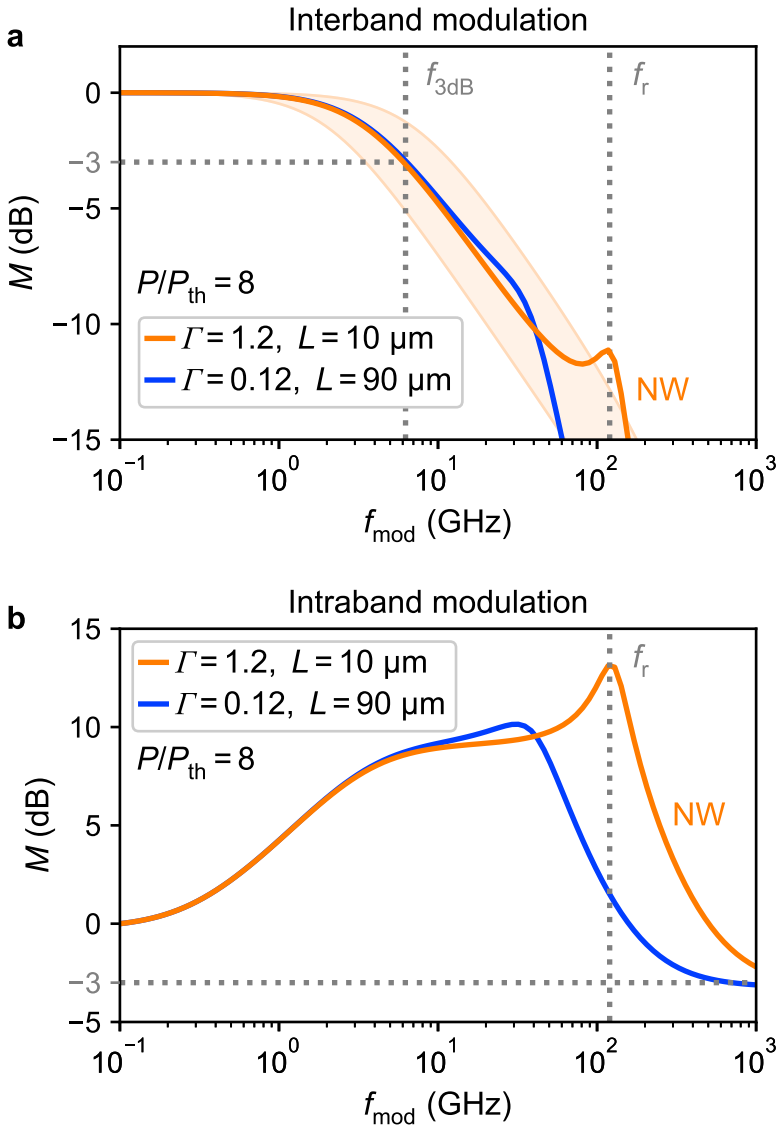

Figure 6.21 | Three-level modulation response. **a**, The orange curve shows the interband modulation response of a NW with a mode confinement factor of $\Gamma = 1.2$ and a length of $L = 10\,\mu\mathrm{m}$. The blue curve shows the corresponding interband modulation response of a similar laser with $\Gamma = 0.12$ and $L = 90\,\mu\mathrm{m}$. The NW exhibits a weak resonance at a frequency of $f_\mathrm{r} = 120\,\mathrm{GHz}$, which is absent in the laser with low mode confinement. Physically, this is a resonance between the carrier temperature and the laser intensity. The orange shaded area indicates the two-level rate equation modulation response of a NW with gain saturation values between $\mathcal{P}_\mathrm{sat} = 100$ (lower bound) and $\mathcal{P}_\mathrm{sat} = 500$ (upper bound). The $3\,\mathrm{dB}$ frequency ($f_\mathrm{3dB} \sim 6\,\mathrm{GHz}$) is in excellent agreement with the expectations from the two-level rate equation model. **b**, For intraband modulation the NW exhibits a strong resonance at $f_\mathrm{r} = 120\,\mathrm{GHz}$. Again, this resonance does not exist for the laser with low mode confinement. For a real laser, the decrease in modulation response at very high modulation frequencies ($f_\mathrm{mod} \gg f_\mathrm{r}$) is likely to be faster than predicted by the simulation due to additional damping mechanisms not captured by the rate equation model [261, 273]. All simulations were performed with a CW excitation power of $P/P_\mathrm{th} = 8$. The simulation parameters that are not explicitely shown in **a**,**b** are listed in Table 6.3.

6.4.2 Time dependence of differential reflectivity

Figure 6.22b shows the differential reflectivity ($\Delta\mathcal{R}$) as a function of time (t) and normalized excitation power (P/P_{th}). With increasing excitation power, $\Delta\mathcal{R}$ increases due to the increasing carrier density. In addition, a pronounced kink appears in the time series above threshold corresponding to the onset of lasing.

This can be clearly seen in Fig. 6.22c, which shows the time dependence of $\Delta\mathcal{R}$ for an excitation power of $P/P_{\mathrm{th}} = 2.25$. The initial short peak near $t = 0\,\mathrm{ps}$ is caused by Pauli blocking due to the carriers excited by the pump pulse. As discussed in Section 3.2.1, carrier-carrier scattering leads to a rapid redistribution of photoexcited carriers within their respective bands on a timescale of a few hundred femtoseconds [106], resulting in a sharp decay of this initial peak. Subsequently, the electron-hole plasma (EHP) cools via carrier-LO-phonon scattering [106], as indicated by the blue shaded region. Consistent with Fig. F.1, this leads to an accumulation of carriers near the probe energy and consequently to an increase in $\Delta\mathcal{R}$. After the electron-hole plasma has cooled sufficiently, the laser turns on at $t_{\mathrm{on}} \sim 18\,\mathrm{ps}$ (vertical dashed line). Stimulated emission then leads to a quick decrease in carrier density and thus $\Delta\mathcal{R}$, producing a pronounced kink in the time series.

6.4.3 Limitations and solutions

We note that there are no oscillations of $\Delta\mathcal{R}$ in the lasing region in this particular measurement. However, such oscillations would be expected based on the results in Section 6.2 and Section 6.3. To understand this, there are several points to consider.

First, the amplitude of the oscillations is expected to be small. Using the simulation data in Fig. 6.9, the oscillation amplitude of absorption/reflection at the probe energy due to carrier temperature changes can be estimated to be $< 5\,\%$ of the total signal.

Second, the oscillation amplitude decreases with increasing probe energy. This means that it is beneficial to measure as close as possible to the band edge and the lasing energy. There is still room for improvement here, as this is only limited by the available filters and by the fact that the pump pulse must still be able to bring the NW into the lasing regime.

Third, the small diameter ($\sim 2\,\mu\mathrm{m}$) of the probe and detection spot makes the experiment susceptible to mechanical noise. A small mechanical displacement of a few hundred nanometers of pump, probe and detection relative to the NW can easily lead to a change in $\Delta\mathcal{R}$ of a few percent. This noise occurs on a time scale similar to the waiting time of the lock-in amplifier (3 s), and therefore can wash out the small oscillations due to carrier temperature changes in the NW laser. As a solution to this problem, the size of all spot diameters (pump, probe and detection) should be increased.

Name	Symbol	Value
Pulse duration of titanium-sapphire laser	Δt_{pump}	200 fs
Photon energy of titanium-sapphire laser	ϵ_{p}	1.542 eV
Pump spot diameter	d_{pump}	17 µm
Probe spot diameter	d_{probe}	2 µm
Detection spot diameter	d_{det}	2 µm
Lattice temperature	T_{L}	10 K
Probe fluence	F_{probe}	3.1 µJ cm^{-2}
Lock-in amplifier: low pass filter slope	-	24 dB oct^{-1}
Lock-in amplifier: integration time	-	300 ms
Lock-in amplifier: wait time	-	3 s

Table 6.4 | Experimental parameters for quasi-degenerate transient reflection spectroscopy. The excitation energy corresponds to an electron excess energy of $\Delta\epsilon_{\mathrm{e}} \sim 20\,\mathrm{meV}$ and a hole excess energy of $\Delta\epsilon_{\mathrm{h}} \sim 4\,\mathrm{meV}$. The wait time of the lock-in amplifier is the settling time between each measurement point. The parameters listed here were used for all transient reflection experiments.

Fourth, and most importantly, this measurement was performed with a probe fluence of $F_{\mathrm{probe}} = 3.1\,\mu\mathrm{J\ cm}^{-2}$, which is quite strong compared to the pump fluence of $F_{\mathrm{pump}} = 4.3\,\mu\mathrm{J\ cm}^{-2}$. Such a strong probe pulse can significantly perturb the NW laser itself [156], potentially obscuring weak internal dynamics. Consequently, the probe pulse must be weaker, but this increases the noise of the measurement. However, this increase in noise can be compensated by increasing the modulation frequency. By replacing the optical chopper wheel with an acousto-optic or electro-optic modulator, the modulation frequency could be increased from 10 kHz to up to 1 MHz.

6.4.4 Excitation power dependence of the turn-on time

Figure 6.22d shows that t_{on} is inversely proportional to the excitation power, consistent with expectations from literature [277]. This inverse proportionality is demonstrated by the excellent agreement between t_{on}^{-1} and a linear fit, as shown in red. Taking into account the lower threshold of NW-G, the data in Fig. 6.22d are also consistent with the turn-on times shown in Fig. 6.12a.

6.5 Summary

In this chapter, we investigated the lasing dynamics of GaAs-AlGaAs core-shell NW lasers with various experimental and theoretical approaches.

In Section 6.1, we first investigated their relaxation oscillation frequency using the two-level rate equation approach. In doing so, we showed that the corresponding

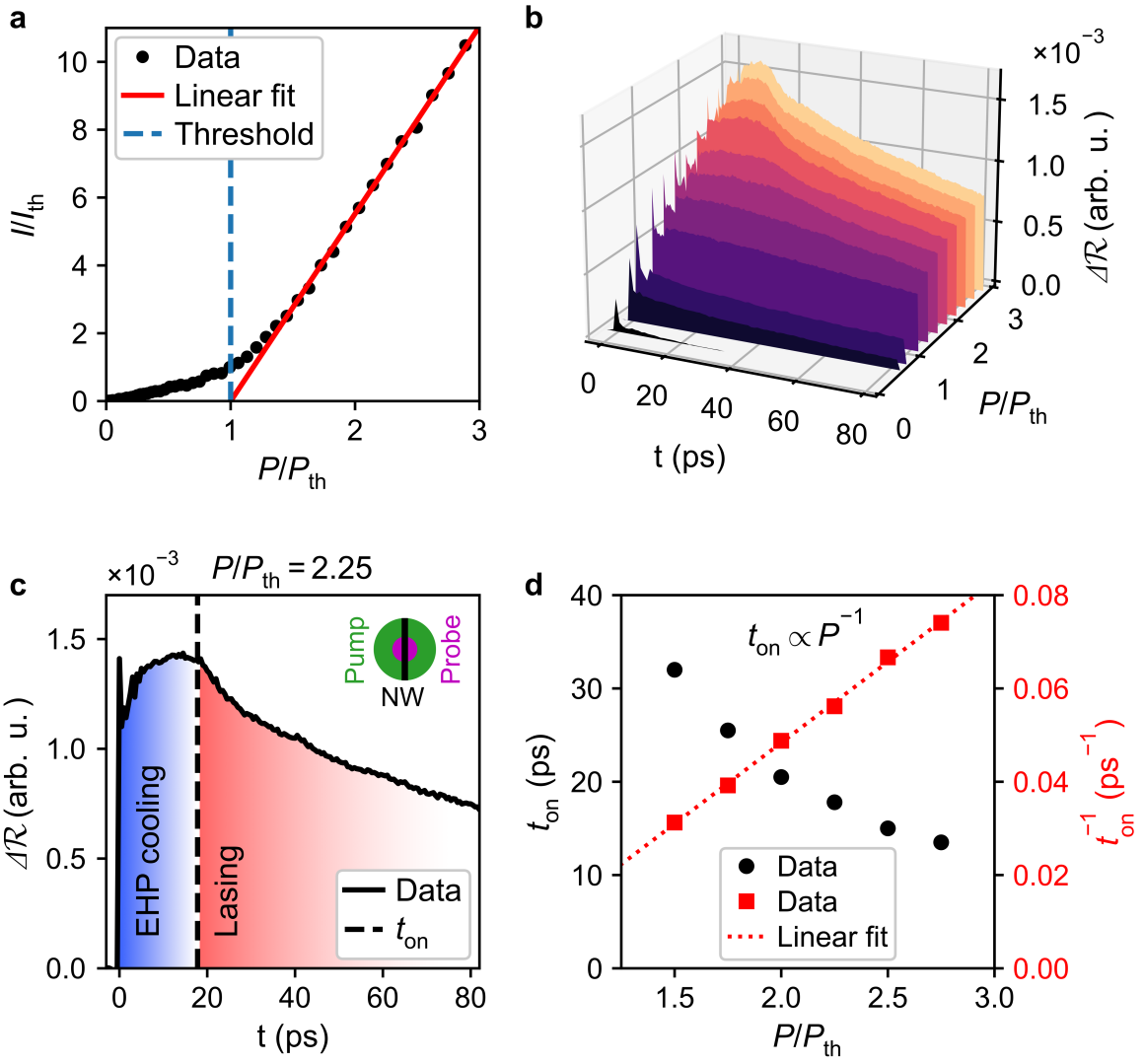

Figure 6.22 | Quasi-degenerate transient reflection spectroscopy. a, Light-in light-out curve of NW-G. Similar to Fig. 6.4b, the threshold was determined by the intersection of the linear fit with the horizontal axis. Here, $P_{\mathrm{th}} = (0.36 \pm 0.02)\,\mathrm{mW}$, which corresponds to a threshold fluence of $F_{\mathrm{th}} = (1.9 \pm 0.1)\,\mu\mathrm{J\ cm^{-2}}$. **b**, Differential reflectivity ($\Delta\mathcal{R}$) of NW-G as a function of time (t) and normalized excitation power (P/P_{th}). As the excitation power increases, a pronounced kink appears in the time series corresponding to the onset of lasing. **c**, Exemplary time dependence of $\Delta\mathcal{R}$ for an excitation power of $P/P_{\mathrm{th}} = 2.25$. The data was taken from **b**. After the initial cooling of the photoexcited and hot electron-hole plasma (EHP), lasing starts at $t_{\mathrm{on}} \sim 18\,\mathrm{ps}$ (vertical dashed line), leading to a pronounced kink in the time dependence of $\Delta\mathcal{R}$. **d**, The turn-on time (t_{on}) is inversely proportional to the excitation power, which is consistent with expectations from literature [277]. The inverse proportionality is demonstrated by the linear fit to the inverse of the turn-on time, as shown in red.

carrier-photon resonance is overdamped when gain saturation is taken into account. We then simulated their impulse response and showed that gain saturation leads to long ($> 50\,\mathrm{ps}$) and strongly asymmetric output pulses with a sharp rise and a long tail, consistent with the results in the subsequent sections.

In Section 6.2, we obtained a detailed understanding of the microscopic processes that govern the NW laser dynamics on picosecond timescales, using a combination of femtosecond pump-probe spectroscopy and simulations based on many-body laser theories. We showed that the output pulses of GaAs-AlGaAs core-shell NW lasers exhibit sustained intensity oscillations with frequencies ranging from 160 GHz to 260 GHz. We found that these non-equilibrium dynamics are intimately linked to the strong mode confinement in these lasers and the resulting strong interaction between the lasing mode and the gain material. Using many-body laser theories, we showed that strong mode confinement combined with a dynamic competition between photoinduced carrier heating and cooling via phonon scattering enables self-induced electron-hole plasma temperature oscillations, explaining the observed experimental results. Since these dynamics involve oscillations of the carrier temperature and not the carrier density, they circumvent the speed limitations inherent in conventional relaxation oscillations [261]. As a result, the combination of THz modulation with NWs or other suitably designed lasers could enable direct laser modulation at previously unachievable speeds, as highlighted in the discussion of Section 6.2.

In a next step, we showed in Section 6.3 that the main results from Section 6.2 can be reproduced by extending the two-level rate equation model to a three-level system. As the main reason for the excellent results of the three-level rate equation approach, we identified the fact that it provides a more accurate description of gain saturation, as it allows for a time delay between G_{mat} and $\mathcal{P}$, in contrast to the two-level rate equation model. This led to the interesting finding that the same effect that strongly dampens the carrier-photon resonance in NWs simultaneously creates a new temperature-photon resonance at higher frequencies. Next, similar to Section 6.1, we investigated the resonance frequency and modulation response of the three-level system. For a NW, the modulation response exhibited a weak resonance for interband modulation and a strong resonance for intraband modulation. In both cases, it had a resonance frequency of $f_{\mathrm{r}} = 120\,\mathrm{GHz}$ at a CW excitation power of $P/P_{\mathrm{th}} = 8$. Consistent with the results of Section 6.2, this resonance disappeared for a laser with weak mode confinement.

Finally, in Section 6.4, we presented the first experimental results of quasi-degenerate transient reflection spectroscopy of a single GaAs-AlGaAs core-shell NW laser. We observed the thermalization of the electron-hole plasma on femtosecond timescales, its subsequent cooling on picosecond timescales, and the following onset of stimulated emission, all in agreement with the results of Section 6.2 and Appendix F. The turn-on time of the laser was shown to be inversely proportional to the excitation power, in

agreement with previous theoretical work [277]. However, the expected oscillations in $\Delta\mathcal{R}$ due to the non-equilibrium dynamics described in Section 6.2 could not be observed yet. Here, we listed four limitations of the current experiment and corresponding suggestions for improvement. The most important issue we identified is the power of the probe pulse, which should be reduced, as it can otherwise significantly disturb the NW laser dynamics [156].

Chapter 7

Summary and outlook

In this thesis, we investigated the lasing characteristics of GaAs-AlGaAs core-shell NW lasers [68]. Chapter 2 to 4 presented the necessary theoretical and experimental background. In the following, we summarize the main findings of this work and conclude with a brief outlook on future research.

Continuous wave lasing characteristics

In Chapter 5, we studied the steady-state properties of GaAs-AlGaAs core-shell NW lasers using microphotoluminescence spectroscopy and showed that the quantum statistical laser theory provides an accurate microscopic description of all experimental results. Thereby, we found that the laser linewidth does not follow the expectations of the well-known Schawlow-Townes-Henry theory. Using the quantum statistical model, this could be explained by significant carrier heating above threshold, resulting in a depinning of the carrier density, which ultimately leads to a strong broadening of the laser linewidth. These results show that the CW lasing characteristics of GaAs-AlGaAs core-shell NW lasers are strongly affected by gain saturation via carrier heating and the resulting non-equilibrium effects.

Lasing dynamics

In Chapter 6, we then employed various experimental and theoretical approaches to investigate their lasing dynamics.

- In Section 6.1, we discussed the impact of gain saturation on the dynamic performance of GaAs-AlGaAs core-shell NW lasers using the two-level rate equation approach. We showed that the carrier-photon resonance is overdamped

and that the output pulses are long ($> 50\,\mathrm{ps}$) and strongly asymmetric in time, with a sharp rise and a long tail.

- In Section 6.2, we investigated the microscopic lasing dynamics of GaAs-AlGaAs core-shell NW lasers. Thereby, we demonstrated how strong mode confinement and the resulting large $\partial G_{\mathrm{mod}}/\partial T_{\mathrm{c}}$ lead to exceptionally strong non-equilibrium laser dynamics that modulate the laser output. In a lattice temperature range between 10 K to 80 K, these manifest themselves as carrier temperature oscillations through a dynamic competition between carrier heating via stimulated emission and carrier cooling via carrier-LO-phonon scattering. The results of our combined experimental and theoretical approach are consistent with oscillation frequencies ranging from 160 GHz to 260 GHz.

- In Section 6.3, we showed that a three-level rate equation approach provides an accurate phenomenological description of these ultrafast non-equilibrium dynamics. By calculating the modulation response, we revealed that while gain saturation due to carrier heating leads to strong damping of the carrier-photon resonance, it simultaneously creates a new resonance between the electron-hole plasma temperature and the laser intensity at even higher frequencies. Consistent with the results in Section 6.2, this new temperature-photon resonance only appears for lasers with strong mode confinement.

- In Section 6.4, we performed quasi-degenerate transient reflection spectroscopy on a single GaAs-AlGaAs core-shell NW laser. Although the limitations of the experimental setup did not allow the direct measurement of carrier temperature oscillations, we observed the thermalization and cooling of the electron-hole plasma and the subsequent onset of lasing. Moreover, we identified an inverse proportionality between the turn-on time of the laser and the excitation power. All experimental results are in agreement with theoretical expectations.

Outlook

This section provides a brief outlook on opportunities for further research.

Transient reflection spectroscopy

Improving the quasi-degenerate transient reflection setup as proposed in Section 6.4 could allow the direct observation of the carrier temperature oscillations discussed in Section 6.2 and Section 6.3. Since the time dependence of the transient reflectivity can be calculated using the quantum statistical laser theory, this allows an even more detailed comparison between experiment and theory. As a variation of this approach,

an optical parametric oscillator could be used to enable non-degenerate transient reflection measurements. The distinct advantage of this approach would be a lower signal-to-noise ratio compared to the quasi-degenerate case. Furthermore, by adjusting the probe energy, it could also allow the NW laser dynamics to be spectrally resolved.

Ultrafast laser modulation using terahertz heating fields

Modulation schemes based on the carrier-photon resonance are currently limited to frequencies $< 60\,\mathrm{GHz}$ [168]. Recently, however, direct laser modulation with a 3 dB frequency of $\sim 100\,\mathrm{GHz}$ has been demonstrated by exploiting a photon-photon resonance [168]. Taking advantage of the temperature-photon resonance discussed in Section 6.2 and Section 6.3 could allow to achieve even faster modulation frequencies ranging from 160 GHz to 260 GHz. This could be achieved by the use of modulation schemes based on THz heating fields [261]. Suitable sources of THz radiation are commercially available. In such a scheme, an externally applied terahertz heating field modulates the carrier temperature and thus the laser output, avoiding the speed bottleneck of interband modulation [261]. This also creates new opportunities for ultrafast pulse shaping of nanoscale semiconductor lasers and, provided the modulation depth is sufficient, would allow the generation of picosecond pulse trains with extremely high repetition rates $> 100\,\mathrm{GHz}$. In perspective, further research could achieve ultrafast modulation of NW lasers integrated into silicon photonic circuits [45].

General laser design considerations

We note that our theoretical models [101, 148] are general and therefore our findings can be applied to the design of other types of semiconductor lasers as well. There are several points to consider in the development of semiconductor lasers, that are intended to be highly susceptible to externally applied terahertz fields. According to the key insight of Section 6.2, such a laser should have strong mode confinement, which can be achieved by an optimized spatial overlap of the lasing mode and the gain material [119, 121]. The choice of the gain material is crucial as well, as it directly affects the cooling rate of the carriers. Moreover, the operating point of the carrier density and temperature should be chosen such that $\partial G_{\mathrm{mod}}/\partial T_{\mathrm{c}}$ is maximized. According to a previous theoretical investigation, this is the case when both the carrier density and temperature are as low as possible [261]. The differential modal gain can further be optimized by tuning the cavity length to place the lasing mode on the high energy side of the gain spectrum [239–241]. Lastly, the laser must have a large enough resonator bandwidth and should preferentially be single modal. Both points can be achieved by making the laser as short as possible, which of course, must be balanced with the simultaneously increasing threshold.

Dynamics of quantum well NW lasers

Practical applications would ultimately require ultrafast modulation of NW lasers at room temperature. In this context, a significant drawback of the non-equilibrium dynamics described in Section 6.2 and Section 6.3 is the limitation to cryogenic temperatures ($T_{\mathrm{L}} \leq 80\,\mathrm{K}$). However, this could be overcome by using a low-dimensional gain medium, such as multi-quantum wells [52, 278, 279]. The use of quantum wells as a gain medium would simultaneously allow the emission wavelength to be tuned to the technologically relevant telecommunication bands [54, 55], which is especially important for on-chip laser devices. In view of their importance for practical applications, it will therefore be of great interest to study the ultrafast dynamics of quantum well NW lasers using the experimental and theoretical tools developed in this thesis.

Appendix $\mathcal{A}$

Natural constants and material parameters

Name	Symbol	Value	Source
Speed of light	c_0	$2.9979 \times 10^8\,\mathrm{m\,s^{-1}}$	[280]
Elementary charge	e_0	$1.6022 \times 10^{-19}\,\mathrm{C}$	[280]
Vacuum permittivity	ε_0	$8.854 \times 10^{-12}\,\mathrm{C\,V^{-1}\,m^{-1}}$	[280]
Vacuum permeability	μ_0	$4\pi \times 10^{-7}\,\mathrm{H\,m^{-1}}$	[280]
Electron mass	m_0	$9.109 \times 10^{-31}\,\mathrm{kg}$	[280]
Boltzmann constant	k_B	$8.617 \times 10^{-5}\,\mathrm{eV\,K^{-1}}$	[280]
Reduced Planck constant	$\hbar$	$6.582 \times 10^{-16}\,\mathrm{eV\,s}$	[280]
Electron effective mass	m_e	$0.067 \times m_0$	[84, 101, 143]
Hole effective mass	m_h	$0.377 \times m_0$	[84, 101, 143]
Transition matrix element	$6\lvert\mathcal{M}_\mathrm{T}\rvert^2/m_0$	28.8 eV	[9]
Bandgap at 10 K	$\epsilon_{\mathrm{g}0}\,(10\,\mathrm{K})$	1.5192 eV	[99]
Relative static dielectric constant	ε_r	12.9	[281]
Relative optical dielectric constant	ε_∞	10.89	[281]
Bohr radius	a_0	12.43 nm	[101, 143]
LO phonon energy	ϵ_LO	36.5 meV	[110]

Table A.1 | Natural constants and material parameters. The listed parameters were used for all theoretical models. (Adapted from [68])

Appendix $\mathcal{B}$

Experimental determination of the turn-on time

This chapter includes material from

A. Thurn, J. Bissinger, S. Meinecke, P. Schmiedeke, S. S. Oh, W. W. Chow, K. Lüdge, G. Koblmüller and J. J. Finley, 'Self-induced ultrafast electron-hole plasma temperature oscillations in nanowire lasers'. *arXiv:2108.11784* submitted (2021)

Here we discuss the method used to experimentally determine t_{on}. Figure B.1a shows the time-integrated spectra of a selected pump-probe measurement belonging to Fig. 3a of the main manuscript. The measurement was performed with an excitation power of $P_{\mathrm{pump}}/P_{\mathrm{th}} \sim 2.9$ and $P_{\mathrm{probe}}/P_{\mathrm{th}} \sim 0.5$, and otherwise the same experimental conditions as for Fig. 3a. We integrated all spectra along the energy axis and plotted the integrated intensity as a function of Δt in Fig. B.1b. From these data a minimum and maximum value (dashed grey lines) was determined by averaging over a suitable number of data points around $\Delta t = 0\,\mathrm{ps}$ and around the respective maximum. Using these values, we defined t_{on} as the time that it takes the integrated intensity to rise from the minimum to $1/e$ of the difference between the maximum and the minimum, as indicated by the horizontal dashed green line in Fig. B.1b. This method relies on the transient reduction of the probe pulse absorption due to a depletion of available states and its subsequent recovery [59]. We attribute this to a non-negligible overlap of the excitation laser ($\epsilon_{\mathrm{p}} \sim 1.588\,\mathrm{eV}$, $\Delta t_{\mathrm{pump}} \sim 200\,\mathrm{fs}$) with the thermalized electron and hole distributions. In this particular example, this method yields $t_{\mathrm{on}} = (6.3 \pm 0.4)\,\mathrm{ps}$, which is indicated by the vertical dashed green lines in Fig. B.1a,b. The error is an overestimate of the 95% CI of the mean, which follows from the averaging used to obtain the minimum and maximum values, and the discreteness of the data (step size

$\sim 0.4\,\mathrm{ps}$).

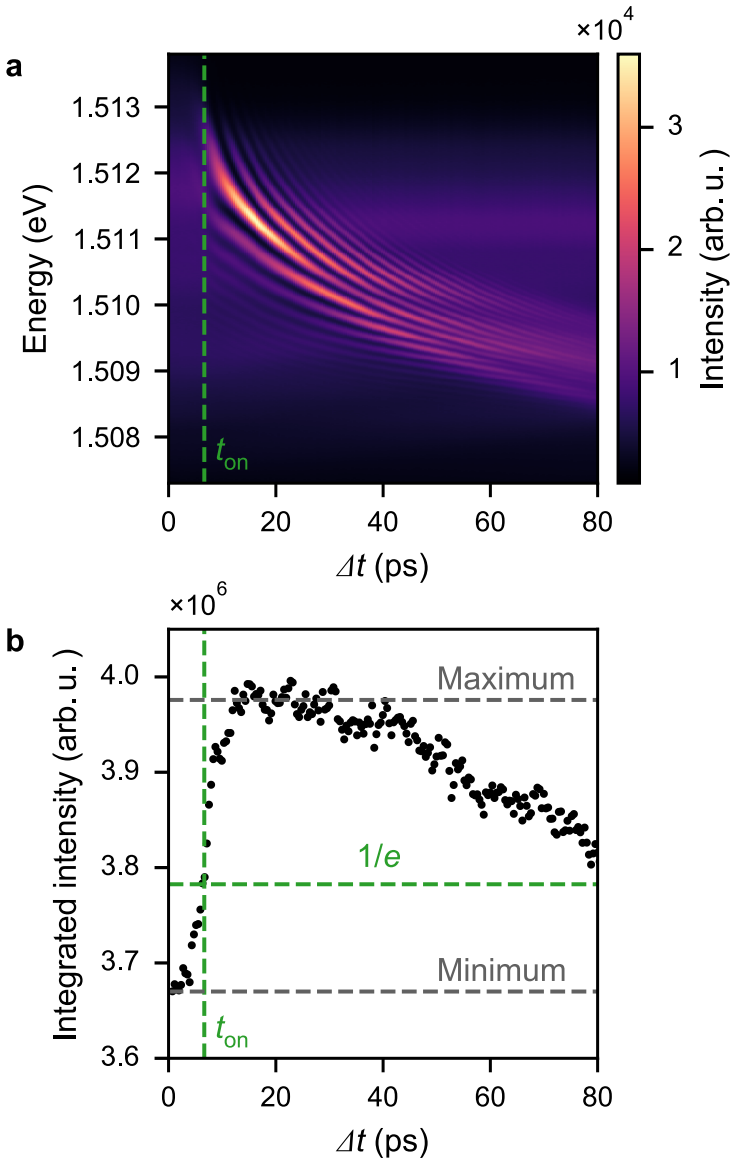

Figure B.1 | Experimental determination of the turn-on time. **a**, Time-integrated pump-probe spectra as a function of Δt. Integration over the energy axis yielded the integrated intensity shown in **b**. **b**, We defined the turn-on time (t_{on}) as the time that it takes the integrated intensity to rise from the minimum to $1/e$ of the difference between the maximum and the minimum. (Adapted from [68])

Appendix C

Influence of the spontaneous emission coupling factor

This chapter includes material from

A. Thurn, J. Bissinger, S. Meinecke, P. Schmiedeke, S. S. Oh, W. W. Chow, K. Lüdge, G. Koblmüller and J. J. Finley, 'Self-induced ultrafast electron-hole plasma temperature oscillations in nanowire lasers'. *arXiv:2108.11784* submitted (2021)

Previous research on nanolasers has shown that the spontaneous emission coupling factor β_{sp} is, in general, a weak function of the carrier density [255, 256]. When the carrier density changes by an order of magnitude from $10^{17}\,\mathrm{cm}^{-3}$ to $10^{18}\,\mathrm{cm}^{-3}$, β_{sp} is expected to change by up to $\sim 25\,\%$ [256].

From Fig. 6.8d, we see that the NW laser operates at carrier densities of $\sim 5 \times 10^{17}\,\mathrm{cm}^{-3}$ and that the total carrier density only decreases by $\sim 15\,\%$ within the first 30 ps. The corresponding expected change in β_{sp} would then be on the order of a few percent. Based on this, it is expected that the carrier density dependence of β_{sp} does not play a significant role for the NW lasers dynamics. Especially not for their ultrafast carrier temperature dynamics, which are main focus of our work.

To check this, we used the quantum statistical model to investigate how the NW laser dynamics depend on β_{sp}. Since the expected influence is small, we changed β_{sp} by four orders of magnitude to make the trend clear. The results of this simulation are shown in Fig. C.1. Generally, a larger β_{sp} leads to faster turn-on times, slightly slower oscillations, and stronger damping. At the same time, however, it is clear that β_{sp} would have to change by at least an order of magnitude to have an appreciable influence on the NW laser dynamics. We therefore conclude that the carrier density dependence of β_{sp} can be neglected for the purposes of our work. This allows us to

approximate β_{sp} as a constant.

Furthermore, a comparison of Fig. 6.8d and Fig. 5.2b shows that the NW laser operates in a similar carrier density range for both pulsed and CW excitation. From this, we conclude that the same β_{sp} can be used to describe the NW laser under both excitation conditions.

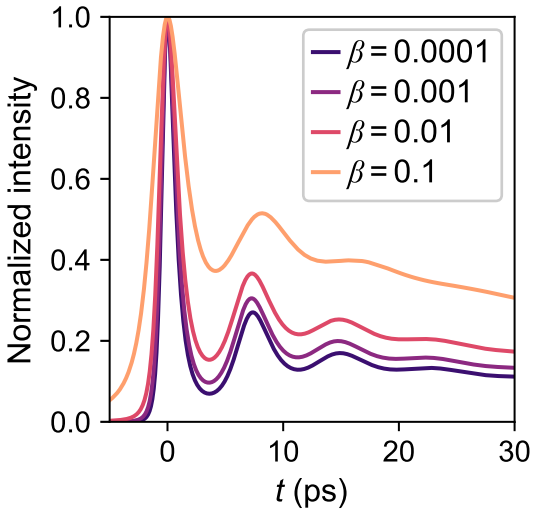

Figure C.1 | Influence of the spontaneous emission coupling factor on the NW lasing dynamics. NW output intensity as a function of time after excitation with a power of $P_{\mathrm{pump}} \sim 2 \times P_{\mathrm{th}}$. For better comparison, the output pulses are normalized and temporally aligned with respect to their maximum intensity. (Adapted from [68])

Appendix $\mathcal{D}$

Semiconductor Bloch simulation of the NW laser dynamics

This chapter includes material from

A. Thurn, J. Bissinger, S. Meinecke, P. Schmiedeke, S. S. Oh, W. W. Chow, K. Lüdge, G. Koblmüller and J. J. Finley, 'Self-induced ultrafast electron-hole plasma temperature oscillations in nanowire lasers'. *arXiv:2108.11784* submitted (2021)

Here we discuss the time-resolved pump-probe response of a NW laser simulated using the semiconductor Bloch model. Figure D.1a presents the output intensity as a function of time for a pump-probe delay of $\Delta t = 40\,\mathrm{ps}$ (grey dashed lines), where we used the same excitation conditions as for Fig. 6.7c,d and Fig. 6.8 in the main manuscript. The NW output pulses are strongly asymmetric in time with a pronounced initial peak, following oscillations ($\nu_\mathrm{S} = 253\,\mathrm{GHz}$, magenta) and a slow decay. Figure D.1b reveals that these intensity oscillations result from oscillations of the carrier temperatures, which mirror the time dependence of the intensity in Figure D.1a. The sudden increase of T_e and T_h at $t = 40\,\mathrm{ps}$ is due to transient heating caused by the injection of additional carriers [156]. The above observations are in qualitative agreement with the quantum statistical simulation in Fig. 6.8a,b, although here the oscillations are more strongly damped. One reason for this is the weaker manifestation of oscillations in T_e and T_h compared to the quantum statistical model. Especially T_h shows only very weak and strongly damped oscillations. This can have several reasons. Firstly, the quantum statistical model self-consistently calculates time-dependent scattering rates, while the scattering rates of the semiconductor Bloch model are kept constant. Secondly, the electron-hole scattering included in the Boltzmann equations used to

calculate the scattering rates allows for an energetic exchange of the two subsystems. Thereby, the periodic oscillation of T_e is partially transferred to the holes in the valence band. This demonstrates the limitations of the relaxation rate approximation and the importance of treating carrier-carrier and carrier-LO-phonon scattering microscopically. Nevertheless, ν_S is not strongly affected by these limitations and the resulting stronger damping, as it mainly reflects the time dependence of T_e in the present case.

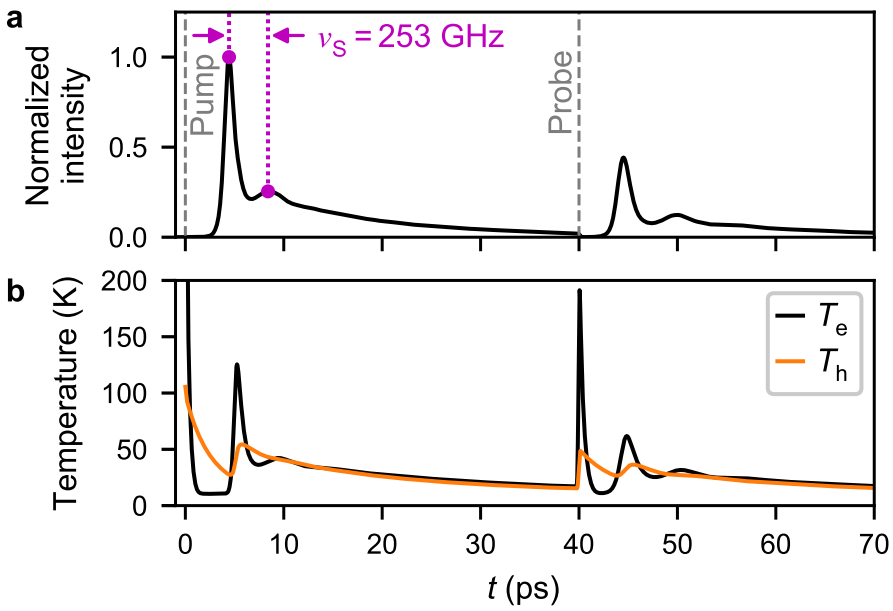

Figure D.1 | Semiconductor Bloch simulation of the time-resolved pump-probe response. **a**, Output intensity as a function of time for pump-probe excitation with $\Delta t = 40\,\mathrm{ps}$. The oscillation frequency (ν_S) of the first output pulse is indicated in magenta. **b**, Corresponding time dependence of the electron (T_e) and hole (T_h) temperatures, reflecting the intensity dynamics in **a**. (Adapted from [68])

In the relaxation rate approximation of the semiconductor Bloch model we used piecewise constant scattering rates, which we chose with guidance from the rates calculated within the quantum statistical simulation, see Fig. 6.8c. We used two sets of scattering rates, one for the initial relaxation of the photoexcited carriers and another for the lasing process. The former gets an additional factor of 1.5 to approximately account for the faster scattering during the initial carrier relaxation, see Fig. 6.8c. Both sets of scattering rates are summarized in Table D.1. Since the k-resolved and time-dependent scattering rates of the quantum statistical model do not directly translate to the relaxation rate approximation of the semiconductor Bloch model, we added a factor ξ for adjustment. We chose ξ such that the simulated t_{on} and f_S approximately match the experiment. For simulations, $\xi = 10$ was used. All other simulation parameters are listed in Table 5.1 and Table A.1.

Symbol	Value during relaxation	Value during lasing	Unit
$\gamma_{\mathrm{cc,e}}$	$1.5 \cdot \xi \cdot 8.5$	$\xi \cdot 8.5$	ps^{-1}
$\gamma_{\mathrm{cc,h}}$	$1.5 \cdot \xi \cdot 16.4$	$\xi \cdot 16.4$	ps^{-1}
γ_{ep}	$1.5 \cdot \xi \cdot 0.4$	$\xi \cdot 0.4$	ps^{-1}
γ_{hp}	$1.5 \cdot \xi \cdot 0.03$	$\xi \cdot 0.03$	ps^{-1}

Table D.1 | Scattering rates used in the semiconductor Bloch model. Summary of the rates for carrier-carrier scattering of electrons ($\gamma_{\mathrm{cc,e}}$), carrier-carrier scattering of holes ($\gamma_{\mathrm{cc,h}}$), electron-LO-phonon scattering (γ_{ep}) and hole-LO-phonon scattering (γ_{hp}). Two sets of constant scattering rates were used. One for the initial relaxation of the photoexcited carriers and another for the lasing process. For our simulations we used $\xi = 10$.

Appendix $\mathcal{E}$

Determination of the carrier temperature

This chapter includes material from

A. Thurn, J. Bissinger, S. Meinecke, P. Schmiedeke, S. S. Oh, W. W. Chow, K. Lüdge, G. Koblmüller and J. J. Finley, 'Self-induced ultrafast electron-hole plasma temperature oscillations in nanowire lasers'. *arXiv:2108.11784* submitted (2021)

Here we discuss how the carrier temperatures are determined and show that they are well-defined parameters. The data presented here belong to the quantum statistical simulation in Fig. 6.8. Figure E.1 shows two selected electron distributions for $t = 6.5\,\mathrm{ps}$ (upper panel) and $t = 8.7\,\mathrm{ps}$ (lower panel). At $t = 6.5\,\mathrm{ps}$ the laser intensity reaches its first maximum (see Fig. 6.8a) and therefore spectral hole burning, if it plays a role, is expected to be strong for this distribution. In contrast, at $t = 8.7\,\mathrm{ps}$ the intensity is at the following local minimum, which means that spectral hole burning should be weak in this case. We fitted each carrier distribution with a Fermi-Dirac function, whereby the carrier density N and the total energy of the carriers served as a constraint. The resulting fits are shown in Fig. E.1 with red dotted lines, together with their respective fit parameters. In both cases, the fit provides a good approximation to the carrier distribution, demonstrating that spectral hole burning does not play a significant role. Thus, for our NW laser T_e is a well defined parameter for all time steps. The only exception to this are very short timeframes after excitation, since the photoexcited carrier distributions need a few hundred femtoseconds to thermalize [177, 178, 188, 194]. A similar discussion to the above applies to holes.

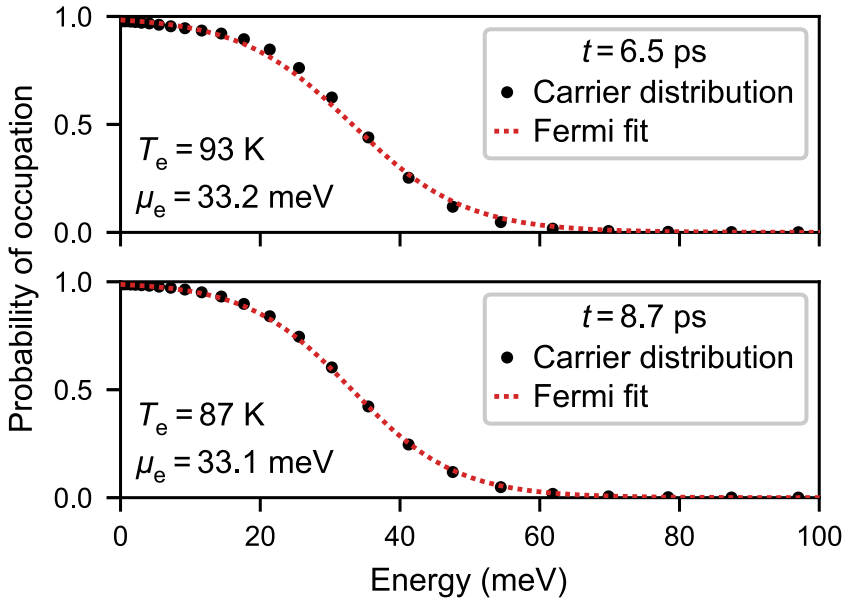

Figure E.1 | Determination of the carrier temperature. Two exemplary electron distributions for $t = 6.5\,\mathrm{ps}$ (upper panel) and $t = 8.7\,\mathrm{ps}$ (lower panel). In each case, the fitted Fermi-Dirac functions are a good approximation. The respective fit parameters (electron temperature T_e and Fermi energy μ_e) are given in each plot. The carrier density in the upper panel is $N = 5.12 \times 10^{17}\,\mathrm{cm}^{-3}$, whereas in the lower panel it is $N = 5.06 \times 10^{17}\,\mathrm{cm}^{-3}$. (Adapted from [68])

Appendix $\mathcal{F}$

Carrier relaxation

This chapter includes material from

A. Thurn, J. Bissinger, S. Meinecke, P. Schmiedeke, S. S. Oh, W. W. Chow, K. Lüdge, G. Koblmüller and J. J. Finley, 'Self-induced ultrafast electron-hole plasma temperature oscillations in nanowire lasers'. *arXiv:2108.11784* submitted (2021)

The data presented here belong to the quantum statistical simulation in Fig. 6.8. Figure F.1a,b shows the relaxation of photoexcited electrons and holes in the conduction band at three different time steps with $t = 0.0\,\mathrm{ps}$ (red), $t = 1.0\,\mathrm{ps}$ (orange) and $t = 5.3\,\mathrm{ps}$ (blue). Shown is the occupation probability as a function of $k \cdot a_0$, where k is the wave number and a_0 the Bohr radius. The electrons and holes are excited at $k \cdot a_0 \sim 4$ with a sech^2 pulse having a full width at half maximum of $\mathrm{FWHM} = 200\,\mathrm{fs}$. This corresponds to an electron excess energy of $\Delta\epsilon_\mathrm{e} \sim 60\,\mathrm{meV}$ and a hole excess energy of $\Delta\epsilon_\mathrm{h} \sim 10\,\mathrm{meV}$ with respect to the non-renormalized band gap [174]. Due to the finite discretization in k-space, this excitation injects the carriers into two k-points. During the excitation process, the carrier distributions are clearly non-thermal, exhibiting a peak where the carriers are injected. At $t = 1.0\,\mathrm{ps}$, the electron and hole distributions are already thermalized and take on the form of hot Fermi-Dirac distributions with temperatures of $T_\mathrm{e} = 154\,\mathrm{K}$ and $T_\mathrm{h} = 122\,\mathrm{K}$, respectively. This is consistent with literature, where thermalization is expected to occur within a few hundred femtoseconds [177, 178, 188, 194]. The subsequent cooling of these hot, thermalized carrier distributions is dominated by carrier-LO-phonon scattering [106], as already discussed in Section 6.2.3. This cooling leads to an accumulation of electrons and holes near the band edge and thus gradually increases the gain. Eventually, this

enables the NW laser to turn-on. In this particular example, $t_{on} = 5.7\,ps$. It is further instructive to see how the carrier distributions change within the respective bands as a function of time. This is illustrated in Figure F.1c,d. From these plots, it is clear that for the pump-probe photoluminescence experiment, it is the good overlap of the probe pulse with the hole distribution that allows the accurate determination of the turn-on time, as described in Appendix B.

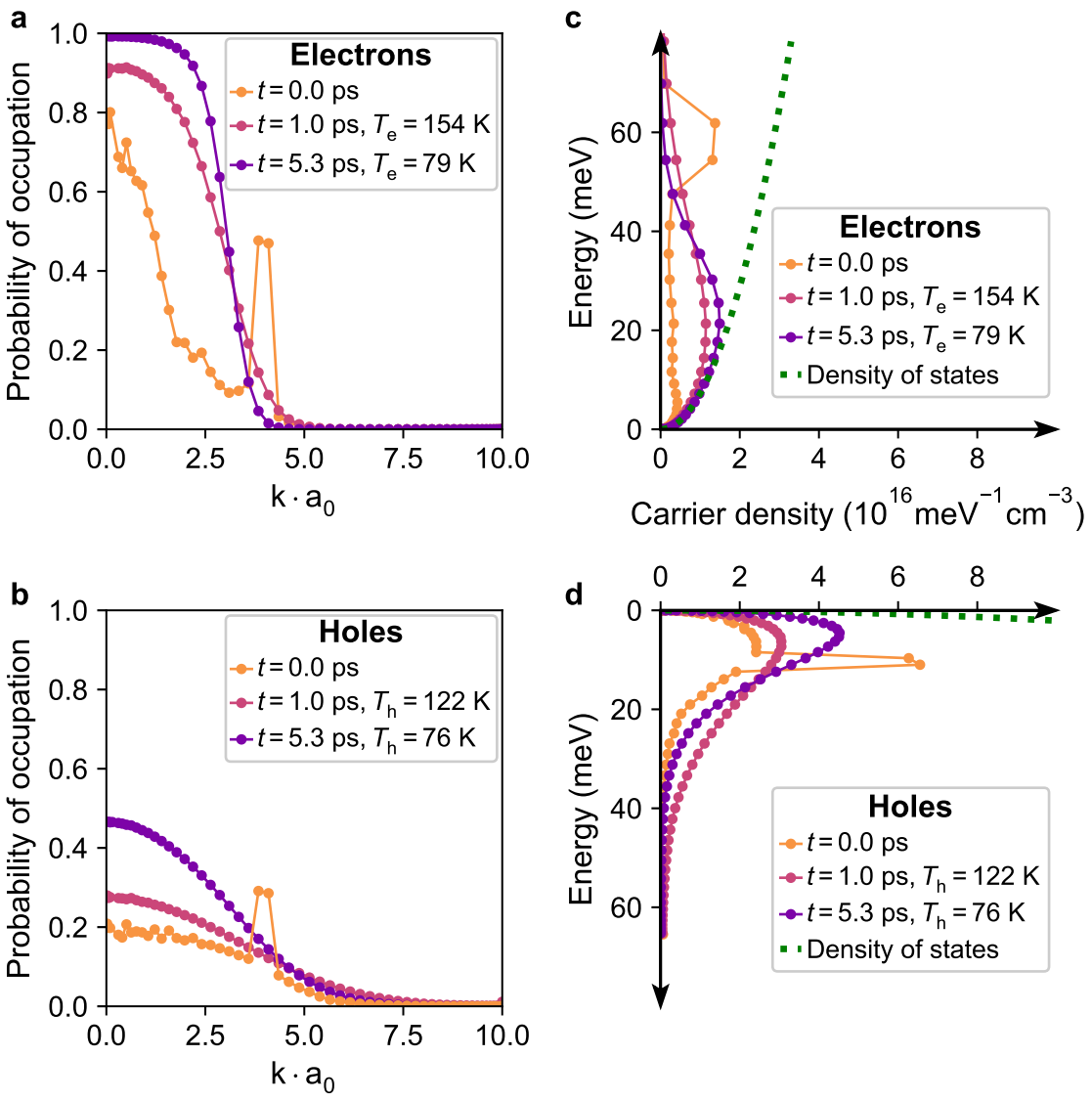

Figure F.1 | Carrier relaxation. **a**,**b**, Probability of occupation for electrons and holes as a function of $k \cdot a_0$, with wave nubmer k and Bohr radius a_0. To illustrate the initial relaxation process, the carrier distributions were extracted from the quantum statistical simulation at $t = 0.0\,\mathrm{ps}$, $t = 1.0\,\mathrm{ps}$ and $t = 5.3\,\mathrm{ps}$. The filled circles indicate the numerical discretization of the conduction band in the model. The temporal origin $t = 0.0\,\mathrm{ps}$ is defined as the moment in time where the maximum of the excitation pulse arrives at the NW. **c**,**d**, Energy-resolved carrier densities in the conduction and valence band. (Subfigure **a** adapted from [68])

Appendix $\mathcal{G}$

Determination of the oscillation frequency

This chapter includes material from

A. Thurn, J. Bissinger, S. Meinecke, P. Schmiedeke, S. S. Oh, W. W. Chow, K. Lüdge, G. Koblmüller and J. J. Finley, 'Self-induced ultrafast electron-hole plasma temperature oscillations in nanowire lasers'. *arXiv:2108.11784* submitted (2021)

Here, we discuss the procedure that is used to determine the experimental (f_{E}) and simulated (f_{S}) oscillation frequency from the respective magnitude of the electric field autocorrelation $|G^{(1)}(\Delta t,\tau)|$. In the following, we use an example that belongs to the experimental excitation power series in Fig. 6.12b. The selected $|G^{(1)}(\Delta t,\tau)|$ is presented in Fig. G.1a and was measured with an excitation power of $P_{\mathrm{pump}}/P_{\mathrm{th}} \sim 2.50$ and $P_{\mathrm{probe}}/P_{\mathrm{th}} \sim 0.63$. We calculated f_{E} from the time interval (indicated by green arrows) between the main sideband (white) and the first oscillation above (yellow). There are three reasons for this. Firstly, this oscillation is mainly influenced by the first output pulse (see Appendix H). Secondly, there the changes with Δt are small, and thirdly, this feature is also pronounced in the simulated $|G^{(1)}(\Delta t,\tau)|$ (see Fig. 6.7d). To avoid outliers, we determined the oscillation frequency over a range of different Δt. In this example, the selected region ranged from $\Delta t \sim 28\,\mathrm{ps}$ to $\Delta t \sim 56\,\mathrm{ps}$ with a step size of 2 ps, as indicated in Fig. G.1a. The obtained oscillation frequencies are presented in Fig. G.1b as a function of Δt (green), whereby the error bars represent an estimate of the standard deviation resulting from the Fourier transform of the spectral data. By averaging, we obtained $f_{\mathrm{E}} = (302 \pm 16)\,\mathrm{GHz}$ (black line). The error represents the 95 % CI of the mean and is indicated in Fig. G.1b by the grey shaded area. The same procedure, as discussed above, is used to determine f_{S} from the simulated $|G^{(1)}(\Delta t,\tau)|$.

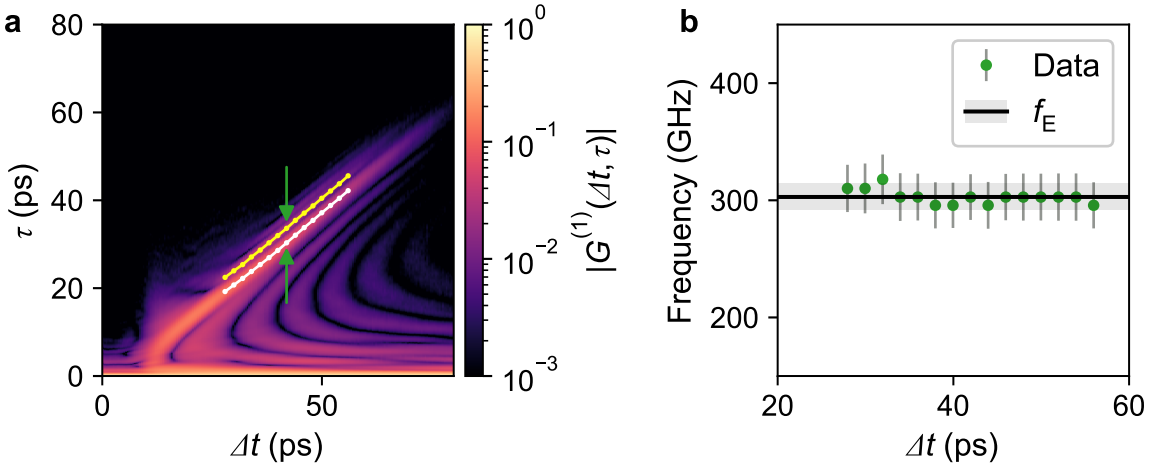

Figure G.1 | Determination of the oscillation frequency. **a**, Measured $|G^{(1)}(\Delta t, \tau)|$ as a function of pump-probe delay Δt and time shift τ. For a selected range of Δt, the white line indicates the maximum of the main sideband, whereas the yellow line indicates the maximum of the first oscillation above. For each selected Δt value (indicated by points), we calculated the oscillation frequency by evaluating the distance between the white and yellow maxima, as indicated by the green arrows. **b**, Resulting oscillation frequencies as a function of Δt. For easier comparison, the frequency axis is scaled in the same way as in Fig. 6.12b. Error bars represent the standard deviation resulting from the Fourier transform of the spectral data. We obtained the oscillation frequency f_{E} by averaging over all green data points and indicated the corresponding $95\,\%$ CI with the grey shaded area. (Adapted from [68])

Appendix $\mathcal{H}$

Comparison of electric field and intensity autocorrelation

This chapter includes material from

A. Thurn, J. Bissinger, S. Meinecke, P. Schmiedeke, S. S. Oh, W. W. Chow, K. Lüdge, G. Koblmüller and J. J. Finley, 'Self-induced ultrafast electron-hole plasma temperature oscillations in nanowire lasers'. *arXiv:2108.11784* submitted (2021)

Here, we compare the electric field autocorrelation $G^{(1)}(\Delta t,\tau)$ with the intensity autocorrelation $G^{(2)}(\Delta t,\tau)$. To facilitate this, we define the emitted electric field as $E(t) = A(t) \cdot \exp[i\Phi(t)]$, where $A(t)$ and $\Phi(t)$ denote the time-dependent amplitude and phase, respectively. With this definition one can write $G^{(1)}(\Delta t,\tau)$ as [254]

$$G^{(1)}(\Delta t,\tau) = \frac{1}{T}\int_T E^*(t)E(t+\tau)dt = \frac{1}{T}\int_T A(t)A(t+\tau)e^{i[\Phi(t+\tau)-\Phi(t)]}dt \tag{H.1}$$

and $G^{(2)}(\Delta t,\tau)$ as

$$G^{(2)}(\Delta t,\tau) = \frac{1}{T}\int_T I(t)I(t+\tau)dt = \frac{1}{T}\int_T [A(t)A(t+\tau)]^2dt \tag{H.2}$$

where T is the range of integration and $I(t) = |E(t)|^2$ the time-dependent laser intensity. From Eq. H.1 and Eq. H.2 it is apparent that $G^{(1)}(\Delta t,\tau)$ depends on both $A(t)$ and $\Phi(t)$, whereas $G^{(2)}(\Delta t,\tau)$ is only influenced by $A(t)$. Here, it is important to note that $A(t)$ and $\Phi(t)$ are not independent of each other, but coupled. This is because the carrier temperature oscillations modulate the complex susceptibility whose

real (χ') and imaginary (χ'') parts are related to the gain and the refractive index change, as can be seen by Eq. 3.63 and Eq. 3.64. In addition, χ' and χ'' are related by Kramers-Kronig relations. Thus, the carrier temperature modulates both $A(t)$ and $\Phi(t)$ with the same periodicity, which then also leads to oscillations in $G^{(1)}(\Delta t,\tau)$ and $G^{(2)}(\Delta t,\tau)$.

An example where this can be observed is shown in Fig. H.1a and Fig. H.1b, where we reproduced the normalized magnitude of the measured and simulated $G^{(1)}(\Delta t,\tau)$ from Fig. 6.7. The corresponding simulated $G^{(2)}(\Delta t,\tau)$ is presented in Fig. H.1c and, as expected, oscillations near the main sideband are also observed there. Comparing Fig. H.1b and Fig. H.1c, the influence of the phase-dependent part of Eq. H.1 is directly apparent, since it is naturally absent in Eq. H.2 and thus Fig. H.1c. To allow for a more detailed comparison, we marked the main sideband of $|G^{(1)}(\Delta t,\tau)|$ and $G^{(2)}(\Delta t,\tau)$ in all panels with white and green dashed lines, respectively. As expected, the sideband of $G^{(2)}(\Delta t,\tau)$, which is only influenced by $A(t)$, scales linearly with Δt and has a slope close to 1. A faint remnant of this sideband is visible in Fig. H.1b, whereas in Fig. H.1a it is completely gone. In contrast, the clearly visible sideband of $|G^{(1)}(\Delta t,\tau)|$ in Fig. H.1a,b only has a slope of ~ 0.8 (white dashed line). This shows that, in the present case, $G^{(1)}(\Delta t,\tau)$ is strongly influenced by the phase-dependent factor in Eq. H.1 and less so by its amplitude-dependent part. In Fig. H.1a we furthermore observe that $|G^{(1)}(\Delta t,\tau)|$ almost completely vanishes above the green dashed line. Due to the long output pulse lengths of up to $\sim 76\,\mathrm{ps}$ (see Fig. 6.7 and Fig. 6.8 of the main manuscript), one would expect a signal in this region, as can be seen when comparing with Fig. H.1c. This reveals that the second output pulse quickly looses its phase coherence with the first output pulse. The simulation in Fig. H.1b shows a similar behaviour, although not as pronounced as in the experiment in Fig. H.1a.

As a consequence, the oscillations near the main sideband of $|G^{(1)}(\Delta t,\tau)|$ are mainly determined by the first output pulse. Using the method described in Appendix G, we obtained an oscillation frequency of $f_\mathrm{S} = 350\,\mathrm{GHz}$ for the simulated $|G^{(1)}(\Delta t,\tau)|$ in Fig. H.1b. Among other effects, f_S does not directly correspond to the intensity oscillation frequency ν_S of the laser output, due to the influence of the carrier density dependent refractive index on the phase evolution. For comparison, in Appendix D we determined $\nu_\mathrm{S} = 253\,\mathrm{GHz}$. The semiconductor Bloch model therefore predicts that, in the present case, the frequencies f_S and ν_S are related by $f_\mathrm{S} = 1.38 \cdot \nu_\mathrm{S}$, which is confirmed by Fig. 6.12b and Fig. 6.14d in the main manuscript.

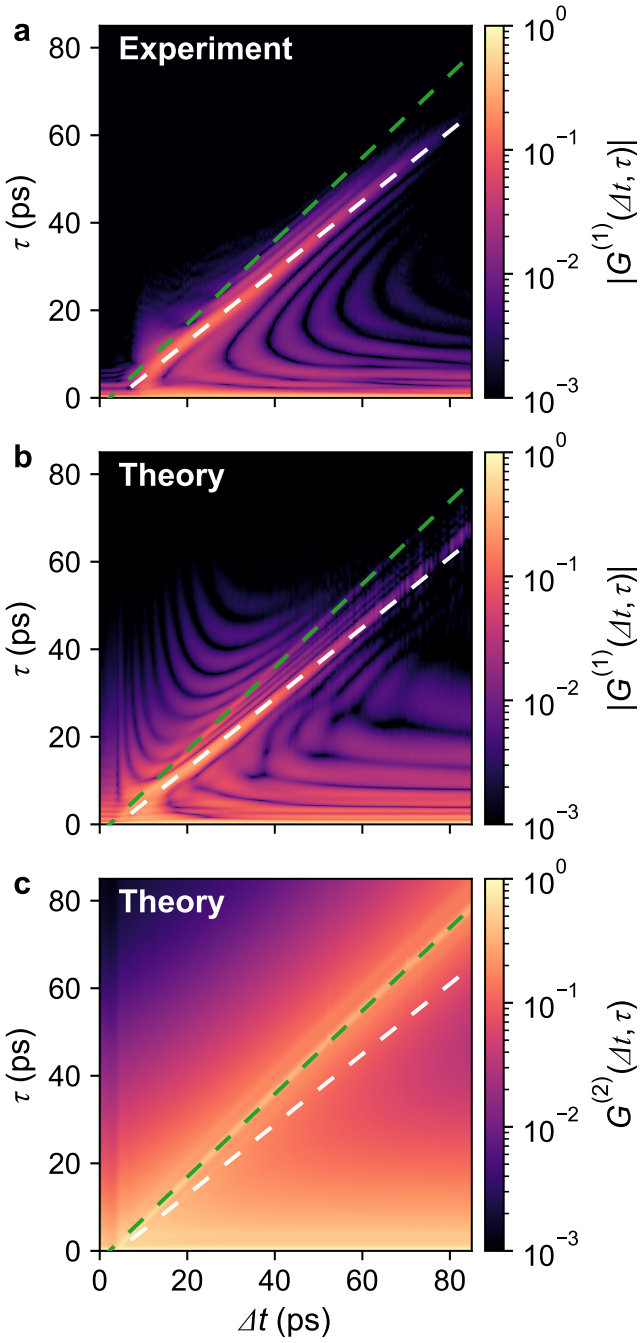

Figure H.1 | Comparison of electric field and intensity autocorrelation. **a**,**b** Experimental and simulated $|G^{(1)}(\Delta t,\tau)|$. **c**, Simulated intensity autocorrelation $G^{(2)}(\Delta t,\tau)$ obtained from the same simulation as in **b**. In all panels, the white and green dashed lines indicate the scaling of the main sideband of $|G^{(1)}(\Delta t,\tau)|$ and $G^{(2)}(\Delta t,\tau)$ with Δt, respectively. (Adapted from [68])

Appendix *I*

Output pulse length as a function of lattice temperature

This chapter includes material from

A. Thurn, J. Bissinger, S. Meinecke, P. Schmiedeke, S. S. Oh, W. W. Chow, K. Lüdge, G. Koblmüller and J. J. Finley, 'Self-induced ultrafast electron-hole plasma temperature oscillations in nanowire lasers'. *arXiv:2108.11784* submitted (2021)

Figure I.1 presents the dependence of $t_{\mathrm{pulse}} \sim t_{\mathrm{off}} - t_{\mathrm{on}}$ on T_{L}. The data correspond to the T_{L} series shown in Fig. 6.13 and Fig. 6.14 and were measured with the excitation powers fixed at $P_{\mathrm{pump}}/P_{\mathrm{th}} \sim 2.5$ and $P_{\mathrm{probe}}/P_{\mathrm{th}} \sim 0.5$. For $T_{\mathrm{L}} \leq 40\,\mathrm{K}$, t_{pulse} remains constant at $\sim 71\,\mathrm{ps}$ and then decreases down to a value of $(32.4 \pm 0.6)\,\mathrm{ps}$ at $T_{\mathrm{L}} = 100\,\mathrm{K}$. This decrease is connected to the shift of the lasing mode towards the high energy side of the gain spectrum as T_{L} increases (see discussion of Fig. 6.14). There, the lasing mode experiences a larger differential material gain with respect to carrier density $(\partial G_{\mathrm{mat}}/\partial N)$ [239], which leads to a decrease of t_{pulse}. This explains the behaviour seen in Fig. I.1 and is in accord with previous work on microcavity lasers [240, 241].

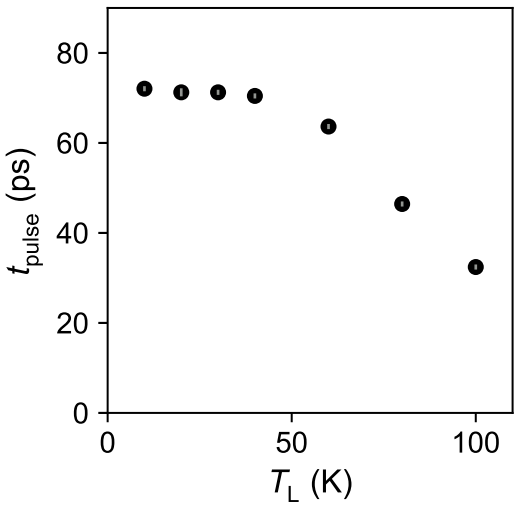

Figure I.1 | Lattice temperature dependence of the output pulse length. As the lattice temperature (T_{L}) increases, the output pulse length (t_{pulse}) is at first constant and then decreases for $T_{\mathrm{L}} > 40\,\mathrm{K}$. The error bars (grey) represent $95\,\%$ CIs of the mean. They result from the errors that are associated with t_{off} and t_{on}, and are smaller than the black data points. (Adapted from [68])

List of acronyms

AlGaAs	Aluminum gallium arsenide
APD	Avalanche photodiode
C	Conduction
CCD	Charge-coupled device
CMOS	Complementary metal-oxide-semiconductor
CW	Continuous wave
FWHM	Full width at half maximum
GaAs	Gallium arsenide
GDD	Group delay dispersion
HH	Heavy-hole
LA	Longitudinal acoustic
LH	Light-hole
LO	Longitudinal optical
MBE	Molecular beam epitaxy
NW	Nanowire
SO	Split-off
SRH	Shockley-Read-Hall
TA	Transverse acoustic
TEM	Transmission electron microscopy
THz	Terahertz
TO	Transverse optical

List of symbols

Symbol	Description
α_{i}	Internal cavity losses
α	Linewidth enhancement factor
α_{m}	Mirror losses
β_{sp}	Spontaneous emission coupling factor
$\gamma_{\mathrm{cc,e}}$	Carrier-carrier scattering rate of electrons
$\gamma_{\mathrm{cc,h}}$	Carrier-carrier scattering rate of holes
γ_{cool}	Cooling rate
γ_{r}	Damping rate of carrier temperature oscillations
γ_{R}	Damping rate of relaxation oscillations
γ	Dephasing rate
γ_{ep}	Electron-LO-phonon scattering rate
γ_{eh}	Energy broadening
γ_0	Energy broadening near the band gap
γ_{heat}	Heating rate
γ_{hp}	Hole-LO-phonon scattering rate
γ_{L}	Landsberg broadening
γ_{ph}	Photon decay rate
γ_{lasing}	Stimulated emission rate
γ_{c}	Total carrier recombination rate
Γ_{R}	Angular damping rate of relaxation oscillations
Γ	Confinement factor
Γ_{N}	Damping rate of carrier number
Γ_{P}	Damping rate of photon number
Γ_0	Energy confinement factor
$\Delta\epsilon_{\mathrm{CH}}$	Coulomb-hole self energy
$\Delta\epsilon_{\mathrm{e}}$	Electron excess energy
Δt_{pump}	FWHM of excitation pulse
$\Delta\epsilon_{\mathrm{h}}$	Hole excess energy
Δf	Laser linewidth

Symbol	Description
$\Delta\mathcal{R}/\mathcal{R}_0$	Normalized differential probe reflectivity
Δt	Pump-probe delay
$\Delta\epsilon_{\mathrm{SX},\mathbf{k}}$	Screened exchange energy
$\epsilon_{\mathrm{c}\mathbf{k}}$	Conduction band energy
$\epsilon_{\mathrm{e}\mathbf{k}}$	Electron energy
ϵ	Energy
ϵ_{L}	Energy of the lasing mode
$\epsilon_{\mathrm{h}\mathbf{k}}$	Heavy hole energy
ϵ_{LO}	Longitudinal optical phonon energy
ε	Permittivity
ϵ_{p}	Photon energy of excitation laser
ε_∞	Relative optical dielectric constant
ε_{r}	Relative static dielectric constant
ϵ_{g}	Renormalized band gap energy
$\epsilon_{\mathrm{g}0}$	Unexcited band gap energy
ε_0	Vacuum permittivity
$\epsilon_{\mathrm{v}\mathbf{k}}$	Valence band energy
$\mu_{\mathbf{k}}$	Dipole matrix element
η_{p}	Pump absorption efficiency
κ	Amplitude loss per round-trip
κ_{sc}	Inverse screening length
λ	Wavelength
μ	Chemical potential
μ_0	Vacuum permeability
ν_{S}	Oscillation frequency from intensity
ρ	Density of states
$\bar{\Sigma}$	Combined carrier-carrier and carrier-phonon scattering rate
Σ	Scattering rate
τ_{spon}	Spontaneous emission lifetime
τ_{stim}	Stimulated emission lifetime
ϕ	Phase of the electric field
χ	Susceptibility
$\omega_{\mathbf{q}}$	Angular effective plasmon frequency
ω	Angular lasing frequency
ω_{pl}	Angular plasma frequency
$\omega_{\mathbf{k}}$	Angular transition frequency
Ω	Angular cavity resonance frequency
$\Omega_{\mathbf{k}}$	Angular Rabi frequency

Symbol	Description
Ω_{R}	Angular relaxation oscillation frequency
$\hbar$	Reduced Planck constant
a_0	Bohr radius
$\hat{a}$	Electron annihilitation operator
$\hat{a}^\dagger$	Electron creation operator
a_{AlGaAs}	Lattice constant of AlGaAs
a_{GaAs}	Lattice constant of GaAs
a_{gain}	Parameter of linear gain approximation
$\hat{b}$	Hole annihilitation operator
$\hat{b}^\dagger$	Hole creation operator
B	Bimolecular recombination coefficient
$\hat{c}$	Photon annihilitation operator
$\hat{c}^\dagger$	Photon creation operator
c_0	Speed of light
e_0	Elementary charge
E	Electric field
$\mathbf{E}$	Electric field vector
EH	Hybrid mode
f	Fermi-Dirac distribution
f_{mod}	Modulation frequency
f_{E}	Oscillation frequency from autocorrelation
f_{R}	Relaxation oscillation frequency
f_{r}	Resonance frequency of carrier temperature oscillations
f_{S}	Simulated f_{E}
f_{3dB}	3 dB frequency
$\tilde{F}$	Approximation for the cavity response function $F_{\mathbf{q}}$
g	Amplitude gain
g_{mat}	Amplitude material gain
$g_{\mathbf{k}}$	Dipole interaction matrix element
$\hat{g}$	LO phonon annihilitation operator
$\hat{g}^\dagger$	LO phonon creation operator
$G_{\mathcal{P}}$	Differential modal gain with respect to photon number
$G_{\mathcal{N}}$	Differential modal gain with respect to carrier number
$G^{(1)}$	Electric field autocorrelation
$G^{(2)}$	Intensity autocorrelation
G	Intensity gain
G_{mat}	Material gain
G_{mod}	Modal gain

Symbol	Description
G_0	Parameter of logarithmic gain approximation
$\bar{G}_{\mathrm{mat}}$	Peak material gain
G_{s}	Saturated modal gain
$G_{\mathrm{th,mat}}$	Threshold material gain
$G_{\mathrm{th,mod}}$	Threshold modal gain
H	Magnetic field
$\mathbf{H}$	Magnetic field vector
$\hat{\mathcal{H}}_{\mathrm{C}}$	Coulomb hamiltonian
$\hat{\mathcal{H}}_{\mathrm{dipole}}$	Dipole interaction hamiltonian
$\hat{\mathcal{H}}_{\mathrm{e-LO}}$	Fröhlich hamiltonian
$\hat{\mathcal{H}}$	Hamiltonian
$\hat{\mathcal{H}}_{\mathrm{kin}}$	Kinetic energy hamiltonian
HE	Hybrid mode
I	Laser intensity
I_{th}	Laser intensity at threshold
k_{B}	Boltzmann constant
k	Wave number
$\mathbf{k}$	Wave vector
$\mathcal{L}_{\mathbf{k}}$	$\mathbf{k}$-dependent Lorentzian lineshape function
L	Nanowire length
$\mathcal{L}$	Lorentzian lineshape function
m_{c}	Conduction band effective mass
m_{e}	Electron effective mass
m_0	Free electron mass
m_{h}	Heavy hole effective mass
m_{r}	Reduced mass
m_{v}	Valence band effective mass
M	Modulation response
$\mathcal{M}$	Fröhlich interaction matrix element
$\mathcal{M}_{\mathrm{T}}$	Transition matrix element
$\tilde{n}$	Complex refractive index
n_{eff}	Effective refractive index
$n_{\mathrm{e}\mathbf{k}}$	Electron distribution
$\hat{n}_{\mathrm{e}\mathbf{k}}$	Electron number operator
n_{g}	Group refractive index
$n_{\mathrm{h}\mathbf{k}}$	Hole distribution
$\hat{n}_{\mathrm{h}\mathbf{k}}$	Hole number operator
n_{PN}	Phonon distribution

Symbol	Description
n	Refractive index
n_{active}	Refractive index of the active material
N	Carrier density
$\mathcal{N}$	Carrier number
$\mathcal{N}_{\mathrm{hot}}$	Hot carrier number
$\mathcal{N}_{\mathrm{s}}$	Parameter of logarithmic gain approximation
$\mathcal{N}_{\mathrm{tr}}$	Transparency carrier number
$p_{\mathbf{k}}$	Microscopic polarization
$\hat{p}_{\mathbf{k}}$	Microscopic polarization operator
p	Polarization
$\Lambda_{\mathrm{a}\mathbf{k}}$	Pump rate
$\hat{\mathbf{P}}$	Macroscopic polarization operator
P	Optical pump power
P_{probe}	Probe pulse power
P_{pump}	Pump pulse power
P_{th}	Threshold pump power
$\mathfrak{P}$	Complex macroscopic polarization amplitude
$\mathcal{P}$	Photon number
$\mathcal{P}_{\mathrm{sat}}$	Saturation photon number
$q_{\mathbf{k}}$	Coulomb enhancement
q_{PN}	Phonon wave number
$\mathbf{q}_{\mathrm{PN}}$	Phonon wave vector
q	Wave number
$\mathbf{q}$	Wave vector
r	Amplitude reflectivity of nanowire end facets
R	Intensity reflectivity of nanowire end facets
R_{NW}	Nanowire radius
$\mathcal{R}$	Probe reflectivity
R_{sp}	Total spontaneous emission rate
S	Photon density of states
$S_{\mathbf{q}}$	Photon lineshape function
t_0	Arrival time of excitation pulse
t_{on}	Turn-on time
T_{c}	Carrier temperature
T_{e}	Electron temperature
T_{h}	Hole temperature
T_{L}	Lattice temperature
TE	Transverse electric mode

Symbol	Description
TM	Transverse magnetic mode
v_{g}	Group velocity
v_{ph}	Phase velocity
v	Velocity
V	Coulomb potential energy
$V_{\mathbf{sq}}$	Fourier transform of screened coulomb potential energy
$V_{\mathbf{q}}$	Fourier transformed coulomb potential energy
V_{NW}	Nanowire volume
W	Spectrally resolved spontaneous emission rate

List of figures

List of tables

Bibliography

[1] Bardeen, J. & Brattain, W. H. Three-electrode circuit element utilizing semiconductive materials. *U.S. patent 2524035.* United States Patent and Trademark Office. (1950) (Cited on page 1.)

[2] Shockley, W. Circuit element utilizing semiconductive material. *U.S. patent 2569347.* United States Patent and Trademark Office. (1951) (Cited on page 1.)

[3] Hall, R. N., Fenner, G. E., Kingsley, J. D., Soltys, T. J. & Carlson, R. O. Coherent Light Emission From GaAs Junctions. *Physical Review Letters* **9,** 366–368 (1962). doi:10.1103/PhysRevLett.9.366 (Cited on page 1.)

[4] Nathan, M. I., Dumke, W. P., Burns, G., Dill, F. H. & Lasher, G. Stimulated emission of radiation from GaAs p-n junctions. *Applied Physics Letters* **1,** 62–64 (1962). doi:10.1063/1.1777371 (Cited on page 1.)

[5] Sze, S. & Ng, K. K. *Physics of Semiconductor Devices* (John Wiley & Sons, Inc., 2006). doi:10.1002/0470068329 (Cited on page 1.)

[6] Horowitz, P. & Hill, W. *The art of electronics* 3rd ed. (Cambridge University Press, 2015). (Cited on page 1.)

[7] *Medical Applications of Lasers* (eds. Vij, D. R. & Mahesh, K.) (Springer US, 2002). doi:10.1007/978-1-4615-0929-5 (Cited on page 1.)

[8] *High Power Diode Lasers* (eds. Bachmann, F., Loosen, P. & Poprawe, R.) (Springer New York, 2007). doi:10.1007/978-0-387-34729-5 (Cited on page 1.)

[9] Coldren, L. A., Corzine, S. W. & Mashanovitch, M. *Diode lasers and photonic integrated circuits* 2nd ed. (Wiley, 2012). doi:10.1002/9781118148167 (Cited on pages 1, 10, 11, 13, 14, 16, 18, 19, 20, 21, 22, 48, 49, 63, 65, 75, and 103.)

[10] Klotzkin, D. J. *Introduction to Semiconductor Lasers for Optical Communications* (Springer New York, 2014). doi:10.1007/978-1-4614-9341-9 (Cited on page 1.)

[11] Miller, D. Rationale and challenges for optical interconnects to electronic chips. *Proceedings of the IEEE* **88,** 728–749 (2000). doi:10.1109/5.867687 (Cited on pages 1 and 2.)

[12] Chen, X. *et al.* The Emergence of Silicon Photonics as a Flexible Technology Platform. *Proceedings of the IEEE* **106,** 2101–2116 (2018). doi:10.1109/JPROC.2018.2854372 (Cited on pages 1 and 2.)

[13] Zhu, D. *et al.* Integrated photonics on thin-film lithium niobate. *Advances in Optics and Photonics* **13,** 242 (2021). doi:10.1364/AOP.411024 (Cited on page 1.)

[14] Gardes, F. *et al.* A Review of Capabilities and Scope for Hybrid Integration Offered by Silicon-Nitride-Based Photonic Integrated Circuits. *Sensors* **22,** 4227 (2022). doi:10.3390/s22114227 (Cited on page 1.)

[15] Smit, M., Williams, K. & van der Tol, J. Past, present, and future of InP-based photonic integration. *APL Photonics* **4,** 050901 (2019). doi:10.1063/1.5087862 (Cited on page 1.)

[16] Miller, D. A. B. Device Requirements for Optical Interconnects to Silicon Chips. *Proceedings of the IEEE* **97,** 1166–1185 (2009). doi:10.1109/JPROC.2009.2014298 (Cited on page 2.)

[17] Bogaerts, W. *et al.* Programmable photonic circuits. *Nature* **586,** 207–216 (2020). doi:10.1038/s41586-020-2764-0 (Cited on page 2.)

[18] Li, H. *et al.* A 112 Gb/s PAM4 Silicon Photonics Transmitter With Microring Modulator and CMOS Driver. *Journal of Lightwave Technology* **38,** 131–138 (2020). doi:10.1109/JLT.2019.2938731 (Cited on page 2.)

[19] Siew, S. Y. *et al.* Review of Silicon Photonics Technology and Platform Development. *Journal of Lightwave Technology* **39,** 4374–4389 (2021). doi:10.1109/JLT.2021.3066203 (Cited on page 2.)

[20] Xu, X. *et al.* Self-calibrating programmable photonic integrated circuits. *Nature Photonics,* 1–8 (2022). doi:10.1038/s41566-022-01020-z (Cited on page 2.)

[21] Carolan, J. *et al.* Universal linear optics. *Science* **349,** 711–716 (2015). doi:10.1126/science.aab3642 (Cited on page 2.)

[22] Sun, C. *et al.* Single-chip microprocessor that communicates directly using light. *Nature* **528,** 534–538 (2015). doi:10.1038/nature16454 (Cited on page 2.)

[23] Zhuang, L., Roeloffzen, C. G. H., Hoekman, M., Boller, K.-J. & Lowery, A. J. Programmable photonic signal processor chip for radiofrequency applications. *Optica* **2,** 854–859 (2015). doi:10.1364/OPTICA.2.000854 (Cited on page 2.)

[24] Soref, R. Mid-infrared photonics in silicon and germanium. *Nature Photonics* **4,** 495–497 (2010). doi:10.1038/nphoton.2010.171 (Cited on page 2.)

[25] Liu, X., Osgood, R. M., Vlasov, Y. A. & Green, W. M. J. Mid-infrared optical parametric amplifier using silicon nanophotonic waveguides. *Nature Photonics* **4,** 557–560 (2010). doi:10.1038/nphoton.2010.119 (Cited on page 2.)

[26] Zlatanovic, S. *et al.* Mid-infrared wavelength conversion in silicon waveguides using ultracompact telecom-band-derived pump source. *Nature Photonics* **4,** 561–564 (2010). doi:10.1038/nphoton.2010.117 (Cited on page 2.)

[27] Shastri, B. J. *et al.* Photonics for artificial intelligence and neuromorphic computing. *Nature Photonics* **15,** 102–114 (2021). doi:10.1038/s41566-020-00754-y (Cited on page 2.)

[28] Shen, Y. *et al.* Deep learning with coherent nanophotonic circuits. *Nature Photonics* **11,** 441–446 (2017). doi:10.1038/nphoton.2017.93 (Cited on page 2.)

[29] Harris, N. C. *et al.* Linear programmable nanophotonic processors. *Optica* **5,** 1623–1631 (2018). doi:10.1364/OPTICA.5.001623 (Cited on page 2.)

[30] Subramanian, A. Z. *et al.* Silicon and silicon nitride photonic circuits for spectroscopic sensing on-a-chip [Invited]. *Photonics Research* **3,** B47–B59 (2015). doi:10.1364/PRJ.3.000B47 (Cited on page 2.)

[31] Yang, K. Y. *et al.* Inverse-designed non-reciprocal pulse router for chip-based LiDAR. *Nature Photonics* **14,** 369–374 (2020). doi:10.1038/s41566-020-0606-0 (Cited on page 2.)

[32] Liang, D. & Bowers, J. E. Recent progress in lasers on silicon. *Nature Photonics* **4,** 511–517 (2010). doi:10.1038/nphoton.2010.167 (Cited on page 2.)

[33] Fang, Z., Chen, Q. Y. & Zhao, C. Z. A review of recent progress in lasers on silicon. *Optics & Laser Technology* **46,** 103–110 (2013). doi:10.1016/j.optlastec.2012.05.041 (Cited on page 2.)

[34] Xu, D.-X. *et al.* Silicon Photonic Integration Platform—Have We Found the Sweet Spot? *IEEE Journal of Selected Topics in Quantum Electronics* **20,** 189–205 (2014). doi:10.1109/JSTQE.2014.2299634 (Cited on page 2.)

[35] Liu, A. Y. & Bowers, J. Photonic Integration With Epitaxial III–V on Silicon. *IEEE Journal of Selected Topics in Quantum Electronics* **24,** 1–12 (2018). doi:10.1109/JSTQE.2018.2854542 (Cited on page 2.)

[36] Tang, M. *et al.* Integration of III-V lasers on Si for Si photonics. *Progress in Quantum Electronics* **66,** 1–18 (2019). doi:10.1016/j.pquantelec.2019.05.002 (Cited on page 2.)

[37] Han, Y. & Lau, K. M. III–V lasers selectively grown on (001) silicon. *Journal of Applied Physics* **128,** 200901 (2020). doi:10.1063/5.0029804 (Cited on page 2.)

[38] Liu, D., Wu, J., Xu, H. & Wang, Z. Emerging Light-Emitting Materials for Photonic Integration. *Advanced Materials* **33,** 2003733 (2021). doi:10.1002/adma.202003733 (Cited on page 2.)

[39] Yan, R., Gargas, D. & Yang, P. Nanowire photonics. *Nature Photonics* **3,** 569–576 (2009). doi:10.1038/nphoton.2009.184 (Cited on page 2.)

[40] Zimmler, M. A., Capasso, F., Müller, S. & Ronning, C. Optically pumped nanowire lasers: invited review. *Semiconductor Science and Technology* **25,** 024001 (2010). doi:10.1088/0268-1242/25/2/024001 (Cited on pages 2, 11, and 13.)

[41] Koblmüller, G., Mayer, B., Stettner, T., Abstreiter, G. & Finley, J. J. GaAs–AlGaAs core–shell nanowire lasers on silicon: invited review. *Semiconductor Science and Technology* **32,** 053001 (2017). doi:10.1088/1361-6641/aa5e45 (Cited on pages 2 and 11.)

[42] Chen, R. *et al.* Nanolasers grown on silicon. *Nature Photonics* **5,** 170–175 (2011). doi:10.1038/nphoton.2010.315 (Cited on page 2.)

[43] Sun, H. *et al.* Nanopillar Lasers Directly Grown on Silicon with Heterostructure Surface Passivation. *ACS Nano* **8,** 6833–6839 (2014). doi:10.1021/nn501481u (Cited on page 2.)

[44] Mayer, B. *et al.* Monolithically Integrated High-β Nanowire Lasers on Silicon. *Nano Letters* **16,** 152–156 (2016). doi:10.1021/acs.nanolett.5b03404 (Cited on pages 2, 38, 53, and 56.)

[45] Stettner, T. *et al.* Direct Coupling of Coherent Emission from Site-Selectively Grown III–V Nanowire Lasers into Proximal Silicon Waveguides. *ACS Photonics* **4,** 2537–2543 (2017). doi:10.1021/acsphotonics.7b00805 (Cited on pages 2 and 101.)

[46] Mayer, B. *et al.* Lasing from individual GaAs-AlGaAs core-shell nanowires up to room temperature. *Nature Communications* **4,** 2931 (2013). doi:10.1038/ncomms3931 (Cited on pages 2, 6, 7, 11, 13, 28, 38, 54, 56, 69, and 72.)

[47] Saxena, D. *et al.* Optically pumped room-temperature GaAs nanowire lasers. *Nature Photonics* **7,** 963–968 (2013). doi:10.1038/nphoton.2013.303 (Cited on pages 2, 6, 7, 11, 12, 13, 14, 20, 38, 53, 54, 56, 69, and 75.)

[48] Ding, J. X. *et al.* Lasing in ZnS nanowires grown on anodic aluminum oxide templates. *Applied Physics Letters* **85,** 2361–2363 (2004). doi:10.1063/1.1791326 (Cited on page 2.)

[49] Zimmler, M. A., Bao, J., Capasso, F., Müller, S. & Ronning, C. Laser action in nanowires: Observation of the transition from amplified spontaneous emission to laser oscillation. *Applied Physics Letters* **93,** 051101 (2008). doi:10.1063/1.2965797 (Cited on page 2.)

[50] Johnson, J. C. *et al.* Single gallium nitride nanowire lasers. *Nature Materials* **1,** 106–110 (2002). doi:10.1038/nmat728 (Cited on pages 2 and 11.)

[51] Huang, M. H. *et al.* Room-Temperature Ultraviolet Nanowire Nanolasers. *Science* **292,** 1897–1899 (2001). doi:10.1126/science.1060367 (Cited on pages 2, 11, and 13.)

[52] Stettner, T. *et al.* Coaxial GaAs-AlGaAs core-multishell nanowire lasers with epitaxial gain control. *Applied Physics Letters* **108,** 011108 (2016). doi:10.1063/1.4939549 (Cited on pages 2, 12, 65, and 102.)

[53] Saxena, D. *et al.* Design and Room-Temperature Operation of GaAs/AlGaAs Multiple Quantum Well Nanowire Lasers. *Nano Letters* **16,** 5080–5086 (2016). doi:10.1021/acs.nanolett.6b01973 (Cited on pages 2 and 12.)

[54] Stettner, T. *et al.* Tuning Lasing Emission toward Long Wavelengths in GaAs-(In,Al)GaAs Core–Multishell Nanowires. *Nano Letters* **18,** 6292–6300 (2018). doi:10.1021/acs.nanolett.8b02503 (Cited on pages 2, 12, 65, and 102.)

[55] Schmiedeke, P. *et al.* Low-threshold strain-compensated InGaAs/(In,Al)GaAs multi-quantum well nanowire lasers emitting near 1.3 µm at room temperature. *Applied Physics Letters* **118,** 221103 (2021). doi:10.1063/5.0048807 (Cited on pages 2, 12, and 102.)

[56] Duan, X., Huang, Y., Agarwal, R. & Lieber, C. M. Single-nanowire electrically driven lasers. *Nature* **421,** 241–245 (2003). doi:10.1038/nature01353 (Cited on page 2.)

[57] Chin, A. H. *et al.* Near-infrared semiconductor subwavelength-wire lasers. *Applied Physics Letters* **88,** 163115 (2006). doi:10.1063/1.2198017 (Cited on page 2.)

[58] Geburt, S. *et al.* Low threshold room-temperature lasing of CdS nanowires. *Nanotechnology* **23,** 365204 (2012). doi:10.1088/0957-4484/23/36/365204 (Cited on page 2.)

[59] Sidiropoulos, T. P. H. *et al.* Ultrafast plasmonic nanowire lasers near the surface plasmon frequency. *Nature Physics* **10,** 870–876 (2014). doi:10.1038/nphys3103 (Cited on pages 2, 69, 71, 72, 82, and 105.)

[60] Röder, R. *et al.* Ultrafast Dynamics of Lasing Semiconductor Nanowires. *Nano Letters* **15,** 4637–4643 (2015). doi:10.1021/acs.nanolett.5b01271 (Cited on pages 2 and 69.)

[61] Röder, R. *et al.* Mode Switching and Filtering in Nanowire Lasers. *Nano Letters* **16,** 2878–2884 (2016). doi:10.1021/acs.nanolett.6b00811 (Cited on page 2.)

[62] Wille, M. *et al.* Carrier density driven lasing dynamics in ZnO nanowires. *Nanotechnology* **27,** 225702 (2016). doi:10.1088/0957-4484/27/22/225702 (Cited on page 2.)

[63] Blake, J. C., Nieto-Pescador, J., Li, Z. & Gundlach, L. Ultraviolet femtosecond Kerr-gated wide-field fluorescence microscopy. *Optics Letters* **41,** 2462 (2016). doi:10.1364/OL.41.002462 (Cited on pages 2 and 91.)

[64] Hollinger, R. *et al.* Enhanced absorption and cavity effects of three-photon pumped ZnO nanowires. *Applied Physics Letters* **111,** 213106 (2017). doi:10.1063/1.4999690 (Cited on pages 2 and 92.)

[65] Mayer, B. *et al.* Long-term mutual phase locking of picosecond pulse pairs generated by a semiconductor nanowire laser. *Nature Communications* **8,** 15521 (2017). doi:10.1038/ncomms15521 (Cited on pages 2, 69, 71, 72, and 85.)

[66] Röder, R. & Ronning, C. Review on the dynamics of semiconductor nanowire lasers. *Semiconductor Science and Technology* **33,** 033001 (2018). doi:10.1088/1361-6641/aaa7be (Cited on pages 2 and 69.)

[67] Blake, J. C., Nieto-Pescador, J., Li, Z. & Gundlach, L. Femtosecond Luminescence Imaging for Single Nanoparticle Characterization. *The Journal of Physical Chemistry A* **124,** 4583–4593 (2020). doi:10.1021/acs.jpca.0c01775 (Cited on pages 2 and 91.)

[68] Thurn, A. *et al.* Self-induced ultrafast electron-hole plasma temperature oscillations in nanowire lasers. *arXiv preprint arXiv:2108.11784* (2021). doi:10.48550/arXiv.2108.11784 (Cited on pages 2, 31, 50, 52, 56, 64, 69, 70, 71, 74, 75, 76, 77, 79, 80, 81, 84, 87, 99, 103, 106, 108, 110, 114, 117, 120, 123, and 126.)

[69] Mayer, B. *Ultrafast Nanowire Lasers as On-Chip Devices* PhD thesis (Technical University of Munich, Munich, 2016) (Cited on pages 6, 7, 12, 22, 38, and 41.)

[70] Titova, L. V. *et al.* Temperature dependence of photoluminescence from single core-shell GaAs–AlGaAs nanowires. *Applied Physics Letters* **89,** 173126 (2006). doi:10.1063/1.2364885 (Cited on pages 6, 7, and 38.)

[71] Demichel, O., Heiss, M., Bleuse, J., Mariette, H. & Fontcuberta i Morral, A. Impact of surfaces on the optical properties of GaAs nanowires. *Applied Physics Letters* **97,** 201907 (2010). doi:10.1063/1.3519980 (Cited on pages 6, 7, and 38.)

[72] Wolford, D. J. Intrinsic recombination and interface characterization in "surface-free" GaAs structures. *Journal of Vacuum Science & Technology B: Microelectronics and Nanometer Structures* **9,** 2369 (1991). doi:10.1116/1.585705 (Cited on pages 6, 7, and 38.)

[73] Hocevar, M. *et al.* Residual strain and piezoelectric effects in passivated GaAs/AlGaAs core-shell nanowires. *Applied Physics Letters* **102,** 191103 (2013). doi:10.1063/1.4803685 (Cited on pages 6, 7, and 38.)

[74] Rudolph, D. *Growth of GaAs-based nanowires on silicon for optical applications* PhD thesis (Technical University of Munich, Munich, 2014) (Cited on pages 6, 7, and 38.)

[75] Saxena, D. *Design and characterization of III-V Nanowire Lasers* PhD thesis (Australian National University, Canberra, 2017) (Cited on pages 6, 7, 12, 20, and 38.)

[76] Welker, H. Über neue halbleitende Verbindungen. *Zeitschrift für Naturforschung A* **7,** 744–749 (1952). doi:10.1515/zna-1952-1110 (Cited on pages 6 and 7.)

[77] Adachi, S. *Properties of semiconductor alloys: group-IV, III-V and II-VI semiconductors* (Wiley, 2009). (Cited on pages 6 and 7.)

[78] Blakemore, J. S. Semiconducting and other major properties of gallium arsenide. *Journal of Applied Physics* **53,** R123–R181 (1982). doi:10.1063/1.331665 (Cited on pages 6, 7, 8, and 9.)

[79] Adachi, S. GaAs, AlAs, and $Al_xGa_{1-x}As$: Material parameters for use in research and device applications. *Journal of Applied Physics* **58,** R1–R29 (1985). doi:10.1063/1.336070 (Cited on pages 6 and 7.)

[80] *Gallium arsenide* (ed. Blakemore, J. S.) (American Institute of Physics, 1987). (Cited on pages 6 and 7.)

[81] Adachi, S. *Physical Properties of III-V Semiconductor Compounds: InP, InAs, GaAs, GaP, InGaAs, and InGaAsP* 1st ed. (Wiley, 1992). doi:10.1002/352760281X (Cited on pages 6 and 7.)

[82] Adachi, S. *GaAs and related materials: bulk semiconducting and superlattice properties* (World Scientific, 1994). doi:https://doi.org/10.1142/2508 (Cited on pages 6 and 7.)

[83] *Properties of Gallium Arsenide* (ed. Brozel, M. R.) 3rd ed. (INSPEC - The Institution of Electrical Engineers, 1996). (Cited on pages 6 and 7.)

[84] Vurgaftman, I., Meyer, J. R. & Ram-Mohan, L. R. Band parameters for III–V compound semiconductors and their alloys. *Journal of Applied Physics* **89,** 5815–5875 (2001). doi:10.1063/1.1368156 (Cited on pages 6, 7, 8, and 103.)

[85] *Properties of aluminum gallium arsenide* (ed. Adachi, S.) (The Institution of Engineering and Technology, 2006). (Cited on pages 6 and 7.)

[86] Persson, A. I. *et al.* Solid-phase diffusion mechanism for GaAs nanowire growth. *Nature Materials* **3,** 677–681 (2004). doi:10.1038/nmat1220 (Cited on page 7.)

[87] Hubmann, J. *GaAs nanowires: epitaxy, crystal structure-related properties and magnetic heterostructures* PhD thesis (University of Regensburg, Regensburg, 2016) (Cited on page 7.)

[88] Soshnikov, I. P. *et al.* Atomic structure of MBE-grown GaAs nanowhiskers. *Physics of the Solid State* **47,** 2213–2218 (2005). doi:10.1134/1.2142881 (Cited on page 7.)

[89] Glas, F., Harmand, J.-C. & Patriarche, G. Why Does Wurtzite Form in Nanowires of III-V Zinc Blende Semiconductors? *Physical Review Letters* **99,** 146101 (2007). doi:10.1103/PhysRevLett.99.146101 (Cited on page 7.)

[90] Hoang, T. B. *et al.* Observation of free exciton photoluminescence emission from single wurtzite GaAs nanowires. *Applied Physics Letters* **94,** 133105 (2009). doi:10.1063/1.3104853 (Cited on page 7.)

[91] Spirkoska, D. *et al.* Structural and optical properties of high quality zinc-blende/wurtzite GaAs nanowire heterostructures. *Physical Review B* **80,** 245325 (2009). doi:10.1103/PhysRevB.80.245325 (Cited on page 7.)

[92] Zardo, I. *et al.* Raman spectroscopy of wurtzite and zinc-blende GaAs nanowires: Polarization dependence, selection rules, and strain effects. *Physical Review B* **80,** 245324 (2009). doi:10.1103/PhysRevB.80.245324 (Cited on pages 7 and 38.)

[93] Jancu, J.-M. *et al.* Type II heterostructures formed by zinc-blende inclusions in InP and GaAs wurtzite nanowires. *Applied Physics Letters* **97,** 041910 (2010). doi:10.1063/1.3473779 (Cited on page 7.)

[94] Rudolph, D. *et al.* Direct Observation of a Noncatalytic Growth Regime for GaAs Nanowires. *Nano Letters* **11,** 3848–3854 (2011). doi:10.1021/nl2019382 (Cited on pages 7 and 38.)

[95] Ackland, G. J. High-pressure phases of group IV and III-V semiconductors. *Reports on Progress in Physics* **64,** 483–516 (2001). doi:10.1088/0034-4885/64/4/202 (Cited on page 7.)

[96] McMahon, M. I. & Nelmes, R. J. Observation of a Wurtzite Form of Gallium Arsenide. *Physical Review Letters* **95,** 215505 (2005). doi:10.1103/PhysRevLett.95.215505 (Cited on page 7.)

[97] Yu, P. Y. & Cardona, M. *Fundamentals of Semiconductors* (Springer Berlin Heidelberg, 2010). doi:10.1007/978-3-642-00710-1 (Cited on pages 7, 8, and 9.)

[98] Cohen, M. L. & Chelikowsky, J. R. *Electronic Structure and Optical Properties of Semiconductors* (Springer Berlin Heidelberg, 1988). doi:https://doi.org/10.1007/978-3-642-97080-1 (Cited on pages 7 and 8.)

[99] Pässler, R. & Oelgart, G. Appropriate analytical description of the temperature dependence of exciton peak positions in GaAs/$Al_xGa_{1-x}As$ multiple quantum wells and the Γ_{8v}-Γ_{6c} gap of GaAs. *Journal of Applied Physics* **82,** 2611–2616 (1997). doi:10.1063/1.366098 (Cited on pages 7, 54, and 103.)

[100] Fox, M. *Optical properties of solids* 2nd ed. (Oxford University Press, 2010). (Cited on pages 8 and 9.)

[101] Chow, W. W., Koch, S. W. & Sargent, M. *Semiconductor-Laser Physics* (Springer-Verlag, 1994). doi:https://doi.org/10.1007/978-3-642-61225-1 (Cited on pages 8, 9, 18, 19, 21, 24, 25, 26, 27, 28, 29, 30, 31, 32, 33, 34, 59, 68, 101, and 103.)

[102] Ashcroft, N. W. & Mermin, N. D. *Solid state physics* (Holt, Rinehart and Winston, 1976). (Cited on page 9.)

[103] Ferry, D. K. *Semiconductors: bonds and bands* (IOP Publishing, 2013). doi:10.1088/978-0-750-31044-4 (Cited on pages 9 and 10.)

[104] Kittel, C. *Introduction to solid state physics* 9th ed. (Wiley, 2018). (Cited on page 9.)

[105] Ridley, B. K. *Quantum Processes in Semiconductors* (Oxford University Press, 2013). doi:10.1093/acprof:oso/9780199677214.001.0001 (Cited on page 9.)

[106] Shah, J. *Ultrafast Spectroscopy of Semiconductors and Semiconductor Nanostructures* 115. (Springer-Verlag, 1999). doi:10.1007/978-3-662-03770-6 (Cited on pages 9, 10, 24, 25, 42, 43, 44, 73, 94, and 115.)

[107] Waugh, J. L. T. & Dolling, G. Crystal Dynamics of Gallium Arsenide. *Physical Review* **132,** 2410–2412 (1963). doi:10.1103/PhysRev.132.2410 (Cited on pages 9 and 10.)

[108] Kunc, K. & Martin, R. M. Density-functional calculation of static and dynamic properties of GaAs. *Physical Review B* **24,** 2311–2314 (1981). doi:10.1103/PhysRevB.24.2311 (Cited on page 9.)

[109] Kunc, K. & Martin, R. M. Ab Initio Force Constants of GaAs: A New Approach to Calculation of Phonons and Dielectric Properties. *Physical Review Letters* **48,** 406–409 (1982). doi:10.1103/PhysRevLett.48.406 (Cited on page 9.)

[110] Strauch, D. & Dorner, B. Phonon dispersion in GaAs. *Journal of Physics: Condensed Matter* **2,** 1457–1474 (1990). doi:10.1088/0953-8984/2/6/006 (Cited on pages 9, 10, and 103.)

[111] Lyon, S. A. Spectroscopy of hot carriers in semiconductors. *Journal of Luminescence* **35,** 121–154 (1986). doi:10.1016/0022-2313(86)90066-9 (Cited on pages 9 and 25.)

[112] Dirac, P. A. M. & Bohr, N. H. D. The quantum theory of the emission and absorption of radiation. *Proceedings of the Royal Society of London. Series A, Containing Papers of a Mathematical and Physical Character* **114,** 243–265 (1927). doi:10.1098/rspa.1927.0039 (Cited on page 10.)

[113] Pelant, I. & Valenta, J. *Luminescence Spectroscopy of Semiconductors* (Oxford University Press, 2012). doi:10.1093/acprof:oso/9780199588336.001.0001 (Cited on pages 10, 11, and 21.)

[114] Shockley, W. & Read, W. T. Statistics of the Recombinations of Holes and Electrons. *Physical Review* **87,** 835–842 (1952). doi:10.1103/PhysRev.87.835 (Cited on pages 10 and 11.)

[115] Hall, R. N. Electron-Hole Recombination in Germanium. *Physical Review* **87,** 387–387 (1952). doi:10.1103/PhysRev.87.387 (Cited on pages 10 and 11.)

[116] Siegman, A. E. *Lasers* (University Science Books, 1986). (Cited on pages 11, 14, and 16.)

[117] Agrawal, G. P. & Dutta, N. K. *Semiconductor Lasers* (Springer, 2013). (Cited on pages 11, 18, 19, 20, 21, 22, 23, 56, 59, 63, 64, 65, 89, and 90.)

[118] Wiersma, D. S. The physics and applications of random lasers. *Nature Physics* **4,** 359–367 (2008). doi:10.1038/nphys971 (Cited on page 11.)

[119] Ning, C. Z. Semiconductor nanolasers. *Physica Status Solidi B* **247,** 774–788 (2010). doi:10.1002/pssb.200945436 (Cited on pages 11, 12, 14, 19, 75, and 101.)

[120] Maslov, A. V. & Ning, C. Z. Reflection of guided modes in a semiconductor nanowire laser. *Applied Physics Letters* **83,** 1237–1239 (2003). doi:10.1063/1.1599037 (Cited on pages 11, 12, and 13.)

[121] Maslov, A. & Ning, C. Modal gain in a semiconductor nanowire laser with anisotropic bandstructure. *IEEE Journal of Quantum Electronics* **40,** 1389–1397 (2004). doi:10.1109/JQE.2004.834767 (Cited on pages 11, 12, 14, 75, and 101.)

[122] Hauschild, R. & Kalt, H. Guided modes in ZnO nanorods. *Applied Physics Letters* **89,** 123107 (2006). doi:10.1063/1.2354427 (Cited on pages 11 and 12.)

[123] Maslov, A. V., Bakunov, M. I. & Ning, C. Z. Distribution of optical emission between guided modes and free space in a semiconductor nanowire. *Journal of Applied Physics* **99,** 024314 (2006). doi:10.1063/1.2164538 (Cited on page 11.)

[124] Wang, M.-Q., Huang, Y.-Z., Chen, Q. & Cai, Z.-P. Analysis of mode quality factors and mode reflectivities for nanowire cavity by FDTD technique. *IEEE Journal of Quantum Electronics* **42,** 146–151 (2006). doi:10.1109/JQE.2005.861823 (Cited on page 11.)

[125] Henneghien, A.-L., Gayral, B., Désières, Y. & Gérard, J.-M. Simulation of waveguiding and emitting properties of semiconductor nanowires with hexagonal or circular sections. *Journal of the Optical Society of America B* **26,** 2396–2403 (2009). doi:10.1364/JOSAB.26.002396 (Cited on pages 11, 12, and 13.)

[126] Van Vugt, L. K., Zhang, B., Piccione, B., Spector, A. A. & Agarwal, R. Size-Dependent Waveguide Dispersion in Nanowire Optical Cavities: Slowed Light and Dispersionless Guiding. *Nano Letters* **9,** 1684–1688 (2009). doi:10.1021/nl900371r (Cited on pages 11 and 13.)

[127] Law, M. *et al.* Nanoribbon Waveguides for Subwavelength Photonics Integration. *Science* **305,** 1269–1273 (2004). doi:10.1126/science.1100999 (Cited on page 11.)

[128] Bissinger, J. *Unknown title* PhD thesis (Technical University of Munich, Munich, 2022) (Cited on pages 11, 12, 13, 14, 15, 19, 20, 21, 22, 24, 26, 27, 28, 32, 33, 34, 35, 48, 56, 58, 59, 63, 64, 65, 66, and 87.)

[129] Senica, U. *Unidirectional Coupling of Light from Nanowire Lasers into Silicon Waveguides* MSc Thesis (Technical University of Munich, Munich, 2017) (Cited on pages 12 and 13.)

[130] Snyder, A. W. & Love, J. D. *Optical Waveguide Theory* (Springer US, 1984). doi:10.1007/978-1-4613-2813-1 (Cited on pages 12 and 13.)

[131] Adams, M. J. *An introduction to optical waveguides* (Wiley, 1981). (Cited on pages 12 and 13.)

[132] Zimmermann, P. *Optical Characterization of Coaxial GaAs_AlGaAs Core-Multishell NWs.pdf* MSc Thesis (Technical University of Munich, Munich, 2016) (Cited on page 12.)

[133] Schmiedeke, P. *Continuous Lasing of GaAs Nanowires* MSc Thesis (Technical University of Munich, Munich, 2018) (Cited on pages 12, 13, 20, 21, 22, 24, 56, 63, 65, and 66.)

[134] Qian, F. *et al.* Multi-quantum-well nanowire heterostructures for wavelength-controlled lasers. *Nature Materials* **7,** 701–706 (2008). doi:10.1038/nmat2253 (Cited on page 12.)

[135] Lu, F. *et al.* Nanopillar quantum well lasers directly grown on silicon and emitting at silicon-transparent wavelengths. *Optica* **4,** 717 (2017). doi:10.1364/OPTICA.4.000717 (Cited on page 12.)

[136] Stettner, T. *GaAs based NW Lasers on Silicon* PhD thesis (Technical University of Munich, Munich, 2019) (Cited on pages 12 and 38.)

[137] Mayer, B. *et al.* Continuous wave lasing from individual GaAs-AlGaAs core-shell nanowires. *Applied Physics Letters* **108,** 071107 (2016). doi:10.1063/1.4942506 (Cited on page 13.)

[138] DeFranzo, A. C. & Pazol, B. G. Index of refraction measurement on sapphire at low temperatures and visible wavelengths. *Applied Optics* **32,** 2224 (1993). doi:10.1364/AO.32.002224 (Cited on pages 13 and 15.)

[139] Reinhart, F. K. A heuristic approach to precisely represent optical absorption and refractive index data for photon energies below, at, and above the band gap of semiconductors: The case of high-purity GaAs. Part I. *Journal of Applied Physics* **97,** 123534 (2005). doi:10.1063/1.1935767 (Cited on pages 13, 15, 33, and 54.)

[140] Visser, T., Blok, H., Demeulenaere, B. & Lenstra, D. Confinement factors and gain in optical amplifiers. *IEEE Journal of Quantum Electronics* **33,** 1763–1766 (1997). doi:10.1109/3.631280 (Cited on page 14.)

[141] Huang, Y.-Z. Comparison of modal gain and material gain for strong guiding slab waveguides. *IEE Proceedings - Optoelectronics* **148,** 131–133 (2001). doi:10.1049/ip-opt:20010519 (Cited on page 14.)

[142] Piprek, J. *Nitride semiconductor devices: principles and simulation* (Wiley-VCH, 2010). (Cited on page 14.)

[143] Chow, W. W. & Koch, S. W. *Semiconductor-Laser Fundamentals* (Springer Berlin Heidelberg, 1999). doi:10.1007/978-3-662-03880-2 (Cited on pages 18, 19, 29, 30, 31, 32, 68, and 103.)

[144] Henneberger, K. *et al.* Spectral hole burning and gain saturation in short-cavity semiconductor lasers. *Physical Review A* **45,** 1853–1859 (1992). doi:10.1103/PhysRevA.45.1853 (Cited on pages 18, 19, and 32.)

[145] Henneberger, K., Jahnke, F. & Herzel, F. Many-Body Effects and Multi-Mode Behaviour in Semiconductor Lasers. *Physica Status Solidi B* **173,** 423–439 (1992). doi:10.1002/pssb.2221730143 (Cited on pages 18, 19, and 32.)

[146] Jahnke, F. & Koch, S. W. Theory of carrier heating through injection pumping and lasing in semiconductor microcavity lasers. *Optics Letters* **18,** 1438 (1993). doi:10.1364/OL.18.001438 (Cited on pages 18, 19, 32, and 75.)

[147] Jahnke, F., Koch, S. W. & Henneberger, K. Dynamic response of short-cavity semiconductor lasers. *Applied Physics Letters* **62,** 2313–2315 (1993). doi:10.1063/1.109402 (Cited on pages 18, 19, and 32.)

[148] Jahnke, F., Henneberger, K., Schäfer, W. & Koch, S. W. Transient nonequilibrium and many-body effects in semiconductor microcavity lasers. *Journal of the Optical Society of America B* **10,** 2394 (1993). doi:10.1364/JOSAB.10.002394 (Cited on pages 18, 19, 32, 33, 34, and 101.)

[149] Jahnke, F. & Koch, S. W. Many-body theory for semiconductor microcavity lasers. *Physical Review A* **52,** 1712–1727 (1995). doi:10.1103/PhysRevA.52.1712 (Cited on pages 18, 19, 32, and 68.)

[150] Schneider, H. C., Jahnke, F. & Koch, S. W. Microscopic theory of nonequilibrium microcavity laser dynamics. *Quantum and Semiclassical Optics: Journal of the European Optical Society Part B* **9,** 693–711 (1997). doi:10.1088/1355-5111/9/5/005 (Cited on pages 18, 19, 32, 62, 67, and 75.)

[151] Henneberger, K. & Haug, H. Nonlinear optics and transport in laser-excited semiconductors. *Physical Review B* **38,** 9759–9770 (1988). doi:10.1103/PhysRevB.38.9759 (Cited on pages 19 and 32.)

[152] Herzel, F., Henneberger, K. & Vogel, W. The semiconductor laser linewidth: a Green's function approach. *IEEE Journal of Quantum Electronics* **29,** 2891–2897 (1993). doi:10.1109/3.259403 (Cited on pages 19, 32, 33, and 59.)

[153] Mohideen, U., Slusher, R. E., Jahnke, F. & Koch, S. W. Semiconductor Microlaser Linewidths. *Physical Review Letters* **73,** 1785–1788 (1994). doi:10.1103/PhysRevLett.73.1785 (Cited on pages 19, 32, 58, 59, and 60.)

[154] Schäfer, W. & Wegener, M. *Semiconductor Optics and Transport Phenomena* (Springer Berlin Heidelberg, 2002). doi:10.1007/978-3-662-04663-0 (Cited on page 19.)

[155] Haug, H. & Koch, S. W. *Quantum theory of the optical and electronic properties of semiconductors* 4th ed. (World Scientific, 2004). (Cited on pages 19, 25, 26, 27, and 31.)

[156] Jahnke, F. & Koch, S. W. Ultrafast intensity switching and nonthermal carrier effects in semiconductor microcavity lasers. *Applied Physics Letters* **67,** 2278–2280 (1995). doi:10.1063/1.115125 (Cited on pages 19, 32, 95, 98, and 109.)

[157] Korenman, V. Nonequilibrium quantum statistics; Application to the laser. *Annals of Physics* **39,** 72–126 (1966). doi:10.1016/0003-4916(66)90137-0 (Cited on pages 19 and 32.)

[158] Schäfer, W. & Treusch, J. An approach to the nonequilibrium theory of highly excited semiconductors. *Zeitschrift für Physik B Condensed Matter* **63,** 407–426 (1986). doi:10.1007/BF01726189 (Cited on pages 19 and 32.)

[159] Agrawal, G. P. Spectral hole-burning and gain saturation in semiconductor lasers: Strong-signal theory. *Journal of Applied Physics* **63,** 1232–1235 (1988). doi:10.1063/1.339990 (Cited on page 21.)

[160] Gomatam, B. & DeFonzo, A. Theory of hot carrier effects on nonlinear gain in GaAs-GaAlAs lasers and amplifiers. *IEEE Journal of Quantum Electronics* **26,** 1689–1704 (1990). doi:10.1109/3.60884 (Cited on pages 21 and 75.)

[161] Huang, J. & Casperson, L. W. Gain and saturation in semiconductor lasers. *Optical and Quantum Electronics* **25,** 369–390 (1993). doi:10.1007/BF00420579 (Cited on page 21.)

[162] Petermann, K. *Laser Diode Modulation and Noise* (Springer, 1988). doi:10.1007/978-94-009-2907-4 (Cited on page 21.)

[163] Rosencher, E. & Vinter, B. *Optoelectronics* (Cambridge University Press, 2002). doi:https://doi.org/10.1017/CBO9780511754647 (Cited on page 21.)

[164] Bowers, J. E. High speed semiconductor laser design and performance. *Solid-State Electronics. Special Issue-Optoelectronics* **30,** 1–11 (1987). doi:10.1016/0038-1101(87)90023-2 (Cited on pages 21 and 22.)

[165] Agrawal, G. Effect of gain and index nonlinearities on single-mode dynamics in semiconductor lasers. *IEEE Journal of Quantum Electronics* **26,** 1901–1909 (1990). doi:10.1109/3.62109 (Cited on page 21.)

[166] Nelson, R. J. & Sobers, R. G. Minority-carrier lifetimes and internal quantum efficiency of surface-free GaAs. *Journal of Applied Physics* **49,** 6103–6108 (1978). doi:10.1063/1.324530 (Cited on page 21.)

[167] Stern, F. Calculated spectral dependence of gain in excited GaAs. *Journal of Applied Physics* **47,** 5382–5386 (1976). doi:10.1063/1.322565 (Cited on page 21.)

[168] Yamaoka, S. *et al.* Directly modulated membrane lasers with 108 GHz bandwidth on a high-thermal-conductivity silicon carbide substrate. *Nature Photonics* **15,** 28–35 (2021). doi:10.1038/s41566-020-00700-y (Cited on pages 22, 65, 80, 82, 91, and 101.)

[169] Lax, M. Classical Noise. V. Noise in Self-Sustained Oscillators. *Physical Review* **160,** 290–307 (1967). doi:10.1103/PhysRev.160.290 (Cited on page 23.)

[170] Haug, H. & Haken, H. Theory of noise in semiconductor laser emission. *Zeitschrift für Physik A Hadrons and nuclei* **204,** 262–275 (1967). doi:10.1007/BF01326200 (Cited on page 23.)

[171] Henry, C. Theory of the linewidth of semiconductor lasers. *IEEE Journal of Quantum Electronics* **18,** 259–264 (1982). doi:10.1109/JQE.1982.1071522 (Cited on pages 23 and 24.)

[172] Agrawal, G. P. & Gray, G. R. Intensity and phase noise in microcavity surface-emitting semiconductor lasers. *Applied Physics Letters* **59,** 399–401 (1991). doi:10.1063/1.105443 (Cited on page 23.)

[173] Toffano, Z. Investigation of threshold transition in semiconductor lasers. *IEEE Journal of Selected Topics in Quantum Electronics* **3,** 485–490 (1997). doi:10.1109/2944.605698 (Cited on pages 23 and 56.)

[174] Shah, J. Hot electrons and phonons under high intensity photoexcitation of semiconductors. *Solid-State Electronics* **21,** 43–50 (1978). doi:10.1016/0038-1101(78)90113-2 (Cited on pages 24, 73, and 115.)

[175] Göbel, E. O. Ultrafast spectroscopy of semiconductors. in *Festkörperprobleme* **30** (ed. Rössler, U.) 269–294. (Springer, 1990). doi:10.1007/BFb0108292 (Cited on page 25.)

[176] Binder, R. *et al.* Carrier-carrier scattering and optical dephasing in highly excited semiconductors. *Physical Review B* **45,** 1107–1115 (1992). doi:10.1103/PhysRevB.45.1107 (Cited on pages 25 and 27.)

[177] Oudar, J. L. *et al.* Femtosecond Orientational Relaxation of Photoexcited Carriers in GaAs. *Physical Review Letters* **53,** 384–387 (1984). doi:10.1103/PhysRevLett.53.384 (Cited on pages 25, 113, and 115.)

[178] Oudar, J. L., Hulin, D., Migus, A., Antonetti, A. & Alexandre, F. Subpicosecond Spectral Hole Burning Due to Nonthermalized Photoexcited Carriers in GaAs. *Physical Review Letters* **55,** 2074–2077 (1985). doi:10.1103/PhysRevLett.55.2074 (Cited on pages 25, 113, and 115.)

[179] Schultheis, L., Honold, A., Kuhl, J., Köhler, K. & Tu, C. W. Optical dephasing of homogeneously broadened two-dimensional exciton transitions in GaAs quantum wells. *Physical Review B* **34,** 9027–9030 (1986). doi:10.1103/PhysRevB.34.9027 (Cited on page 25.)

[180] Schultheis, L., Kuhl, J., Honold, A. & Tu, C. W. Picosecond Phase Coherence and Orientational Relaxation of Excitons in GaAs. *Physical Review Letters* **57,** 1797–1800 (1986). doi:10.1103/PhysRevLett.57.1797 (Cited on page 25.)

[181] Schultheis, L., Kuhl, J., Honold, A. & Tu, C. W. Ultrafast Phase Relaxation of Excitons via Exciton-Exciton and Exciton-Electron Collisions. *Physical Review Letters* **57,** 1635–1638 (1986). doi:10.1103/PhysRevLett.57.1635 (Cited on page 25.)

[182] Becker, P. C. *et al.* Femtosecond Photon Echoes from Band-to-Band Transitions in GaAs. *Physical Review Letters* **61,** 1647–1649 (1988). doi:10.1103/PhysRevLett.61.1647 (Cited on page 25.)

[183] Kuhl, J., Honold, A., Schultheis, L. & Tu, C. W. Optical dephasing and orientational relaxation of wannier-excitons and free carriers in GaAs and GaAs/$Al_xGa_{1-x}As$ quantum wells. in *Festkörperprobleme* **29** (ed. Rössler, U.) 157–181. (Springer, 1989). doi:10.1007/BFb0108011 (Cited on page 25.)

[184] Gurevich, V. L., Muradov, M. I. & Parshin, D. A. On the Theory of Femtosecond Photon Echoes from Band-to-Band Transitions in Semiconductors. *Europhysics Letters (EPL)* **12,** 375–379 (1990). doi:10.1209/0295-5075/12/4/016 (Cited on page 25.)

[185] Snoke, D. W., Rühle, W. W., Lu, Y.-C. & Bauser, E. Evolution of a nonthermal electron energy distribution in GaAs. *Physical Review B* **45,** 10979–10989 (1992). doi:10.1103/PhysRevB.45.10979 (Cited on page 25.)

[186] Kane, M. G., Sun, K. W. & Lyon, S. A. Ultrafast dynamics of non-thermal carriers in GaAs. *Semiconductor Science and Technology* **9,** 697–699 (1994). doi:10.1088/0268-1242/9/5S/079 (Cited on page 25.)

[187] Sun, K. W., Kane, M. G. & Lyon, S. A. Dynamics of Nonthermal-Carrier Distributions in GaAs Generated by Femtosecond Laser Pulses. *Europhysics Letters (EPL)* **26,** 123–128 (1994). doi:10.1209/0295-5075/26/2/008 (Cited on page 25.)

[188] Kane, M. G., Sun, K. W. & Lyon, S. A. Ultrafast carrier-carrier scattering among photoexcited nonequilibrium carriers in GaAs. *Physical Review B* **50,** 7428–7438 (1994). doi:10.1103/PhysRevB.50.7428 (Cited on pages 25, 113, and 115.)

[189] Young, J. F., Gong, T., Fauchet, P. M. & Kelly, P. J. Carrier-carrier scattering rates within nonequilibrium optically injected semiconductor plasmas. *Physical Review B* **50,** 2208–2215 (1994). doi:10.1103/PhysRevB.50.2208 (Cited on page 25.)

[190] Goebel, E. O. & Hildebrand, O. Thermalization of the Electron-Hole Plasma in GaAs. *Physica Status Solidi (b)* **88,** 645–652 (1978). doi:10.1002/pssb.2220880231 (Cited on page 25.)

[191] Knox, W. H. *et al.* Femtosecond Excitation of Nonthermal Carrier Populations in GaAs Quantum Wells. *Physical Review Letters* **56,** 1191–1193 (1986). doi:10.1103/PhysRevLett.56.1191 (Cited on page 25.)

[192] Tsang, J. C. & Kash, J. A. Picosecond spectroscopy of hot anti-Stokes luminescence in GaAs. *Physical Review B* **34,** 6003–6006 (1986). doi:10.1103/PhysRevB.34.6003 (Cited on page 25.)

[193] Schoenlein, R. W., Lin, W. Z., Ippen, E. P. & Fujimoto, J. G. Femtosecond hot-carrier energy relaxation in GaAs. *Applied Physics Letters* **51,** 1442–1444 (1987). doi:10.1063/1.98651 (Cited on page 25.)

[194] Elsaesser, T., Shah, J., Rota, L. & Lugli, P. Initial Thermalization of Photoexcited Carriers in GaAs Studied by Femtosecond Luminescence Spectroscopy. *Physical Review Letters* **66,** 1757–1760 (1991). doi:10.1103/PhysRevLett.66.1757 (Cited on pages 25, 113, and 115.)

[195] Snoke, D. W., Rühle, W. W., Lu, Y.-C. & Bauser, E. Nonthermalized distribution of electrons on picosecond time scale in GaAs. *Physical Review Letters* **68,** 990–993 (1992). doi:10.1103/PhysRevLett.68.990 (Cited on page 25.)

[196] Lifshitz, E. M. & Pitaevskij, L. P. *Physical kinetics* (Pergamon Press, 1981). doi:https://doi.org/10.1016/C2009-0-25523-1 (Cited on page 25.)

[197] Leheny, R. F., Shah, J., Fork, R. L., Shank, C. V. & Migus, A. Dynamics of hot carrier cooling in photo-excited GaAs. *Solid State Communications* **31,** 809–813 (1979). doi:10.1016/0038-1098(79)90393-4 (Cited on pages 25, 73, and 78.)

[198] Rosenwaks, Y. *et al.* Hot-carrier cooling in GaAs: Quantum wells versus bulk. *Physical Review B* **48,** 14675–14678 (1993). doi:10.1103/PhysRevB.48.14675 (Cited on page 25.)

[199] Prabhu, S. S., Vengurlekar, A. S., Roy, S. K. & Shah, J. Nonequilibrium dynamics of hot carriers and hot phonons in CdSe and GaAs. *Physical Review B* **51,** 14233–14246 (1995). doi:10.1103/PhysRevB.51.14233 (Cited on page 25.)

[200] Pötz, W. & Kocevar, P. Electronic power transfer in pulsed laser excitation of polar semiconductors. *Physical Review B* **28,** 7040–7047 (1983). doi:10.1103/PhysRevB.28.7040 (Cited on page 25.)

[201] Riddoch, F. A. & Ridley, B. K. On the scattering of electrons by polar optical phonons in quasi-2D quantum wells. *Journal of Physics C: Solid State Physics* **16,** 6971–6982 (1983). doi:10.1088/0022-3719/16/36/012 (Cited on page 25.)

[202] Leo, K. & Rühle, W. W. Influence of carrier lifetime on the cooling of a hot electron-hole plasma in GaAs. *Solid State Communications* **62,** 659–662 (1987). doi:10.1016/0038-1098(87)90211-0 (Cited on pages 25 and 73.)

[203] Polland, H.-J., Rühle, W. W., Ploog, K. & Tu, C. W. Fröhlich interaction in two-dimensional GaAs/$Al_xGa_{1-x}As$ systems. *Physical Review B* **36,** 7722–7725 (1987). doi:10.1103/PhysRevB.36.7722 (Cited on page 25.)

[204] Leo, K., Rühle, W. W., Queisser, H. J. & Ploog, K. Hot carrier cooling in gaas quantum wells. *Applied Physics A* **45,** 35–39 (1988). doi:10.1007/BF00618761 (Cited on page 25.)

[205] Leo, K., Rühle, W. W., Queisser, H. J. & Ploog, K. Reduced dimensionality of hot-carrier relaxation in GaAs quantum wells. *Physical Review B* **37,** 7121–7124 (1988). doi:10.1103/PhysRevB.37.7121 (Cited on page 25.)

[206] Collet, J. & Amand, T. Model calculation of the laser-semiconductor interaction in subpicosecond regime. *Journal of Physics and Chemistry of Solids* **47,** 153–163 (1986). doi:10.1016/0022-3697(86)90125-3 (Cited on pages 27 and 28.)

[207] Collet, J., Amand, T. & Pugnet, M. Numerical approach to non-equilibrium carrier relaxation in picosecond and subpicosecond physics. *Physics Letters A* **96,** 368–374 (1983). doi:10.1016/0375-9601(83)90012-9 (Cited on page 28.)

[208] Collins, C. L. & Yu, P. Y. Generation of nonequilibrium optical phonons in GaAs and their application in studying intervalley electron-phonon scattering. *Physical Review B* **30,** 4501–4515 (1984). doi:10.1103/PhysRevB.30.4501 (Cited on page 28.)

[209] Kadanoff, L. P. & Baym, G. *Quantum Statistical Mechanics: Green's Function Methods in Equilibrium and Nonequilibrium Problems* 1st ed. (CRC Press, 1962). doi:10.1201/9780429493218 (Cited on page 32.)

[210] Keldysh, L. V. Diagram technique for nonequilibrium processes. *Soviet Physics JETP* **20,** 1018–1026 (1965) (Cited on page 32.)

[211] Reinhart, F. K. A heuristic approach to determine the modifications of electronic and optical properties of "intrinsic" GaAs under free-carrier injection. Part II. *Journal of Applied Physics* **97,** 123535 (2005). doi:10.1063/1.1935746 (Cited on pages 33 and 54.)

[212] Fontcuberta i Morral, A. *et al.* Prismatic Quantum Heterostructures Synthesized on Molecular-Beam Epitaxy GaAs Nanowires. *Small* **4,** 899–903 (2008). doi:10.1002/smll.200701091 (Cited on page 38.)

[213] Hertenberger, S. *et al.* Growth kinetics in position-controlled and catalyst-free InAs nanowire arrays on Si(111) grown by selective area molecular beam epitaxy. *Journal of Applied Physics* **108,** 114316 (2010). doi:10.1063/1.3525610 (Cited on page 38.)

[214] Rudolph, D. *et al.* Spontaneous Alloy Composition Ordering in GaAs-AlGaAs Core–Shell Nanowires. *Nano Letters* **13,** 1522–1527 (2013). doi:10.1021/nl3046816 (Cited on page 38.)

[215] Aspnes, D. E. & Studna, A. A. Dielectric functions and optical parameters of Si, Ge, GaP, GaAs, GaSb, InP, InAs, and InSb from 1.5 to 6.0 eV. *Physical Review B* **27,** 985–1009 (1983). doi:10.1103/PhysRevB.27.985 (Cited on page 38.)

[216] Dobrovinskaya, E. R., Lytvynov, L. A. & Pishchik, V. Properties of Sapphire. in *Sapphire: Material, Manufacturing, Applications* (eds. Pishchik, V., Lytvynov, L. A. & Dobrovinskaya, E. R.) 55–176. (Springer US, 2009). doi:10.1007/978-0-387-85695-7_2 (Cited on page 38.)

[217] Hauer, P., Grand, J., Djorovic, A., Willmott, G. R. & Le Ru, E. C. Spot Size Engineering in Microscope-Based Laser Spectroscopy. *The Journal of Physical Chemistry C* **120,** 21104–21113 (2016). doi:10.1021/acs.jpcc.6b04574 (Cited on page 40.)

[218] Bor, Z. Distortion of Femtosecond Laser Pulses in Lenses and Lens Systems. *Journal of Modern Optics* **35,** 1907–1918 (1988). doi:10.1080/713822325 (Cited on page 40.)

[219] Bor, Z. Distortion of femtosecond laser pulses in lenses. *Optics Letters* **14,** 119–121 (1989). doi:10.1364/OL.14.000119 (Cited on page 40.)

[220] Radzewicz, C., la Grone, M. J. & Krasinski, J. S. Interferometric measurement of femtosecond pulse distortion by lenses. *Optics Communications* **126,** 185–190 (1996). doi:10.1016/0030-4018(96)00060-0 (Cited on page 40.)

[221] Born, M. & Wolf, E. *Principles of optics* 7th ed. (Cambridge University Press, 1999). (Cited on page 40.)

[222] Auston, D. H., McAfee, S., Shank, C. V., Ippen, E. P. & Teschke, O. Picosecond spectroscopy of semiconductors. *Solid-State Electronics* **21,** 147–150 (1978). doi:10.1016/0038-1101(78)90129-6 (Cited on page 44.)

[223] McLean, D. G., Roe, M. G., D'Souza, A. I. & Wigen, P. E. Picosecond recombination of charged carriers in GaAs. *Applied Physics Letters* **48,** 992–993 (1986). doi:10.1063/1.96634 (Cited on page 44.)

[224] Davydova, D., de la Cadena, A., Akimov, D. & Dietzek, B. Transient absorption microscopy: advances in chemical imaging of photoinduced dynamics. *Laser & Photonics Reviews* **10,** 62–81 (2016). doi:10.1002/lpor.201500181 (Cited on page 44.)

[225] Knowles, K. E., Koch, M. D. & Shelton, J. L. Three applications of ultrafast transient absorption spectroscopy of semiconductor thin films: spectroelectrochemistry, microscopy, and identification of thermal contributions. *Journal of Materials Chemistry C* **6,** 11853–11867 (2018). doi:10.1039/C8TC02977F (Cited on page 44.)

[226] Zhu, Y. & Cheng, J.-X. Transient absorption microscopy: Technological innovations and applications in materials science and life science. *The Journal of Chemical Physics* **152,** 020901 (2020). doi:10.1063/1.5129123 (Cited on page 44.)

[227] Klopf, J. *Ultrafast Carrier Dynamics Measured by the Transient Change in the Reflectance of InP and GaAs Film* PhD thesis (Thomas Jefferson National Accelerator Facility (TJNAF), Newport News, 2005) (Cited on page 44.)

[228] Kang, K., Koh, Y. K., Chiritescu, C., Zheng, X. & Cahill, D. G. Two-tint pump-probe measurements using a femtosecond laser oscillator and sharp-edged optical filters. *Review of Scientific Instruments* **79,** 114901 (2008). doi:10.1063/1.3020759 (Cited on page 44.)

[229] Berera, R., van Grondelle, R. & Kennis, J. T. M. Ultrafast transient absorption spectroscopy: principles and application to photosynthetic systems. *Photosynthesis Research* **101,** 105–118 (2009). doi:10.1007/s11120-009-9454-y (Cited on page 44.)

[230] Hartland, G. V. Ultrafast studies of single semiconductor and metal nanostructures through transient absorption microscopy. *Chemical Science* **1,** 303–309 (2010). doi:10.1039/C0SC00243G (Cited on page 44.)

[231] Virgili, T. *et al.* Confocal ultrafast pump–probe spectroscopy: a new technique to explore nanoscale composites. *Nanoscale* **4,** 2219–2226 (2012). doi:10.1039/C2NR11896C (Cited on page 44.)

[232] Grumstrup, E. M., Gabriel, M. M., Cating, E. E., Van Goethem, E. M. & Papanikolas, J. M. Pump–probe microscopy: Visualization and spectroscopy of ultrafast dynamics at the nanoscale. *Chemical Physics* **458,** 30–40 (2015). doi:10.1016/j.chemphys.2015.07.006 (Cited on page 44.)

[233] Landsberg, P. T. Electron Interaction Effects on Recombination Spectra. *Physica Status Solidi B* **15,** 623–626 (1966). doi:10.1002/pssb.19660150223 (Cited on page 49.)

[234] Martin, R. & Stormer, H. On the low energy tail of the electron-hole drop recombination spectrum. *Solid State Communications* **22,** 523–526 (1977). doi:10.1016/0038-1098(77)91406-5 (Cited on page 49.)

[235] Kalt, H. & Rinker, M. Band-gap renormalization in semiconductors with multiple inequivalent valleys. *Physical Review B* **45,** 1139–1154 (1992). doi:10.1103/PhysRevB.45.1139 (Cited on page 49.)

[236] Röder, R. *et al.* Continuous Wave Nanowire Lasing. *Nano Letters* **13,** 3602–3606 (2013). doi:10.1021/nl401355b (Cited on page 51.)

[237] Saxena, D. *et al.* Mode Profiling of Semiconductor Nanowire Lasers. *Nano Letters* **15,** 5342–5348 (2015). doi:10.1021/acs.nanolett.5b01713 (Cited on pages 53 and 56.)

[238] Langrieger, F. *Continuous Wave Lasing of Semiconductor Nanowire Lasers* MSc Thesis (Technical University of Munich, Munich, 2017) (Cited on page 56.)

[239] Grabmaier, A. *et al.* Linewidth enhancement factor and carrier-induced differential index in InGaAs separate confinement multi-quantum-well lasers. *Journal of Applied Physics* **70,** 2467–2469 (1991). doi:10.1063/1.349402 (Cited on pages 56, 101, and 125.)

[240] Michler, P., Lohner, A., Rühle, W. W. & Reiner, G. Transient pulse response of $In_{0.2}Ga_{0.8}As$/GaAs microcavity lasers. *Applied Physics Letters* **66,** 1599–1601 (1995). doi:10.1063/1.113864 (Cited on pages 56, 75, 101, and 125.)

[241] Michler, P. *et al.* Emission dynamics of $In_{0.2}Ga_{0.8}As$/GaAs λ and 2λ microcavity lasers. *Applied Physics Letters* **68,** 156–158 (1996). doi:10.1063/1.116132 (Cited on pages 56, 75, 101, and 125.)

[242] Ongstad, A. P., Dente, G. C. & Tilton, M. L. Carrier heating and the power independent linewidth in semiconductor lasers. *Journal of Applied Physics* **82,** 84–88 (1997). doi:10.1063/1.365852 (Cited on pages 56 and 60.)

[243] Chang, R. K. & Campillo, A. J. *Optical Processes in Microcavities* 3. (World Scientific, 1996). doi:10.1142/2828 (Cited on page 58.)

[244] Hamel, W. A. & Woerdman, J. P. Observation of enhanced fundamental linewidth of a laser due to nonorthogonality of its longitudinal eigenmodes. *Physical Review Letters* **64,** 1506–1509 (1990). doi:10.1103/PhysRevLett.64.1506 (Cited on page 59.)

[245] Van Exter, M. P., Kuppens, S. J. M. & Woerdman, J. P. Theory for the linewidth of a bad-cavity laser. *Physical Review A* **51,** 809–816 (1995). doi:10.1103/PhysRevA.51.809 (Cited on page 59.)

[246] Redlich, C. *et al.* Linewidth Rebroadening in Quantum Dot Semiconductor Lasers. *IEEE Journal of Selected Topics in Quantum Electronics* **23,** 1–10 (2017). doi:10.1109/JSTQE.2017.2701555 (Cited on page 59.)

[247] Köster, F. *et al.* Temperature dependent linewidth rebroadening in quantum dot semiconductor lasers. *Journal of Physics D: Applied Physics* **53,** 235106 (2020). doi:10.1088/1361-6463/ab7ca5 (Cited on page 59.)

[248] Morthier, G., Schatz, R. & Kjebon, O. Extended modulation bandwidth of DBR and external cavity lasers by utilizing a cavity resonance for equalization. *IEEE Journal of Quantum Electronics* **36,** 1468–1475 (2000). doi:10.1109/3.892568 (Cited on page 63.)

[249] Takiguchi, M. *et al.* Continuous-wave operation and 10-Gb/s direct modulation of InAsP/InP sub-wavelength nanowire laser on silicon photonic crystal. *APL Photonics* **2,** 046106 (2017). doi:10.1063/1.4977927 (Cited on pages 63 and 65.)

[250] Pompe, G., Rappen, T. & Wegener, M. Transient response of an optically pumped short-cavity semiconductor laser. *Physical Review B* **51,** 7005–7009 (1995). doi:10.1103/PhysRevB.51.7005 (Cited on pages 65 and 75.)

[251] Wang, J. & Schweizer, H. A quantitative comparison of the classical rate-equation model with the carrier heating model on dynamics of the quantum-well laser: the role of carrier energy relaxation, electron-hole interaction, and Auger effect. *IEEE Journal of Quantum Electronics* **33,** 1350–1359 (1997). doi:10.1109/3.605558 (Cited on page 65.)

[252] Hua, B., Motohisa, J., Kobayashi, Y., Hara, S. & Fukui, T. Single GaAs/GaAsP Coaxial Core-Shell Nanowire Lasers. *Nano Letters* **9,** 112–116 (2009). doi:10.1021/nl802636b (Cited on page 69.)

[253] Burgess, T. *et al.* Doping-enhanced radiative efficiency enables lasing in unpassivated GaAs nanowires. *Nature Communications* **7,** 11927 (2016). doi:10.1038/ncomms11927 (Cited on page 69.)

[254] Loudon, R. *The quantum theory of light* 3rd ed. (Oxford University Press, 2000). (Cited on pages 71 and 121.)

[255] Gregersen, N., Suhr, T., Lorke, M. & Mørk, J. Quantum-dot nano-cavity lasers with Purcell-enhanced stimulated emission. *Applied Physics Letters* **100,** 131107 (2012). doi:10.1063/1.3697702 (Cited on pages 72, 82, and 107.)

[256] Romeira, B. & Fiore, A. Purcell Effect in the Stimulated and Spontaneous Emission Rates of Nanoscale Semiconductor Lasers. *IEEE Journal of Quantum Electronics* **54,** 1–12 (2018). doi:10.1109/JQE.2018.2802464 (Cited on pages 72, 82, and 107.)

[257] Shah, J. & Leite, R. C. C. Radiative Recombination from Photoexcited Hot Carriers in GaAs. *Physical Review Letters* **22,** 1304–1307 (1969). doi:10.1103/PhysRevLett.22.1304 (Cited on pages 73 and 78.)

[258] Kesler, M. P. & Ippen, E. P. Subpicosecond gain dynamics in GaAlAs laser diodes. *Applied Physics Letters* **51,** 1765–1767 (1987). doi:10.1063/1.98515 (Cited on page 75.)

[259] Stix, M. S., Kesler, M. P. & Ippen, E. P. Observations of subpicosecond dynamics in GaAlAs laser diodes. *Applied Physics Letters* **48,** 1722–1724 (1986). doi:10.1063/1.96814 (Cited on page 75.)

[260] Jahnke, F., Schneider, H. C. & Koch, S. W. Combined influence of design and carrier scattering on the ultrafast emission dynamics of quantum well microcavity lasers. *Applied Physics Letters* **69,** 1185–1187 (1996). doi:10.1063/1.117405 (Cited on page 75.)

[261] Li, J. & Ning, C. Z. Plasma heating and ultrafast semiconductor laser modulation through a terahertz heating field. *Journal of Applied Physics* **88,** 4933–4940 (2000). doi:10.1063/1.1315613 (Cited on pages 80, 82, 90, 91, 92, 93, 97, and 101.)

[262] Altug, H., Englund, D. & Vučković, J. Ultrafast photonic crystal nanocavity laser. *Nature Physics* **2,** 484–488 (2006). doi:10.1038/nphys343 (Cited on page 82.)

[263] Khurgin, J. B. & Sun, G. Comparative analysis of spasers, vertical-cavity surface-emitting lasers and surface-plasmon-emitting diodes. *Nature Photonics* **8,** 468–473 (2014). doi:10.1038/nphoton.2014.94 (Cited on page 82.)

[264] Pellegrino, D. *et al.* Mode-field switching of nanolasers. *APL Photonics* **5,** 066109 (2020). doi:10.1063/5.0006767 (Cited on page 82.)

[265] Suhr, T., Gregersen, N., Yvind, K. & Mørk, J. Modulation response of nanoLEDs and nanolasers exploiting Purcell enhanced spontaneous emission. *Optics Express* **18,** 11230–11241 (2010). doi:10.1364/OE.18.011230 (Cited on page 82.)

[266] Ning, C. Z., Indik, R. A. & Moloney, J. V. Self-consistent approach to thermal effects in vertical-cavity surface-emitting lasers. *Journal of the Optical Society of America B* **12,** 1993–2004 (1995). doi:10.1364/JOSAB.12.001993 (Cited on page 82.)

[267] Arnold, G. & Petermann, K. Self-pulsing phenomena in (GaAl) As double-heterostructure injection lasers. *Optical and Quantum Electronics* **10,** 311–322 (1978). doi:10.1007/BF00620119 (Cited on pages 89 and 90.)

[268] Dixon, R. & Joyce, W. A possible model for sustained oscillations (pulsations) in (Al,Ga)As double-heterostructure lasers. *IEEE Journal of Quantum Electronics* **15,** 470–474 (1979). doi:10.1109/JQE.1979.1070024 (Cited on pages 89 and 90.)

[269] Hakki, B. W. Instabilities in output of injection lasers. *Journal of Applied Physics* **50,** 5630–5637 (1979). doi:10.1063/1.326737 (Cited on pages 89 and 90.)

[270] Van der Ziel, J. P., Merz, J. L. & Paoli, T. L. Study of intensity pulsations in proton-bombarded stripe-geometry double-heterostructure $Al_xGa_{1-x}As$ lasers. *Journal of Applied Physics* **50,** 4620–4637 (1979). doi:10.1063/1.326572 (Cited on pages 89 and 90.)

[271] Henry, C. H. Theory of defect-induced pulsations in semiconductor injection lasers. *Journal of Applied Physics* **51,** 3051–3061 (1980). doi:10.1063/1.328092 (Cited on pages 89 and 90.)

[272] Van der Ziel, J. Self-focusing effects in pulsating $Al_xGa_{1-x}As$ double-heterostructure lasers. *IEEE Journal of Quantum Electronics* **17,** 60–68 (1981). doi:10.1109/JQE.1981.1070631 (Cited on pages 89 and 90.)

[273] Ning, C. Z., Hughes, S. & Citrin, D. S. Ultrafast modulation of semiconductor lasers through a terahertz field. *Applied Physics Letters* **75,** 442–444 (1999). doi:10.1063/1.124402 (Cited on pages 90, 91, 92, and 93.)

[274] Shah, J. Ultrafast luminescence spectroscopy using sum frequency generation. *IEEE Journal of Quantum Electronics* **24,** 276–288 (1988). doi:10.1109/3.124 (Cited on page 92.)

[275] Puthussery, J., Lan, A., Kosel, T. H. & Kuno, M. Band-Filling of Solution-Synthesized CdS Nanowires. *ACS Nano* **2,** 357–367 (2008). doi:10.1021/nn700270a (Cited on page 92.)

[276] Yang, C., Chih-Ta, C., Hung-Ying, C., Gwo, S. & Kung-Hsuan, L. Ultrafast carrier dynamics in GaN nanorods. *Applied Physics Letters* **105,** 212105 (2014). doi:10.1063/1.4902927 (Cited on page 92.)

[277] Buschlinger, R., Lorke, M. & Peschel, U. Coupled-Mode Theory for Semiconductor Nanowires. *Physical Review Applied* **7,** 034028 (2017). doi:10.1103/PhysRevApplied.7.034028 (Cited on pages 95, 96, and 98.)

[278] Hess, K., Vojak, B. A., Holonyak, N., Chin, R. & Dapkus, P. D. Temperature dependence of threshold current for a quantum-well heterostructure laser. *Solid-State Electronics* **23,** 585–589 (1980). doi:10.1016/0038-1101(80)90040-4 (Cited on page 102.)

[279] Arakawa, Y. & Sakaki, H. Multidimensional quantum well laser and temperature dependence of its threshold current. *Applied Physics Letters* **40,** 939–941 (1982). doi:10.1063/1.92959 (Cited on page 102.)

[280] Tiesinga, E., Mohr, P. J., Newell, D. B. & Taylor, B. N. CODATA recommended values of the fundamental physical constants: 2018. *Reviews of Modern Physics* **93,** 025010 (2021). doi:10.1103/RevModPhys.93.025010 (Cited on page 103.)

[281] Samara, G. A. Temperature and pressure dependences of the dielectric constants of semiconductors. *Physical Review B* **27,** 3494–3505 (1983). doi:10.1103/PhysRevB.27.3494 (Cited on page 103.)

Publications and conference contributions

Peer-reviewed journal articles

1. **A. Thurn**, J. Bissinger, S. Meinecke, P. Schmiedeke, S. S. Oh, W. W. Chow, K. Lüdge, G. Koblmüller, and J. J. Finley. Self-induced ultrafast electron-hole plasma temperature oscillations in nanowire lasers. *arXiv:2108.11784* (2021) (**under peer review at Nature Communications**).

2. P. Schmiedeke, **A. Thurn**, S. Matich, M. Döblinger, J. J. Finley, and G. Koblmüller. Low-threshold strain-compensated InGaAs/(In,Al)GaAs multi-quantum well nanowire lasers emitting near 1.3 µm at room temperature. *Applied Physics Letters* **118,** 221103 (2021) (**Editor's Pick**)

3. T. Stettner, **A. Thurn**, M. Döblinger, M. O. Hill, J. Bissinger, P. Schmiedeke, S. Matich, T. Kostenbader, D. Ruhstorfer, H. Riedl, M. Kaniber, L. J. Lauhon, J. J. Finley, and G. Koblmüller. Tuning Lasing Emission toward Long Wavelengths in GaAs-(In,Al)GaAs Core-Multishell Nanowires. *Nano letters* **18,** 6292–6300 (2018)

Conference contributions

1. Talk (**best student paper award, honorable mention**), Self-induced ultrafast electron-hole plasma temperature oscillations in GaAs-based nanowire lasers, *Compound Semiconductor Week*, June 2022, Ann Arbor, USA

2. Talk, Self-induced ultrafast electron-hole plasma temperature oscillations in nanowire lasers, *Nanowire Week 2022*, April 2022, Chamonix, France

3. Talk (**invited**), Self-induced ultrafast electron-hole plasma temperature oscillations in nanowire lasers, *Photonics West*, January 2022, San Francisco, USA

4. Talk (**SIOE merit award for oral presentations**), Ultrafast non-equilibrium dynamics in GaAs-based nanowire lasers, *Semiconductor and Integrated Opto-Electronics (SIOE) Conference*, March 2021, Cardiff, United Kingdom

5. Poster, Dynamics of GaAs-based Nanowire Lasers - Experiments and Comprehensive Modeling, *11th International Conference on Quantum Dots*, December 2020, Munich, Germany

6. Talk, Ultrafast Dynamics of Ga(In)As-Al(Ga)As based Nanowire Lasers. *Photonics West*, February 2020, San Francisco, USA.

7. Poster, Dynamics of GaAs-based Nanowire Lasers – Experiments and Comprehensive Modeling. *21st International Winterschool on New Developments in Solid State Physics*, February 2020, Mauterndorf, Austria

8. Poster, Long Term Phase Locking of Pulse Pairs Emitted by Individual GaAs-based Nanowire Lasers. *TUM-IAS Focus Workshop, Hot Carrier Dynamics in Advanced Concept Solar Cells*, Oktober 2019, Munich, Germany

9. Poster, Nanowire Lasers for Information Technologies. *Conference of the Nanoinitiative Munich*, September 2018, Tutzing, Germany

10. Poster, Long Term Phase Locking of Pulse Pairs Emitted by Individual GaAs-based Nanowire Lasers on Silicon. *20th International Winterschool on New Developments in Solid State Physics*, February 2018, Mauterndorf, Austria

11. Poster, Long Term Phase Locking of Pulse Pairs Emitted by Individual GaAs-based Nanowire Lasers on Silicon. *34th International Conference on the Physics of Semiconductors (ICPS)*, July 2018, Montpellier, France

Acknowledgements

During my PhD, I had the opportunity to work with many great people without whose support this work would not have been possible. For this, I would like to thank:

- **Prof. Jonathan J. Finley** for giving me the opportunity to do my PhD in your group and for being a great supervisor. I very much appreciate your enthusiasm for new results, your sense of humour and that you always had an open door for scientific discussions despite your busy schedule. Thank you for your support and giving me the creative freedom to explore the ideas I was curious about.
- **PD Dr. Gregor Koblmüller** for creating a great atmosphere in his research group and for being a great mentor. I highly appreciate the time and effort you devote to support the growth and fabrication of our samples. Without this, the results in this thesis would not have been possible.
- **Prof. Kai Müller** for the great time at conferences and especially for supporting me in my future endeavors while on holidays.
- **Jochen Bissinger** for being the mastermind of our numerical simulations. I would say the only thing even more impressive than your talent for theory is that you did not despair in the face of my silly puns.
- **Paul Schmiedeke** for being the best co-developer of our awesome data analysis script and also a great scientific discussion partner. After each of our countless and endless discussions we had a better understanding of the physical problem - regardless of the specific topic.
- **Stefan Meinecke**, **Kathy Lüdge**, **Sang Soon Oh** and **Weng W. Chow** for being great collaborators and for their valuable scientific insights.
- **Jakob Wierzbowski** and **Lukas Hanschke** for teaching me your experimental skills in the optics lab, lending me your optical equipment and being awesome lab colleagues.
- **Fabio Del Giudice**, **Sergej Fust**, **Tobias Schreitmüller**, **Daniel Ruhstorfer**, **David Busse**, **Jona Zöllner**, **Steffen Meder**, **Jonathan Becker**, **Hyowon Jeong** and **Akhil Ajay** for really being a remarkable bunch of characters that

created a great working environment in the group. Thank you for all the fun moments we shared, either in the lab, on conferences, or in bars.

- **Philipp Moser** and **Ade Ziegltrum**. It was a pleasure sharing an office with both of you. Philipp, I will certainly not forget your fishing skills. Thank you Ade for helping me countless times with fixing optical table legs, broken laser coolers and much more. At this point I would also like to thank **Johannes Seitz**, **Nick Schröder**, **Linda Mora**, **Claudia Paulus**, **Leon Arnold** and **Hubert Riedl** for taking care of all technical aspects in the institute.
- **Irmgard Neuner**, **Martina Schmidt** and **Daniela Huber** for their administrative support.
- **William Rauhaus**, **Julian Klein** and **Lukas Wolz** for being the best gym buddies I could think of. Whether it was early in the morning or on the weekend, you guys were always there to motivate me.

A big thank you also goes to all the other group members I had the pleasure of getting to know and who have helped me over the years in many ways: **Marko Petrić**, **Bianca Scaparra**, **Lucio Zugliani**, **Matteo Barbone**, **Viviana Villafane**, **Rasmus Flaschmann**, **Stefan Strohhauer**, **Malte Kremser**, **Katarina Boos**, **Friedrich Sbresny**, **Riccardo Silvioli**, **Michele Bissolo**, **Marco Dembecki** and **Frederik Bopp**. All of you were always there to help and support, for which I am very grateful.
Lastly and most importantly, I would like to thank my family and friends for their unwavering support.

Statement

With the submission of this thesis I testify that I have written it independently and did not use other sources than the cited references.

Munich, 09.09.2022 Andreas Thurn